

## ABSTRACT

Title of Dissertation: A THERMOMECHANICAL FATIGUE LIFE PREDICTION METHODOLOGY FOR BALL GRID ARRAY COMPONENTS WITH REWORKABLE UNDERFILL

Maxim Serebreni, Doctor of Philosophy, 2019

Dissertation directed by: Professor Patrick McCluskey, Department of Mechanical Engineering

Underfill materials were originally developed to improve the thermo-mechanical reliability of flip-chip devices due to the large coefficient of thermal expansion (CTE) mismatch between the silicon die and substrate. More recently, underfill materials, specifically reworkable underfills, have been used to improve reliability of second level interconnects in ball grid array (BGA) packages in harsh end-use environments such as automotive, military and aerospace. In these environments, electronic components are exposed to mechanical shock, vibration, and large fluctuations in temperatures. Although reworkable underfills improve the reliability of BGA components under mechanical shock and vibration, some reworkable underfills have been shown to reduce reliability during thermal cycling environments.

Consequently, this research employs experimental and numerical approaches to investigate the impact of reworkable underfill materials on thermomechanical fatigue life of solder joints in BGA packages. In the first section of the analysis, material

characterization of a reworkable underfill is performed to determine appropriate material models for reworkable underfills. In the second analysis section, a variety of underfill materials with different properties are exposed to harsh and benign thermal cycles to determine the stress state responsible for reducing fatigue life of solder joints in BGA packages. In the final analysis section, simulations are performed on the BGAs with reworkable underfill to develop a fatigue life predication methodology that implements a modified mode separation scheme. The model developed in this work provides a working fatigue life approach for BGA packages with reworkable underfills exposed to thermal loading. The results of this study can be utilized by the automotive, military, and aerospace industries to optimize underfill material selection process and provide reliability assessment of BGA components in real world environments.

A THERMOMECHANICAL FATIGUE LIFE PREDICTION METHODOLOGY  
FOR BALL GRID ARRAY COMPONENTS WITH REWORKABLE  
UNDERFILL

by

Maxim Serebreni

Dissertation submitted to the Faculty of the Graduate School of the  
University of Maryland, College Park, in partial fulfillment  
of the requirements for the degree of  
Doctor of Philosophy  
2019

Advisory Committee:  
Professor Patrick McCluskey, Chair  
Professor Abhijit Dasgupta  
Professor Bongtae Han  
Professor Hugh Bruck  
Professor Mohamad Al-Sheikhly

© Copyright by  
Maxim Serebreni  
2019

## Dedication

To Izzy, my family, and friends for their encouragement and support throughout this journey.

## Acknowledgements

I would like to thank my advisor professor Patrick McCluskey for his unwavering support and mentorship throughout my graduate studies. I would also like to thank my committee members professors Abhijit Dasgupta, Bongtae Han, Hugh Bruck and Mohamad Al-Sheikhly for their time and effort in supporting and providing guidance on my research.

I would like to thank the CALCE staff and graduate students for providing state-of-the-art research facilities and collegial working environment. A special thanks goes to the members of the McCluskey research group: Subramani Manoharan, Erick Gutierrez, Yonatan Saadon, Zhaoxi Yao, He Yun and Jennifa Li. I would also like to thank Deng Chen and Luis Santos for their fruitful discussions.

Lastly, I would like to thank Dr. Craig Hillman, CEO of DfR Solutions, for supporting my dissertation research and without whom this research would not be possible. I would like to say special thanks to my professional mentors Dr. Nathan Blattau and Dr. Gil Sharon, also of DfR Solutions, for sharing their tremendous expertise and industry experience.

# Table of Contents

Dedication .....	ii
Acknowledgements .....	iii
Table of Contents .....	iv
List of Figures .....	vi
List of Tables .....	x
<b>INTRODUCTION</b> .....	1
1.1 Thermo-mechanical Fatigue in Solder Interconnects .....	1
1.2 Application of underfill in ball grid array packages .....	5
1.2.1 Improvement Under Mechanical Loading .....	9
1.2.2 Thermal Fatigue of Underfilled Components .....	10
1.2.3 Problem Statement and Motivation .....	15
1.2.4 Scope of Dissertation .....	16
<b>LITERATURE REVIEW</b> .....	17
2.1 Influence of loading condition on fatigue life of solder alloys .....	17
2.1.1 Effect of Multiaxial Cyclic Loading on Pb-free Solder Alloys .....	18
2.1.1.2 Fatigue Behavior of Joint Scale Solder .....	22
2.1.2 Effect of Thermomechanical loading on solder joints in BGA Packages ..	24
2.1.2.1 BGAs without Underfill .....	25
2.1.2.2 BGAs with Underfill .....	29
2.3 Empirical trends in thermal fatigue life of ball grid array packages with underfill .....	32
2.3.1 Thermal Fatigue of 1st level solder joints in Flip-Chip Packages .....	32
2.3.2 2nd level solder joints in BGA packages .....	35
2.4 Review of Existing Fatigue Life Prediction Methods .....	44
2.4.1 Empirical and Analytical Models .....	44
<b>MATERIAL CHARACTERIZATION</b> .....	51
3.1 Underfill Material Selection .....	51
3.2 Inelastic characterizations of a reworkable underfill .....	57
3.2.1 Temperature Dependent Elastic Properties .....	57
3.2.2 Plastic deformation .....	65
3.2.3 Creep Deformation of Reworkable Underfill .....	68
3.3 BGA Package Material Characterization .....	72
3.4 Pb-free Solder Alloy .....	76
<b>THERMAL CYCLING OF UNDERFILLED BALL GRID ARRAY COMPONENTS</b> .....	80
4.1 Thermal fatigue of BGAs with high expansion materials .....	80
4.1.1 Experimental procedure .....	80
4.1.2 Experimental results .....	84
4.1.3 Failure analysis .....	88
4.2 Thermal cycling of BGAs with underfill under mean temperature conditions	92
4.2.1 Experimental procedure .....	92
4.2.2 Test vehicles Assembly .....	93
4.2.3 Experimental results .....	96

4.2.4 Failure analysis .....	98
4.3 Thermal cycling of BGAs with reworkable underfill .....	104
4.3.1 Experimental procedure .....	105
4.3.2 Experimental results.....	107
4.3.3 Failure Analysis .....	110
<b>FINITE ELEMENT MODELING AND FATIGUE LIFE PREDICTION</b>	
<b>MODEL DEVELOPMENT</b> .....	113
5.1 Finite Element Modeling .....	113
5.1.1 Thermal mechanical simulations .....	114
5.1.2 Mesh Convergence Study .....	121
5.2 Stress State in BGA Solder Joints.....	122
5.2.1 Effect of Underfill Properties on Energy Density.....	122
5.2.2 Interaction of Underfill and Solder .....	136
5.3 Fatigue Life Prediction of BGA with Underfill.....	140
5.3.1 Fatigue Life Prediction of Existing Models.....	140
<b>SUMMARY, CONTRIBUTIONS AND FUTURE WORK</b> .....	153
6.1 Summary .....	153
6.2 Contributions.....	156
6.3 Future Work .....	158
<b>APPENDIX</b> .....	160



## List of Figures

Figure 1- 1: CTE mismatch in electronic assemblies at elevated temperatures. ....	2
Figure 1- 2: Fatigue cracks in solder joints of 2512 chip resistors after thermal cycling from -40°C to 125°C [4].....	3
Figure 1- 3: Trends in electronic package evolution driven by increase I/O density, miniaturization and functionality [5]. ....	4
Figure 1- 4: Illustration of Flip-Chip package with board level underfill. ....	6
Figure 1- 5: Underfill application methods on BGA package. ....	7
Figure 1- 6: Conformal Coating as underfill in BGA package in Nexus S mobile phone.....	8
Figure 1- 7: Cross-section of flip chip device in Nexus S mobile phone illustrating first level underfill and second level underfill with conformal coating.....	9
Figure 1- 8: Dominant loading mode in BGA with and without underfill. ....	11
Figure 2- 1: Relationship between ratcheting and the number of cycles: (a) $\Delta\gamma/2 = 0.692\%$ , different axial stress; (b) $\Delta\gamma/2 = 1.732\%$ , different axial stress; (c) $\sigma = 2$ MPa, different shear strains and (d) $\sigma = 8$ MPa, different shear strains [32]. ....	19
Figure 2- 2: Axial tension creep deformation at 1.5 and 3ksi during shear monotonic shear test [36].....	21
Figure 2- 3: Shear strain vs. stress with axial stress of 0, 1.5, 3.0 ksi at a shear strain rate of $1.3 \times 10^{-4}$ S-1 for SAC387 [36] .....	22
Figure 2- 4: Anand model vs. experimental results at temperature of 90C with 225 second dwell with peak force of 90N [35].....	23
Figure 2- 5: Fatigue life versus displacement range for Sn3.5Ag0.75Cu by 50% load drop [38].....	24
Figure 2- 6: Anand model vs. experimental results at temperature of 90C with 225 second dwell with peak force of 90N [35].....	26
Figure 2- 7: Experimental shear strain-stress hysteresis loops for each thermal cycling condition [44].....	27
Figure 2- 8: Effect of BGA ball geometry and chip size on fatigue life of SnPb eutectic solder balls [47]. ....	28
Figure 2- 9: Characteristic thermal cycling life cycle number depends on the package design. [48] .....	29
Figure 2- 10: Strain components of the nodal point in the chip edge solder ball with the maximum equivalent plastic strain [49].....	30
Figure 2- 11: Average normal and shear strain for three flip-chip solder bumps with underfills [25].....	31
Figure 2- 12: Fatigue life multiplier as function of CTE for flip-chip package taken from Table 2.....	33
Figure 2- 13: Various flip-chip package types subjected to thermal cycling [53].....	34
Figure 2- 14: Fatigue life multiplier as function of underfill CTE for BGA packages. ....	43
Figure 2- 15: Several 2-D and 3-D FEA models of a PBGA package [74].....	48
Figure 3- 1: CTE and maximum operation temperature of commercial underfills and molding compounds [89]. ....	52
Figure 3- 2: Conformal coating materials poured and cured for testing.....	55

Figure 3- 3: Cured bulk specimen of Henkel 3808 for creep and plasticity testing. ..	56
Figure 3- 4: Stainless steel mold block for underfill sample preparation .....	56
Figure 3- 5: Final shape of Henkel 3808 underfill samples for characterization.....	57
Figure 3- 6: Principles of DMA [91] .....	58
Figure 3- 7: Volumetric expansivity with temperature for polymers [92].....	59
Figure 3- 8: CTE measurements using TMA (left) and modulus measurements using DMA (right).....	60
Figure 3- 9: Temperature dependent elastic modulus of group A conformal coating materials.....	61
Figure 3- 10: Strain vs. temperature of group A conformal coating materials. ....	62
Figure 3- 11: Temperature dependent CTE and modulus of group B .....	63
Figure 3- 12: Temperature dependent CTE and modulus of group C reworkable underfills. ....	64
Figure 3- 13: Sample of Henkel 3808 under monotonic tensile loading. ....	66
Figure 3- 14: Stress-strain curves of Loctite 3808 at strain rate of $10^{-3}$ and various temperatures.....	67
Figure 3- 15: Stress-strain curves of Loctite3808 underfill at 20 and 60°C at three strain rates. ....	<b>Error! Bookmark not defined.</b>
Figure 3- 16: DMA Q800 (left) with Henkel 3808 underfill sample loaded in tensile fixture (right).....	68
Figure 3- 17: Creep deformation of Loctite 3808 underfill. ....	69
Figure 3- 18: Steady state creep behavior of Loctite 3808 underfill. ....	70
Figure 3- 19: Steady state creep strain rate vs. $1/T(K)$ . ....	70
Figure 3- 20: BGA package deconstruction process using serial grinding steps.....	72
Figure 3- 21: PCB sample tested with DMA Three-point bending fixture.....	73
Figure 3- 22: Temperature dependent elastic modulus and CTE for BGA mold compound.....	74
Figure 3- 23: Measurement of package Effective CTE using TMA.....	75
Figure 3- 24: Comparison between measured and calculated effective BGA package CTE.....	76
Figure 3- 25: Curve fitting of SAC creep data to hyperbolic sine model Eq. 2 based on 108 data points from own measurements and literature [103].....	78
Figure 3- 26: Thermal stress simulations of 96.5Sn3.5Ag solder incorporating progressively more complex constitutive relations [104].....	79
Figure 4- 1: Underfilling of BGAs with conformal coating using pneumatic syringe. .....	81
Figure 4- 2: Assembled test vehicle showing two halves of the board with one side applied with Thick conformal coating. ....	82
Figure 4- 3: Test board placed inside Sun thermal chamber with thermocouples.....	83
Figure 4- 4: Temperature profile measured from four thermocouples places throughout the chamber. ....	83
Figure 4- 5: Weibull distribution of Silicone and acrylic Thick conformal coating at the two thermal profiles. ....	85
Figure 4- 6: Weibull distribution of urethane and epoxy Thick and Spray conformal coating tested at -55°C to 125°C.....	87

Figure 4- 7: Cross-section along DNP for control BGA with no conformal coating tested at -55°C to 125°C. ....	88
Figure 4- 8: Failure of SAC305 BGA with acrylic coated using a) standard spray and b) Thick application from -55°C to 125°C. ....	89
Figure 4- 9: Cross-section and X-ray image of BGAC with SAC305 solder with Thick application of Acrylic 1B31 from -55°C to 125°C.....	91
Figure 4- 10: Cross-section of BGA with Thick acrylic coating (left) and Spray.....	91
Figure 4- 11: Temperature profiles with High and Low mean temperatures. ....	93
Figure 4- 12: MPM Stencil Printer (left), Universal GC-120 Machine (right).....	94
Figure 4- 13: Assembled test board with 20 components.....	95
Figure 4- 14: Hakko FR-1012 preheater with sample test board.....	95
Figure 4- 15: Components underfilled with (a)Silicone 1-2577 (b) EP1238 (c) Loctite 3808 (d) U8437-2.....	96
Figure 4- 16: Thermal cycling results for underfilled BGAs at the two thermal profiles. ....	97
Figure 4- 17: Cross-section of single-sided control BGA after 4000 thermal cycles at High Mean thermal profile.....	99
Figure 4- 18: Cross-section of double-sided BGA at High Mean temperature profile after 1862 cycles. ....	100
Figure 4- 19: Cross-section of BGA with UF2 underfill at (a) corner joint (b) 8 <sup>th</sup> joint from the corner with High Mean thermal profile.....	101
Figure 4- 20: Cross-section of two corner joints in BGA with UF1 at High Mean temperature profile (a) bottom interface (b) diagonal cracking.....	102
Figure 4- 21: Cross-section of BGA packages with UF3 at High Mean profile (a) Fifth solder joint from package corner, (b) third solder joint from package corner .	103
Figure 4- 22: Cross-section of underfilled BGA package (a) control (b) UF1 (c) UF3 (d) UF2.....	104
Figure 4- 23: Hot plate preheating test board for underfilling.....	105
Figure 4- 24: Techon Systems 700 series manual underfilling syringe gun.....	106
Figure 4- 25: -55°C to 125°C temperature profile.....	107
Figure 4- 26: Weibull plot of BGAs with five reworkable underfills.....	108
Figure 4- 27: characteristic life vs. $T_g$ for BGAs with reworkable underfill. ....	<b>Error!</b>
<b>Bookmark not defined.</b>	
Figure 4- 28: Cross-section of BGA with Henkel 3808. ....	111
Figure 4- 29: Cross-section of BGA with Namics XSUF1594-6F.....	111
Figure 5- 1: Global quarter symmetric model with tied underfill UF2 (Left) solder joint in package center with coarse mesh (Right).....	114
Figure 5- 2: Displacement boundary conditions for the quarter symmetric BGA model.....	115
Figure 5- 3: Cross-sectional view of underfilled BGA along the distance to neutral axis to the center of the package. ....	117
Figure 5- 4: Various layers in FEA model corresponding to location of crack propagation in solder joint. ....	117
Figure 5- 5: Accumulated creep strain energy density for the various solder joint volumes in control BGA. ....	118
Figure 5- 6: Filler size for group B underfill materials.....	119

Figure 5- 7: FEA models of BGA with underfills including accurate representation of underfill fillet geometry for group B materials. ....	120
Figure 5- 8: Mesh convergence of corner most solder joint in BGA without underfill. ....	122
Figure 5- 9: Dissipated energy density in corner solder as function of underfill CTE and modulus. ....	123
Figure 5- 10: Volume of solder used for energy density partitioning and fatigue prediction. ....	126
Figure 5- 11: Mode I and Mode II energy density for 30 and 60 ppm underfills as function of elastic modulus. ....	126
Figure 5- 12: Energy density Mode I and Mode II components for each 32 $\mu\text{m}$ thick layer in corner joint of BGA package without underfill. ....	128
Figure 5- 13: Energy density Mode I and Mode II components for each 32 $\mu\text{m}$ thick layer in corner joint of BGA package with Loctite 3808 underfill. ....	129
Figure 5- 14: Mode I and Mode II energy densities on the distance to neutral line for BGA with and without Loctite 3808 underfill. ....	130
Figure 5- 15: Average creep strain in corner solder joint for 15 thermal cycles for BGA with Loctite3808 underfill -50°C to 125°C. ....	131
Figure 5- 16:Hydrostatic stress as a function of time for control BGA from -50 to 125°C thermal cycles for 376 elements at the PCB side of the corner solder joint..	133
Figure 5- 17: Average hydrostatic stress for the first three thermal cycle for control BGA and Loctite 3808 from -55°C to 125°C. ....	134
Figure 5- 18: Average mean hydrostatic stress in corner most solder joint for BGA with group B and C underfills at different thermal profiles. ....	135
Figure 5- 19: Boundary conditions for underfill tied to package and solder (left) tied to package and component only (right). ....	137
Figure 5- 20: Von-mises stress distribution in underfill without interaction with solder (left) with interaction with solder (right) and strain energy density in corner solder joint after three thermal cycles. ....	137
Figure 5- 21: Normalized energy density as function of temperature for thermal profiles with mean temperature conditions with Group B underfills. ....	138
Figure 5- 22: Fatigue life predictions for group B underfills at High Mean temperature profile. ....	141
Figure 5- 23: Fatigue life predictions for group B underfills at Low Mean temperature profile. ....	143
Figure 5- 24: Mode I vs. Mode II energy densities for linear elastic underfill materials. ....	144
Figure 5- 25: Characteristic life as function of Mode I and Mode II energy density for group C underfill from -55 to 125°C. ....	145
Figure 5- 26: Fatigue life prediction comparison for group C underfills. ....	146
Figure 5- 27: Process flow of energy density partitioning approach for underfilled BGA. ....	148
Figure 5- 28: Predicted vs. experimental characteristic life for group B and C underfills. ....	149
Figure 5- 29: thermal profile with consideration to underfill shrinkage. ....	150

Figure 5- 30: Accumulated energy density with time for BGA with Loctite3808 underfill using elastic, plastic and creep material behavior. ....	151
Figure 5- 31: Accumulated energy density as function of temperature for BGA with Loctite3808 with elastic, plastic and creep behavior. ....	152

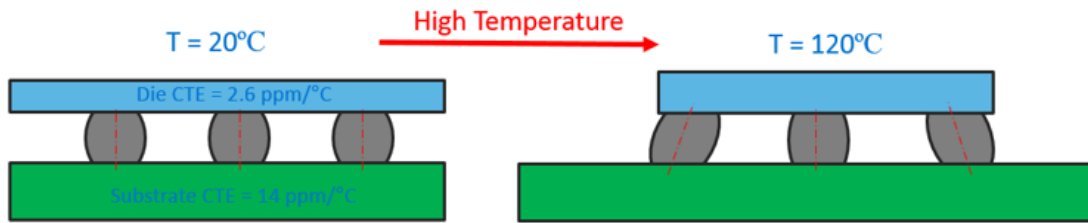
## List of Tables

Table 1- 1: Field Conditions for various industries [2].....	2
Table 2- 1: Torsional (left) and multiaxial (right) fatigue test results for Sn-3.5Ag [33].....	20
Table 2- 2: Published thermal cycling fatigue life of Flip-Chip packages. ....	32
Table 2- 3: Underfill properties and thermal cycling results of CBGAs [54]. ....	35
Table 2- 4: Predicted and measured values of Weibull characteristic life [54]. ....	36
Table 2- 5: Thermal cycle results for corner/edge bonded SAC305 BGAs [55]. ....	37
Table 2- 6: Thermal cycle results for underfilled SAC305 BGAs [55]. ....	37
Table 2- 7: Underfill properties and application method, full underfill, partial underfill [56]. ....	38
Table 2- 8: Thermal cycling results for underfilled BGAs [56]. ....	38
Table 2- 9: Underfill properties and cure time (top), package dimensions (bottom) [57]. ....	39
Table 2- 10: Predicted and measured values of Weibull characteristic life for 280-lead fleXBGA assemblies with and without underfill. [57]. ....	40
Table 2- 11: Underfill material properties used in [58]. ....	41
Table 2- 12: Temperature cycling results after 2525 cycles [58]. ....	42
Table 3- 1: Material properties taken from manufacturer’s data sheets. ....	53
Table 3- 2: Properties of underfills provided by manufacturer data sheets. ....	54
Table 3- 3: Group A Conformal coating material properties.....	61
Table 3- 4: Coefficient for hyperbolic sine model for Loctite 3808.....	71
Table 3- 5: Schubert’s constitutive model coefficients [103]. ....	78
Table 4- 1: Thermal cycling results for Silicone and Acrylic Thick applications at two temperature cycles. ....	86
Table 4- 2: Thermal cycling results for epoxy and urethane Thick and Spray applications at temperature profile 1.....	88
Table 4- 3: Test matrix for thermal cycling of group B underfills. ....	92
Table 4- 4: Characteristic life for thermal cycling experiments of underfilled BGAs at two thermal profiles. ....	98
Table 4- 5: Weibull plot of BGAs with five reworkable group C underfills. ....	109

# INTRODUCTION

## 1.1 Thermo-mechanical Fatigue in Solder Interconnects

Solder materials are the most widely used second level interconnects in electronic packaging. Solder interconnects, often referred to as solder joints, provide the mechanical and electrical connection between electronic packages and printed circuit boards (PCBs). Electronic packages are assembled onto PCBs using a soldering process. This soldering process results in the formation of solder joints, which vary in shape and size, based on package style, stencil thickness, and board pad size. A large percentage of electronic failures are due to thermally induced stresses and strains that are caused by differences in the coefficient of thermal expansion (CTE) mismatch between the components and boards. A study by the United States Air-Force on field failures, related to operating environments, shows that about 55% of the failures are due to high temperatures and temperature cycling, 20% of the failures are attributed to vibration and shock, and finally, 20% are caused by humidity [1]. Under fluctuating temperature conditions, the large CTE mismatch can cause cyclic fatigue failure to occur in solder joints. Due to the geometry of the surface mount component, thermo-mechanical fatigue is induced by the accumulation of shear stress on the solder joints as shown in Figure 1-1. The distance from the center of the package to the solder joint is called the distance to the neutral point (DNP). In general, components with larger DNP will be more affected by CTE mismatch, which means that the farthest joint from the package center will experience the highest shear strains.



**Figure 1- 1: CTE mismatch in electronic assemblies at elevated temperatures.** Some operating service conditions subject components to high temperatures during the dwell time. This allows creep to become the dominant inelastic deformation mechanism. Table 1-1 lists the temperature range experienced during field conditions for several electronic product categories.

**Table 1- 1: Field Conditions for various industries [2].**

	Temp range	Cycles/year	Service time	Failure rate
Consumer	0 to 60 °C	365	1 year	1 %
Computer	15 to 60 °C	1460	5 years	0.1 %
Telecom	-40 to 85 °C	365	7 to 20 years	0.01 %
Aircraft	-55 to 95 °C	365	20 years	0.001 %
Automotive	-55 to 95 °C	100	10 years	0.1 %

Field conditions differ based on device usage and application, even for the same products and components. Specific applications have detailed specifications that define 1) the maximum and minimum temperature range, and 2) the dwell time at each temperature extreme. In some products there are different requirements for each life phase. The difference between field conditions and accelerated thermal cycling will be illustrated in Chapter 2. In situations where the given CTE mismatch is large enough and the temperature range and cyclic frequency are such that solder joints will experience plastic or creep deformation, low cycle fatigue failure can occur as shown in Figure 1-2. In this figure, 2512 chip resistors were assembled on 1.6 mm thick PCB and subjected to accelerated thermal cycling with a temperature range of -40°C to 125°C according to IPC standard 9701A [3]. Often, the accelerated thermal cycling

tests are used to qualify the performance and reliability of surface mount solder attachments of electronic assemblies. During the accelerated thermal cycling tests, creep strain in solder joint is induced due to CTE mismatch between the PCB and the component. For the case illustrated in Figure 1-2, solder joints in chip resistors predominantly experience shear strains due to the rigid alumina component and PCB with a CTE of 7.8 ppm/°C and 17 ppm/°C, respectively.

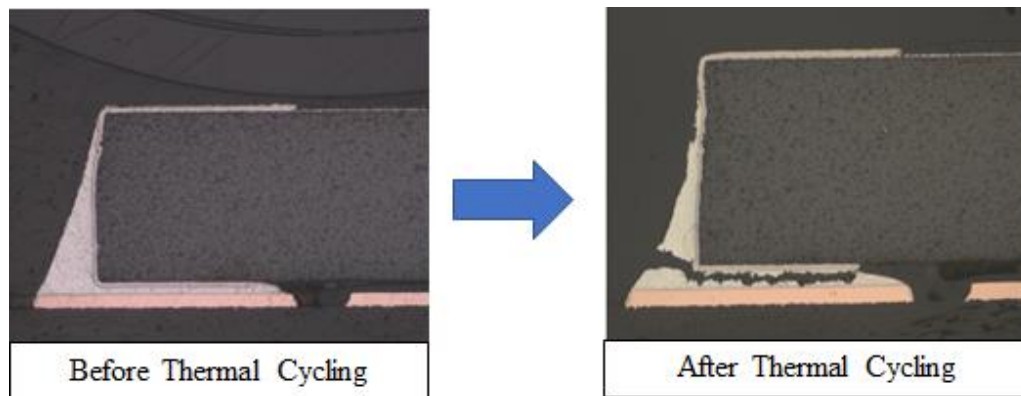


**Figure 1- 2: Fatigue cracks in solder joints of 2512 chip resistors after thermal cycling from -40°C to 125°C [4].**

After a sufficiently long number of cycles, a fatigue crack will nucleate and start to propagate through the solder joint resulting in a mechanical failure of the joint. The interruption in the physical connection of the solder joint disrupts the electrical signal path, which renders the component or device inoperable. Figure 1-3 shows the evolution in electronic packaging trends that are driven by increasing demand for higher I/O, miniaturization and improved functionality. Ball Grid Array (BGA) technology is utilized to meet the ever-growing demands of electronic packages. BGA components use the bottom side of the package to provide an increased foot print for second level solder interconnects in variety of configurations to meet specific application requirements. BGA laminate technology has enabled the use of both flip



chip and wire bonds (1<sup>st</sup> level interconnects) in a small form factor referred to as Chip-Scale Packages (CSPs).

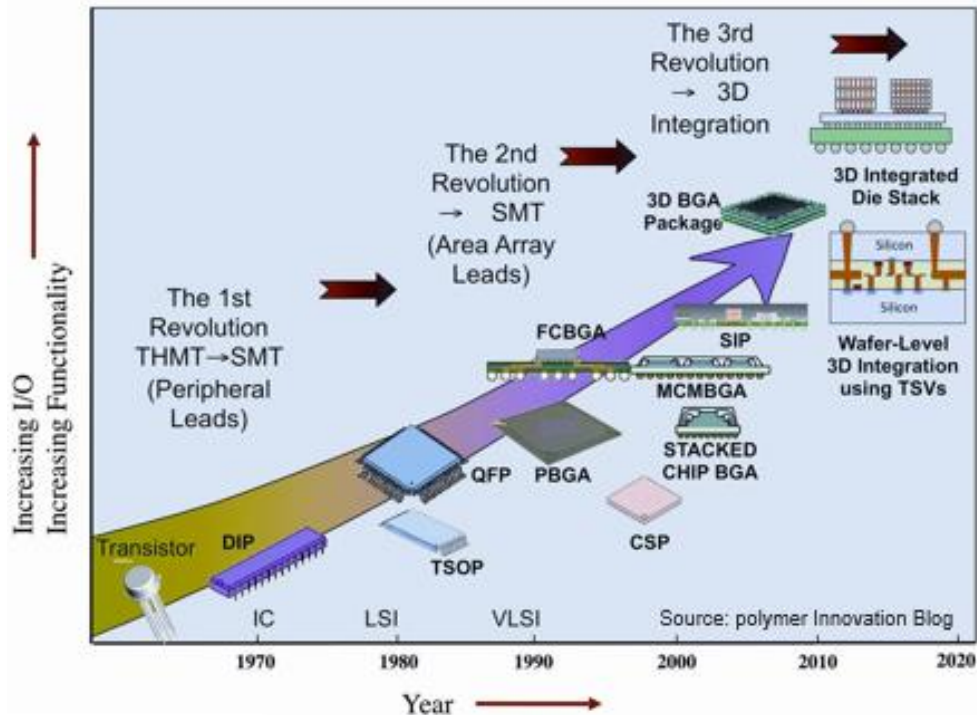


**Figure 1- 3: Trends in electronic package evolution driven by increase I/O density, miniaturization and functionality [5].**

Electronic components are often exposed to large temperature fluctuations in harsh use environments found in the automotive, military, and aerospace. Repeated temperature fluctuations induce cyclic loading in solder interconnects. CTE mismatch is intrinsic to electronic components and assemblies due to the variety of materials used in their construction. The repeated CTE mismatch causes thermally induced mechanical stresses in solder joints that results in fatigue failure of the interconnects. Such advance electronic packages as BGAs are sensitive to thermo-mechanical fatigue failure due to the previously mentioned factors. Fatigue failure is a wear-out phenomenon that depends on the repeatability and magnitude of loading. Predicting the time to failure of solder interconnects requires an understanding of the mechanisms behind low cycle

fatigue failure in solder alloys. The subsequent sections of this chapter discuss fatigue lifetime assessment of BGA components with underfill and the current models used to predict the reliability within certain environments.

## **1.2 Application of underfill in ball grid array packages**

Underfill technology for flip-chip devices has matured since the introduction of Controlled Collapse Chip Connection (C4), also referred to as solder bumps for flip-chip devices by IBM in the 1960's [6]. Underfills were originally developed to enhance the thermal cycling solder fatigue of flip-chip bumps (first-level interconnects). Later, its usage was extended to the BGA (second-level interconnect) due to strong demand for increasing drop-reliability (portable devices). Reworkable underfills were developed to reduce the cost of conventional underfills, but the nature of reworkability (low  $T_g$  and high CTE) causes a detrimental effect on the thermal cycling solder fatigue although drop reliability was not compromised. There is only limited literature that deals with the quantitative effect of the properties of reworkable underfills on BGA thermal cycling solder fatigue. Flip-Chip underfills address thermo-mechanical concerns by distributing the load from thermal expansion mismatch between the silicon die and organic substrate. Manufacturers optimize underfill mechanical properties by adjusting the epoxy resin formulation and increasing silica filler particles volume fraction. Lower expansion, high glass transition temperature ( $T_g$ ), and high elastic modulus, have been reported as the optimal properties for underfills in flip-chip devices [7]. Indeed, research documents how underfills with lower CTE mismatch with the solder alloy provide higher thermo-mechanical reliability for solder bumps [8]. Figure 1-4 demonstrates an overmolded flip-chip package with board level underfill. The

overmold is applied to the flip-chip after underfilling to provide structural integrity and protection. The board level underfill is applied after the package reflow to the board and acts as an adhesive that binds the package to the board. A dramatic size difference in the underfill applied to 1<sup>st</sup> and 2<sup>nd</sup> level solder joint can be seen. This size difference depends on the height of solder joints and solder mask thickness and vary from 50 to 100 $\mu\text{m}$  in solder bumps and 300 to 500 $\mu\text{m}$  for board level solder balls. Pb-free solder alloys for flip-chip bumps usually utilizes binary alloys such as SnAg due to metallization process requirements compared to ternary SnAgCu used for board level reflow process [9].

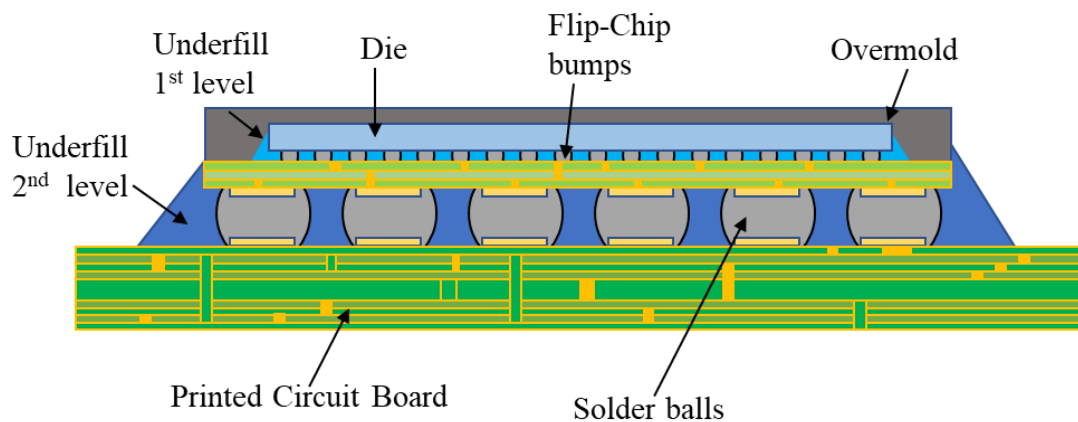


**Figure 1- 4: Illustration of Flip-Chip package with board level underfill.**

Implementing underfill materials for reliability improvement of second level solder joints can be achieved using different application techniques, process parameters, and materials. The first step of underfilling is the application method. Figure 1-5 illustrates the three common methods used to apply underfill to BGA devices. These methods include full area coverage, edge bonding, and corner staking. Each of these methods offers advantages and benefits depending on reliability requirements and process parameters. Corner staking offers the utilization of the least amount of material, thereby

enabling lower production cost, however, it does not provide complete encapsulation of the interconnects against moisture and contamination. Full area underfilling and edge or perimeter bonding are similar in nature. Although edge bonding utilizes the least amount of underfill material, compared to full area application as certain load environments, it might not provide as high of reliability improvement.

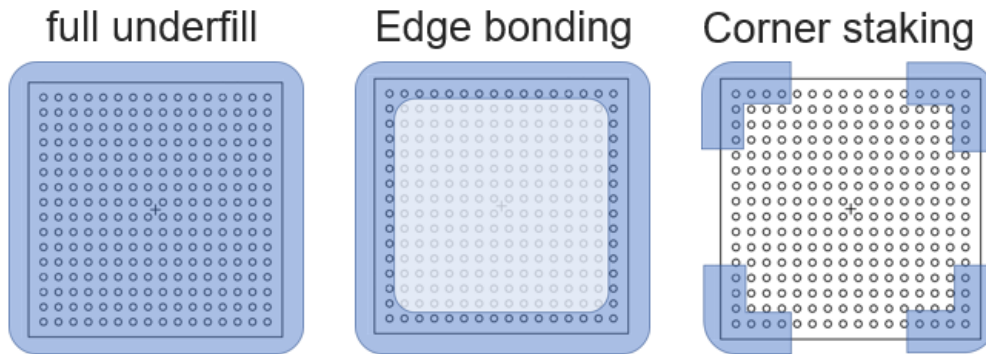


**Figure 1- 5: Underfill application methods on BGA package.**

Underfill material selection is another important parameter that needs to be considered. Adhesion characteristic, cure, and viscosity properties are considered prior to investigating the impact on reliability. The first step of improving reliability is selecting a material that will minimize such process induced defects as delamination and voiding, both of which compromise the effectiveness of underfills [10,11]. When reworkable underfills are considered for board level underfilling the material choices will vary significantly for different application types. Commercial off-the-shelf (COTS) electronics are considered more cost-effective, with material chemistries that offer such high through-put capabilities as UV curable underfills. Conversely, such high reliability industries as automotive and aerospace, consider epoxy-based materials that still offer low expansion characteristics. Figure 1-5 shows conformal coating application on BGA devices in Nexus S mobile phone. In this application, the

conformal coating was applied in a manner that enabled capillary flow underneath the BGA package effectively underfilling the device. In such application, non-conventional underfill materials are used to provide waterproofing and protection from mechanical loads to BGA packages. These non-conventional underfill materials can range from soft silicone resins, polyurethane, acrylics or epoxies. The availability of such a large variety of materials makes reliability assessment under different load environments particularly challenging. Failure of solder bumps in modern flip-chip devices have been reduced due to proper underfill

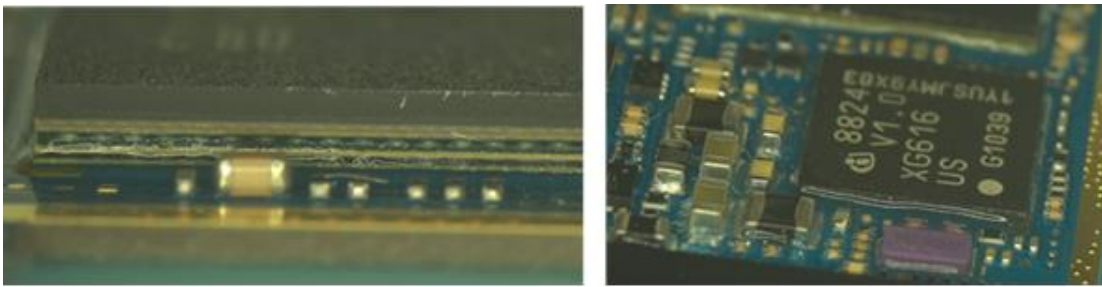


**Figure 1- 6: Conformal Coating as underfill in BGA package in Nexus S mobile phone.**

Material selection, which is also designed to prevent failure of the Low-K dielectric materials and in die passivation [12]. The same effort to study failure modes of flip-chip solder bumps has not been applied to board level underfilling, particularly with non-conventional reworkable underfills for BGA components. As in the previous figure, Figure 1-7 illustrates a cross-section of the same conformally coated BGA package. The cross-section reveals an overmolded flip-chip package with underfill and second level solder balls that have been underfilled with a conformal coating material. This example demonstrates the popularity of non-conventional material chemistries used as underfills in mobile applications. The implementation of these soft, high expansion materials in mobile devices intends to prevent failure due to drop impact,

which accounts for the most common cause of failure in portable electronic products [13].

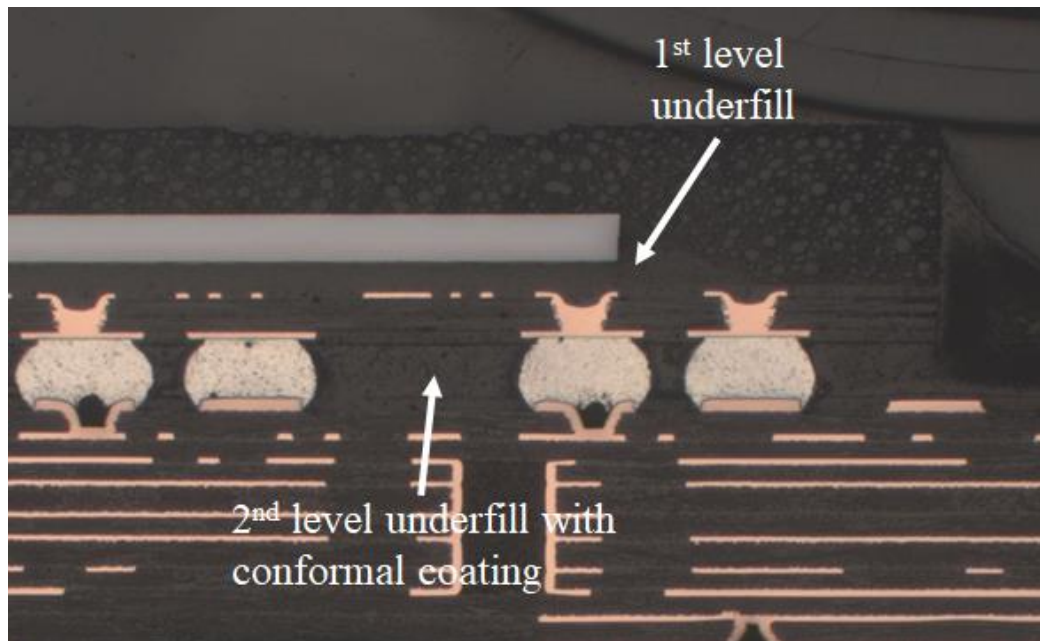


**Figure 1- 7: Cross-section of flip chip device in Nexus S mobile phone illustrating first level underfill and second level underfill with conformal coating.**

### *1.2.1 Improvement Under Mechanical Loading*

One of the common usages for underfills in BGA components is reliability improvements under shock and vibration loading. Mechanical loading, in the form of drop impact or mechanical vibration, results in board bending, which induces mechanical strains in solder joints. Usually, failure of solder joints, due to vibration loading, occurs over a high number of loading reversals that then causes a high cycle fatigue failure. High cycle fatigue failure is characterized by stresses that are in the elastic regime of the load curve, while thermo-mechanical loading result in low cycle fatigue failure that is driven by plastic deformation. Analysis of various underfill materials using monotonic three-point bending found that all underfill types used in their study improve the bending load a BGA package can sustain compared to a non-

underfilled counterpart [9]. Another investigation on the impact of reworkable underfills on thermal cycling and three-point cyclic loading found that all underfills used in the study improved high cycle fatigue loading compared to non-underfilled parts, while some of the reworkable underfills reduced thermal cycle fatigue compared to non-underfilled parts [15]. This finding supports that notion that certain reworkable underfills reduce thermal fatigue life, although no particular attention was given to the specific properties of underfills that are found to reduce thermal fatigue life, nor to the failure mechanism between the two different deformation mechanisms. Similar behavior was found by other studies where reworkable underfill reduced thermal fatigue life and it improved the mechanical loading fatigue of the tested components under flex testing and drop impact [16,17]. Other studies using low expansion underfill materials with CTE of 29.7 ppm/°C found improvement under both random vibration and thermal cycling [18].

### *1.2.2 Thermal Fatigue of Underfilled Components*

Some of the underfill selection guidelines previously mentioned for flip-chip devices can be applied to improve thermal cycling fatigue life. Low CTE and high elastic modulus are the key parameters in underfill selection that improves fatigue life, however, not as much attention has been placed on the glass transition temperature of underfills. Non-conventional and reworkable underfill materials often possess a  $T_g$  that is substantially lower than epoxy based non-reworkable underfills. Low  $T_g$  underfills are used in flip-chip devices to reduce the risk of low-K cracking and also improve thermo-mechanical reliability [19]. The implementation of underfill with similar properties that possess low  $T_g$  have been shown to reduce the board level reliability in

various BGA packages [20,21]. The shift in underfill effectiveness in improving thermal fatigue between 1<sup>st</sup> level and 2<sup>nd</sup> level solder joints is dependent on a multitude of factors that range from underfill properties to package and solder characteristics. Consequently, in this dissertation a particular focus is placed on the influence of reworkable underfill on thermal fatigue life of board level solder joints of BGA components. Figure 1-8 shows the global loading conditions of BGA package with and without underfill. Higher volume of board level underfill can shift the dominant loading condition of the corner most solder joint from predominantly shear to an axial one.

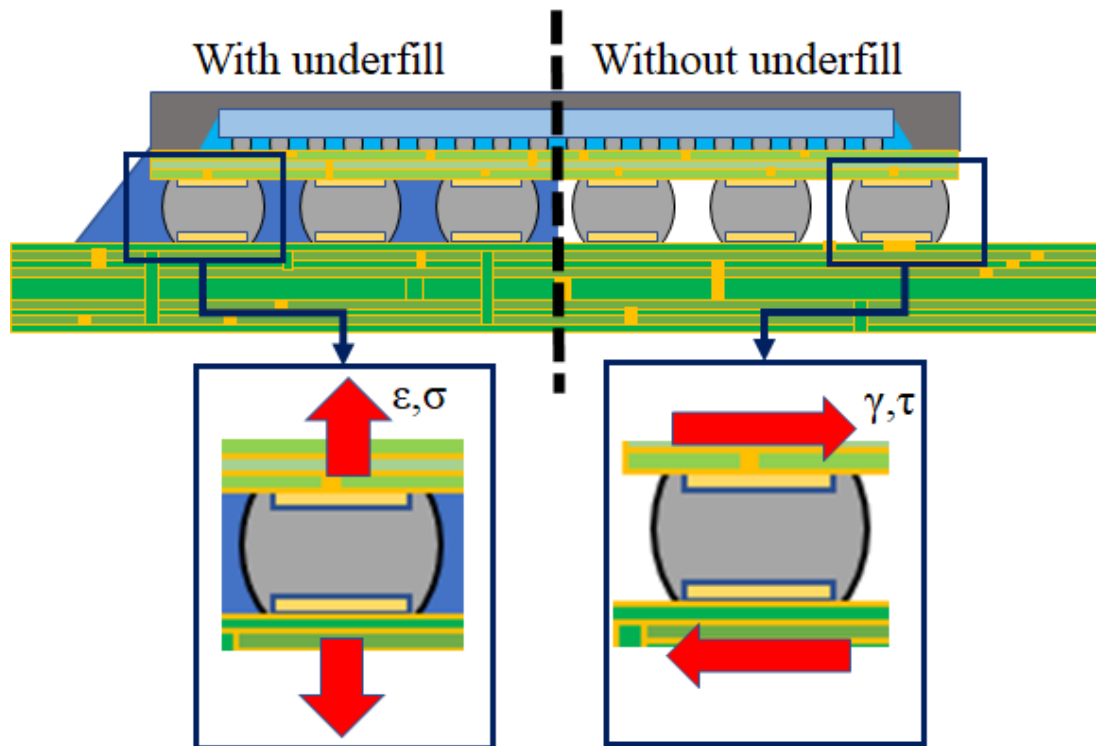


**Figure 1- 8: Dominant loading mode in BGA with and without underfill.**

The idealization of the stress state shown in Figure 1-8 is done for visualization purposes. Actual stress state solder joint experience varies between each solder joint. Some areas of the solder can experience both axial and shear loading throughout the



thermal cycle. The global loading conditions indicated by the red arrows are meant to represent mode I and mode II loading conditions. These two loading modes are illustrated in Figure 1-9 and are two of three ways of applying force to enable fracture. Although these representation is borrowed from linear elastic fracture mechanics, thermal cycling induced crack growth in solder joints is driven by inelastic deformation.

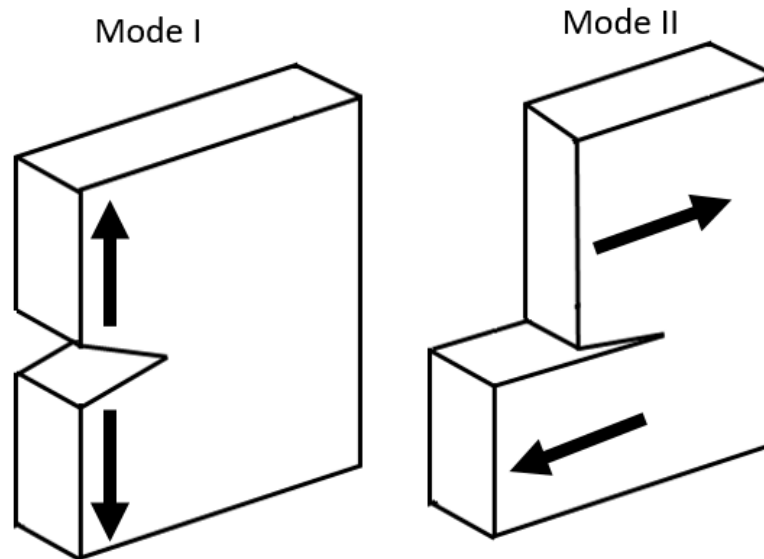


**Figure 1-9: Fracture modes in materials**

Mode I is the tensile stress normal to the plane of the crack while mode II is the sliding shear force parallel to the plane of crack. The third mode of fracture is defined as the tearing mode where the cracked surfaces slide past another. These pure fracture modes rarely occur by themselves in complex geometries. Real structures often experience mixed-mode loading where any of the three modes of fracture can occur simultaneously. Fracture mechanics of solder alloy is not the focus of this research and therefore the two loadings modes discussed here will be later used to classify the stress state in the solder.

One of the reasons to investigate the influence of reworkable underfill materials is to study the failure mechanism of the solder compared to non-underfilled components. Figure 1-10 demonstrates cross-section of a land grid array (LGA) device that was underfilled with an acrylic conformal coating material using heavy spray coating application and subjected to thermal cycling. The cross-section of the conformally coated part demonstrate extruded solder joints. The difference between fatigue cracks in the coated and non-coated LGA components is quite dramatic. Notably, because the acrylic underfill in the LGA device occupies a much narrower gap than available in BGA devices. This is due to stencil printing process that LGA devices are soldered with.

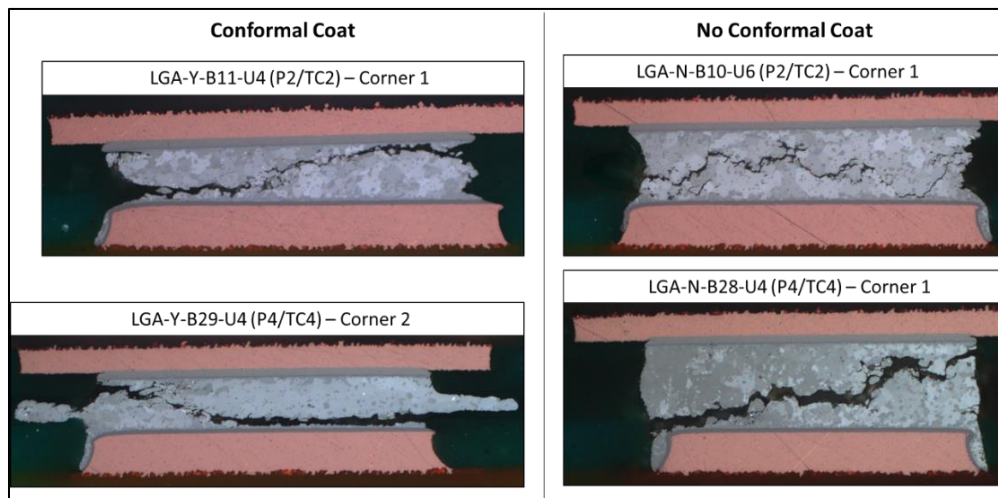


**Figure 1- 10: Cross-section of Land Grid Array (LGA) Failed Component with and without conformal coating [Courtesy of DfR Solutions].**

Results on the effect of various underfill materials on thermal cycling reliability of 23mm flip chip BGA package are shown in Figure 1-11. In this study a variety of materials have been used with  $T_g$  ranging from 45°C to 180°C and CTEs below the  $T_g$  of 29 to 70 ppm/°C [22]. It can be seen that materials with low CTE and high  $T_g$ , which is outside the tested thermal cycle range of -40°C to 125°C slightly improve fatigue

life. This study combined several different underfill application methods as edge bonding, corner fill, and full area underfill. They found that underfill materials that were applied to the full area and resulted in reduce fatigue life compared to non-underfilled parts can result in increasing fatigue life by moving to edge bonding application method.

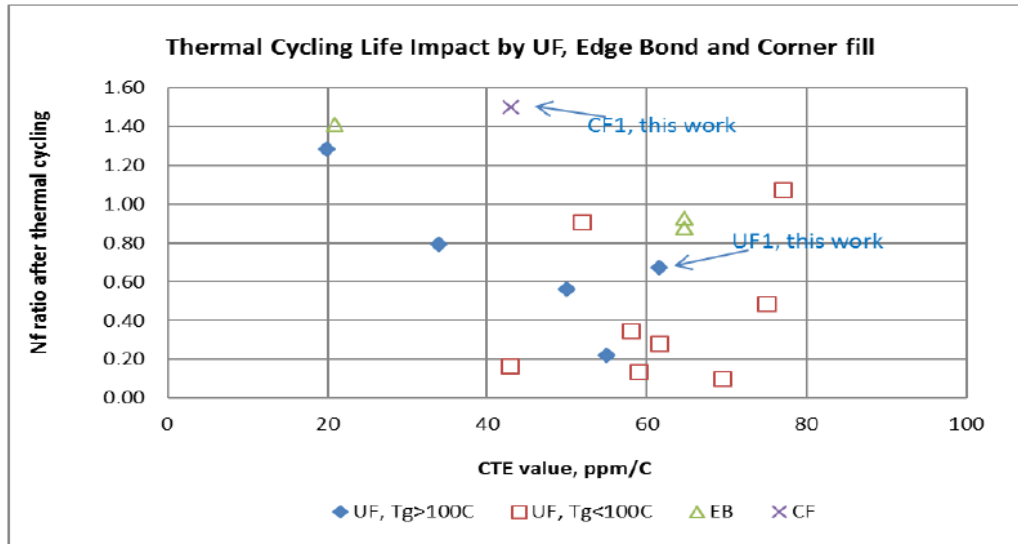


**Figure 1- 11: CTE contribution for thermal cycling fatigue life of solder joints for underfill materials [22].**

The leverage of underfill expansion and interaction with BGA packages under thermal loading has not been rigorously addressed. There is currently a lack of details that address the reasons that cause high expansion underfill to reduce fatigue life compared to non-underfilled ones. Additionally, the published empirical evidence for underfill and BGA package configurations that result in decrease of thermal cycling reliability has not been quantitatively explained. A more detailed correlation between temperature dependent underfill properties, BGA package, and solder characteristics, is necessary to understand the stress state that solder joints are subjected to under both fatigue life reduction and improvement with and without underfill.

### *1.2.3 Problem Statement and Motivation*

As previously discussed, the addition of underfill materials to BGA components can either increase or decrease board level reliability of solder joint in BGA packages [23, 24]. The CTE of underfill has been shown to be the driving factor on influencing thermal cycling reliability of BGA packages. Additionally, explanation to the influence of the underfill  $T_g$  on board level reliability of BGA components has been lacking from the literature. Unlike flip-chip packages that show improvements in fatigue life even when underfill  $T_g$  is within the temperature range, reliability of solder balls has been shown to suffer when the underfill  $T_g$  falls within the temperature range. Deformation and strain measurements of flip-chip solder joints with underfill have shown that higher tensile strains can develop in solder joints compared to shear strain with no distinct distance to neutral effect [25]. This indicates that the presence of underfill materials contributes to the development of an axial loading components. The exact combination of axial and shear loading in BGA packages that show decrease in fatigue life compared to non-underfilled ones is largely unknown. The exact magnitude of axial and shear loading responsible for fatigue life improvement or reduction in BGA packages across the  $T_g$  with reworkable underfills has not been extensively investigated for second level interconnects in BGA components.

An extensive analysis of the applicability of existing fatigue models for predicting the thermomechanical fatigue life of BGAs with reworkable underfill has not been performed. Conventional fatigue models for non-underfilled BGAs have been calibrated using shear dominant cycling loading conditions. It is not known if these current energy-based models would apply for the reliability assessment of BGAs with

reworkable underfill that exhibit a predominantly axial loading direction or require modification to damage indicators. Therefore, there is a need for a new fatigue life prediction model that can incorporate the approach of existing fatigue models by accounting for the complicated stress state solder joints experience with reworkable underfill during thermal cycling. The complicated loading conditions investigated in this study are mainly driven by the temperature dependent properties of various underfill materials. Therefore, an emphasis is placed on modeling the underfill material behavior and its influence of the prediction of stress state in solder joints.

#### *1.2.4 Scope of Dissertation*

The main objective of this dissertation is to develop a fatigue life prediction model that can accurately predict the fatigue life of solder joints in BGA packages with reworkable underfill under thermal cycling. Development of a fatigue life model for solder joints requires thorough understanding of temperature dependent material properties of materials used in electronic packaging. An FEA based methodology is used in order to define how the damage indicator used for fatigue life prediction is influenced by the stress state of the solder during thermo-mechanical loading. Experimental data of BGA component with variety of underfills and thermal environments is necessary for calibration and validation of empirical model parameters. Therefore, this study provides an extensive experimental approach to subject BGA solder joints to complex loading conditions using underfills with various materials properties and behaviors. Failure analysis investigation of the failure mode in solder joints is performed to understand how different underfill materials result in fatigue failure of solder joints. Extensive material characterization of a single reworkable underfill is performed and

used in FEA simulations to determine influence of different material models on stress state of solder joints under thermal cycling. The results from this dissertation will disseminate on performing reliability assessment of BGAs with reworkable underfills by demonstrating the impact of material properties, thermal cycling environments and modelling approaches.

## **LITERATURE REVIEW**

This chapter focuses on the influence of underfill materials on thermal fatigue life of solder interconnects in BGA packages. The influence of complex loading conditions on cyclic behavior of Pb-free solder is discussed with respect to isothermal and thermomechanical loading ranging from dog-bone specimens to joint scale solder used in electronic packaging. The focus is then placed on review of fatigue life of BGAs with various underfills to explore the extent of current research and influence of underfill material properties on solder joint fatigue. Several fatigue life prediction models for solder joints in electronic packages are introduced and discussed with respect to application in underfilled components.

### **2.1 Influence of loading condition on fatigue life of solder alloys**

Low cycle fatigue in Pb-free solder is largely dependent on the stress state responsible for accumulating inelastic deformation. Solder alloys have been shown to exhibit creep deformation even at low temperatures and stresses. In addition, the deformation mode such as tension, shear or bending can result in contribution to damage accumulation in solder interconnects. In the following sections, creep and fatigue behavior of solder

alloys will be discussed based on experimental investigations of Pb-free solder under complicated loading conditions.

### *2.1.1 Effect of Multiaxial Cyclic Loading on Pb-free Solder Alloys*

#### *2.1.1.1 Fatigue Behavior of Bulk Solder*

The influence of mean tensile stress on fatigue behavior is known to cause a ratcheting behavior that results in detrimental effect on both low and high cycle fatigue of metallic alloys [29, 30]. Ratcheting deformation usually occurs under asymmetric cyclic stress loading conditions and refers to the progressive accumulation of secondary deformation that is proceeded cycle by cycle [31]. Gao et al. performed a series of fatigue experiments on Sn-3.5Ag solder at room temperature under a strain rate of 0.005/s [32]. Fatigue tests under fully reversible torsion and cyclic torsion with constant tensile stress were performed in order to investigate multiaxial stress state on fatigue endurance of solder material and ratcheting behavior. Figure 2-1 shows axial ratcheting strain results for various values of shear strain and tensile stress

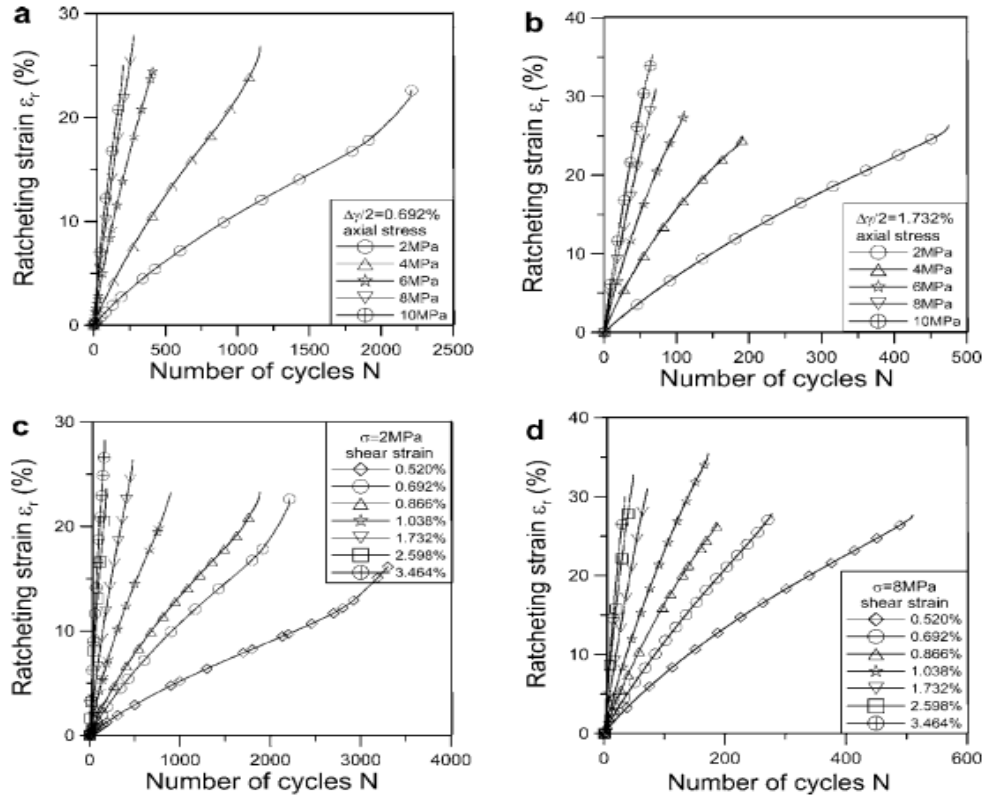


**Figure 2- 1: Relationship between ratcheting and the number of cycles: (a)  $\Delta\gamma/2 = 0.692\%$ , different axial stress; (b)  $\Delta\gamma/2 = 1.732\%$ , different axial stress; (c)  $\sigma = 2 \text{ MPa}$ , different shear strains and (d)  $\sigma = 8 \text{ MPa}$ , different shear strains [32].**

Ratcheting deformation usually occurs under asymmetric cyclic stress loading conditions and refers to the progressive accumulation of secondary deformation that is proceeded cycle by cycle [33]. It was previously shown that ratcheting deformation lead to a reduction in fatigue life [34]. Table 2-1 lists the number of cycles to failure performed under cyclic torsion with no tensile stress (left) and with constant tensile stress (right). It can be seen that even with small axial stress the number of cycles



significantly drops. Gao and Chen determined that even low axial stress can cause high ratcheting strain in Sn-3.5Ag solder. The trend of shakedown doesn't occur at room temperature and strain

**Table 2- 1: Torsional (left) and multiaxial (right) fatigue test results for Sn-3.5Ag [33].**

rate of their experiment. They observed that increase in axial stress or shear strain would lead to the increase in ratcheting strain that have detrimental effects on cyclic

$\Delta\gamma/2$ (%)	Load drop = 35%		$\Delta\gamma/2$ (%)	$\sigma$ (MPa)	Load drop = 35%				
	$\Delta\tau/2$ (MPa)	$N_f$			$\Delta\tau/2$ (MPa)	$\epsilon_r$ (%)	$N_f$		
0.346	10.40	16900	1.732	2	14.45	16.25	266		
0.520	10.94	6850			14.94	17.06	112		
0.692	12.49	3880			14.64	21.23	76		
0.866	13.50	3280			14.63	25.06	55		
1.038	13.01	1960			14.64	26.08	45		
1.732	13.74	1240			2.598	2	15.18	17.31	127
2.598	15.63	618					14.58	21.17	80
3.464	15.01	500					15.01	25.32	55
							14.31	26.11	36
							15.00	22.57	26
			3.464	2			14.88	21.92	120
							16.51	20.24	47
							15.44	23.75	35
							15.60	23.25	25
							15.36	21.27	16

fatigue life of materials. The presence of creep ratcheting in cyclic loading at elevated temperature is evident even when the load is below the material theoretical yield limit [35]. This indication of localized plasticity occurring at far lower loads and may be caused due to stress concentration, solder-intermetallic boundary and localized CTE mismatch. Creep response is more significant than the ratcheting response in solder joints. Liang et al investigated the effect of axial stress on shearing deformation behavior of Pb-free SAC387 and SnPb eutectic alloys at shearing strain rates of  $1.3 \times 10^{-4}$  1/s and  $1.3 \times 10^{-2}$  1/s. Figure 2-2 illustrates the test profile with the application of constant axial stress prior to performing monotonic shear strain testing. Unlike the lap shear tests performed by Hsieh et al, in this experiment solid ingots of the solder were re-melted and cast into 4" by 3/4" bars which were then machined into samples about 3"

long with thin wall (5/128", or 1mm), 1" gauge length and 0.5" outside and 27/64" inside diameters. Specimens were aged as room temperature for a month prior to tests. As a result of the constant axial stress a ratcheting strain in the axial direction is developed during the monotonic shear loading as shown in Figure 2-3. The extent of ratcheting strain is highly sensitive to loading rate and stress magnitude in the tensile direction.

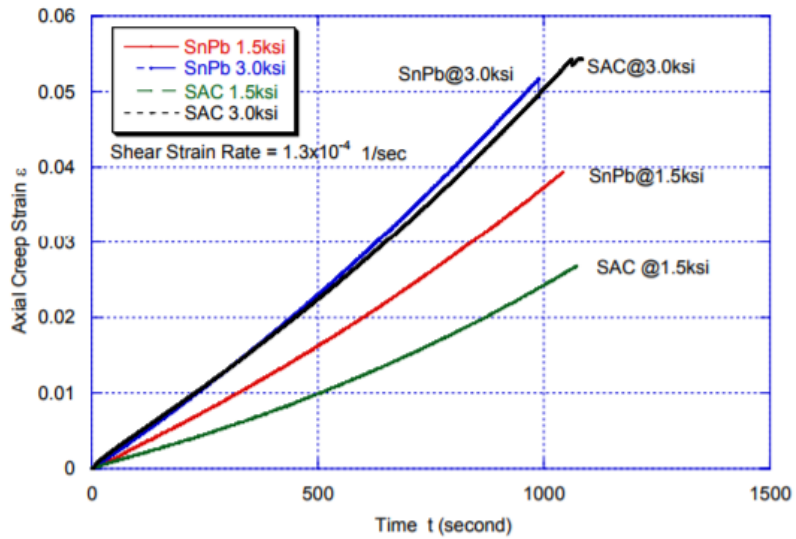


**Figure 2- 2: Axial tension creep deformation at 1.5 and 3ksi during shear monotonic shear test [36]**

The effect of the constant axial stress on during shear behavior is shown in Figure 2-3. In this experiment the impact of constant axial stress results in reducing the flow stress and strain hardening. Slight degree of softening is evident for the condition with constant axial stress of 3 ksi. It is important to note that under higher strain rates the extent by which flow stress was influenced is lower compared to the slower strain rates of  $1.3 \times 10^{-4}$  which allow for creep deformation to fully develop. This behavior is supported by the viscoplastic strain rate sensitive nature of solder alloys.

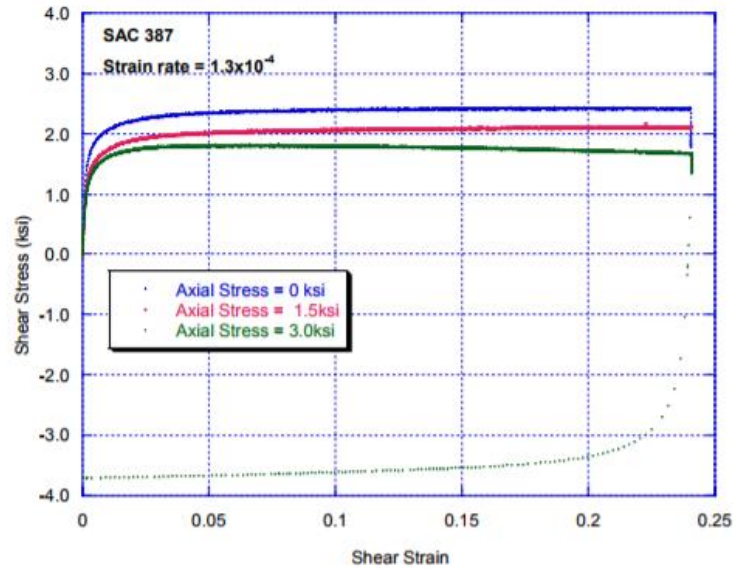


**Figure 2- 3: Shear strain vs. stress with axial stress of 0, 1.5, 3.0 ksi at a shear strain rate of  $1.3 \times 10^{-4}$  S-1 for SAC387 [36]**

#### 2.1.1.2 Fatigue Behavior of Joint Scale Solder

Andersson et al. performed isothermal fatigue experiments on bulk and macroscale solder joints and observed an inverse fatigue life performance at low and high strain ranges [37]. A significant factor that could have manipulated results from their study was the type of strain used in cyclic experiments. Bulk solder was tested in cyclic tension/compression and solder joints were tested under cyclic shear conditions. It is known that fatigue crack propagation rate in solder alloys is dependent both on the geometry, intermetallic layer thickness and loading mode.

Figure 2-4 shows the experimental tests setup and ratcheting displacement performed by Hsieh et al. Cyclic loading was performed on double-lap shear specimen with nine BGA solder joints mounted to a ceramic substrate [35]. FEA simulations of the double lap shear specimen using the Anand constitutive model for SAC387 compared with experimental results obtained using double lap shear specimen. Simulations results

shown in Figure 2-4 are able to capture the ratcheting effect obtained from experiment within acceptable limits.

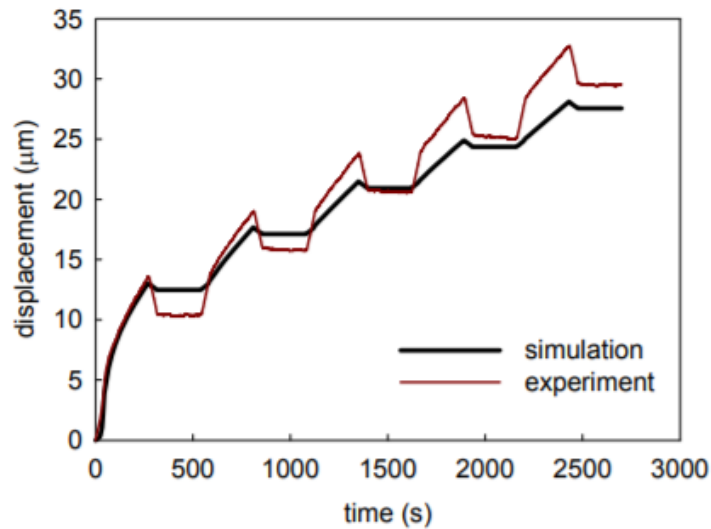


**Figure 2- 4: Anand model vs. experimental results at temperature of 90C with 225 second dwell with peak force of 90N [35].**

Hsieh et al. indicate in their study that an accurate representation of creep constitutive using hyperbolic sine model can adequately capture the ratcheting behavior experienced by solder joints under cyclic loading even at elevated temperatures.

Park and Lee [38] performed isothermal low cycle fatigue loading on SAC305 solder joints at room temperature under several loading angles. A small area array consisting of nine solder joints was soldered between two FR-4 substrates was attached to grips which have specific angle to the loading directions. Figure 2-5 shows the measured fatigue life for the different orientations with 0° having purely uniaxial loading and 90° having pure shear loading. Their results indicate lower fatigue life for 0° loading by a factor of 5X compared to 90° loading orientation at equivalent displacements.

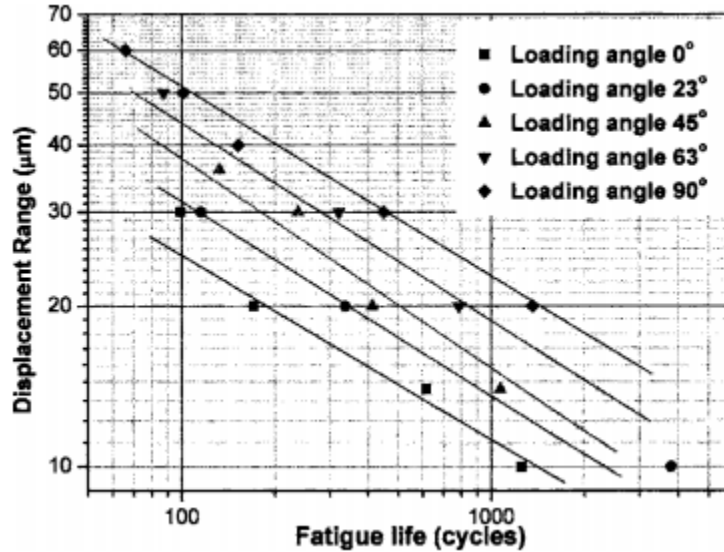


**Figure 2- 5: Fatigue life versus displacement range for Sn3.5Ag0.75Cu by 50% load drop [38].**

Additionally, they showed that the fracture surface direction were about 45 and 0 degrees to the loading direction under tension and shear loading conditions, respectively along the plane of maximum shear stress. This study directly emphasis the importance of loading direction on fatigue life of solder joints in BGA packages.

### 2.1.2 Effect of Thermomechanical loading on solder joints in BGA Packages

Stresses and strain solder joints in BGAs experience under thermal cycling depends on a combination of intrinsic and extrinsic parameters. The intrinsic factors include solder alloy chemical composition, creep resistance behavior, and material degradation sensitivity to complicated multiaxial stress and strain. Extrinsic factors include magnitude of loads, thermal environment, joint geometry and package material properties as well as field and test conditions [39, 4]. As the package and assembly undergo thermal cycling, solder joint deformation and fatigue is driven by global and

local CTE mismatch. The global CTE mismatch is introduced from the mismatch between PCB and effective package CTE, while the local mismatch is introduced by the solder (22 ppm/°C) and copper pads (17 ppm/°C). Global CTE mismatch introduces in-plane shear and out of plane bending loads in solder joints. It has been previously shown that the fatigue damage done by local and global mismatches is comparable in magnitude [41]. Therefore, complicated loading conditions in BGA solder joints are inherently complicated although fatigue damage is assumed to be driven primarily by shear loading [42]. Idealization of shear load has been proven to be an acceptable for many BGA packages; however, the following section will demonstrate situations where the dominant loading conditions no longer hold true to the assumption.

In this section the influence of thermo-mechanical deformation of BGA components will be reviewed. A distinction will be made between the stress state and fatigue life of BGAs with underfill and BGAs without underfill. Examples from both 1<sup>st</sup> level interconnects in flip-chip packages will be reviewed as well as ones from 2<sup>nd</sup> level solder interconnects.

#### *2.1.2.1 BGAs without Underfill*

Studies of crack propagation in solder joints in surface mount components with short leads have shown that shear straining dominates the creep-fatigue damage as shown in Figure 2-6 by the larger hysteresis curve of the shear loading compared to the axial loading.

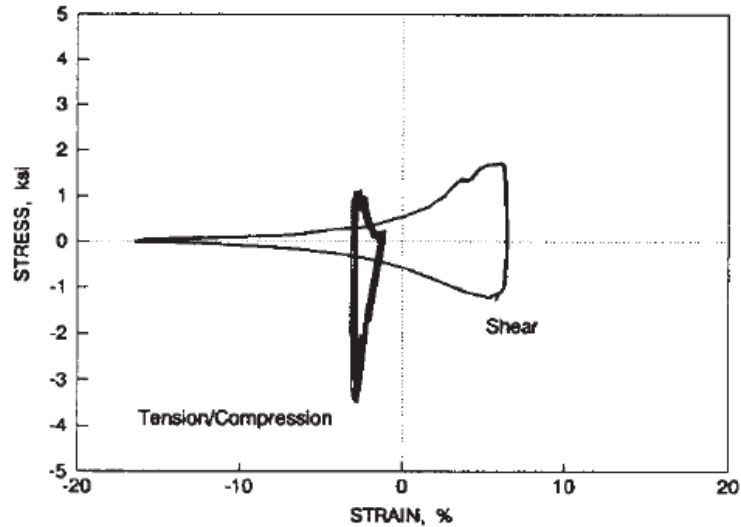


**Figure 2- 6: Anand model vs. experimental results at temperature of 90°C with 225 second dwell with peak force of 90N [35].**

The hysteresis curves from the shear strain and stress accumulate as result of fully reversed cyclic shear behavior during thermal cycling are used to determine the energy density. This energy density can then be used as a damage indicator within fatigue life models. Libot et al. experimentally measured the shear hysteresis behavior for a CBGA76 package using strain gauges mounted on both sides of the package and PCB [44]. Figure 2-7 shows the experimentally measured shear stress-strain curves for different thermal cycles that not only exhibit different strain ranges but also different mean shear stress and strain. As temperature increases, solder joints become less resistant to viscoplastic deformation while at lower temperatures the solder is more resistant to creep deformation and can absorb higher plastic deformation. The shift in the mean stress in different cycles depends on the stress-free temperature of the solder balls in the BGA, temperature range and creep behavior of the alloy that is highly dependent on temperature.

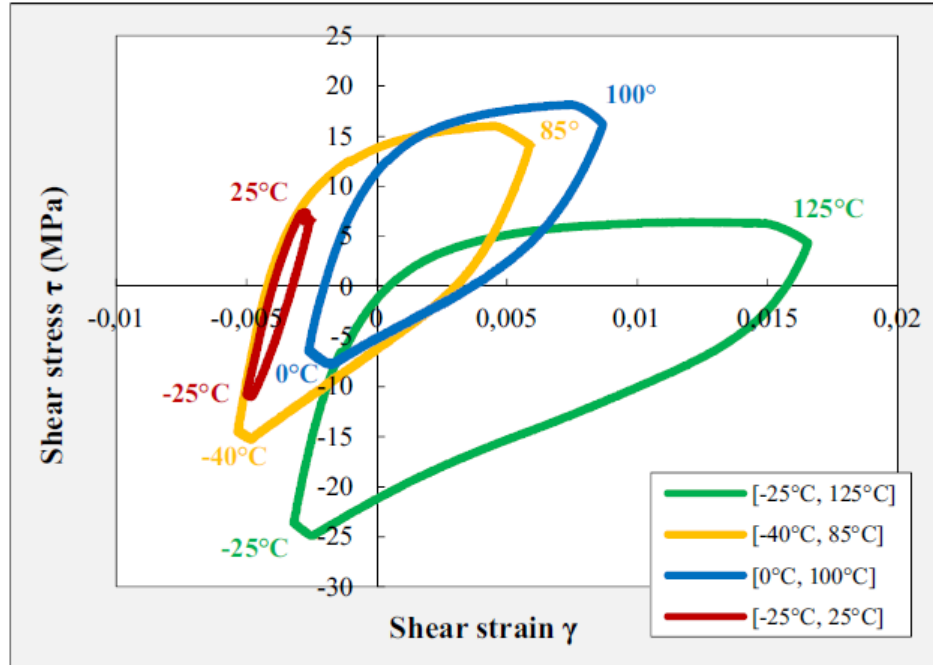


**Figure 2- 7: Experimental shear strain-stress hysteresis loops for each thermal cycling condition [44].**

Influence on thermo-mechanical fatigue life of BGA packages has also been shown to be largely influenced by the package characteristic such as mold compound and die size [45, 46]. Larger die size such as in chip-scale packages will reduce the effective component CTE and result in the increase of the CTE mismatch between the component and the board.

The BGA solder joint geometry can greatly influence fatigue life of BGA packages as shown in Figure 2-8. The two most critical geometric parameters responsible for controlling the fatigue life of solder joints in BGA packages are the ball height and area of the ball soldered to the component or boards pads. Solder ball height is directly proportional to shear strain the corner most joint will experience while the area soldered to the pad will dictate the area crack propagation has to progress in to achieve full failure.



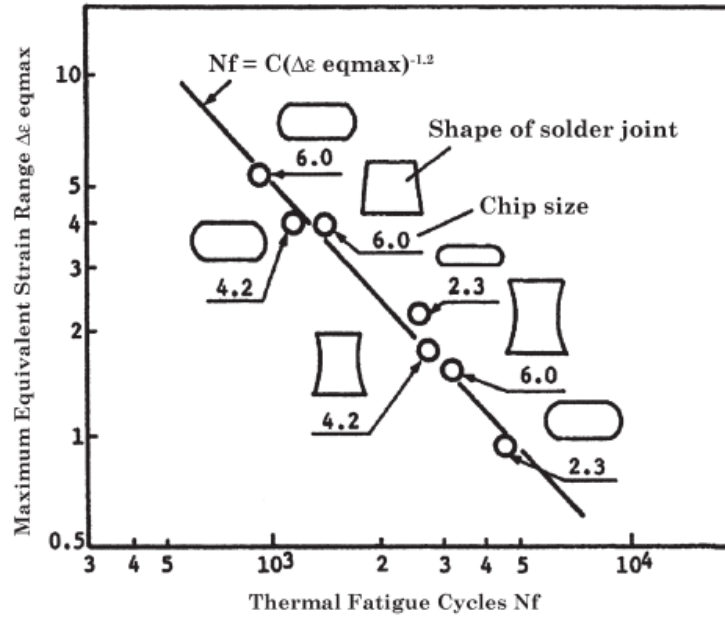


**Figure 2- 8: Effect of BGA ball geometry and chip size on fatigue life of SnPb eutectic solder balls [47].**

The microstructural feature of solder joints has also been found to influence fatigue life. Figure 2-9 illustrates the characteristic life of various BGA packages for thermal profile of 0°C to 100°C on single sided and double-sided boards with three different board thicknesses. A distinct trend in fatigue life as function of die size to package size ratio is evident. Chip scale packages with die size that is 60% of greater of the package area tend to fail sooner on both thicker and double-sided board compared with even larger packages that have a die that is 50% of the package size or smaller.

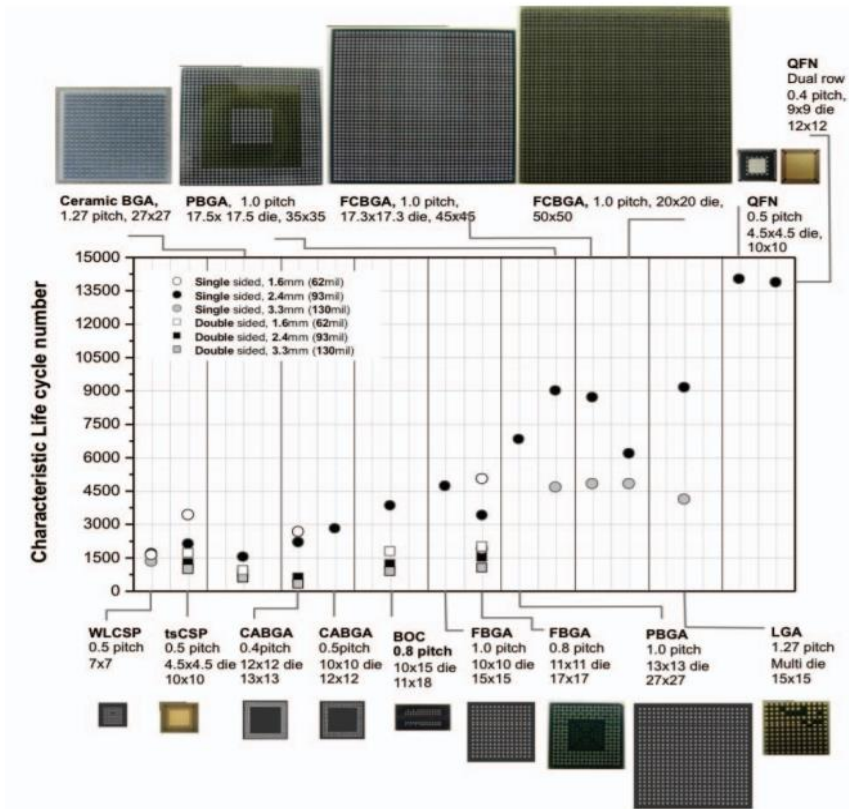


**Figure 2- 9: Characteristic thermal cycling life cycle number depends on the package design. [48]**

Alternatively, large variation in material properties between BGA package types is not discussed and could largely affect the effective CTE of components and warpage characteristics. Other intrinsic factors influencing thermo-mechanical fatigue life of solder joints have been found to be the pad metallization and even the thermal preconditioning of the package during thermal aging.

#### 2.1.2.2 BGAs with Underfill

Verma et al. measured strain in 2<sup>nd</sup> level solder joint of FC-PBGA package using moire interferometry while cooling from the underfill curing temperature to -40°C [49]. Their results found that the third solder ball from the edge of the chip (die shadow) has the

largest normal strain as shown in Figure 2-10 below with the remaining solder balls under the bare substrate having almost uniform strain regardless of distance to neutral point effect. The axial strain was correlated to an inflection point in the warpage characteristic of the investigated package that did not contain overmold material.

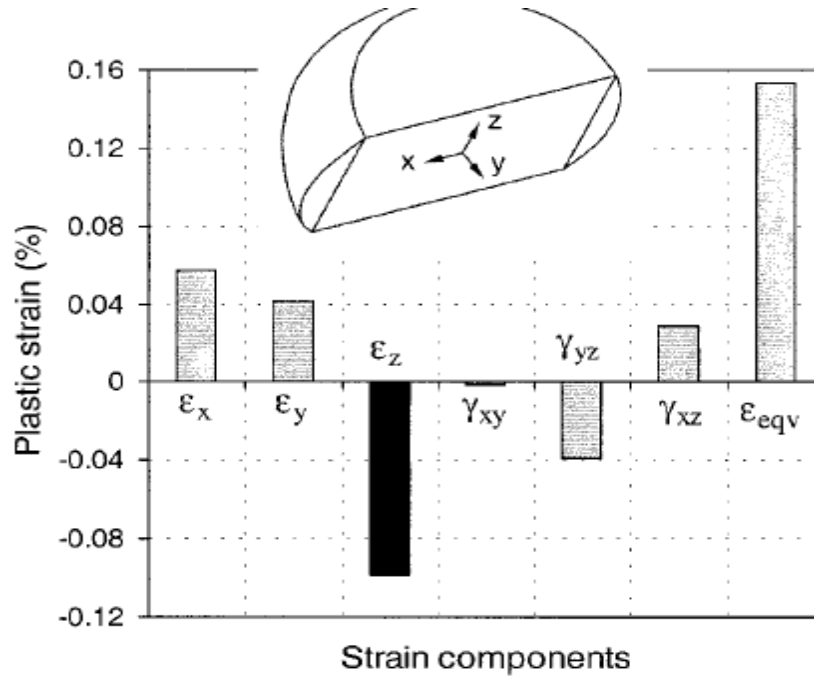


**Figure 2- 10: Strain components of the nodal point in the chip edge solder ball with the maximum equivalent plastic strain [49]**

Strain measurements in flip-chip solder bumps with low  $T_g$  underfill during thermal heating was measured by Kwak et al. using digital image correlation (DIC) technique [25]. Their measurements were performed using low expansion underfill with a CTE of 30ppm/°C and a  $T_g$  of 90°. Figure 2-11 below illustrates the average normal and shear strains in solder bumps. The results from this study illustrate that normal strains do not exhibit the same distance to neutral dependence as the shear strains along the package corner. The magnitude of the normal strains steadily increases with temperature and is of higher magnitude compared to shear strains.

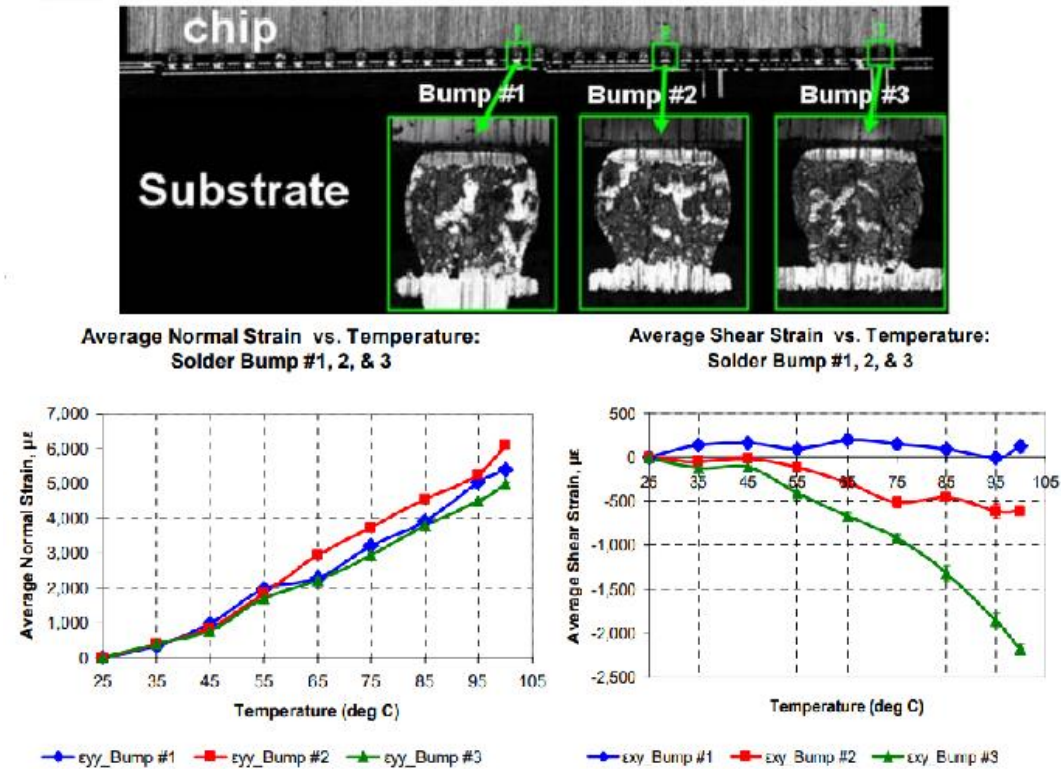


**Figure 2- 11: Average normal and shear strain for three flip-chip solder bumps with underfills [25].**

Two investigations reviewed here on flip-chip solder bumps demonstrated the presence of higher axial strain component in solder bumps during thermal loading. The higher axial strain is shown to be on compressive nature during thermal contraction of the flip-chip package and tensile nature during thermal expansion. The presence of underfill is assumed to contribute to the increase in axial strain on solder joints rather than change in the package warpage of the underfills flip-chip package. Strain measurements on larger solder balls in BGA packages with underfill have not been reported in literature to the best of the author's knowledge. Therefore, it is not possible to compare the strain field of an underfilled flip-chip package with that of an underfilled BGA package.

## 2.3 Empirical trends in thermal fatigue life of ball grid array packages with underfill

Published accelerated thermal cycling experiments on underfilled flip-chip and BGA packages can provide a qualitative assessment on the impact of underfill on the reliability of solder bumps and balls. The subsequent sections will review fatigue results from thermal cycling experiments of flip-chip and BGA packages with and without underfill and outline empirical observations that are unique to each of these package types.

### 2.3.1 Thermal Fatigue of 1st level solder joints in Flip-Chip Packages

The information listed in table 2-2 was taken from three different publications on accelerated thermal cycling of flip-chip packages with different thermal cycling range, solder alloy and package dimensions and underfills. These select publications on the reliability of flip-chip packages performed accelerated thermal cycling on flip-chip components with and without underfill.

**Table 2- 2: Published thermal cycling fatigue life of Flip-Chip packages.**

Ref	Underfill Properties			Thermal Cycle	Package Size	Solder Alloy	Nf Control	Nf w/UF	Experimental Multiplier
	CTE	E (MPa)	T <sub>g</sub>						
50	57	3500	125	0 to 125	7.5x4.8mm die	SAC387	68	1228	18.06
50	30	8500	80	0 to 125	7.5x4.8mm die	SAC388	68	1716	25.24
50	28	10700	119	0 to 125	7.5x4.8mm die	SAC389	68	5476	80.53
50	28	7600	161	0 to 125	7.5x4.8mm die	SAC390	68	6110	89.85
51	45	NA	NA	-40°C to 125	2x2mm die	SnAg	88	1600	18.18
51	46	NA	NA	-40°C to 125	2x2mm die	SnAg	120	3287	27.39
52	22	NA	150	-55 to 125	5x5 mm	SnPb	300	3978	13.26
52	54	NA	90	-55 to 125	5x5 mm	SnPb	300	2700	9.00

Each of the three data sets represents a unique combination of thermal cycle, die size, solder alloy and underfill material. A common factor between the three distinct data sets is that all underfilled flip-chip packages demonstrate a large improvement in fatigue life with the underfill compared to the non-underfilled one. Figure 2-12. shows the fatigue life multiplier as a function of underfill CTE as listed in Table 2-2. The data set which illustrates lowest improvement in characteristic life belongs to the harshest thermal cycle with the highest underfill CTE. The lowest fatigue life multiplier for this data is by a factor of 9 compared with the highest fatigue life improvement with a factor of 89 for the thermal cycle with shortest temperature range and low CTE. This figure demonstrates a

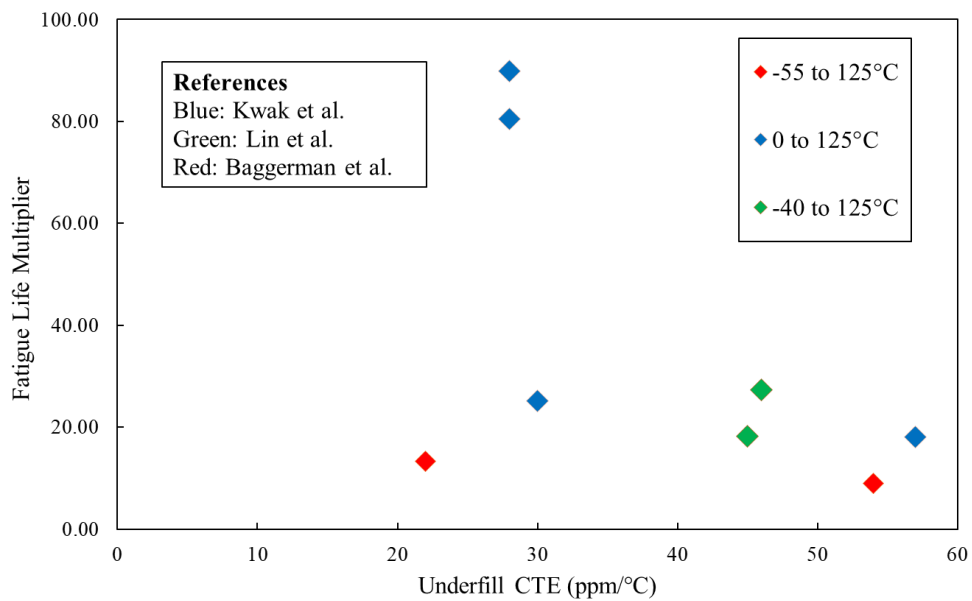


**Figure 2- 12: Fatigue life multiplier as function of CTE for flip-chip package taken from Table 2.**

trend in fatigue life improvement for flip-chip packages regardless of underfill CTE, solder alloy, package configuration and thermal cycle. Sharp increase in the fatigue life multiplier occurs at a CTE of 30ppm/°C at which the improvement increases from a

factor of 20 to 80 for underfills with a CTE of 20ppm/°C. Other investigators have shown even larger improvement in fatigue life for flip-chip devices with underfill that increase the characteristic life beyond a factor of 200 for some combination of flip-chip devices and underfill materials shown in Figure 2-13 [53].

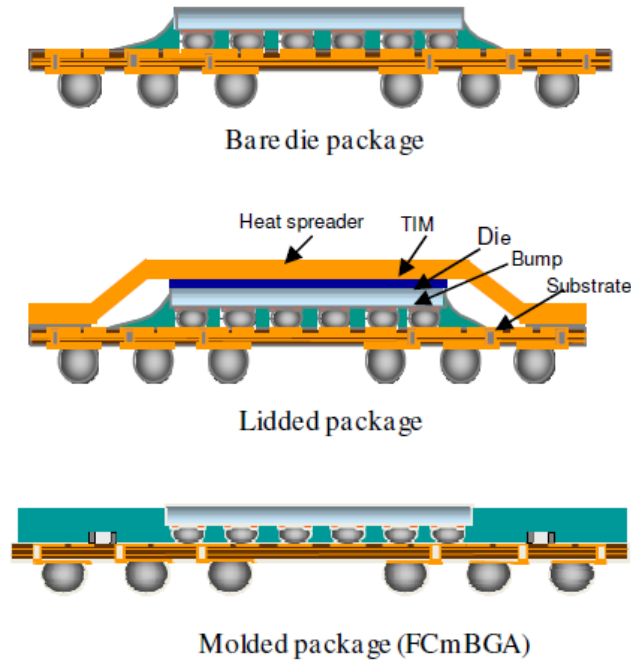


**Figure 2- 13: Various flip-chip package types subjected to thermal cycling [53].**

All the reviewed published experiments on thermal cycling of flip-chip devices demonstrate dramatic increase in fatigue life with underfill, although not every published research provides detailed information on the underfill material used in their test vehicle. Taking into consideration the available information of fatigue life improvement of flip-chip devices an empirical relationship can be defined using the underfill  $T_g$ , modulus and CTE.

$$\frac{N_{f,UF}}{N_{f,no UF}} = e^{-0.05E} \times 9000CTE^{-2} \times (0.6 \ln T_g - 1.8) \quad (2-1)$$

Where E and CTE are the underfill properties defined before the  $T_g$ . Equation 2-1 is comprised of three distinct terms for each of the underfill properties influencing the stress state of solder bumps in a flip-chip package. The limitations of these empirical acceleration life model is that it does not depend on package or substrate properties not the solder alloy and geometry of the flip-chip bump nor information regarding the thermal properties. This empirical acceleration factor is used to demonstrate the usefulness of experimental data while still reminding of the broad limitation empirical models have in reliability assessment of electronic packages.

### 2.3.2 2nd level solder joints in BGA packages

The effect of underfill on thermal cycling reliability of BGA components has been thoroughly investigated using both experimental and numerical techniques on a variety of BGA package types and underfill materials. In this section, a detailed summary of previous experiments on the effect of underfilling on fatigue life of BGA packages is presented. Burnette et al. investigated the board level reliability of ceramic BGAs (CBGA) with various underfills using a thermal cycle of 0°C to 100°C [54]. 21mm 256IO CBGAs assembled onto 1.55 mm PCBs. Underfill material properties used in their study along with thermal cycling results shown in Table 2-3.

**Table 2- 3: Underfill properties and thermal cycling results of CBGAs [54].**

			Epoxy	50%	1%	0.1%
Epoxy	CTE	Modulus	Control	2426	1980	1851
A	75	2.6	A	2070	931	713
B	44	5.6	B	5160	3013	2518
C	40	8.5	C	5097	3100	2626
D	26	5.5	D	No Fails		

It is important to note that underfill material  $T_g$  was not discussed in their analysis.

Based on the CTEs and failure range, it is not possible to assume if the  $T_g$  of the



underfilled used in this study was within the thermal cycling range. Nonetheless, an obvious trend can be seen in which lowest CTE underfill resulted in improvement of fatigue life by a factor greater than 2X and progressively decreased with increase of underfill CTE. The point at which underfill starts to reduce fatigue life in CBGA under this thermal profile is somewhere between 44 and 75 ppm/°C. Fatigue life predictions using FEA and Darveaux's model were also performed in an attempt to predict experimentally determined characteristic life as shown in Table 2-4.

**Table 2- 4: Predicted and measured values of Weibull characteristic life [54].**

Epoxy	Predicted $\eta$ (in cycles)	Measured $\eta$ (in cycles)	Ratio Pred./Meas.
A	3690	2320	1.59
B	7390	5420	1.36
C	7630	5440	1.40
D	9470	>6000	n/a
none	6690	2490	2.69

In their analysis, predictions for underfilled BGAs consistently overpredicted experimental values but were within 2X range. Prediction for the control BGA deviated the most by a factor of almost 3X. Burnette et al. noted that simulation results indicated highest creep strain energy while failure analysis found that all underfilled BGAs failed at the PCB side. Their investigation demonstrates the need to properly characterize the temperature dependent properties of underfill materials for FEA analysis.

Borgesen et al. performed thermal cycling from -40°C to 125°C on 30 mm flip chip with 27 mm square die BGAs with 256I/O with SAC305 solder balls [55]. Components were assembled onto 1.5 mm thick PCB and underfilled using several reworkable and

non-reworkable underfills materials with full underfilling and corner bonding. Table 2-5 lists the thermal cycling results for corner bonded BGAs

**Table 2- 5: Thermal cycle results for corner/edge bonded SAC305 BGAs [55].**

	Drop	N <sub>63</sub>	Beta
Encapsulant B, full fillets	Yes	1298	11.64
Encapsulant B, corner fillets	Yes	1159	4.22
Encapsulant A, full fillets	No	884	3.96
No encapsulant	No	824	4.66

Underfill A has a T<sub>g</sub> of 0 °C with CTE of 77 ppm/°C before and 222 ppm/°C after transition and an elastic modulus of 7 MPa. Underfill B has a T<sub>g</sub> of 150 °C with CTE of 21 ppm/°C before transition with no reported modulus. It can be seen that underfill B increased fatigue life by 57% at most depending on fillet and underfill A provided an insignificant increase in fatigue life. Borgesen et al. repeated thermal cycling using full area underfill with additional materials shown in Table 2-6.

**Table 2- 6: Thermal cycle results for underfilled SAC305 BGAs [55].**

	Drop	N <sub>63</sub>	Beta
No underfill	No	824	4.66
Underfill H	No	655	4.67
Underfill G	No	462	3.99
Underfill C	No	403	4.59
Underfill E	Yes	330	6.31
Underfill F	Yes	285	2.83
Underfill D	Yes	229	2.22

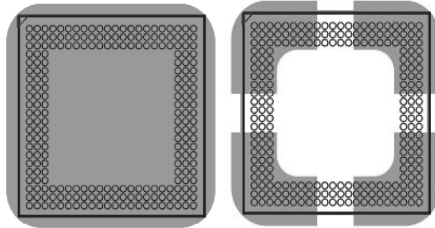
In this test, underfill C had a T<sub>g</sub> of 15°C with CTE of 75 ppm/°C before transition. Underfill D had a T<sub>g</sub> of 15°C and CTE of 80 ppm/°C before and CTE of 210 ppm/°C after transition with 50 MPa elastic modulus. Underfill E has a T<sub>g</sub> 55°C and CTE of 66 ppm/°C before and CTE of 201 ppm/°C transition with a modulus of 2.3 GPa. Underfill G is non-reworkable and had a T<sub>g</sub> of 110°C with CTE of 50 ppm/°C and 160 ppm/°C before and after transition, respectively with a modulus of 2.0 GPa. Underfill H had a

$T_g$  of 115°C with CTE of 34 ppm/°C. It can be seen that all high CTE reworkable underfills resulted in decreasing the thermal fatigue life by a factor of 2 to 3. Underfill H was found to decrease fatigue life the least out of all the combinations. This can be attributed to a higher  $T_g$  and lowest CTE before the transition. Fatigue life is progressively decreasing for underfills with higher CTE and lower  $T_g$ .

The reduction of thermal fatigue life with underfill  $T_g$  that is within the thermal profile range was clearly illustrated in study performed by Shi et al. In their study, a 12 mm CSP BGA with 228 perimeter soldered board assembled onto a 1 mm thick PCB and subjected to a thermal profile range of -40°C to 125°C [56]. Table 2-7 lists the two underfill materials used in their study and application method.

**Table 2- 7: Underfill properties and application method, full underfill, partial underfill [56].**

Underfill	Viscosity at 25°C (mPa.s)	$T_g$ (°C)	CTE (ppm/°C)		Modulus (GPa)	Typical curing performance
			$\alpha_1$	$\alpha_2$		
A	375	69	52	188	3.080	8 minutes at 130°C
B	2000~4500	85	60	200	3.500	5 minutes at 120 °C



Both underfills A and B are reworkable and exhibit large CTE prior to their respective  $T_g$ . Thermal cycling results shown in Table 2-8 indicate that both underfills at either application method thermal cycling fatigue life with respect to the control components.

**Table 2- 8: Thermal cycling results for underfilled BGAs [56].**

Sample	FCFU-A	FCFU-B	PCFU-A	PCFU-B	Control
$\alpha$ or $N_{63.2\%}$	3206	3640	3406	3932	4268
$N_{50\%}$	2844	3281	3100	3694	4059
$N_{1\%}$	712	988	1046	1796	2272
$N_{\text{First failure}}$	960	1046	1519	2251	2650
$\beta$	3.056	3.527	3.895	5.871	7.296
# Failures /# Samples	41/45	43/45	39/45	37/45	19/45

Interesting to note that the decrease in the characteristic fatigue life (63.2%) was observed for underfill A with the lower CTE which is contrary to previous observation. This result could be attributed to cure dependent characteristics or to the lower  $T_g$  of the underfill which enables for the higher CTE for longer temperature duration. The influence of underfill cure characteristics on thermal fatigue life has been previously investigated by Burnette et al. Three types of BGA were underfilled with the properties listed in Table 2-9 and subjected to thermal cycling with the temperature range of -40°C to 125°C. Similar to a previous study, the  $T_g$  of underfills was not reported in here.

**Table 2- 9: Underfill properties and cure time (top), package dimensions (bottom) [57].**

Epoxy	CTE	E	Cure
A	70 ppm/K	2.6 GPa	7 min/165 °C
B	44	5.6	7 min/165 °C
C	40	8.5	7 min/165 °C
D	26	5.5	7 min/165 °C
E	33	8.5	1.5 hours
F	42	5.4	3 hours

I/O	Body Size	Pitch	Die Size
280	16x16 mm	0.80 mm	10.7x10.1 mm
232	12x12	0.65	9.3x8.4
196	15x15	1.00	10.2x9.6

Thermal cycling results were reported in Table 2-10 below along with FEA predictions using the Darveaux model. Again, predictions are found to deviate the most for control BGA and provide good agreement with experimental data for the underfilled BGAs.

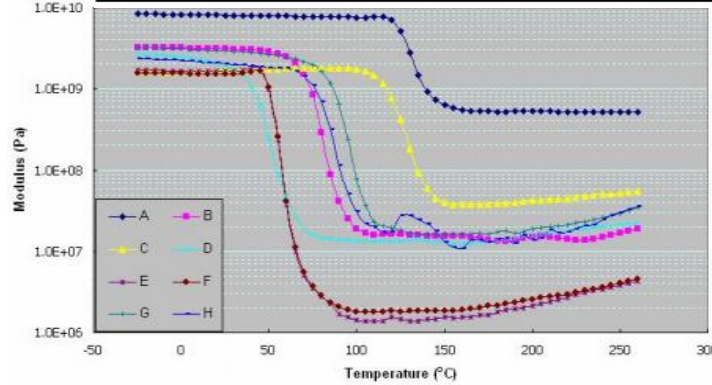
**Table 2- 10: Predicted and measured values of Weibull characteristic life for 280-lead fleXBGA assemblies with and without underfill. [57].**

Epoxy	Predicted $\eta$ (in cycles)	Measured $\eta$ (in cycles)	Ratio Pred./Meas.
A	1150	2230	0.52
B	3030	3720	0.81
C	2360	2090	1.13
D	5930	5600	1.06
none	6950	1030	6.72

The discrepancy between predictions of non-underfilled and underfilled BGAs indicates an inconsistency in either the validity of the fatigue model to the tested configuration or the inappropriate application of the model to the package type by the authors. As the two investigations where this inconsistency was found was reported by the same author, one could conclude that the author's inappropriate utilization of the Darveaux's model was a larger contributor to the deviation in results between control and underfilled BGAs. A detailed investigation on the influence of underfill on second level interconnects in package-on-package BAGs was performed by Lee at al. In their investigation, various reworkable underfills were applied to a 14 mm BGA with 353 IO. As shown in Figure 2-14 below.

**Table 2- 11: Underfill material properties used in [58].**

Underfill name	Dispensing pattern	Filler content (wt%)	T <sub>g</sub> by TMA (°C)	CTE, α1 (ppm/°C)	CTE, α2 (ppm/°C)
A	Full	70	113.1	19.9	83
B	Full	0	67.0	61.5	129
C	Corner dot & L	0	123.9	64.7	180
D	Full	0	62.9	69.4	195
E	Full	65	50.3	51.9	181
F	Full	50	60.1	42.8	125
G	Full	0	89.0	58.0	193
H	Full	0	94.4	59.0	195



Underfill material properties used in their analysis subjected to a standard accelerated thermal cycle of -40°C to 125°C. Table 2-11 lists underfill material properties along with temperature dependent modulus obtained from DMA. Underfill A used in their study was a non-reworkable, capillary underfill with low CTE and high T<sub>g</sub>. Thermal cycling results obtained in their study are shown in Table 2-12. As expected, the low CTE capillary underfill did not exhibit any failures compared to the reworkable underfills. Underfill D with CTE of 69.4 ppm/ °C before and 195 ppm/ °C after a T<sub>g</sub> of 62.9°C reduced characteristic life by a factor of 6.7X compared to control configuration. Underfills F and H followed closely behind with a decrease in characteristic life of 5.1X and 4.7X, respectively. This indicates that the CTE of underfill above the T<sub>g</sub> is as significant as the CTE below the T<sub>g</sub> and the temperature range across the T<sub>g</sub>.

**Table 2- 12: Temperature cycling results after 2525 cycles [58].**

Underfill name	NBR of failure	1 <sup>st</sup> failure	MTTF	63.2%, $\eta$	Slope, $\beta$
No underfill	8/28	1968	2727	2858	10.74
A	0/30				
B	27/30	555	1334	1481	3.58
C (dot)	20/30	1738	2369	2470	12.22
C (L)	22/30	1832	2470	2348	11.75
D	30/30	202	394	426	5.67
E	4/30	1791			
F	30/30	329	512	560	4.75
G	29/30	681	1110	1209	5.02
H	30/30	270	539	597	3.77

This study also indicated that the application method of underfill is just as significant as the CTE and  $T_g$  of underfill. The lowest impact on reduction of characteristic life was observed for the CTE with corner staking and progressively decreased with corner staking through full area underfill.

The above literature review demonstrates the effect of underfill materials on the board level thermo-mechanical fatigue of different BGA components. A common trend can be observed between high CTE underfills that reduce fatigue life while low CTE underfills with high  $T_g$  improve the fatigue life. It can be deduced that the addition of underfill materials strongly influences the stress-strain solder joints exhibit during thermal cycling. The temperature dependent properties of underfills are shown to significantly influence the fatigue life by modifying the stress-strain solder joints experience.

A summary of the experimental data reviewed in this section is plotted along with additional references in figure 2-15 [59-61].

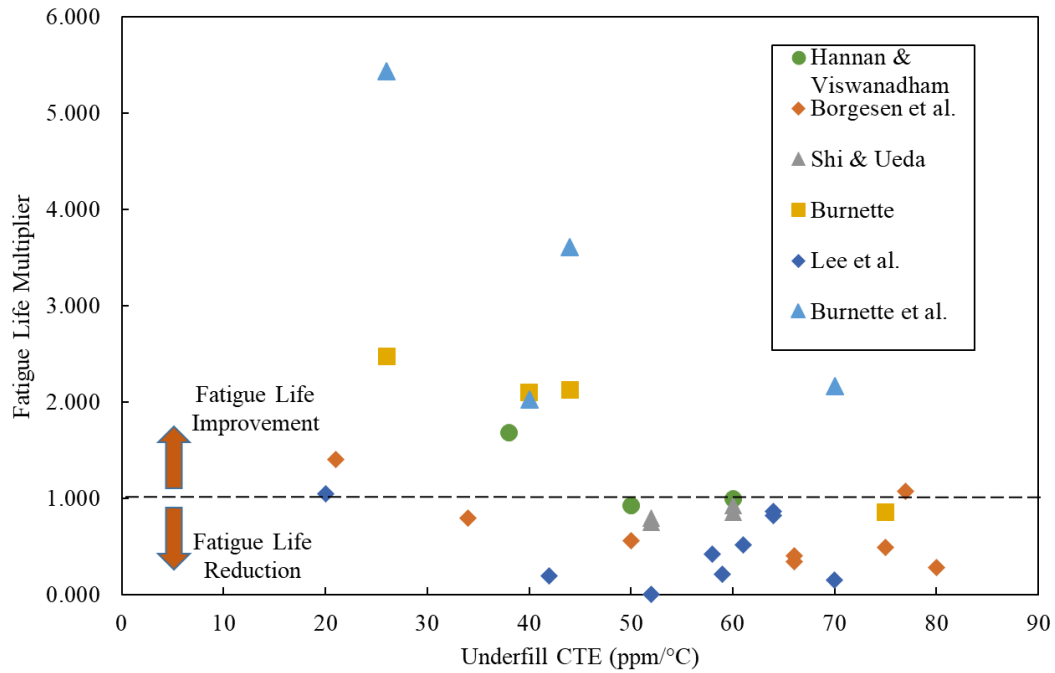


**Figure 2- 14: Fatigue life multiplier as function of underfill CTE for BGA packages.**

Similar to the acceleration factor equation calibrated for flip-chip devices a similar relationship can be defined for BGA devices from the data shown in Figure 2-14. Equation 2-2 demonstrates an empirical acceleration factor equation for BGA devices. Unlike equation 2-1, the dependence on underfill properties changes for BGA devices that demonstrate transition between fatigue life improvement and reduction.

$$\frac{N_{f,UF}}{N_{f,no UF}} = (50 \cdot CTE^{-1.15}) \times (0.45LN(E) - 0.25) \times (0.18e^{0.01T_g}) \quad (2-2)$$

The same limitations that are defined for flip-chip devices hold true for equation 2-2 that exclude additional material properties on the package level.



## 2.4 Review of Existing Fatigue Life Prediction Methods

### 2.4.1 Empirical and Analytical Models

One of them most widely used empirical models for reliability assessment of solder interconnects in electronic packaging is the Norris-Landzberg (NL) model shown in equation 2-3 [62]. The NL model was originally developed in the 1960's to predict fatigue failure of SnPb solder joints in flip-chip devices. The NL model assumes proportionality between plastic strain range and temperature range in the following relationship.

$$AF = \frac{N_1}{N_2} = \left(\frac{f_1}{f_2}\right)^{-m} \left(\frac{\Delta T_1}{\Delta T_2}\right)^{-n} e^{\frac{E_a}{K}\left(\frac{1}{T_{max,1}} - \frac{1}{T_{max,2}}\right)} \quad (2-3)$$

Where  $N_1$ , and  $N_2$  are fatigue life at two different thermal environments,  $f_1$  corresponds to temperature cycling frequency,  $m$  and  $n$  are constants,  $\Delta T$  is the temperature range,  $E_a$  is the activation energy for the solder,  $K$  is the Boltzmann's constant, and  $T_{max}$  is the maximum temperature at each thermal environment. Once the model constants are determined from experimental data the projected reliability of other thermal environments can be predicted. The NL model has been found to provide good correlation when the model has been calibrated for specific packages, solders and use conditions [63]. Other researchers have identified weaknesses in the NL model between various package types and Pb-free solder alloys [64]. They indicated that damage accumulation in solder joints occurs throughout the duration of the thermal cycle and varies for each segment of the cycle and that a simple acceleration factor cannot be taken as a damage indicator for the complex loading conditions solder joints experience during thermal cycling.

Semi-empirical fatigue life predictions models such as the Engelmaier model implemented first order analytical equations to correlate the plastic strain in solder joints as damage indicator for empirical Coffin-Manson type fatigue equations [65]. Engelmaier approximated the plastic strain in solder joint using the first-order approximation due to temperature range, solder joint height and CTE mismatch and distance to neutral point

$$\Delta\gamma = F \frac{D\Delta\alpha\Delta T}{2h} \quad (2-4)$$

$F$  is an empirical factor accounting for second-order effects,  $D$  is the distance to neutral point,  $\Delta\alpha$  is the CTE mismatch between component and PCB,  $\Delta T$  is the temperature range and  $h$  is the solder joint height. After the plastic shear strain is determined fatigue life prediction is made using the following relationship

$$N_f = \frac{1}{2} \left( \frac{\Delta\gamma}{2\varepsilon'_f} \right)^{\frac{1}{c}} \quad (2-5)$$

Where  $\varepsilon'_f$  is the fatigue life ductility coefficient and  $c$  is the fatigue ductility exponents given by the following equation 2-6:

$$c = -0.442 - 6x10^{-4}\bar{T} + 1.74x10^{-2}\ln(1 + f) \quad (2-6)$$

$\bar{T}$  is the mean cyclic temperature and  $f$  is the cyclic frequency. The popularity of the Engelmaier model by the electronics industry enabled its adoption into industry standards such as IPC-D-279 and IPC SM-785 [66, 67]. Although the Engelmaier model has been found to follow fatigue life trends of certain package types it did not provide sufficient accuracy for leadless package types where the solder joint height could be substantially lower than leaded packages [68]. Shear and axial strain in

underfill BGA package can be calculated by the following equations from Suhir's model [69]:

$$\gamma_{zx}(x) = k \frac{3\Delta\alpha\Delta T \sinh kx}{3G_2\lambda \cosh kl} \quad (2-7)$$

$x$  distance from chip center

$2l$  chip length

$t_i$  thickness of layer  $i$

$G_i = E_i/2(1 + \nu_i)$  shear modulus of layer

$D_i = E_i t_i^3 / 12(1 + \nu_i^2)$  Flexural rigidity  $i$

$D = D_1 + D_2 + D_3$  Flexural rigidity

$t = t_1 + t_2 + t_3$  Assembly thickness

$\lambda = \frac{(1-\nu_1)}{E_1 t_1} + \frac{(1-\nu_3)}{E_3 t_3} + \frac{t^2}{4D}$  Axial compliance

$K = \frac{t_1}{3G_1} + \frac{2t_2}{3G_2} + \frac{t_3}{3G_3}$  interfacial compliance

$k = \sqrt{\lambda/k}$

The axial strain can be calculated with the following equation

$$\varepsilon_z = \left( (\alpha_{uf} - \alpha_{sold}) + (\alpha_{uf} - \alpha_{eff}) \frac{2\nu}{(1 - \nu)} \right) \Delta T \quad (2-8)$$

Where  $\alpha_{uf}$  is the thermal expansion of the underfill,  $\alpha_{sold}$  is the thermal expansion of the solder, and  $\alpha_{eff}$  is an “effective” thermal expansion reflecting the in-plane forced deformation of the underfill layer in between the die and substrate. The shear and normal strain components are then used to calculate the effective plastic strain

$$d\varepsilon_p = \frac{\sqrt{2}}{3} \sqrt{d\varepsilon^2 + \frac{3}{2} d\gamma^2} \quad (2-9)$$

$$d\varepsilon^2 = (d\varepsilon_x - d\varepsilon_y)^2 + (d\varepsilon_y - d\varepsilon_z)^2 + (d\varepsilon_z - d\varepsilon_x)^2 \quad (2-10)$$

$$d\gamma^2 = d\gamma_{xy}^2 + d\gamma_{yz}^2 + d\gamma_{zx}^2 \quad (2-11)$$

The cycle to failure can then be calculated using Solomon's equation [70] that provides a relationship between the number of cycles to failure and equivalent plastic strain as shown in equation 2-12:

$$N_f = C(d\varepsilon_p)^n \quad (2-12)$$

With  $C$  and  $n$  are constants.

Regardless of the complexity of semi-empirical models to predict the plastic strain in solder joints certain limitations toward package type, loading environments, solder alloys will always be present. Accelerated testing between SnPb and SAC305 solders have shown SAC305 solder is more reliable than eutectic Sn37Pb solder alloy at more benign thermal environments but proves to be less reliable at more aggressive temperature ranges [71]. Capturing such complex behavior under thermal cycling requires a more accurate modeling of material behavior and geometry in addition to identifying a more suitable damage indicator to correlate with cycles to failure using empirical data.

#### *2.4.2 Numerical Models*

Numerical models provide a quantitative approach to predict failure in solder interconnects in electronic packages. FEA methods has been extensively used to investigate and optimize thermal and mechanical performance of electronic packages [72]. Through-out the decades many simulation techniques and model types have been used to analyze complex microelectronic packages. Some researcher found that thermal cycling simulations of flip-chip packages using simplified axisymmetric, 2D or strip

models can provide comparable fatigue life predictions [38]. Figure 2-16 below demonstrates the different model geometries of a PBGA package.

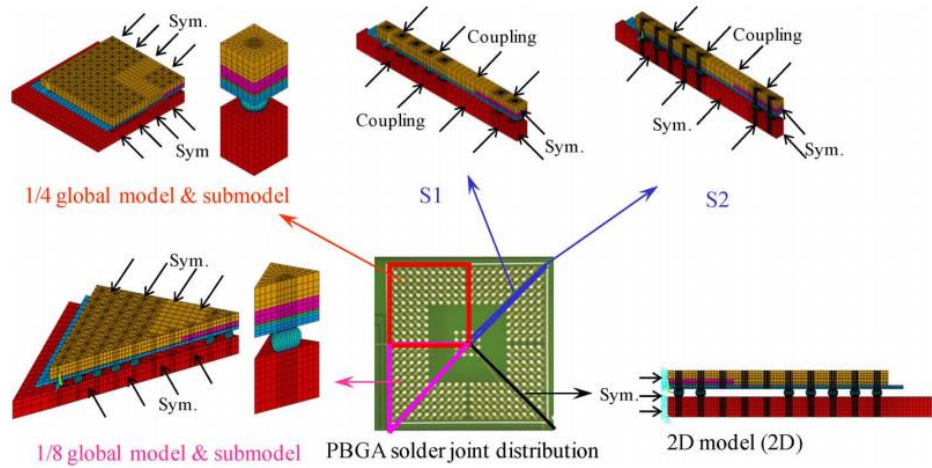


**Figure 2- 15: Several 2-D and 3-D FEA models of a PBGA package [74].**

In addition to modeling technique, constitutive material models of the solder alloy itself can account for a significant role on the accuracy of the prediction [75]. Fatigue life models implement a damage indicator that correlates with the number of cycles to failure. FEA simulations are used to approximate the value of the damage indicator that will be substituted into the fatigue equation. Coefficients in fatigue equations are calibrated using combination of empirical data and simulations. Therefore, experimental data of failure is necessary for any fatigue life prediction methodology and is not exclusive to semi-empirical models that were previously discussed.

One of the first energy-based models was developed by Morrow that predicted fatigue life by taking the plastic strain energy density as a damage indicator [76].

$$N_f^m W_p = C \quad (2-13)$$

Where  $m$  is the fatigue exponent and  $C$  is the material ductility coefficient. The plastic energy density  $W_p$  is obtained from the observed area of the hysteresis loop during cyclic

loading. Some of the popular energy-based fatigue models for SnAgCu solder in microelectronic were proposed by Schubert and Syed [77,78]. Equation x represents Schubert's model and equation x represents Syed's model.

$$N_f = 345W_{cr}^{-1.02} \quad (2-14)$$

$$N_f = (0.0019W_{cr})^{-1} \quad (2-15)$$

In both models the coefficients and exponents were determined by combining FEA simulations results and real test data. A notable difference between the two models is that Schubert's model was calibrated using failure data of flip-chip packages with underfill while Syed's data was calibrated using data from chip-scale packages. Both models used accumulated creep strain energy density as damage indicator. Other models partition the elastic, plastic and creep component responsible for accumulation of energy density as developed by Dasgupta [79].

$$1/N_f = 1/N_{fe} + 1/N_{fp} + 1/N_{fc} \quad (2-16)$$

This model predicts the creep-fatigue damage from the deviatoric energy densities of the elastic, plastic and creep components. The motivation behind energy partitioning is that plastic and creep deformation mechanism result in different types of material damage. Solder joints experience creep at elevated temperature and plastic deformation at colder temperatures. Dasgupta's model was calibrated using separate sets of cyclic tests on small scale test specimens at various temperatures and strain rates to account for creep and plastic deformation regimes [80].

Alternatively, Darveaux correlated measured crack growth data and correlated inelastic strain energy density in solder [81]. This method yielded in two models that predict number of cycles to crack initiation and crack propagation.

$$N_0 = k_1 \Delta W_{ave}^{k_2} \quad (2-17)$$

$$\frac{da}{dN} = k_3 \Delta W_{ave}^{k_4} \quad (2-18)$$

Where  $\Delta W_{ave}$  is the volume averaged inelastic strain energy density per stabilized cycle at the interface layer. The volume averaging calculation of energy density per element is carried out using the following equation.

$$\Delta W_{ave} = \frac{\sum \Delta W V}{\sum V} \quad (2-19)$$

Where  $\Delta W$  is the inelastic energy density accumulated per cycle and  $V$  is the volume of each element in the layer of interest. This model provided a set of empirical constants  $k_1$  through  $k_4$  for various modelling methodologies of geometry and solder constitutive model. The characteristic life can be predicted knowing the area of the solder joints through which crack will propagate to cause complete failure.

$$\eta_w = N_0 + \frac{a}{da/dN} \quad (2-20)$$

Where  $a$  is the solder joint diameter at the interface and  $\eta_w$  is the characteristic life. Since its inception, the Darveaux model was adopted for various BGA package types and solder alloys by calibrating the model constants using experimental data [82,83,84]. Each of the models discussed here can have advantages and limitations depending on the model methodologies, assumption and accuracy of the empirical data used for calibration of model parameters. Fatigue prediction of underfilled BGA packages can be carried using these models. Comparison of the Syed and Darveaux models will be performed in subsequent section for experimental data obtained in this

dissertation for BGA packages with reworkable underfill at different thermal environments.

## **MATERIAL CHARACTERIZATION**

### **3.1 Underfill Material Selection**

This chapter will discuss material selection and characterization of a variety of underfilling materials comprising of conventional reworkable epoxy underfills and high expansion materials such as acrylics, urethanes and silicones. Three materials groups will be individually characterized that pertain to three distinct thermal cycling experiments that are discussed in chapter 4.

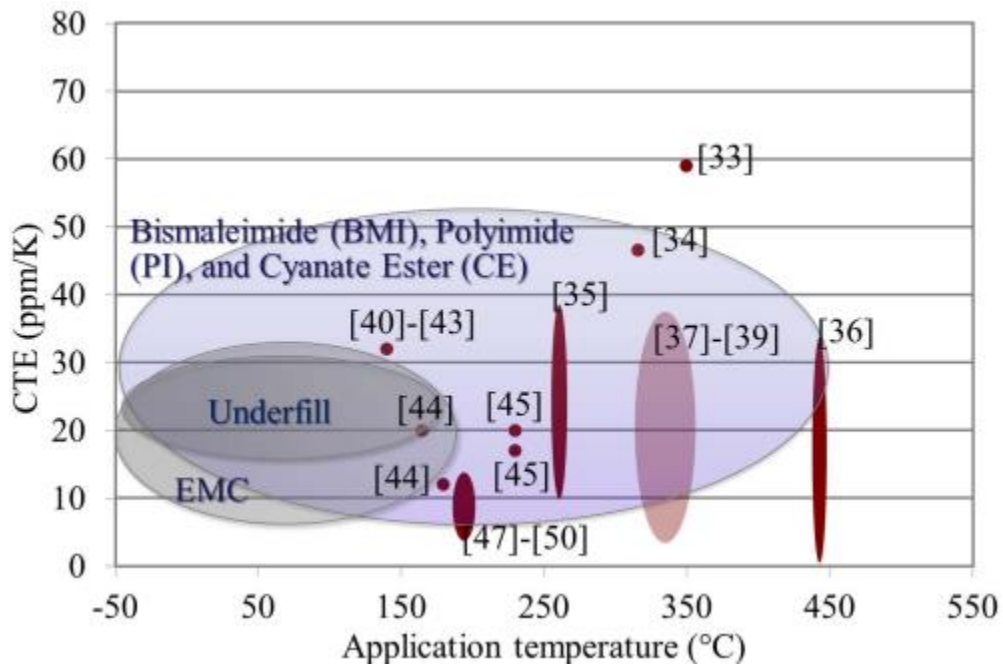
As previously discussed, conformal coating can intentionally or unintentionally flow under BGAs during processing. Coatings are used to protect PCBs and components from moisture, dust, vibration and chemical contamination in harsh end-use environments. Conformal coatings can be used in extreme chemical conditions and adverse environments. Coating can be applied to PCBs using a number of methods including spray, brush and dip coating. Some specialized coatings such as parylene are applied using a specialized vapor deposition process [85].

Commercial underfills and molding compounds typical CTE range per application temperature is shown in Figure 3-1. Low expansion underfills typically match the CTE of solder that is between 20-30ppm/°C. CTE for most molding compounds is usually under 20ppm/°C due to higher filler volume fraction compared to underfill materials. Most underfills are epoxy based but in some instances epoxy underfill are limited to



operating temperature of 200°C. Selection of underfill materials is specific to the device type, application and reliability requirements [86, 87].

The conformal coating selected in this study represent the most common commercially available materials used for protecting electronic devices from moisture and contamination. Each conformal coating material possesses unique properties. The main types of conformal coating used for underfilling BGA components are silicone, acrylic, urethane and epoxy. For the acrylic coating, Humiseal 1B31 was selected as it is a commonly used coating in the industry due to its easy application, favorable rework



properties and short cure time [88].

**Figure 3- 1: CTE and maximum operation temperature of commercial underfills and molding compounds [89].**

Hysol PC12-007M was selected for the epoxy group and provides good moisture, dielectric and abrasion resistance. Dow Corning 1-2577 is a silicone coating popular in high temperature applications due to its soft nature. Two urethane coatings Conatahen CE-1155 and Humiseal 1A33 were selected. Urethane coatings possess excellent

hydrophobic properties and moisture protection. The first group of materials comprised of conformal coatings is referred to as group A.

The second group of materials (Group B) used for underfilling consists of mixed lower expansion and stiffer materials shown in Table 3-1. The first material used is manufactured by United Adhesives EP1238 as a low viscosity epoxy adhesive for bonding electronic devices. This material can be cured at room and elevated temperatures. The second material is the Silicone conformal coating carried over from group A. The third material is a dedicated capillary reworkable underfill manufactured by Henkel Loctite 3808. The fourth material is Namics U8437-2 that is a high  $T_g$ , low CTE underfill. It offers Low-K protection and high temperature reliability. This underfill uses an epoxy-amine curing system with 55% weight filler particle. Both Loctite 3808 and Namics U8437-2 are one component heat cured materials. It is important to note that the Namics underfill has a 150°C cure temperature compared to Loctite 3808's 130°C cure temperature. This second group of materials was specifically selected with gradual variability in CTE and  $T_g$ .

**Table 3- 1: Material properties taken from manufacturer's data sheets.**

	Units	United Adhesive EP1238	Dow Corning 1-2577	Henkel Loctite 3808	Namics U8437-2
Viscosity	@ 25°C Pa.s	3000	750	360	65
Density	g/cm <sup>3</sup>	1.01	1.11	1.16	1.4
CTE	ppm/°C	75	200	55	35
$T_g$	°C	55	NA	113	128

Material selection of conventional reworkable underfill was necessary to provide a variety of material properties such as  $T_g$ , CTE and elastic modulus. All selected materials are commercially available underfilled designed for capillary flow

application specifically for BGA and flip-chip devices. Table 3-2 lists the volume fraction and size of filler particles in the selected underfill of group C. All materials were cast in bulk form for characterization were cured using the same conditions as board level underfilling applications for consistency. Both Henkel underfills used in the study have no filler materials while all three Namics underfills come with a filler content of 30 to 50 percent by weight. The Namics underfills used in this study are designed to be used in both flip-chip applications with narrow gap between the die and substrate as well as fine-pitch board level BGAs. The reworkable underfills are tailored for higher throughput and thermal cycling reliability requirements compared to the previous materials used for underfilling in this study.

**Table 3- 2: Properties of underfills provided by manufacturer data sheets.**

		<b>Namics SUF157 5-9</b>	<b>Namics XSUF159 4-6</b>	<b>Namics XSUF159 4-6F</b>	<b>Henkel E1216 M</b>	<b>Henkel 3808</b>
<b>Filler</b>	<b>Content (Wt%)</b>	<b>30</b>	<b>35</b>	<b>50</b>	<b>0</b>	<b>0</b>
	<b>Size (mean)</b>	<b>0.6</b>	<b>2</b>	<b>2</b>	<b>0</b>	<b>0</b>
	<b>Size (max)</b>	<b>3</b>	<b>10</b>	<b>10</b>	<b>0</b>	<b>0</b>
<b>Curing Condition</b>	<b>Temperature/Time</b>	<b>130°C/15 minutes</b>				
<b>Viscosity</b>	<b>@25°C Pa.s</b>	<b>3.5</b>	<b>0.6</b>	<b>2.0</b>	<b>4.0</b>	<b>3.6</b>
<b>Density</b>	<b>g/cm<sup>3</sup></b>	<b>1.4</b>	<b>1.4</b>	<b>1.5</b>	<b>1.4</b>	<b>1.4</b>

### 3.1.1 Sample Preparation for Characterization

A total of 13 materials were characterized to determine their temperature dependent elastic modulus and CTE. Temperature dependent elastic properties were determined using thin strip tensile specimens. The conformal coating materials were first cast into plastic container and cured at room temperature over night as shown in Figure 3-2.

After the bulk conformal coating were fully cured, they were cut into thin strips using a Buhler Isomet low speed cutting saw.

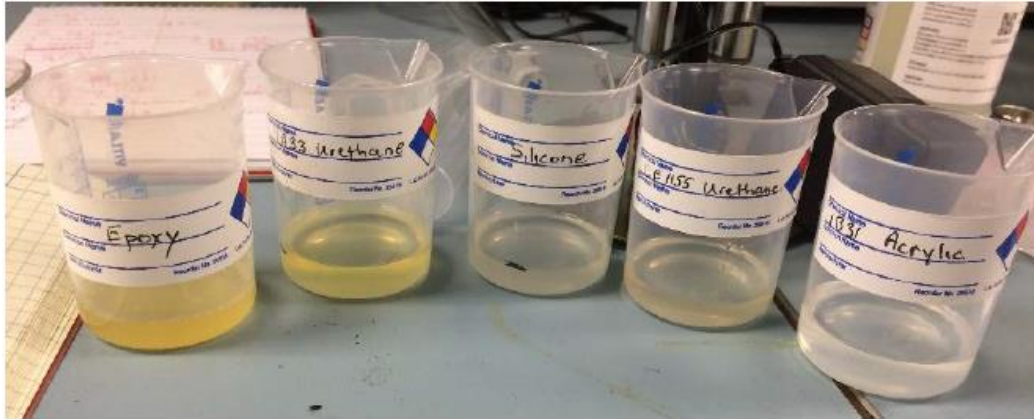


**Figure 3- 2: Conformal coating materials poured and cured for testing.**

Underfill materials from Group B and C were also cast and cured into bulk vessels and cut into smaller strips using the low speed saw. Figure 3-3 illustrates the bulk specimen of Loctite 3808 one part reworkable underfill. Thin strip specimens for plasticity and creep testing were cut from the these bulk castings. No mold release agents was used during the curing of the bulk underfill since it has been previously shown to chemically alter the surface of the underfill samples [90]. Instead, the underfills were cast and cured in thin aluminum foil pants that are easily peeled off after the curing process. To obtain the necessary thickness for the thin strip sample geometry another fixture was prepared to obtain consistent geometry from sample to sample. A stainless-steel fixture was prepared by laser etching thin grooves into the surfaces of the block as shown in Figure 3-4. The etched reliefs of the stainless-steel block are designed to hold the strip of underfill material during grinding procedure. After the thickness of an individual strip was achieved, the sample was inserted into the thinner grooves that held the sample during the second grinding step that achieved the desired sample width.

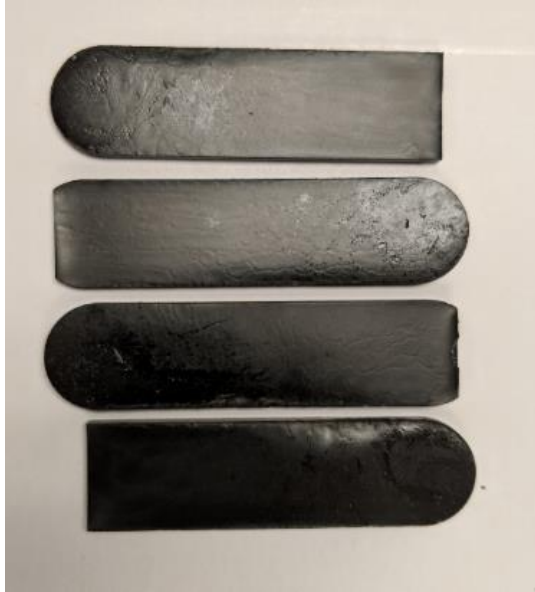


**Figure 3- 3: Cured bulk specimen of Henkel 3808 for creep and plasticity testing.**

Grinding of thin strip samples to required thickness and width was accomplished using an Allied M-PREP manual polisher with 600 grit sanded paper at a speed of 150 rpm. The fine grit and velocity of the polishing head provides a consistent sample variation and does not grind away the hard surface of the stainless-steel fixture.

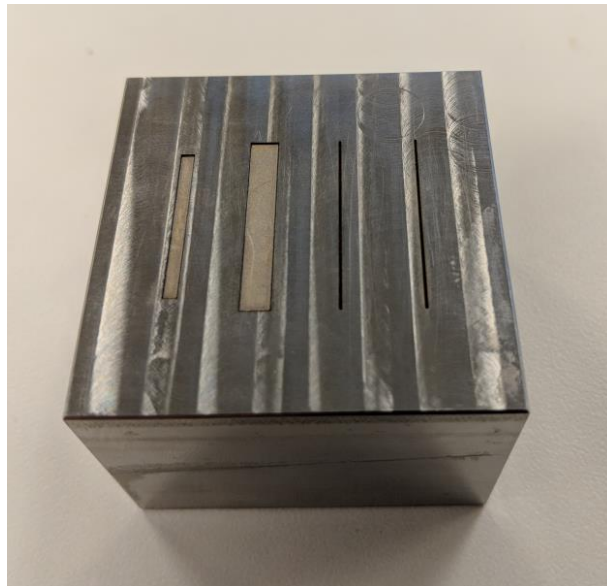


**Figure 3- 4: Stainless steel mold block for underfill sample preparation**

The final specimen geometry is shown in Figure 3-5. Wider 3.5mm samples of all materials were used for temperature dependent modulus measurements while the narrower 1.5mm samples were used for plasticity and creep tests. Any notches and inconsistencies in the samples were cut off prior to testing.

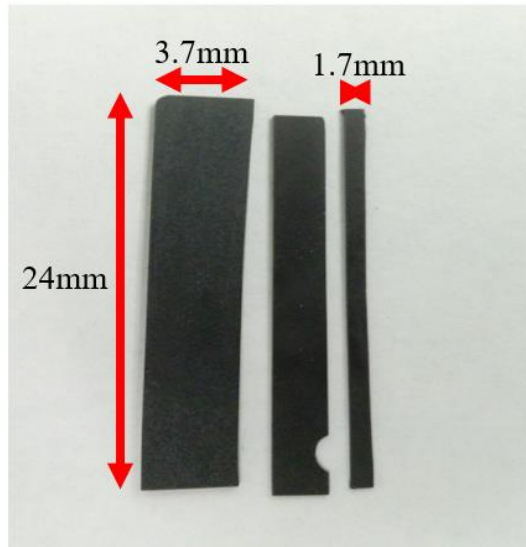


**Figure 3- 5: Final shape of Henkel 3808 underfill samples for characterization.**

## **3.2 Inelastic characterizations of a reworkable underfill**

### *3.2.1 Temperature Dependent Elastic Properties*

Temperature dependent elastic modulus and CTE of all materials used in this study were measured using TA Instruments RSA3 Dynamic Mechanical Analyzer (DMA) and TA Instruments Q400 Thermomechanical Analyzer (TMA), respectively. CTE measurements using the TMA device were performed using a temperature ramp rate of 3°C/minute. A constant compressive force was applied to material samples using the TMA probe during temperature ramp. The constant force varied between materials as to avoid probe penetration in the sample for the softer materials.

Elastic modulus was determined using the DMA device by applying a linear heating rate to the thin strip sample at a rate of 3°C/minute. DMA measures the stiffness and damping of materials under oscillating sinusoidal force. This allows for the material response to be represented as in-phase component by the storage modulus and an out-of-phase component by the loss modulus shown in Figure 3-6. The storage modulus often represented by  $E'$  provides a measure of the materials elastic response while the loss modulus represented by  $E''$  provides a measure on the dissipated energy of a material.

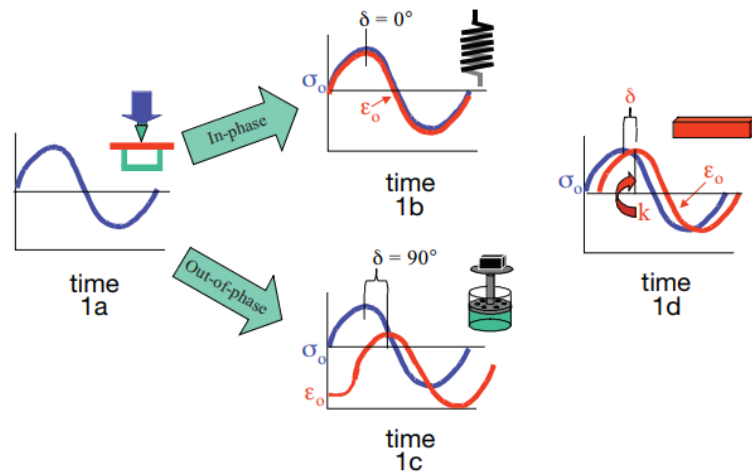


**Figure 3- 6: Principles of DMA [91]**

The elastic modulus can be calculated from the loss ( $E''$ ) and storage ( $E'$ ) moduli using equation 3-1:

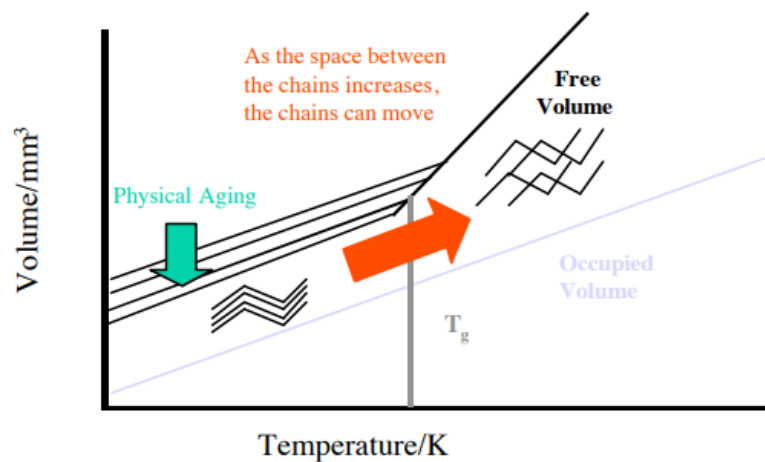
$$E = (E'^2 + E''^2)^{\frac{1}{2}} \quad (3-1)$$

Temperature sweep is performed on materials during DMA to determine the glass transition region. This transition region often differs between TMA and DMA as they measure different physical processes to each other. Changes in the CTE in polymers tend to be driven by changes in the free volume while change in the modulus tend to

be driven by increase in translational and rotational movement of the polymer chain. Change in CTE tends to initiate before a significant decrease in the modulus since lower levels of energy are required to increase the free volume compared to increase motion along polymer chain

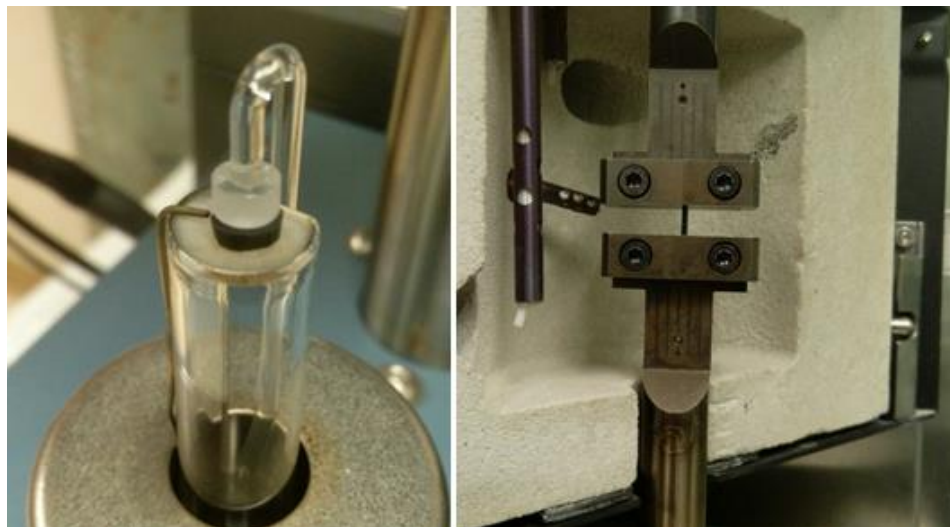
The glass transition in thermosetting polymers that is observed with a DMA in reduction of the storage modulus is driven by change in the molecular mass. This transition occurs between a phase change from a crystalline to a rubbery state. In addition to a phase change, a melting and freezing behavior can occur that mimics the glass transition but occurs at different temperatures.

TMA works by measuring a sample height during temperature change. Changes of polymeric materials height during expansion or contraction are driven by changes of the free volume of the polymer. TMA is used primarily for determining the CTE and  $T_g$  of polymers along with information on the viscoelasticity of materials. Figure 3-7 illustrates the transition of these properties driven by changes in the free volume. Isotropic materials are measured by single dimension change such as sample height.



**Figure 3- 7: Volumetric expansivity with temperature for polymers [92].**





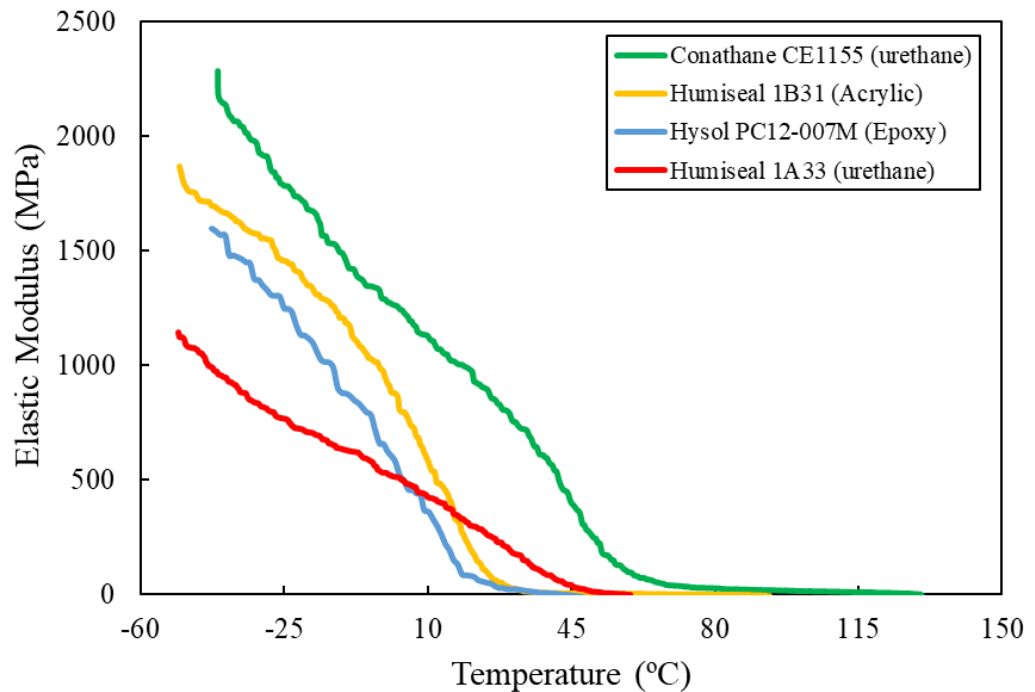
**Figure 3- 8: CTE measurements using TMA (left) and modulus measurements using DMA (right).**

Figure 3-8 illustrates the TMA quartz glass stage and probe with underfill sample on the left side and a sample of underfill loading in the DMA device for measuring the elastic modulus. In both devices, thermocouples are placed as close as possible to the sample surface to ensure consistent temperature reading. Figure 3-9 illustrates the change in elastic modulus with temperature for the four conformal coating materials for which the CTE was determined using the previously described procedure. These materials exhibit a stable linearly decreasing modulus with temperature up to the onset of their respective transition region at which the elastic modulus decrease by an order of magnitude. The end of the glass transition region for Humiseal 1B31, 1A33 coincides with the material's melting point at which complete liquid state is achieved preventing measurement and resulting in fracture or overextension of the thin film samples. DMA tests were performed using TA instruments RSA3 DMA with 3°C/minute ramp for all measurements. Measured CTE, modulus and  $T_g$  values of conformal coating of Group A materials is listed in Table 3-3.

**Table 3- 3: Group A conformal coating material properties.**

Material	Commercial Name	Tg (°C)	CTE (ppm/°C)	E (MPa)
Silicone	Dow Corning 1-2577	-90	210	350
Epoxy	Hysol PC12-007M	26	83	2500
Acrylic	Humiseal 1B31	15	145	1800
Urethane 1	Humiseal 1A33	57	124	1600
Urethane 2	Conathane CE-1155	37	95	2180

The elastic modulus of each conformal coating reported in Table 3-3 is taken from the lowest measured temperature to demonstrate the large difference in material crystallinity at cold temperatures. Polyurethane demonstrates the largest elastic modulus at cold temperature while the silicone exhibits the lowest elastic modulus. The epoxy conformal coating possesses the lowest CTE with the silicone having the highest expansion.



**Figure 3- 9: Temperature dependent elastic modulus of group A conformal coating materials.**

Figure 3-11 illustrates additional DMA measurements for various potting and underfill materials used in the second thermal cycling test (experiment B). The Dow Corning

Silicone exhibits an unusually high melting temperature at approximately 50°C. The Silicone conformal coating  $T_g$  was measured to be about -90°C using TMA. Materials with experiment B were selected with larger variation in mechanical properties as those for experiment A to induce a higher variation in mechanical stresses. Variation in modulus at room temperature between the stiffest and softest materials accounts for about 35X and change in their CTE is approximately an order of 6.6X. The measured elastic modulus of the silicone and urethane conformal coatings is found to be in agreements with those obtained for similar materials [93].

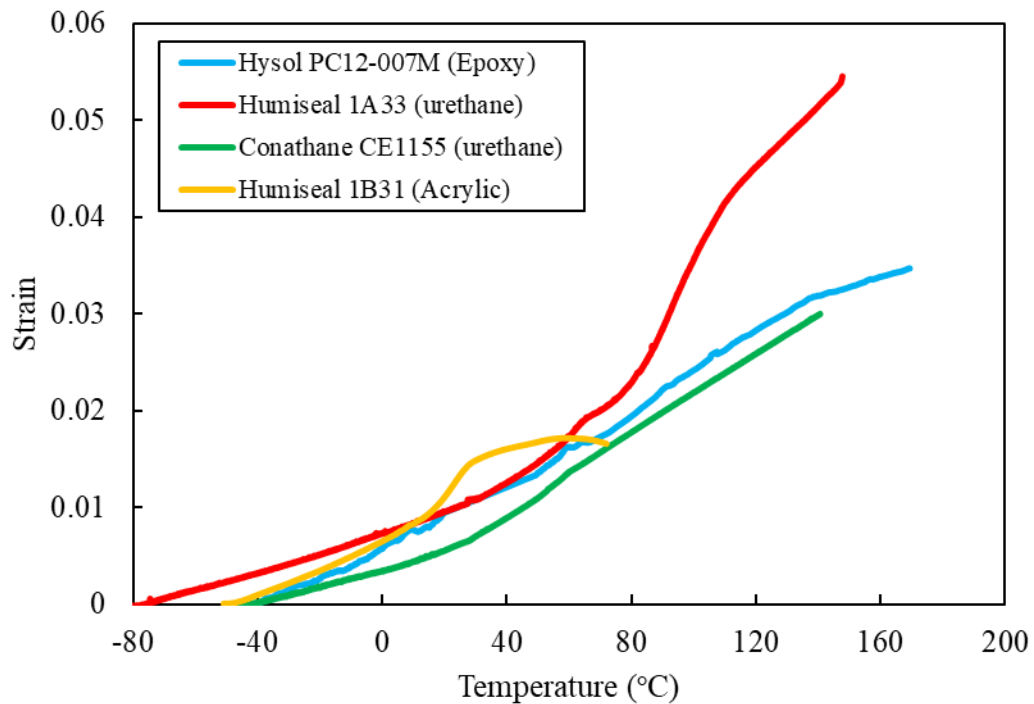


**Figure 3- 10: Strain vs. temperature of group A conformal coating materials.**

The linear CTE is calculated by determining the slope of the strain vs. temperatures curve measured by the TMA. The first method to calculate the CTE from the slope of the strain vs. temperature curve is called the differential CTE. A second method to calculate the CTE is called the mean CTE show in the following equations.

$$\bar{\alpha}(\Delta T) = \frac{1}{l_o} \cdot \frac{l_2 - l_1}{T_2 - T_1} = \frac{1}{l_o} \frac{\Delta l}{\Delta T} \quad (3-2)$$

$$\alpha(\Delta T) = \frac{1}{l_o} \cdot \frac{dl}{\Delta T} \quad (3-3)$$

Where  $l_2$  is the length increment for a given temperature increase of  $T_2$ . When the material crosses the  $T_g$  the strain vs. temperature curve deviates from linearity and can result in erroneous calculation of CTE. Therefore, the differential CTE was calculated for all materials in this study using the differential method. Figure 3-11 shows temperature dependent elastic modulus and CTE of group B materials superimposed on the same temperature scale. This behavior demonstrates that higher changes in the CTE occurs prior to sufficient reduction of the elastic modulus occur within the transition region.

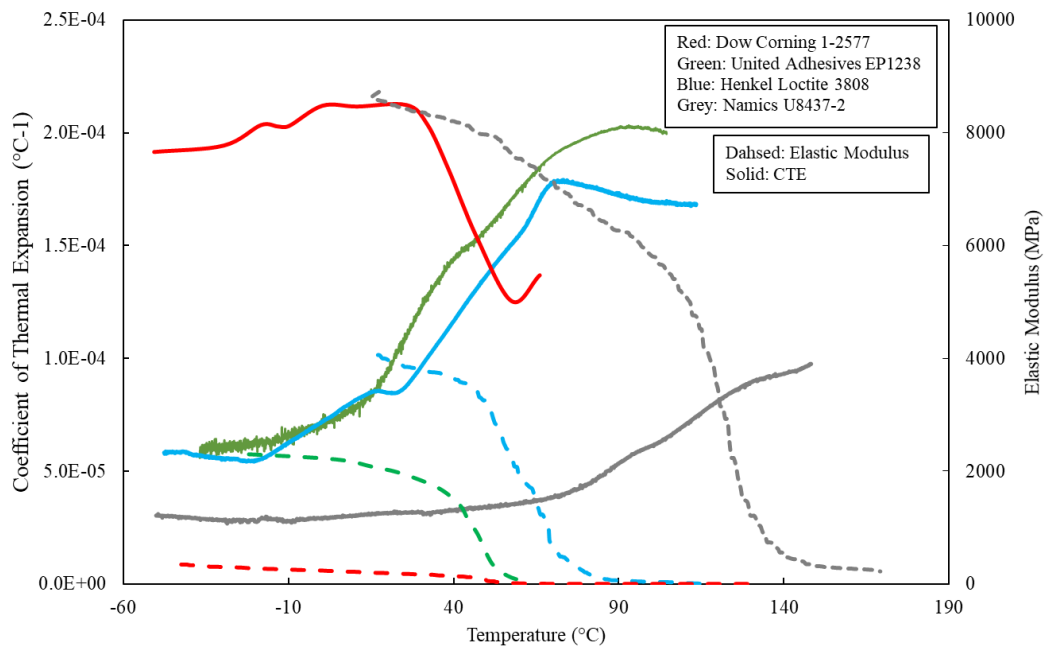


**Figure 3- 11: Temperature dependent CTE and modulus of group B Underfills.**

A notable decrease in the silicone conformal coating CTE and modulus is observed at a temperature of 45°C. This transition occurs due to material crossing the melting point.

The melting point of the silicone further decreases the elastic modulus beyond the point to carry the weight of the quartz probe from free thermal expansion. As a result, the quartz probe sinks into the sample and measures decrease in thermal strain. Additional material properties such as Poisson's ratio has been shown to change with temperature for epoxy resin. Some epoxy resins demonstrate a Poisson's ratio of around 0.5 at the material  $T_g$  [94]. This behavior is indicative of rubbery materials that exhibit nearly incompressible behavior.

Temperature dependent material properties of group C materials is shown in Figure 3-12. In this group a higher consistency between the CTE and modulus is observed with lower variation in materials  $T_g$ .

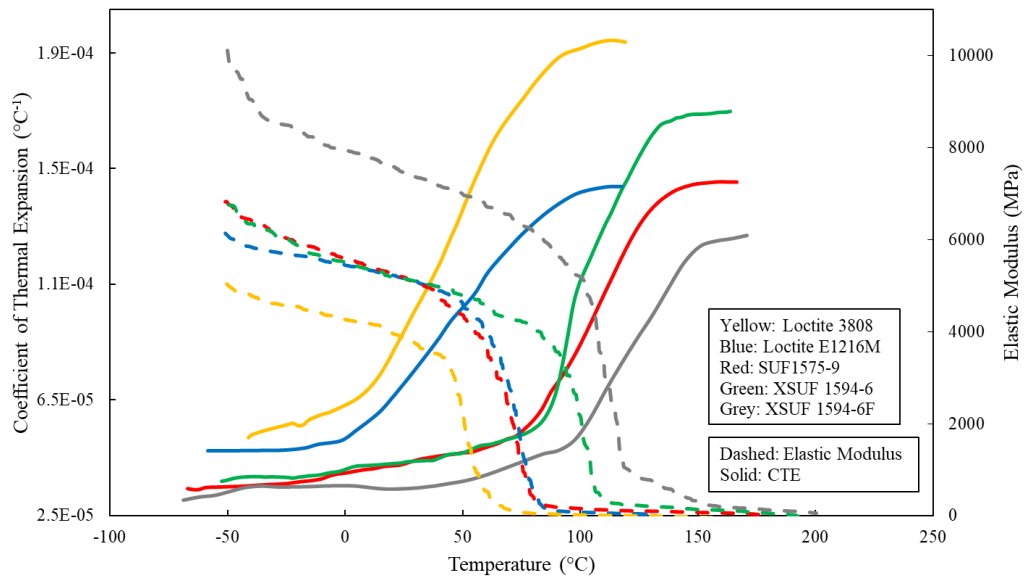


**Figure 3- 12: Temperature dependent CTE and modulus of group C reworkable underfills.**

Most of the epoxy underfills in group C demonstrate similar behavior in which the  $T_g$  from TMA was found to be lower than that of DMA measurements. Interestingly, only the Namics XSUF 1594-6F demonstrates a higher  $T_g$  from TMA compared with that

measured using the DMA. Consequentially, the XSUF 1594-6F demonstrates the higher  $T_g$  amongst the group C materials; although Namics U8437-2 from group B has a higher  $T_g$  and does not follow the same trend. This behavior is believed to belong to the specific chemical formulation of each proprietary underfill material.

### 3.2.2 Plastic deformation

Plastic deformation of Henkel 3808 was measured using the TA Instruments RSA3 DMA device that was used to measure temperature dependent elastic modulus for the same underfills. Modeling plastic behavior of underfills has been shown to fit an empirical three-parameter hyperbolic tangent model that can capture that nonlinear stress-strain curves shown by equations 3-4 and 3-5 [95].

$$\sigma(\varepsilon) = C_1 \tanh(C_2 \varepsilon) + C_3 \varepsilon \quad (3-4)$$

$$E = C_1 C_2 + C_3 \quad (3-5)$$

Where  $C_1$ ,  $C_2$  and  $C_3$  are all material constants. These three constants are determined using a nonlinear regression analysis through experimentally obtained stress-strain curves. Constants for the three-parameter hyperbolic tangent models are unique for every strain rate and temperature combination. Specimen used for monotonic tensile loading had a gauge length of 10mm, thickness of 0.20mm and a width of 1 mm. Figure 3-13 illustrates a failed specimen of Loctite 3808 loaded monotonically in tension with the breaking point at the center of the gauge length. Three or more replicants were performed at each temperature and strain rate until consistency in the stress-strain response was observed. Due to the rectangular sample geometry there was no distinct stress concentration region for necking to occur. Data from samples that fractured at

one of the clamping points were dismissed. Failure of the specimen other than at the center of the gauge length in rectangular samples is a result of sample alignment, variation in the grip pressure and or differences in material properties within the samples. Underfills samples that were used for characterization were not annealed after sanding to achieve final thickness. It is assumed that any residual stress in the underfill material introduced into the bulk sample during the cure process was relieved during singulation process using the low speed saw. Therefore, the polishing is believed to have no further influence on the residual stress state of the prepared samples.

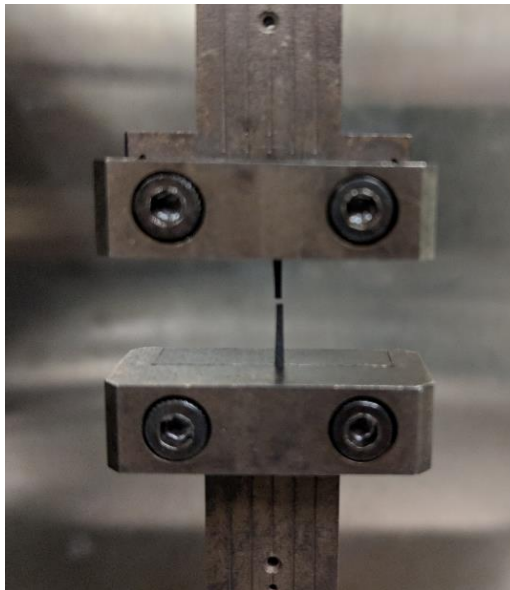


**Figure 3- 13: Sample of Henkel 3808 under monotonic tensile loading.**

Figure 3-14 shows the measured engineering stress and strain for Loctite 3808 at a strain rate of  $10^{-3}$  at different temperatures. The underfill exhibits small plastic deformation and low strain to failure below the  $T_g$ . As soon as the temperature increases above the underfill's  $T_g$  flow stress decreases dramatically and the ductility increases by an order of magnitude. This behavior demonstrates the drastic temperature dependent plastic flow behavior of the reworkable underfill. At temperature below the

glass transition the material exhibit a glassy brittle like behavior that is exacerbated by the lower strain to failure compared to elevated temperatures. At temperature above 80°C the flow stress is not possible to achieve due to the rubbery almost liquid like state of the material.

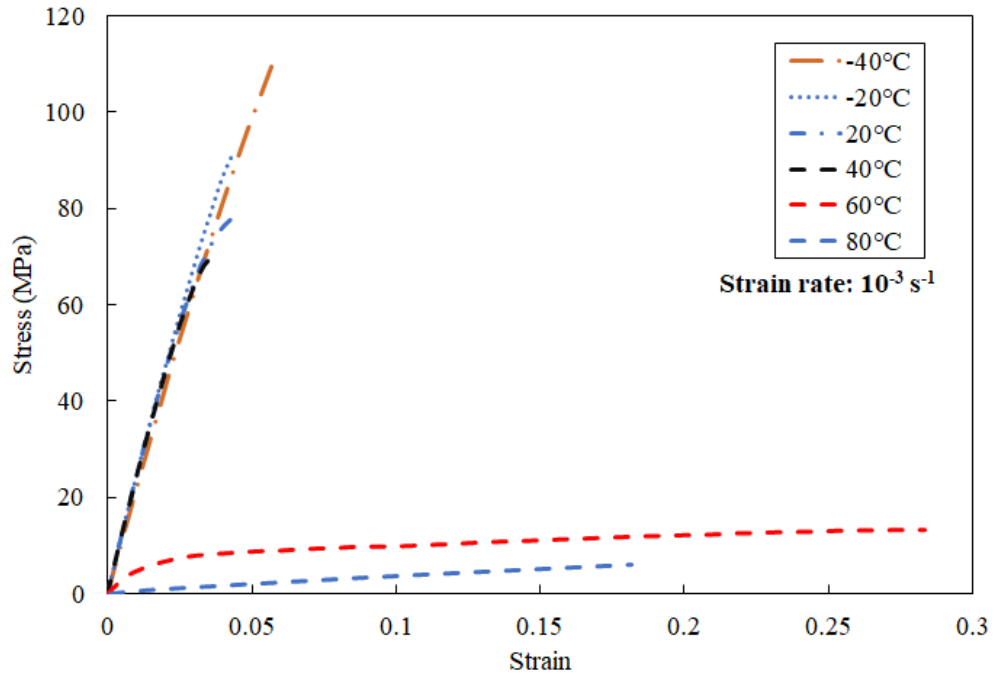


**Figure 3- 14: Stress-strain curves of Loctite 3808 at strain rate of  $10^{-3}$  and various temperatures.**

Strain rate sensitivity of polymers is an important aspect for accelerated life testing.

Accelerated thermal cycling

As strain rates decrease the potential energy required to promote rotational and translational motion of the chain segments is reduced. This causes reorientation of the chain segments that relieve local strain imposed by the stress [96]. The increase in temperature enables the material to change from the glassy to rubbery state due to the distortion of the cross-linked network of polymer long molecular structure.



### 3.2.3 Creep Deformation of Reworkable Underfill

Measurements of creep deformation was performed using TA Instruments Q800 DMA as shown in Figure 3-16. Samples for creep testing were similar to dimensions of specimen used for plastic deformation but with a larger width of 3mm to prevent prematurely rupturing the samples at higher temperatures and stress levels. Performing creep experiments past the underfill materials  $T_g$  require careful monitoring of the load level during test to prevent unintended failure of the specimen. Figure 3-16 illustrates comparison between steady state creep rate as a function of stress and temperature. Equations 3-6 and 3-7 are the Norton's power law and the Arrhenius power law equations [97]. These equations provide a rudimentary behavior for creep activation.

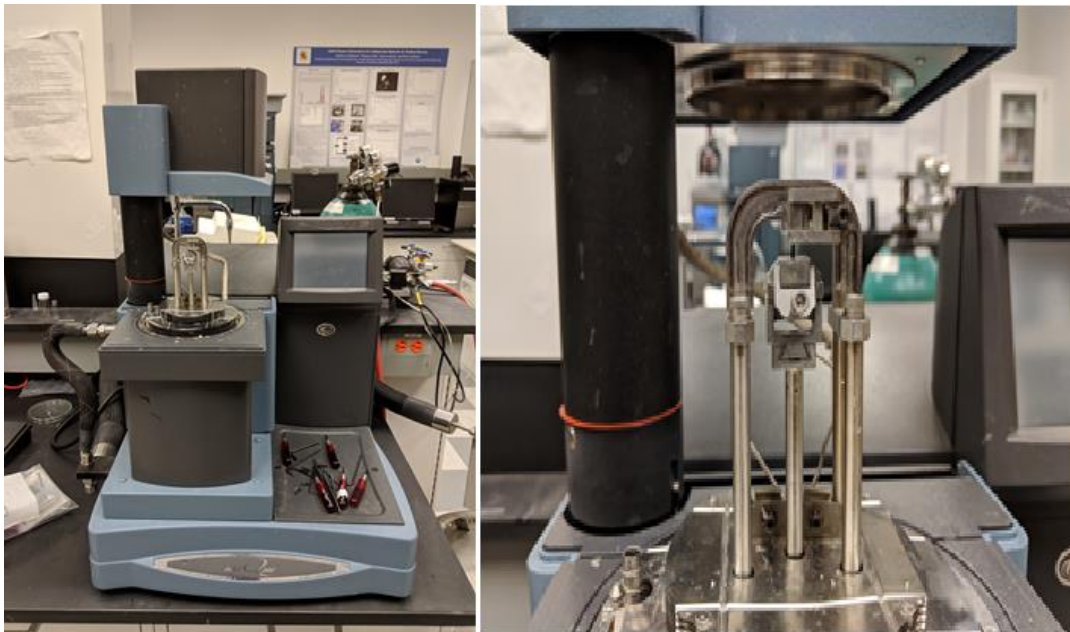
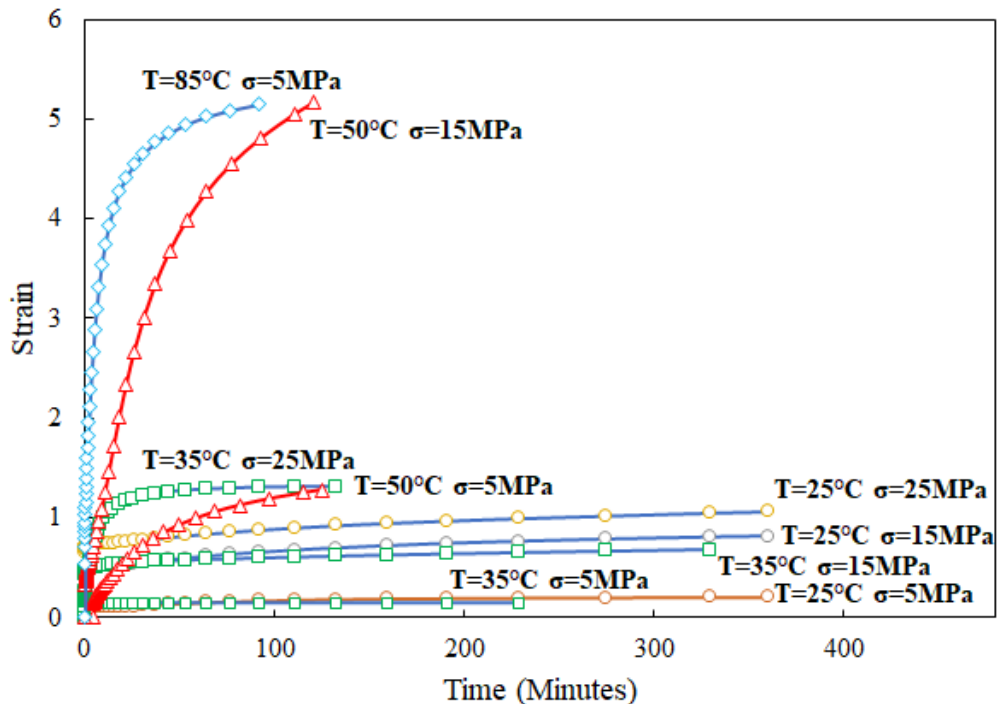


**Figure 3- 15: DMA Q800 (left) with Henkel 3808 underfill sample loaded in tensile fixture (right).**

$$\dot{\epsilon}_S = A_1 \sigma^n e^{\left(-\frac{Q}{RT}\right)} \quad (3-6)$$

$$\dot{\epsilon}_S = A_2 \frac{E}{T} \left( \frac{\sigma}{E} \right)^n e^{\left( -\frac{Q}{RT} \right)} \quad (3-7)$$

Where  $n$  is the stress exponent,  $Q$  is the activation energy,  $R$  is the Boltzmann's constant, and  $A_1$  and  $A_2$  are constants. Figure 3-17 shows these two equations in logarithmic form with a linear relationship between creep strain rate and applied stress. The slope of the curve represents the stress exponent  $n$  that increases with temperature indicating dependence on creep flow mechanism. The creep curves shown in equation 3-16 demonstrate samples that achieved creep rupture at higher stress and temperature levels as well as ones that did not fracture and achieved steady-state strain rate. A direct



comparison between samples that achieved creep rupture and ones that achieved steady state creep strain rate and did not fail during the test duration is not practical as it compares two distinct creep mechanism responsible for secondary (steady-state) and tertiary creep regimes.

**Figure 3- 16: Creep deformation of Loctite 3808 underfill.**

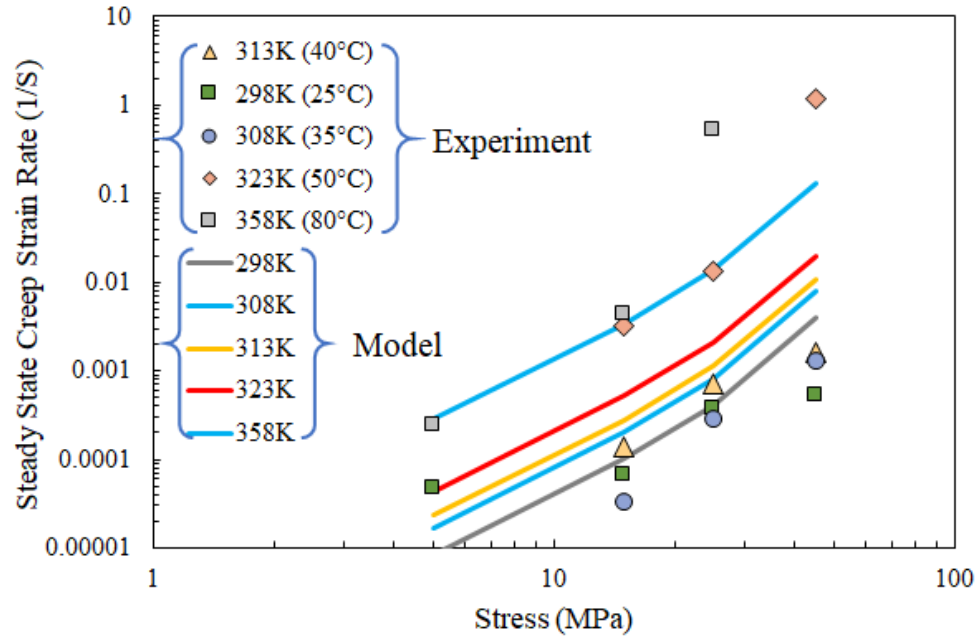


**Figure 3- 17: Steady state creep behavior of Loctite 3808 underfill.**

The logarithmic steady state creep strain rate is plotted vs the reciprocal of the absolute temperature in figure 3-18. The ratio between activation energy and Boltzmann's constant corresponds to the slope of the linear relationship between creep strain rate and the reciprocal of the absolute temperature in Norton's law and the Arrhenius equation. The slope of this curve varies with temperature non-linearly as function of

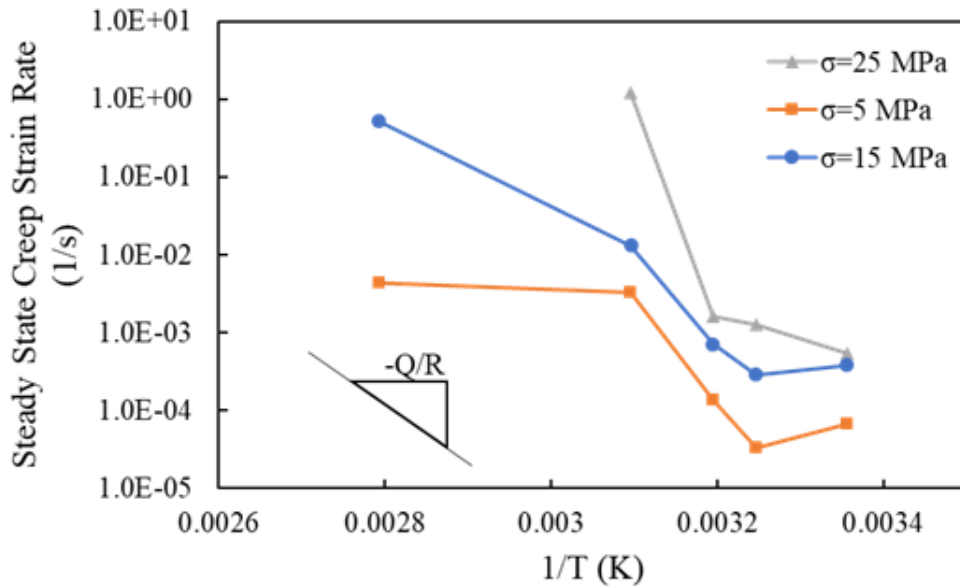


**Figure 3- 18: Steady state creep strain rate vs. 1/T(K).**

temperature or stress level which means that there could be more than one process driving creep deformation mechanism throughout the temperature range as the underfill crosses the  $T_g$ . This means that the Arrhenius equation and Norton's law are not suitable for modeling the creep behavior of reworkable underfill. The power law breakdown phenomenon can be evident from the temperature dependent  $n$  value shown in Figure 3-17. To capture the power law breakdown behavior a single hyperbolic sine power expression can be used as in equation 3-8:

$$\dot{\epsilon}^{cr} = A_1(\sinh\alpha\sigma)^n \exp\left(-\frac{Q}{RT}\right) \quad (3-8)$$

Fitting the hyperbolic sine equation to the test data provides the following coefficients for the reworkable underfill Loctite 3808 listed in Table 3-4.

**Table 3- 4: Coefficient for hyperbolic sine model for Loctite 3808.**

Underfill	$A_1(K/S/MPa)$	$\alpha (MPa^{-1})$	$n$	$Q$ KJ/mol
Loctite 3808	0.005	0.028	2.2	6.5

Underfill materials are exposed to isothermal aging conditions during the repeated high temperatures dwells in thermal cycling conditions. It has been shown that an increase in effective elastic modulus and ultimate tensile strength with the isothermal aging time or temperature regardless if it occurs below or above the underfill  $T_g$  [98]. In addition, thermal aging has also been found to significantly reduce the steady state creep rate of underfills. From Figure 3-17, the hyperbolic sine model is found to fit well with the creep behavior of reworkable underfills below the  $T_g$  while a significant deviation of model occurs at temperatures above the  $T_g$ .

### 3.3 BGA Package Material Characterization

Temperature dependent material behavior of other package constituents are important to know in order to fully determine the factors responsible for inducing strain on BGA solder joints. The largest components are the BGA package materials and PCB to which the package is soldered to. The dummy BGA package analyzed in this dissertation is comprised of a an over molded silicon die that is soldered to an organic substrate using a silver sintered die attach adhesive. Deconstruction of the BGA package was performed in order to measure the temperature dependent elastic properties that will be later implemented in simulations. Figure 3-19 illustrates sequential images of a planar grinding process used to separate the mold compound from the substrate. The grinding process is destructive and only one package material is able to be extracted from a single BGA component.

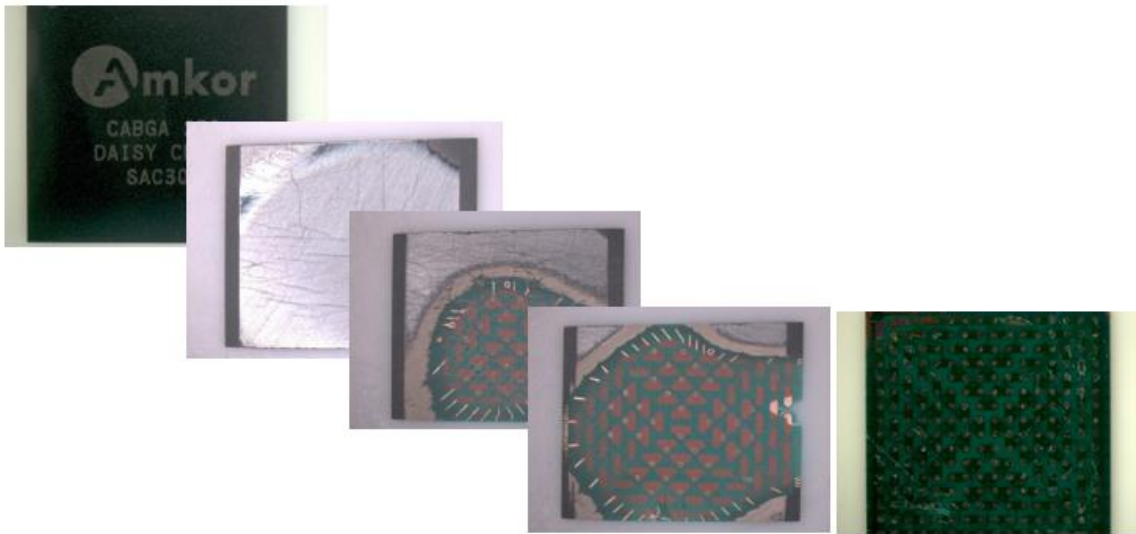


**Figure 3- 19: BGA package deconstruction process using serial grinding steps.  
Steps.**

The two packaging materials that were able to be characterized using the methods used in this study are the over mold material and organic substrate of the BGA package. The

total package thickness of 1.0mm means that the substrate and overmold thickness after planar grinding results in extremely thin samples. Measurement of such thin samples requires delicate manipulation during tests. Both the substrate and mold compound were then cut into thin strip specimen for DMA testing. Measurements of the PCB using DMA was performed with three-point bending fixture. Tensile loading of the PCB in the RSA3 DMA was not possible as the force necessary to perform the measurements exceeds the devices load cell limits. Therefore, the three-point bend shown in Figure 3-21 provides a suitable configuration to test the elastic modulus.

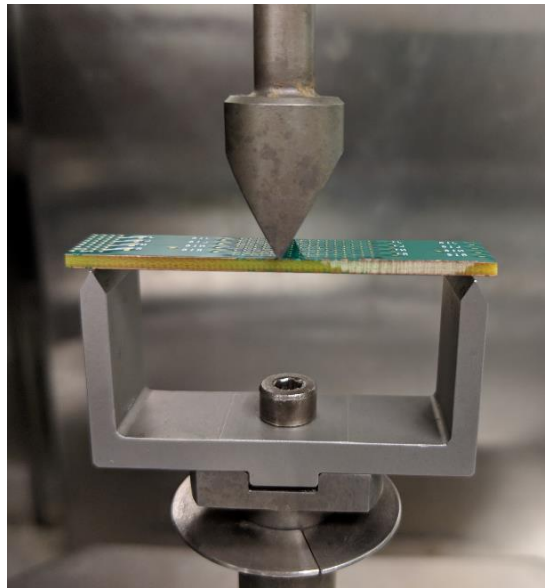


**Figure 3- 20: PCB sample tested with DMA Three-point bending fixture.**

The CTE of the PCB test board was measured to be 15.6 and 17. ppm/°C in the in-plane directions using TMA. Figure 3-21 shows the temperature dependent properties of the BGA overmold material. Overmold materials are highly filler epoxy resins that provide strong coupling to BGA substrate and die during the mold transfer process.

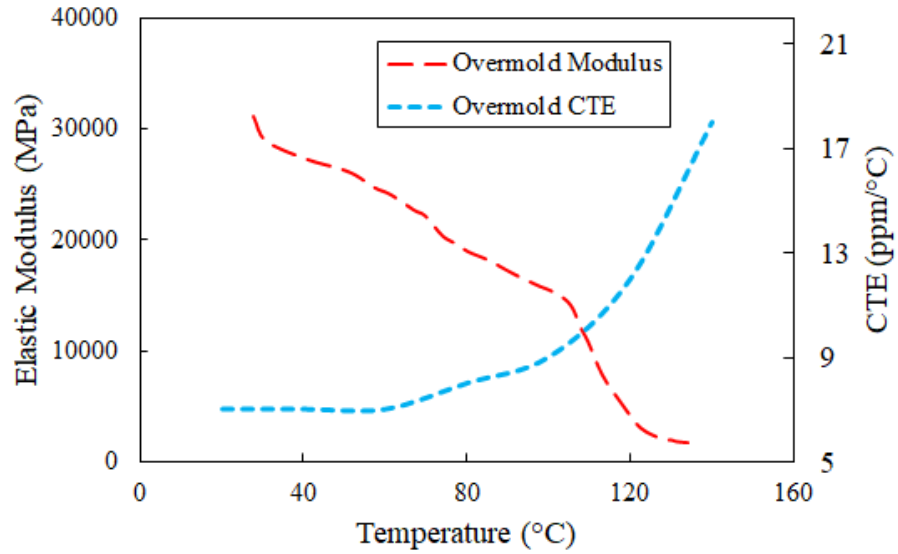


**Figure 3- 21: Temperature dependent elastic modulus and CTE for BGA mold compound.**

Temperature dependent materials properties of the BAG substrate were performed up to a temperature that is below the substrate  $T_g$ . The in-plane CTE of the substrate was found to be within 18-20ppm/°C with an elastic modulus of 14 GPa that did not vary much throughout the temperature range of -40°C and 120°C. To verify the effective CTE of the BGA package a sample of the BGA was cut in half and placed under the probe of the TA as shown in Figure 3-22. Cutting of the BAG package can relieve some of the internal stresses of the package and alter the measurement of the effective properties

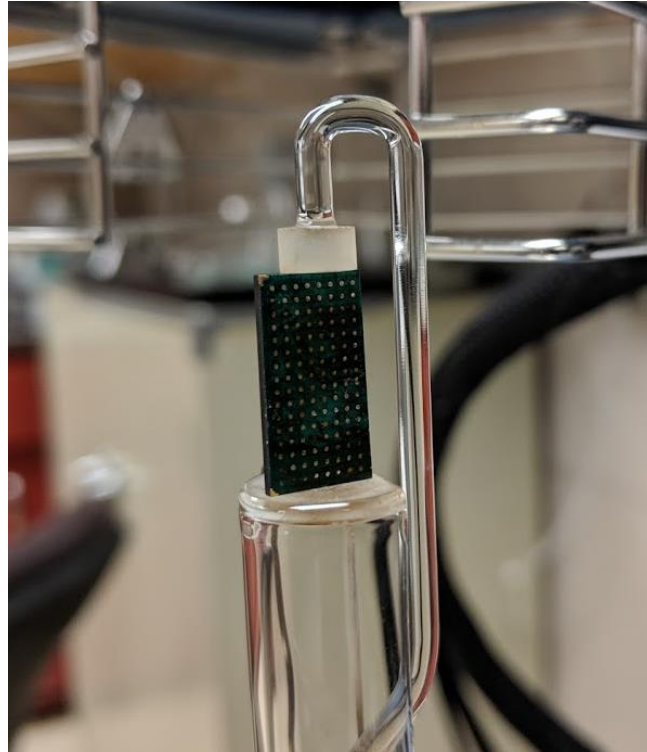


**Figure 3- 22: Measurement of package Effective CTE using TMA.**

Measurement of the effective property was performed for verification of modeling accuracy by implementing the material properties that were determined from individual package constituents during the deconstruction process. A simple, half symmetric model was constructed to simulate the thermal expansion of the BGA package using inputs obtained from the BGA mold and substrate. Silicone die was assumed to have a CTE of  $2.6\text{ppm}/^{\circ}\text{C}$  with an elastic modulus of 130 GPa. Figure 3-23 shows the measured and modeled temperature dependent CTE of the BGA package. A large decrease in strain is observed around the  $T_g$  of the mold compound that indicates a possible inflection point.



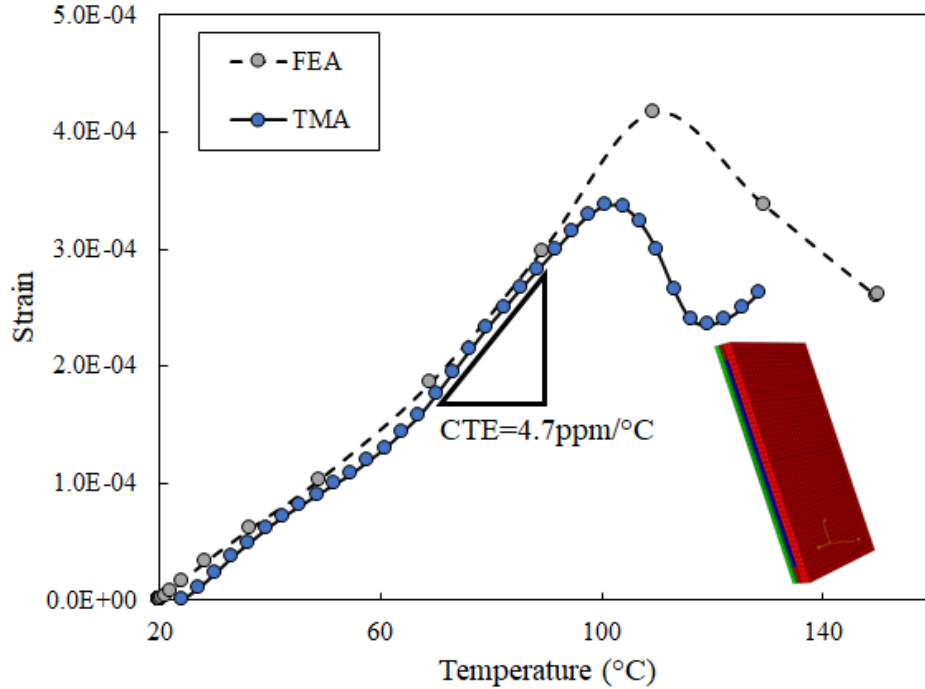


**Figure 3- 23: Comparison between measured and calculated effective BGA package CTE.**

The reason for the inflection point can be attributed to change in the package characteristic warpage that results in the strain decreasing under the TMA probe force and then increasing again. A similar increase past the mold compound Tg is not captured in the FEA since the exact probe force contact was not simulated and the effective CTE of the package increases while the effective modulus decreases.

### **3.4 Pb-free Solder Alloy**

The SnPb eutectic consists of solid solution strengthened Sn and Pb mixed crystals that have similar deformation resistance. The biomaterial system of Sn, Ag and Cu solidifies in a complex system forming various intermediate phases namely Ag<sub>3</sub>Sn and Cu<sub>6</sub>Sn<sub>5</sub>. The deformation resistance of these intermetallic phases is significantly higher than the β-Sn matrix surrounding them. As plastic deformation occurs,

dislocations are arrested or pinned down as they reach the hard-intermetallic phases increasing the creep deformation resistance forcing dislocations to climb around the hard particles.

Wiese et al. found that an improved accuracy in simulation of stress-strain hysteresis behavior can be obtained when plastic flow incorporated into the finite element model [99]. In their experiments, three specimen types of SnAg and SnAgCu solder were tested for creep characterization. Although, the microstructure of the specimens was significantly different, a good agreement in creep behavior was found for the SAC solder. The proposed double power law creep model was found to fit well with the three data sets shown in equation 3-9.

$$\dot{\varepsilon}_{cr} = A_1 \left( \frac{\sigma}{\sigma_N} \right)^{n_1} \exp \left( -\frac{Q_1}{RT} \right) + A_2 \left( \frac{\sigma}{\sigma_N} \right)^{n_2} \exp \left( -\frac{Q_2}{RT} \right) \quad (3-9)$$

Where  $Q_1$  and  $Q_2$  are the activation energies obtained from creep test for low stress and high stress regimes. Weise et al. reported that flip-chip solder joints cast with SAC solder were found to deviate from creep behavior of dog-bone and PCB types creep specimens [100].

Schubert's constitutive model based on a hyperbolic sine function, which is shown as Equation 3-10 was implemented for both SAC305 and SnPb37solder. In this equation  $\dot{\varepsilon}^{cr}$  is the steady state creep strain rate,  $k$  is Boltzmann's constant,  $T$  is the absolute temperature and  $\sigma$  is the applied stress. The constants  $A_1$ ,  $\alpha$ ,  $n$  and  $H_1$ , which is the apparent activation energy, are material properties that depend on the material and define the power law relationship between creep strain rate and applied stress. Published values for SAC305 and SnPb37 are listed in Table 3-5 [101].

$$\varepsilon^{cr} = A_1(\sinh a\sigma)^n \exp\left(-\frac{Q}{RT}\right) \quad (3-10)$$

**Table 3- 5: Schubert’s constitutive model coefficients [103].**

Solder	A <sub>1</sub> (S <sup>-1</sup> )	A (MPa <sup>-1</sup> )	n	Q
SAC305	277984	0.02447	6.41	54041
SnPb37	23343480	0.06699	3.30	67515

In another study, Schubert et al, found that the measured creep behavior of solder joints is different from that measured by bulk solder specimen. They compared different literature creep data of bulk and joint material and determined that scatter in the data due to sample preparation, test methods (shear versus tensile), alloy composition and microstructure were determined to be more pronounced as due to a real geometrical effect with a small number of grains per joint compared to bulk material [102]. The steady state creep behavior modeled using equation 3-10 has been previously shown to fit the secondary creep response of various SAC solders well at different strain rates and temperatures as shown in Figure 3-25 [103].

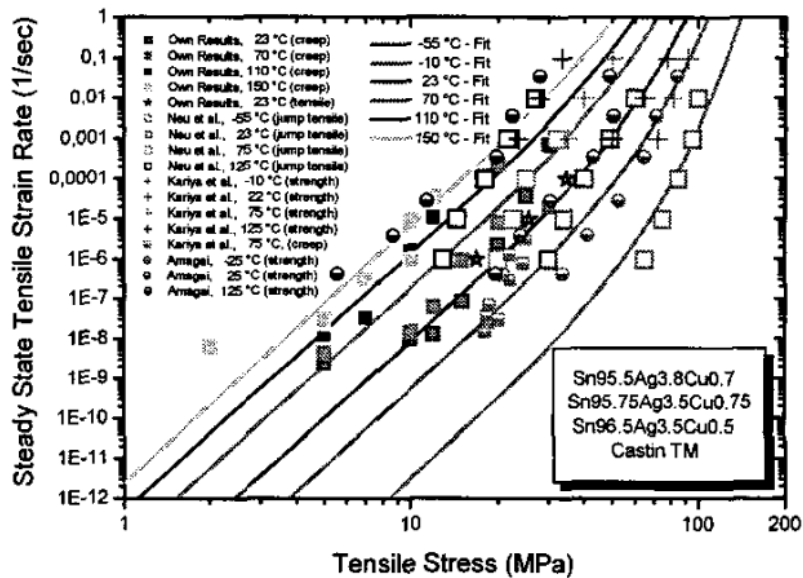


**Figure 3- 24: Curve fitting of SAC creep data to hyperbolic sine model Eq. 2 based on 108 data points from own measurements and literature [103].**

Darveax demonstrated that significant error can result if only the steady state creep were accounted for [104]. Figure 3-26 illustrates the simulated hysteresis loops using a combination of constitutive relations. It is known that time-independent plastic flow and primary creep can occur before steady state creep is achieved. The significance of this in calculating the hysteresis loops for solder joints undergoing thermal cycling is important since most BGAs subjected to accelerated thermal cycling tests experience strains less than 0.05 and even lower in field conditions.

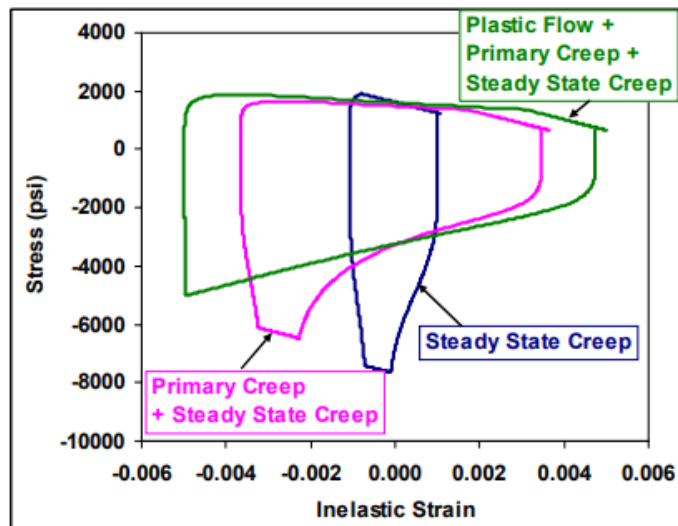


**Figure 3- 25: Thermal stress simulations of 96.5Sn3.5Ag solder incorporating progressively more complex constitutive relations [104].**

# **THERMAL CYCLING OF UNDERFILLED BALL GRID ARRAY COMPONENTS**

## **4.1 Thermal fatigue of BGAs with high expansion materials**

Conformal coatings are used to protect electronics from moisture, dust, vibration chemical contamination and temperatures in harsh end-use environments. Coatings can be applied to circuit boards using several ways such as spray, brush and deep coatings. In this study industry standard spray coating was applied to represent a control configuration and underfilling of BGAs as performed using a pneumatic syringe. Prior to injection of the conformal coating underneath the BGAs using syringe, the coatings were prepared by mixed with thinning agents to reduce their viscosity. Thinning agents were selected for each coating to avoid influencing the chemical structure of coating during cure and is shown in the Appendix.

### *4.1.1 Experimental procedure*

The test vehicles included daisy-chained, 1mm pitch, 256 IO BGA components with a package size of 17mm x 17mm. Each test board was populated with 60 individual components. The FR4 test boards were 2.05mm (81 mil) thick and included 8 dummy inner layers to simulate circuitry. BGA components assembled using a 0.127mm (5 mil) thick stencil. Two conformal coating configurations were applied to the two halves of each test vehicle as shown in Figure 4-1.



**Figure 4- 1: Assembled test vehicle showing two halves of the board with one side applied with Thick conformal coating**

The left half of each board was coated using “Standard” production spray process while the right half of the boards was coated with a manual process using pneumatic syringe to completely fill the conformal coating material under each BGA. This configuration, which is referred to as “Thick” application in this paper, represents a worst-case scenario of conformal coating application that can occur in dipping method and heavy spray coating applications. Additional “Control” boards with no conformal coating were also included in the test to compare to the reliability of components that were not coated. Figure 4-2 shows the underfilling application process using the pneumatic syringe.

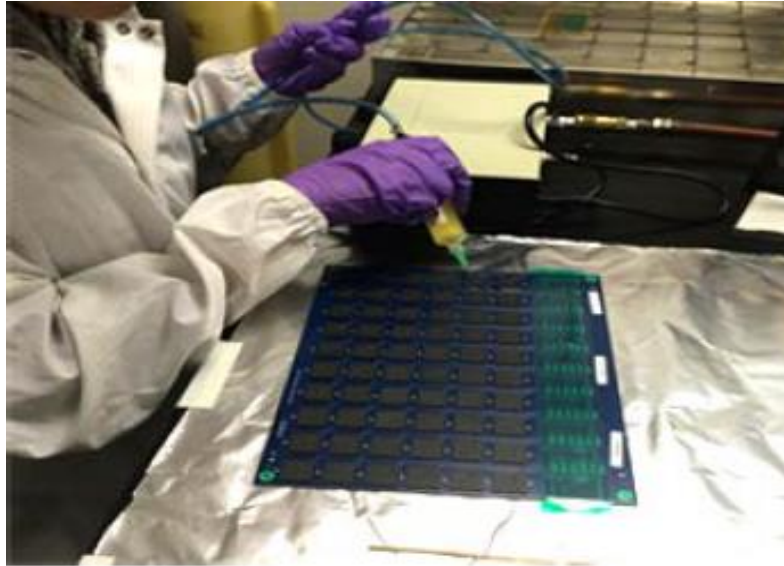


**Figure 4- 2: Application of Thick conformal coating using pneumatic syringe.**

Each test vehicle was subjected to one of two different thermal cycling ranges. Temperature Profile 1 had a temperature range of  $-55^{\circ}\text{C}$  to  $+125^{\circ}\text{C}$  for 620 cycles while Temperature Profile 2 used a temperature range of  $-20^{\circ}\text{C}$  to  $+80^{\circ}\text{C}$  for 2020 cycles. The two profiles, which are shown in Figure 4-3, used a minimum 15-minute dwell time at each temperature extreme and a ramp rate of  $5\text{-}10^{\circ}\text{C}/\text{minute}$ , per IPC- 9701.

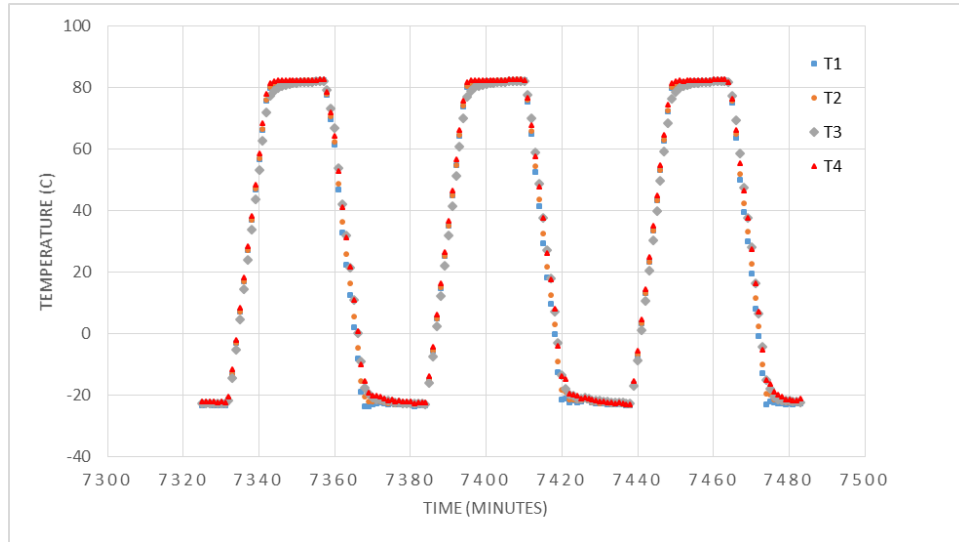


**Figure 4- 3: Temperature profile measured from four thermocouples places throughout the chamber.**

Test boards were placed inside the thermal chamber with thermocouples as shown in Figure 4-4. Adequate spacing was provided to ensure airflow is not prevented in impeded which can result in uneven heating and cooling of the PCB.



**Figure 4- 4: Test board placed inside Sun thermal chamber with thermocouples.**



#### 4.1.2 Experimental results

Reliability data of BGA components were analyzed using regression analysis to determine the Weibull shape factor ( $\beta$ ) and characteristic life ( $\eta$ ) for each configuration. The Weibull function correlates the cumulative failure distribution  $F(t)$  to the number of thermal cycles at which failure occurs shown in equation (4-1).

$$F(t) = 1 - \exp\left(-\frac{t}{\eta}\right)^\beta \quad (4-1)$$

The reported characteristic life corresponds to number of cycles at which 63.2% of the population is expected to have failed.

Figure 4-5 shows the cumulative failure distribution for BGAs with SAC305 solder joints and compares the reliability of Thick application for Acrylic and Silicone coatings at both temperature profiles. In addition, data for SnPb BGA is included with Thick Acrylic coating at the -20°C to 80°C profile. For the Control samples and those with Standard coating application, the thermal cycling profile significantly affected the reliability, with the samples subjected to the less severe temperature excursions exhibiting much longer fatigue life. However, the poor reliability of the samples with Thick coating was essentially just as low with Temperature Profile 1 as with Temperature Profile 2. Weibull slope changes more so between the two temperature profiles and is more consistent for different materials with the Thick coating application. The characteristic life for the two temperature profiles is found to fall closely for the Silicone and Acrylic Thick coating application although the two profiles

have an 80°C difference in temperature range. This observation might be indicative of the temperature dependent material properties of the Acrylic and Silicone coatings.

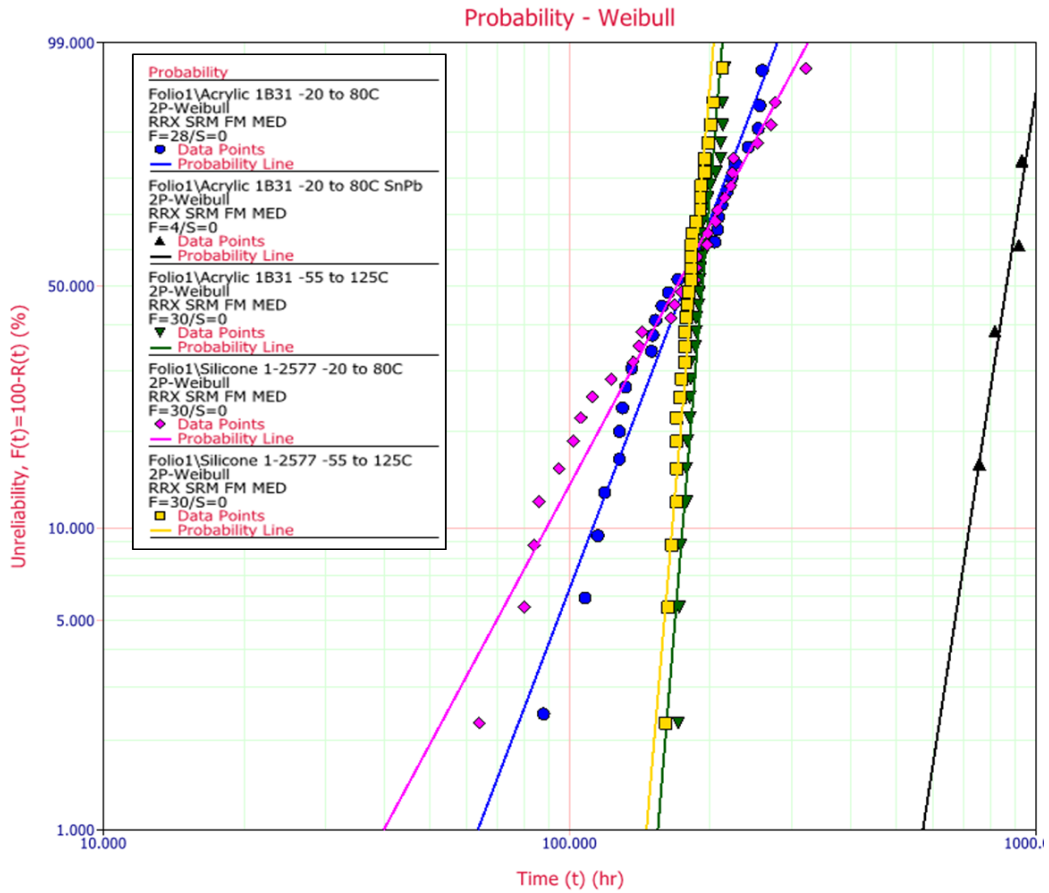


**Figure 4- 5: Weibull distribution of silicone and acrylic Thick conformal coatings at the two thermal profiles**

Another observation in Figure 4-5 indicates the number of cycles to first failure. The cycles to first failure for both the Acrylic and Silicone Thick coating was found to be approximately 50% lower at temperature profile 2 compared with cycles to first failure at temperature profile 1. This observation is indicating of the lower beta values that result in longer cycles between first and last failures of the tested population. These figures are listed in Table 4-1 along with the characteristic life of the SnPb BGA that indicate a 6.4X increase in characteristic life at temperature profile 2 compared to the

equivalent SAC305 configuration. Control BGAs that were not coated with any conformal coating did not exhibit failure throughout the applied number of cycles in each of the thermal profiles. The characteristic life of the 17mm BGA package is dependent on-board thickness, solder mask definition, copper pad plating chemistry.

**Table 4- 1: Thermal cycling results for Silicone and Acrylic Thick applications at two temperature cycles.**

<b>Alloy</b>	<b>SAC305</b>	<b>SAC305</b>	<b>SAC305</b>	<b>SAC305</b>	<b>SnPb</b>
<b>Temperature</b>	<b>-20°C to 80°C</b>	<b>-55°C to 125°C</b>	<b>-20°C to 80°C</b>	<b>-55°C to 125°C</b>	<b>-20°C to 80°C</b>
<b>Coating</b>	Acrylic 1B31	Acrylic 1B31	Silicone 1-2577	Silicone 1-2577	Acrylic 1B31
<b>Application</b>	Thick	Thick	Thick	Thick	Thick
<b># of samples</b>	30	30	30	30	30
<b># of failures</b>	30	30	30	30	4
<b>First Failure</b>	88	171	64	161	756
<b><math>\eta</math></b>	191	197	193	188	1234
<b><math>\beta</math></b>	3.78	17	2.84	16.7	7.21

Figure 4-6 shows failure distribution of three conformal coating materials with standard spray process and thick coating. The three conformal coatings are the Hysol epoxy and the two urethane coatings. The largest difference between the characteristic life of the spray coated and thick coated applications is found for the Humiseal 1A33 material. The difference between 400 and 153 cycles amounts for a factor of 2.6X. The ratio between the characteristic lives of the epoxy and urethane conformal coatings are 1.55 and 1.66, respectively. The lowest characteristic life was found for the Thick coated epoxy conformal coating which consequentially possessed the lowest time to first failure along with the highest beta value of the group.

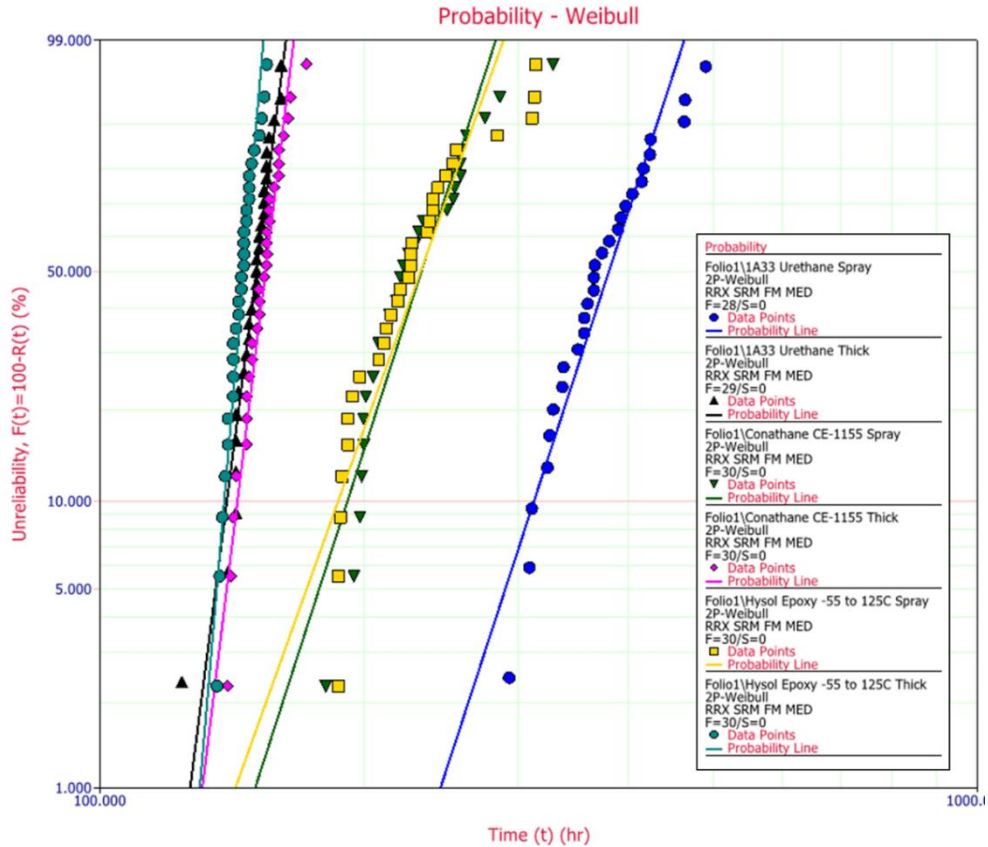


**Figure 4- 6: Weibull distribution of urethane and epoxy Thick and Spray conformal coating tested at -55°C to 125°C.**

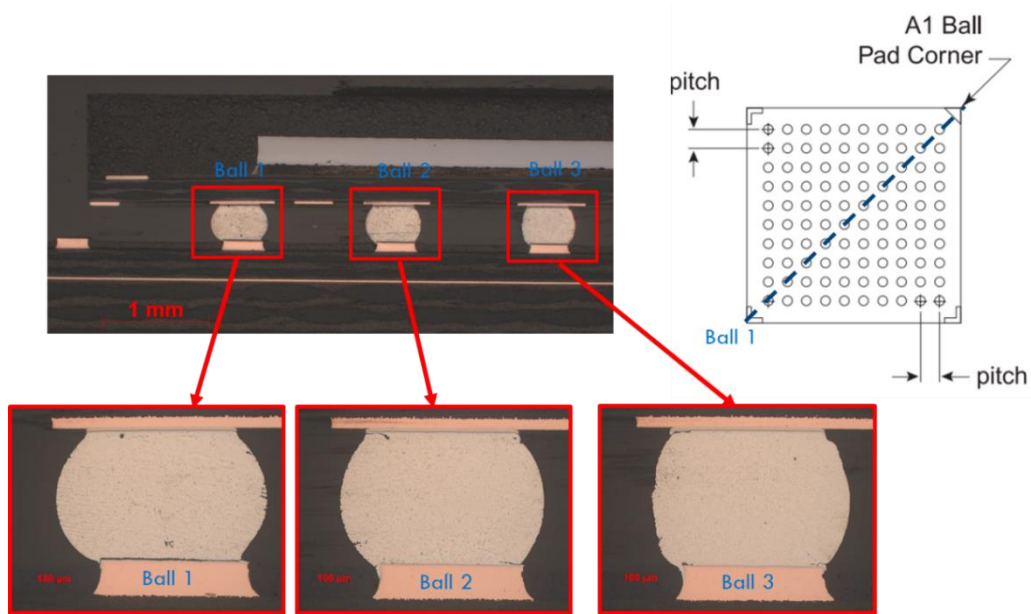
The values of the Weibull distribution shown in Figure 4-6 are listed in Table 4-2. This experiment provides a first account not only to the impact of standard conformal coating process on the reliability of BGA components but also on the effect of certain conformal coatings when used as non-traditional underfill materials with different thermal cycling range. Some investigators reported no adverse effects of conformal coatings on thermal cycling of surface mount components. The findings in thermal cycling of group A materials demonstrate that the impact of conformal coatings is highly dependent on the application type, the package and PCB it is applied to, thermal cycling range and most importantly the material type itself.

**Table 4- 2: Thermal cycling results for epoxy and urethane Thick and Spray applications at temperature profile 1.**

Alloy	SAC305	SAC305	SAC305	SAC305	SAC305	SAC305
Temperature	-55°C to 125°C	-55°C to 125°C	-55°C to 125°C	-55°C to 125°C	-55°C to 125°C	-55°C to 125°C
Coating	Hysol Epoxy	Hysol Epoxy	1A33 Urethane	1A33 Urethane	Conatahen CE-155	Conathane CE-1155
Application	Thick	Spray	Thick	Spray	Thick	Spray
# of samples	30	30	30	30	30	30
# of failures	30	30	29	30	30	30
First Failure	136	187	124	293	140	181
$\eta$	147	245	153	400	157	244
$\beta$	34.48	7.12	22.39	8.69	23.8	8.17

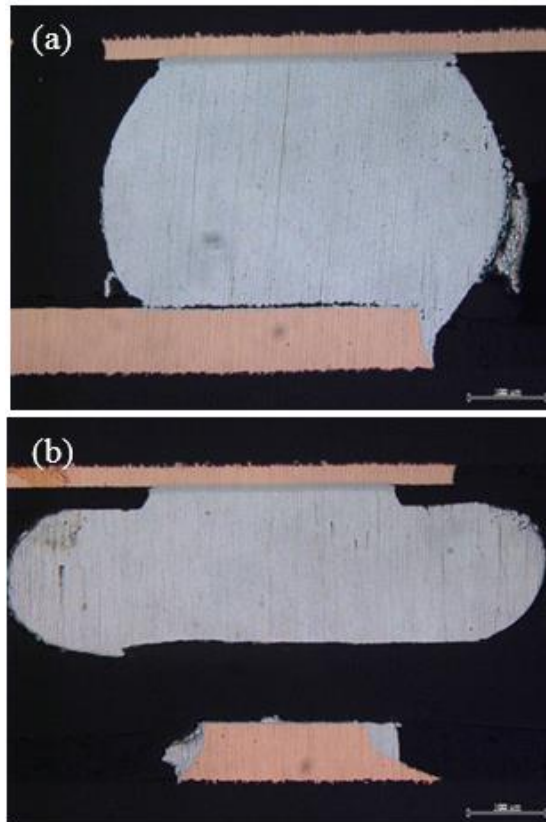
#### 4.1.3 Failure analysis

Post thermal cycling metallographic cross sectioning was performed on SAC305 and SnPb37 BGAs to assess the solder joint damage and crack locations. Figure 4-7 shows a solder ball from a SAC305 Control sample that exhibits cracking at the (lower) circuit board pad interface. SnPb37 Control components more typically had cracks at the (upper) package interface.



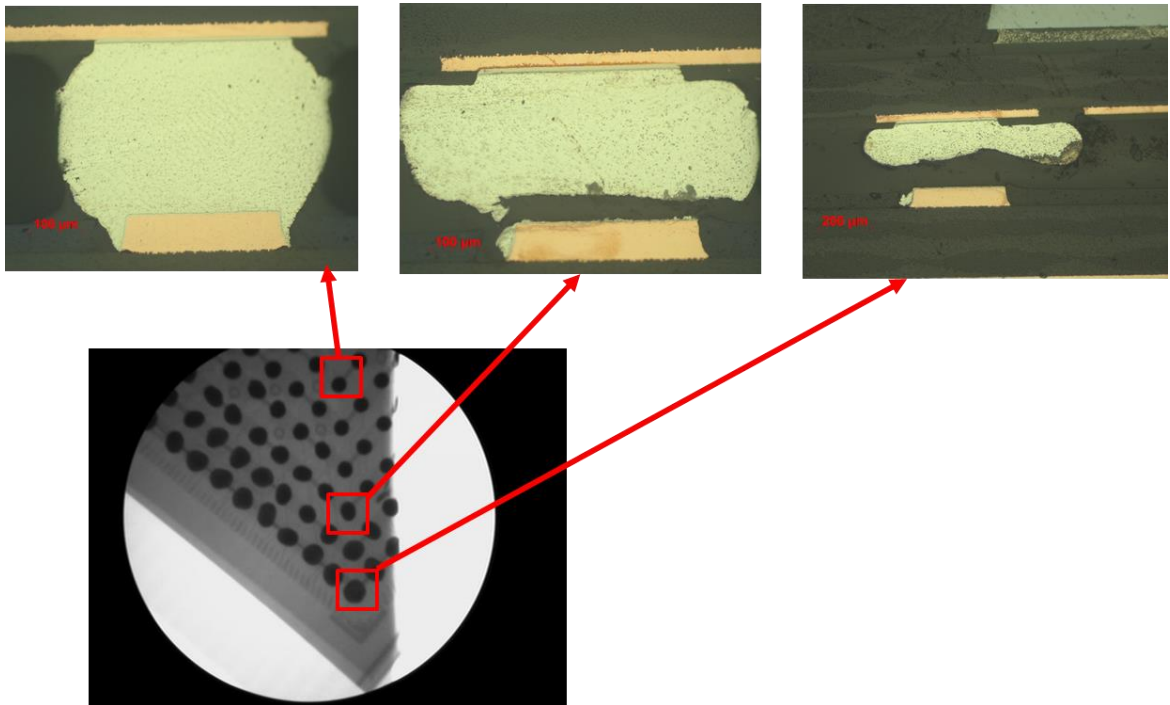
**Figure 4- 7: Cross-section along DNP for control BGA with no conformal coating tested at -55°C to 125°C.**

Figure 4-8 shows cross sections of failed SAC305 components for both Standard and Thick coating applications. The appearance of the solder joint and locations of the crack for the Control and Standard conformal coating samples is quite similar, suggesting that they encountered the same failure mechanism. However, the Thick conformal coating introduced a new failure mechanism that significantly compressed the solder joint, which ultimately separated away from the circuit board a considerable distance. It appears that the acrylic conformal coating, which occupied a much larger portion of the package than the solder joints, placed mechanical stresses on the solder joints, likely due to thermal expansion of the conformal coating itself.



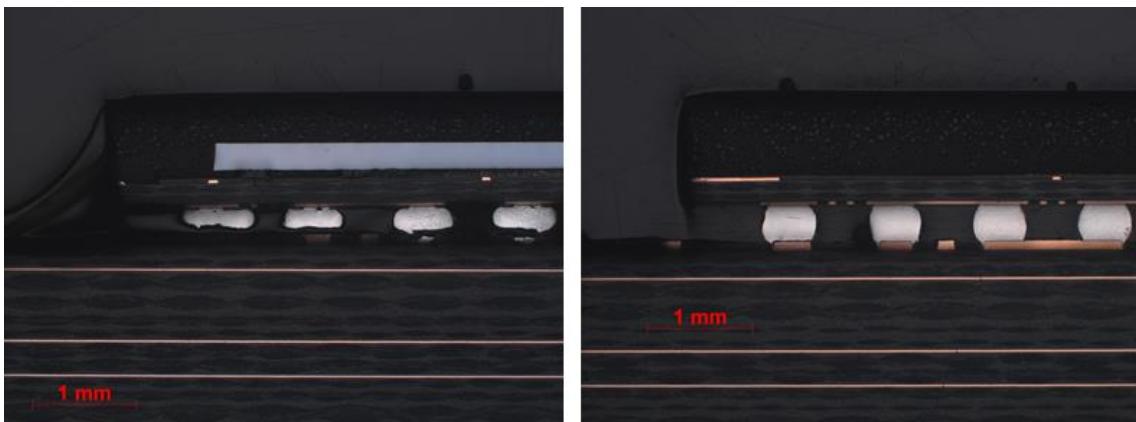
**Figure 4- 8: Failure of SAC305 BGA with acrylic coated using a) standard spray and b) Thick application from -55°C to 125°C.**

Figure 4-8b shows severe plastic deformation in the SAC305 solder joints and no evident distance to neutral effect. Similar cracking at the board pad was observed for the -20°C to 80°C thermal cycle, but with less plastic deformation as in Figure 4-8b. Large compressive strains caused solder joint to be extruded outwards. This failure mode is also attributed to the lack of adhesion and interaction between the conformal coating and solder alloy during the low and high temperature extremes. At the high temperature dwell, solder joints creep and conformal coating softens and eliminates any possible adhesion between solder and the acrylic material. At the cold temperature extreme, the solder is compressed and squeezed outward in the normal direction to the applied load. The lack of hydrostatic stress on solder joints during low temperature dwell implies that no physical constraint is being placed on the solder and allows for the deformation to occur. This solder/conformal coating interaction is greatly dependent on the conformal coating CTE and modulus at the dwell temperature. It should be noted that the cross-sections shown in Figure 4-8 were made after the samples had accumulated more than 1000 thermal cycles. Since the SAC305 component exhibited a solder joint electrical open at ~100 thermal cycles, it is reasonable to assume that the majority of the severe deformation evident in Figure 4-8 occurred well after the initial solder joint failure. Figure 4-9 shows an x-ray image of the same BGA package with Thick acrylic coating. The outline of the squished solder balls is seen to be dependent on the distance to neutral effect. The edge of the package is less constrained as the package center due to edge effects and die shadow effect. Therefore, solder joints toward the center of the package did not experience as much plastic deformation as solder joint on the perimeter rows of the package.



**Figure 4- 9: Cross-section and X-ray image of BGAC with SAC305 solder with Thick application of Acrylic 1B31 from -55°C to 125°C.**

Figure 4-10 shows cross-section of the BGA with thick conformal coating that was cut on the second row of balls and a BGA package with standard spray conformal coating. Although some spray coating end up bridging the gap between the package and PCB the failure mode of the standard spray coating was different than the thick coating.



**Figure 4- 10: Cross-section of BGA with Thick acrylic coating (left) and Spray coating (right) after thermal cycling.**



## 4.2 Thermal cycling of BGAs with underfill under mean temperature conditions

### 4.2.1 Experimental procedure

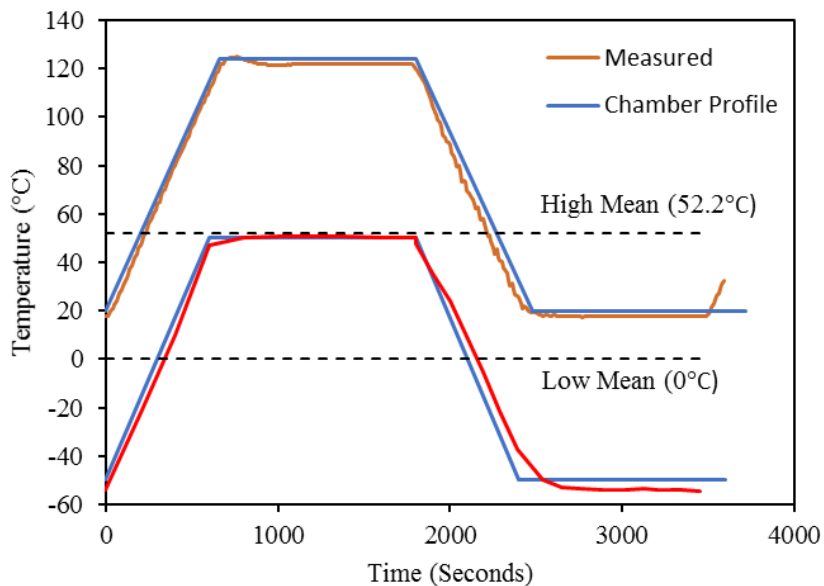
Table 4-3 lists the test matrix indicating the number of components used for each thermal cycle and underfilling material. Two boards with 20 (Figure 4-13) components on each board were used for each temperature and underfill material combination. All BGA components with underfill applied were for single sided assemblies. One double-sided configuration was assembled and placed at the High Mean temperature conditions for comparison. The boards with double-sided components were placed with a checkered pattern to provide spacing between components and avoid influencing neighboring parts during the thermal cycling tests. Therefore only 20 mirrored sets of components were used compared to 40 individual parts that were used for each underfill material.

**Table 4- 3: Test matrix for thermal cycling of group B underfills.**

	Low Mean (-50°C to 50°C)	High Mean (20°C to 125°C)
Configuration	Number of Components	Number of Components
Control (No underfill)	40	40
UF1	40	40
UF2	40	40
UF3	40	40
UF4	40	40
Double Sided (No underfill)		40

Test boards were placed inside thermal chambers and each of the chamber profiles was calibrated prior to start of test. Figure 4-11 shows the measured temperatures and set temperatures for each of the mean conditions. The “High Mean”

temperature profile consisted of temperature range of 20°C to 125°C with 20-minute dwells at each extreme and had a mean cyclic temperature of 52.2°C. The “Low Mean” temperature profile consisted of a temperature range of -50°C to 50°C with similar dwell times and mean temperature of 0°C. Both thermal profiles utilized a ramp rate of 10°C/minute. Boards were hung inside the thermal chambers and spaced to allow adequate airflow. Resistance monitoring was performed using an Agilent 34980 multifunction switch/measure unit. Failure definition was taken according to criteria defined in IPC-SM-785 [14]. Complete failure was considered at the number of cycles coinciding with recording 9 consecutive measurements of resistance values that



increased by 10 percent above the baseline resistance measurement.

**Figure 4- 11: Temperature profiles with High and Low mean temperatures.**

#### 4.2.2 Test vehicles Assembly

The test vehicles were assembled at the Rockwell Collins Coralville production facility.

An MPM UltraPrint 2000 automated MPM stencil printer using a 0.004 inch thick

stainless steel stencil applied Indium 8.9 SAC305 solder paste to the test vehicles. Figure 4-12 illustrates the MPM stencil printer. The BGA components were placed on the test vehicles using Universal GC-120 machine. The test vehicles were reflowed with a 14 zone Heller 1912EXL Convection Reflow Oven using a ramp-to-spike profile. The conveyor speed was 43 inches per minute and the nitrogen flow was 1500 cubic feet per hour. The oven used the high convection setting, and the boards were placed on the rails.

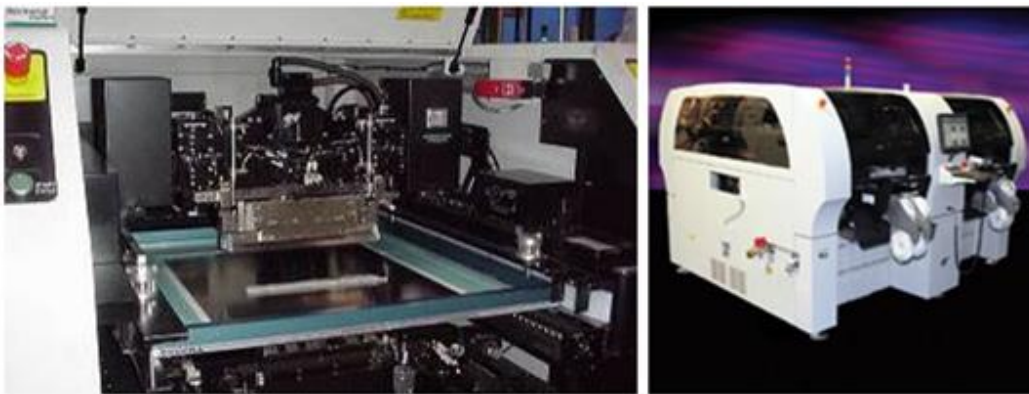


**Figure 4- 12: MPM Stencil Printer (left), Universal GC-120 Machine (right)**

The underfill materials were applied manually using an EFD Dispensing Products syringe and dispensing needle with a 27-gauge opening. The boards were heated, using the Hakko FR-1012 (Figure 4-14) preheater station to 60°C prior to the application of underfill material. The underfill materials were cured according to manufacturer recommendations. Henkel Loctite 3808 was cured at 130°C for 15 minutes, with the cure time started once the test vehicles had reached the specified cure temperature. Namics was cured at 140°C for 6 minutes. Silicone and EP1238 were subjected to room temperature cure.

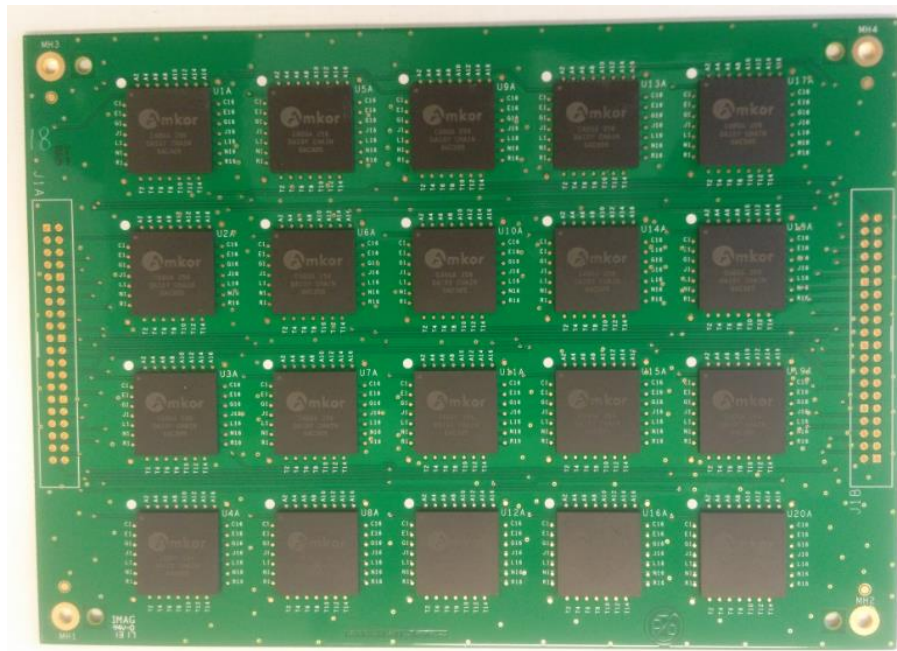


**Figure 4- 13: Assembled test board with 20 components.**



**Figure 4- 14: Hakko FR-1012 preheater with sample test board.**

Figure 4-15 shows the components after underfilling for each material. It is evident that the fillet size of both the silicone and EP1238 materials are larger than the dedicated underfill materials as they are not designed to be applied as capillary underfills unlike the Namics and Loctite3808. It could be possible to adjust the size of the fillet of these

non-underfill materials by carefully controlling cure time, temperature and syringe application method; however, the method used for this study is indicative of the capillary flow that these materials could experience by dip or heavy coating applications in various electronic products.

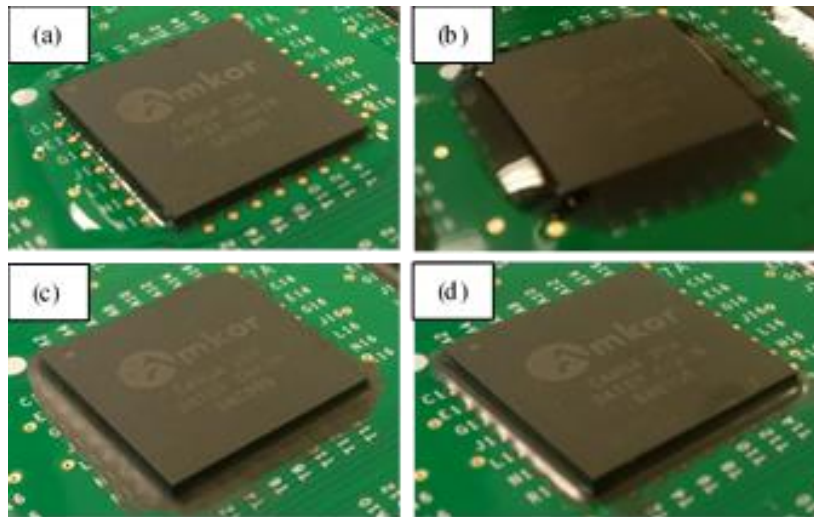


**Figure 4- 15: Components underfilled with (a)Silicone 1-2577 (b) EP1238 (c) Loctite 3808 (d) U8437-2.**

#### *4.2.3 Experimental results*

BGA components with silicone underfill materials exhibit lowest characteristic life at the High Mean Temperature along with EP1238 which shows equally low characteristic life. Compared to the single sided control components, the addition of the soft underfill materials led to an almost 20X reduction in fatigue life. BGAs with the Loctite3808 resulted in 2.5X reduction of fatigue life similar to the mirrored components configuration while BGAs with the Namics underfill did not show failures at either temperature profiles. Figure 4-16 shows the failure rate as function of thermal cycles. In addition to characteristic life, the first failures demonstrate lowest probability of failure of a component with a certain underfill and thermal profile. In general, first

failures under accelerated thermal cycling tests are expected to occur at approximately 1/3 of the projected characteristic life. The  $\beta$  from the plot of the 2-parameter Weibull distribution provides information on the scatter of the failure rate. For the underfilled BGAs,  $\beta$  is found to be approximately 3 while control and mirrored configuration indicate values of 9 and 6, respectively. The higher the slope of the failure rates, the smaller the time between first and last failures. Inclusion of first failures and suspension point (non-failed sample population) in failure rate is necessary in order to project the estimated time to failure at which 63.2% of the population is expected to be failed as was the case of the control BGAs at the High Mean temperature profile.

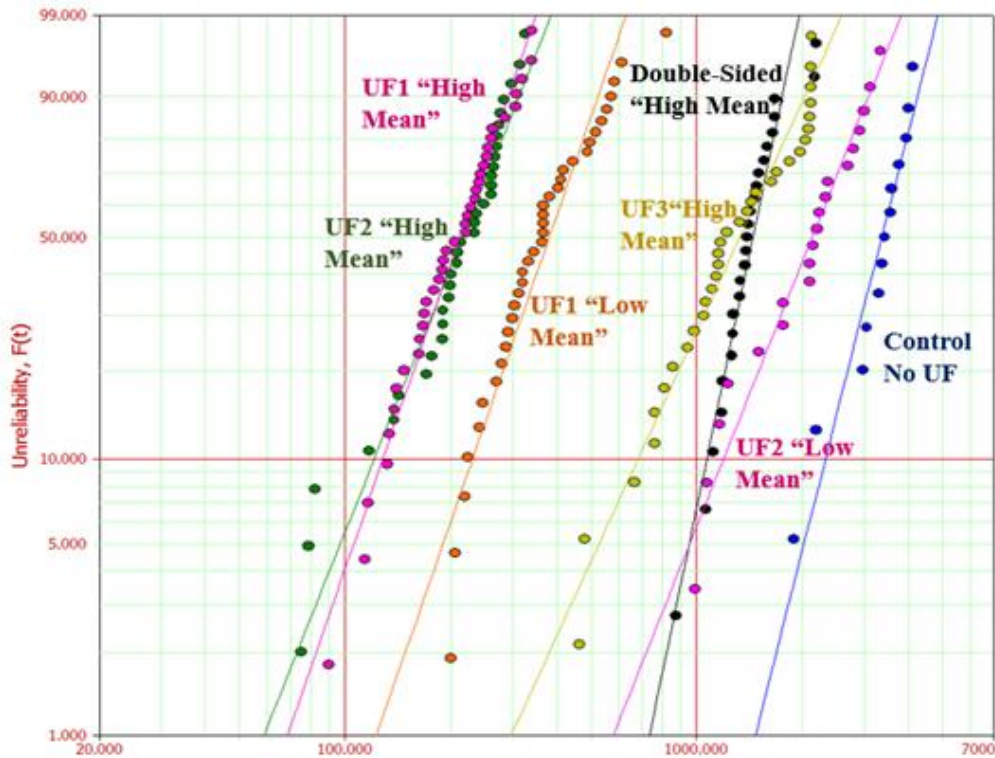


**Figure 4- 16: Thermal cycling results for underfilled BGAs at the two thermal profiles.**

A total of 4400 thermal cycles have been performed with both thermal profiles. Summary of failure results are listed in Table 2 for the underfilled materials, control boards with no underfill and a double-sided (mirrored) configuration with no underfill.

NA indicates no failure recorded during tested cycles. The mirrored configuration was placed only in the High Mean temperature profile in order to compare failure rates with the single sided control configuration. Mirrored components experienced a reduction of 2.8X in characteristic life compared to single sided control boards. Similar trends in the reduction of fatigue life in mirrored components have been previously demonstrated in literature [15]. The reduced number of cycles in double-sided condition is direct result of components constraining PCB which results in increasing the in-plane shear strain solder joints experience during thermal cycling.

**Table 4- 4: Characteristic life for thermal cycling experiments of underfilled BGAs at two thermal profiles.**

	Low Mean (-50°C to 50°C)		High Mean (20°C to 125°C)		Decrease in N63 (High Mean)
	N <sub>63</sub>	$\beta$	N <sub>63</sub>	$\beta$	
Control	NA	NA	4441	9.10	1
Silicone	419	3.74	232	3.77	19X
EP1238	3494	2.71	241	3.25	18X
Loctite3808	NA	NA	1776	2.55	2.5X
Namics U8437-2	NA	NA	NA	NA	NA
Double sided	NA	NA	1532	6.24	2.8X

#### 4.2.4 Failure analysis

Select components were cut from test boards for cross-sectioning after thermal cycling. Figure 4-17 shows a cross-section of the control BGA after 4400 thermal cycles. Cracking in the corner solder joints is found at the lower interface with the PCB. All four corners of the control BGA were found to be partially or fully cracked with minor cracking evident at the subsequent solder joints along the distance to neutral direction. Crack location in the control BGA was also found to shift from the lower

PCB side of the ball to the component side by the third solder joint; the extent of cracking by the third solder joint toward the package center shows much less damage than the corner joints. All fatigue cracks in the control BGA with the High Mean temperature profile occurred in the bulk of the solder and not through the intermetallic interface.

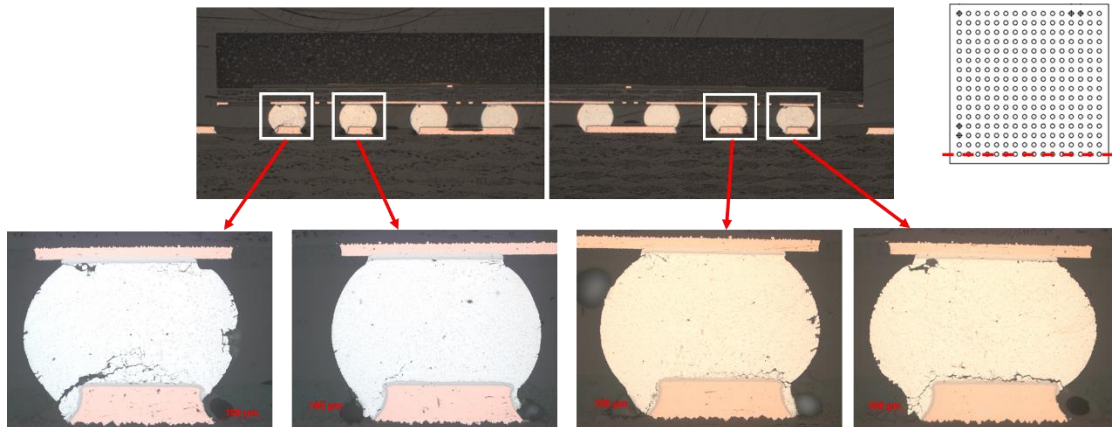


**Figure 4- 17: Cross-section of single-sided control BGA after 4000 thermal cycles at High Mean thermal profile.**

A cross-section of the double-sided configuration which was subjected only to the High Mean temperature profile is shown in Figure 4-18. Cracks in mirrored components follow the trend observed in the single sided control BGA. Fully cracked solder joints are found only at the corners of the mirrored BGA packages with progressively decreasing degree of cracking toward the package center. A similar shift in crack location from the PCB interface to the upper component interface is found in joints that lay inward in the package. Figure 4-19 shows cracks in a BGA component underfilled with the United Adhesives EP1238 material at the high Mean Temperature profile. Figure 4-19 (left) shows cracking for the corner joint and matches that of the control BGA; however, Figure 4-19 (right) illustrates cracks in a joint located at the center of the package. Additional cracks occurred in the BGA package with the EP1238 underfill



at both package and PCB interfaces. No preferential cracking pattern was found at the High Mean temperature profile. Fatigue cracks were found to alternate between the upper and lower solder joint interfaces with some joints showing cracks that are propagated diagonally toward the center of the solder joint. Unlike the single sided control BGA, the BGA with the EP1238 underfill did not exhibit distance-to-neutral effect with reduction of fatigue cracks toward the package center.

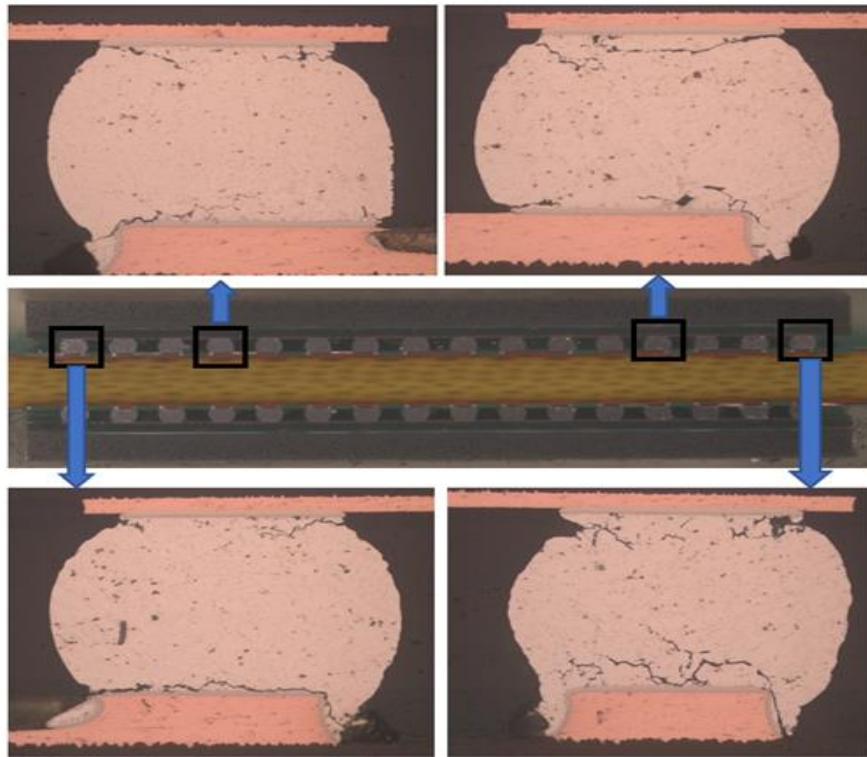


**Figure 4- 18: Cross-section of double-sided BGA at High Mean temperature profile after 1862 cycles.**

A reason behind the irregular crack paths and location at the High Mean temperature profile are attributed to the underfill materials  $T_g$  which falls within the temperature profile. Across this temperature EP1238 exhibits a CTE increase from 75 to 200 ppm/ $^{\circ}$ C. Although the CTE of this material before crossing the  $T_g$  is substantially large the increased expansion contributes to the axial loads during heating and cooling

regimes which explains the low characteristic life obtained with this material. Even with slightly lower life demonstrated at the Low Mean profile with UF2, fatigue crack damage was found to align with the one observed in the equivalent control configuration.

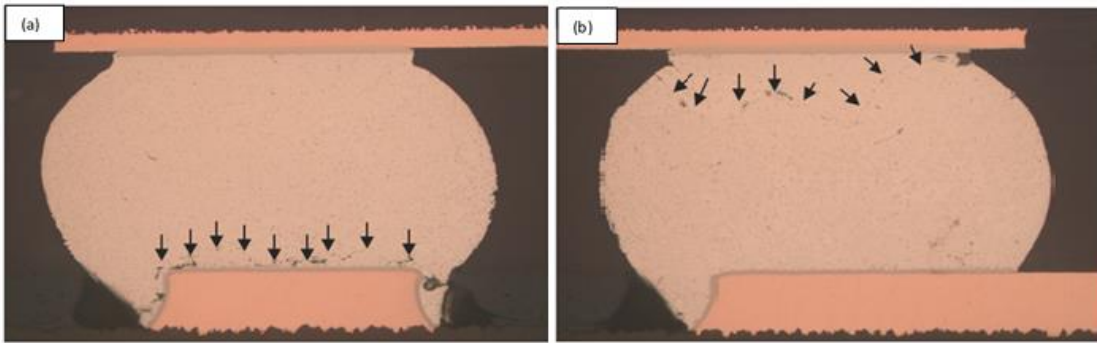


**Figure 4- 19: Cross-section of BGA with EP1238 underfill at (a) corner joint (b) 8<sup>th</sup> joint from the corner with High Mean thermal profile.**

Fatigue cracking with the Silicone underfill material exhibited different characteristics compared to the other configurations. Figure 4-20 shows fatigue cracks at both corners of BGA cross-section with the Silicone underfill material at the High-Mean temperature profile. The characteristic lives at both temperature profiles with underfill are closer to each other than any other underfill material configuration. Fatigue cracks are found to be consistent in solder joints with silicone underfill between the two profiles. Only the corner solder joints exhibit cracks which run along either the diagonal of the joint or the bottom interface as shown in Figure 4-20. Further observation of the BGA package exterior with the silicone underfill was found delamination of the silicone fillet from the package surface as well as cracks. Cracking and delamination of the silicone fillet was found only for the Low Mean temperature profile. No cracking or deadhesion of the silicone was observed for the High Mean temperature profile. A reason for the

cracking could be attributed to the high stiffness of the silicone at low temperature which results in higher interfacial loads during the contraction of the material. the silicone

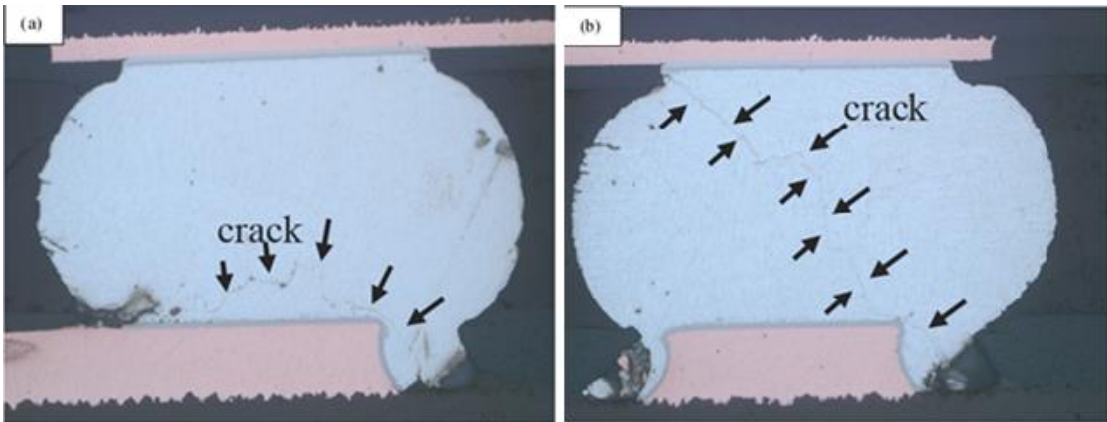


**Figure 4- 20: Cross-section of two corner joints in BGA with silicone at High Mean temperature profile (a) bottom interface (b) diagonal cracking.**

Figure 4-21 shows a cross-section of BGA package with Loctite3808 underfill material after 2414 cycles with High Mean temperature profile. Cracks in solder joints of the BGA package with the Loctite3808 are Similar to those observed in BGA package with EP1238 underfill at the High Mean temperature profile. No distinct pattern can be observed with fatigue cracks alternating between the top and lower interfaces of solder joints through the bulk region of the solder. Figure 4-21(b) shows cross-polarized image of the 3<sup>rd</sup> solder joint from the edge with cracking observed at the upper interface. Crack path at this instance progresses down toward the center of the joint before shifting direction and changing path toward the other edge of the joint. In some joints, fatigue cracks were found to progress diagonally and emanate from both interfaces. The occurrence of recrystallization at the central region of the solder joint at the High Mean temperature profile indicates that substantial deformation occurs at the central region of the joint rather than the localized interfacial regions of the solder and copper pads. No particular location along the cross-sectional edge of the BGA

package indicates a pattern that would explain the cracking phenomenon that was observed.

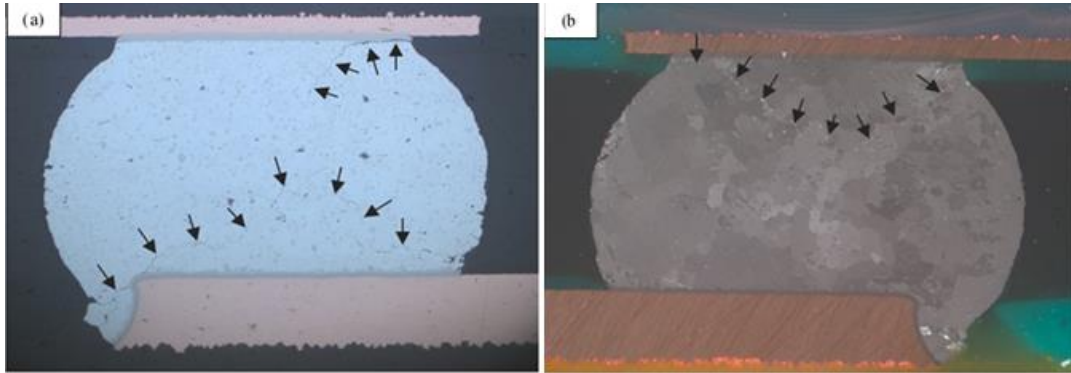


**Figure 4- 21: Cross-section of BGA packages with Loctite3808 at High Mean profile (a) Fifth solder joint from package corner, (b) third solder joint from package corner**

The underfill application method used in this study resulted in distinct fillet shape formation for each of the underfill materials. The difference between the fillet formed for each material is depicted in Figure 4-22. Fillet geometry measurements were taken from cross-sectional images of the BGA package with each underfill material. Namics U8437-2 and Loctite3808 were found to have nearly identical fillet shapes which extend from the PCB up the center of the assembled BGA package. The two non-dedicated underfill materials EP1238 and silicone resulted in large fillet sizes that extended up to the top of the BGA package and away from the package to a distance with excess of 1.5mm. Such large fillet size is not ideal for BGA with dedicated underfill materials. Under vibration fatigue or mechanical shock loading the large fillet geometry might not have any adverse effects on the time to failure of solder interconnect. The same assumption could not be applied for the influence of the fillet geometry under thermal cycling since material expansion is responsible for physically

constraining the package thermal expansion itself which in turn influences the loads transmitted to the solder joints.

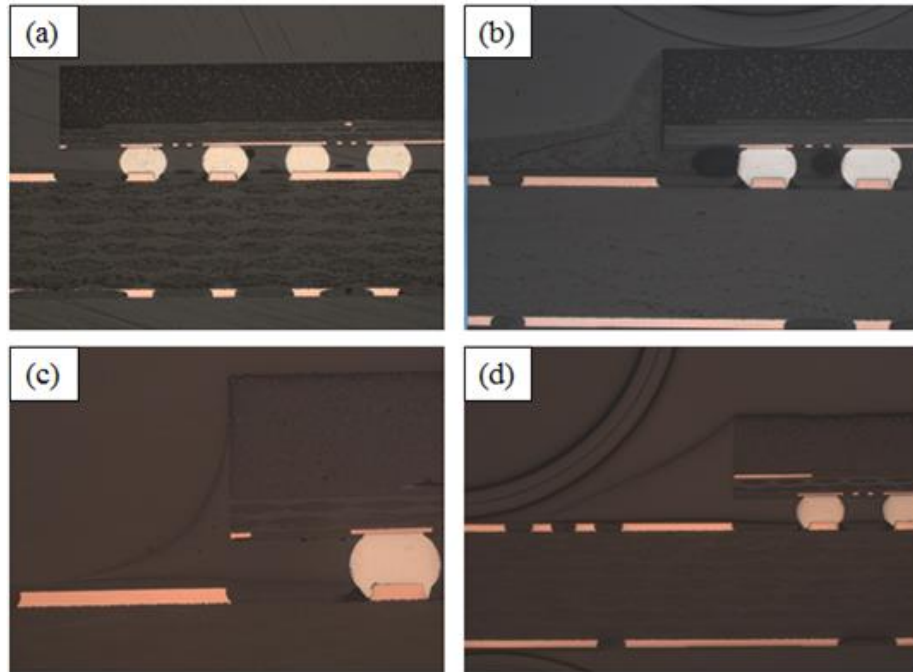


**Figure 4- 22: Cross-section of underfilled BGA package (a) control (b) UF1 (c) UF3 (d) UF2.**

### **4.3 Thermal cycling of BGAs with reworkable underfill**

The process of reworking underfilled BGAs consist of heating the electronic PCB and components to a temperature that is higher than the solder melt temperature. This rework temperature for Pb-free solder is typically around 230°C to 260°C. Underfills classified for reworkable purposes are designed to minimize damage to copper pads and residues on the PCB to ensure that no interference with the reflow of the new BGA package. Reworkable underfills can come in variety of material properties and volume fraction of filer particles.

#### 4.3.1 Experimental procedure

Each test board was preheated to manufacturer recommended temperature of 70°C prior to underfilling using a BIPEE SH-4 hot plate. A thermocouple was placed on the surface of test boards to monitor preheating temperature. Each thermocouple was calibrated using a Fluke -140 Dry-well temperature calibrator. To ensure even temperature distribution between the hot plate and the PCB a thermally conductive material is used as shown in Figure 4-23. Laird Tflex HR400 series 0.5mm thick thermal interface material made of filled silicone rubber with thermal conductivity of 1.8 W/m-k provides sufficient heat transfer for underfill application process.

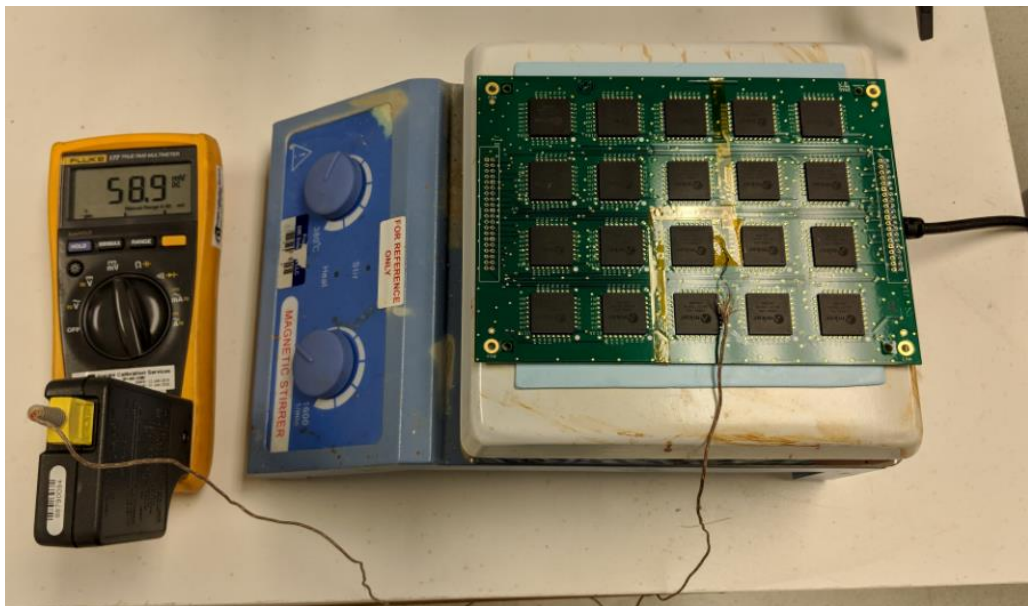


**Figure 4- 23: Hot plate preheating test board for underfilling.**

Underfill application was manually performed using Tehcon Systems 700 series manual syringe gun as shown in Figure 4-24. Underfill cartridges of 10 cm in volume were loaded to the syringe and applied to the gap between the PCB and BGA using an L pattern. This pattern utilizes the underfills capillary flow characteristics. The underfill is applied to two perpendicular sides of the BGA package and the heated PCB increased

underfills capillary flow by reducing its viscosity which pulls it all the way underneath the package to the other two sides that were not been applied resulting in uniform void free epoxy interface between the PCB and package.



**Figure 4- 24: Techon Systems 700 series manual underfilling syringe gun.**

An accelerated thermal profile with a range of  $-55^{\circ}\text{C}$  to  $125^{\circ}\text{C}$  was used according to IPC 9701 standard similar to thermal cycling of group A materials as shown in Figure 4-25. The high range of the thermal cycle is chosen such that the both temperature peaks are above the glass transition temperature of all underfill materials and the obtained results from this experiment will provide information on the effect of reworkable underfill properties such as glass transition temperature, CTE and modulus.

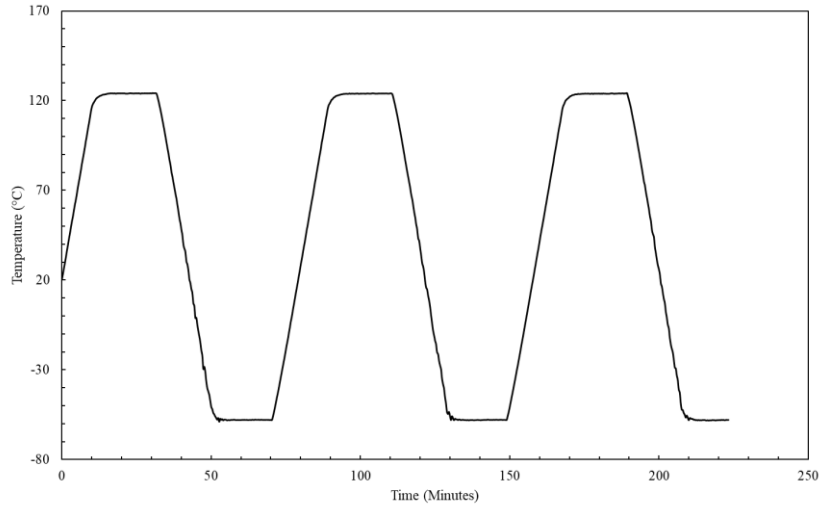


**Figure 4- 25: -55°C to 125°C temperature profile.**

#### *4.3.2 Experimental results*

Test boards with different underfills were removed once all components met failure criteria defined by increase in the electrical resistance. The test boards with the control components and Namics XSUF1594-6 were exposed to a total of 2272 thermal cycles. The remaining test boards comprising of BGA with Henkel E1216M and Loctite 3808, Namics 1575-9 and 1594-6F underfills were removed after 1442 thermal cycles. The failure rate of this experiments is plotted using 2-parameter Weibull distribution as for the previous thermal cycling experiments shown in Figure 4-26.



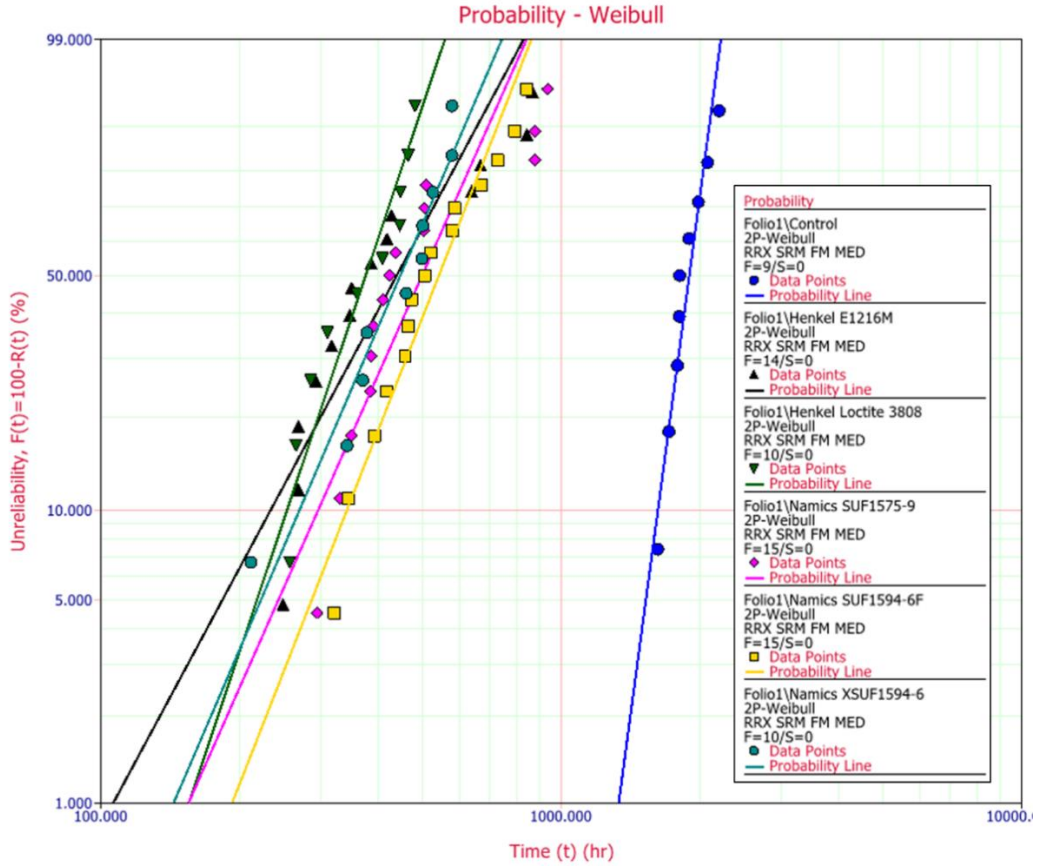


**Figure 4- 26: Weibull distribution of group C underfills and control BGA under -55°C to 125°C thermal profile.**

From first observation it can be seen that the failures of all underfills are clustered in one group that is substantially earlier than the control group. Table 4-5 provides the characteristic life, Weibull beta value, first failure and respective CTE and glass transition temperature measured with both TMA and DMA for each underfill material. It is directly evident that the characteristic life increases with underfill  $T_g$ . The center of the glass transition region was found to be higher using DMA measurements than ones measured using TMA.

**Table 4- 5: Weibull plot of BGAs with five reworkable group C underfills.**

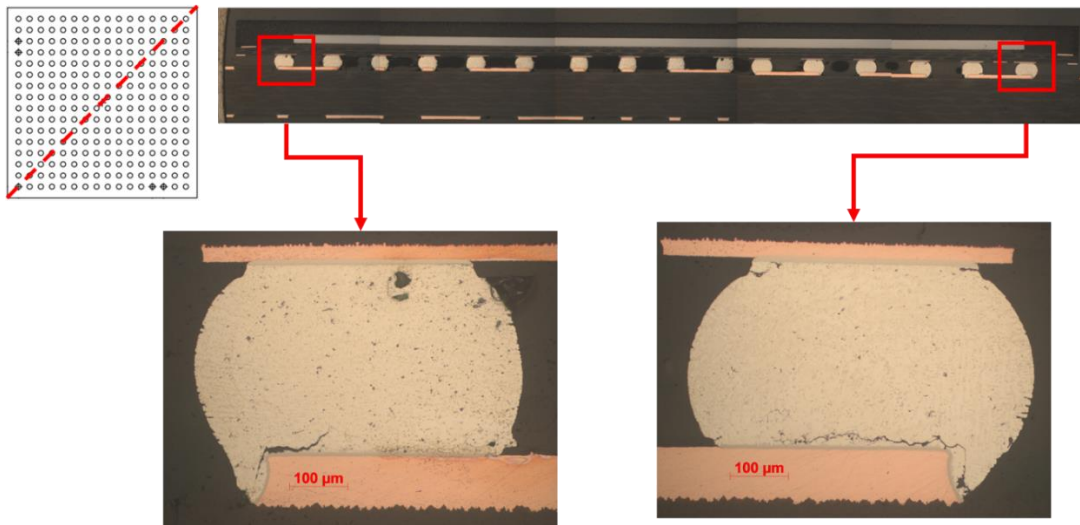
Underfill	$\eta$	$\beta$	1 <sup>st</sup> Failure	CTE ( $\alpha1/\alpha2$ )	T <sub>g</sub> (TMA/DMA)
Control	1955	11.99	1624	NA	NA
Henkel Loctite 3808	405	4.78	258	60/189	32/51
Henkel E1216M	421	3.90	249	47/138	39/71
Namics SUF1575-9	438	6.74	295	41/140	92/71
Namics XSUF1594-6	493	3.73	212	41/164	97/102
Namics SUF1594-6F	518	5.28	322	35/120	111/114

The beta value of 11.99 for the control BGA is higher than the beta of all underfilled BGA similar to the one found for group B underfills under mean temperature conditions. This means that for a sample population of the same size the underfilled component result in longer spread between first and last to fail components. The smaller beta value inevitably increases the proportion of characteristic life to first failure compared with the higher beta values of the non-underfilled BGAs.

Figure 4-27 shows the characteristic life and underfill CTE prior to the glass transition temperature on the vertical axis with the T<sub>g</sub> plotted on the horizontal axis. A distinct non-linear relationship can be seen in the characteristic life dependence on T<sub>g</sub> more so than just the CTE alone. Namics 1575-9 and 1594-6 with closely measured T<sub>g</sub> values have closer characteristic life even though their CTE after the glass transition are different. It is important to note that the ratio between the control and BGA with Loctite 3808 underfill was 4.8X for -55°C to 125°C profile compared with only 2.5X reduction in characteristic life in the 20°C to 125°C profile. This observation supports the limitation of empirical models and illustrates the dependence of characteristic life on the combination of underfill material properties and temperature range.

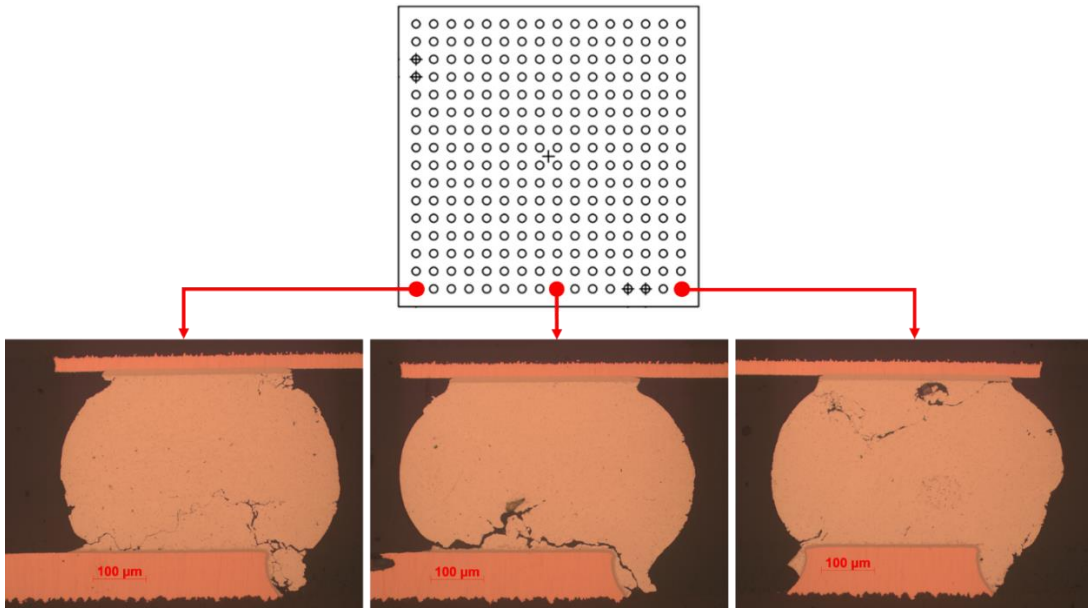
### 4.3.3 Failure Analysis

Underfilled test boards were taken out of the thermal chamber after 1441 thermal cycles from -50°C to 125°C to ensure complete failure in all underfilled BGAs. No extruded solder joints were observed in any of the reworkable underfilled BGAs in this study compared to the ones observed with high expansion conformal coatings. Figure 4-27 shows diagonal cross-section of control BGA that failed at 1896. The two corner most joints indicate fatigue cracking at the PCB side through the bulk of the solder near the intermetallic region. No damage was observed except for the corner most solder joints. This observation is consistent with control BGA with the high mean temperature profile.



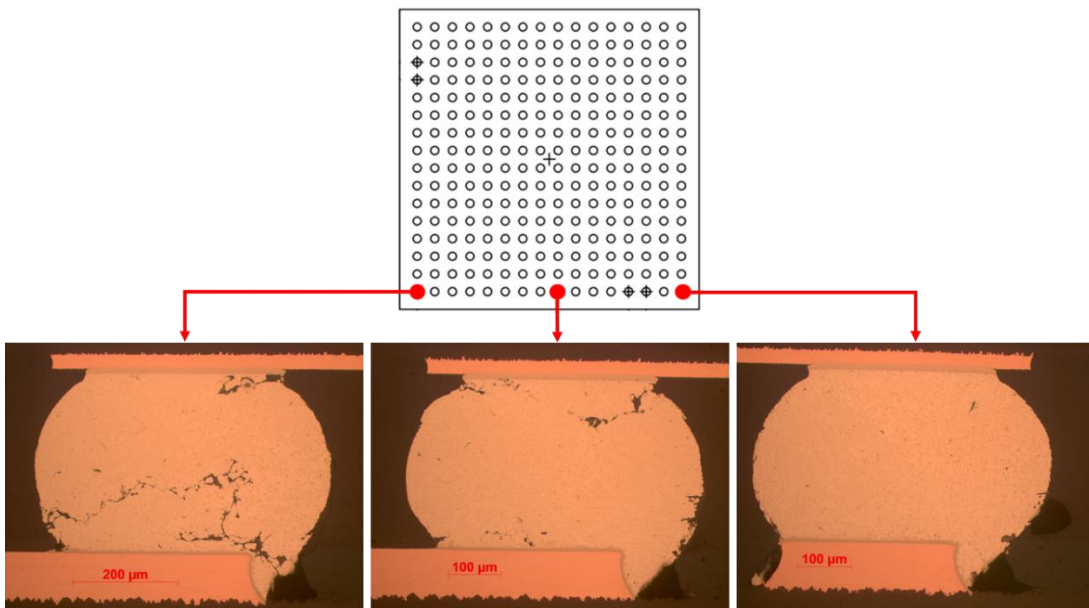
**Figure 4- 27: Cross-section of control BGA along package diagonal.**

Figure 4-28 shows cross-section of BGA with Loctite3808 underfill along the perimeter of the package. Fatigue cracking is found to occur throughout the perimeter solder balls without distinct pattern. Crack location is found to alternate between the component and board sides.



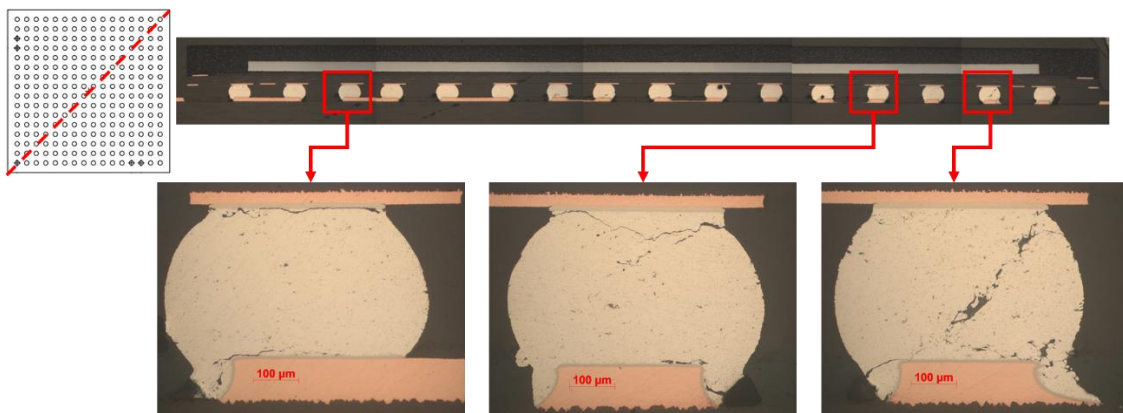
**Figure 4- 28: Cross-section of BGA with Henkel 3808 along package side.**

Figure 4-29 shows cross-section of BGA with Namics XSUF1594-6F that has the highest glass transition among group C underfills. Cracking behavior is found to be consistent among all group C underfills with no distance to neutral effect that was observed for the control components.



**Figure 4- 29: Cross-section of BGA with Namics XSUF1594-6F along the package side.**

Figure 4-30 shows cross-sections of BGA with Namics 1594-6 along the diagonal of the package to provide a better indication of cracking behavior along the distance to neutral line. Again, no distinct dependence on ball position and crack occurrence is shown. Cracked solder joints are found throughout the package with cracking alternating between PCB, package side and cracks that run diagonally in the solder joint.



**Figure 4- 30: Cross-section of BGA with Namics 1594-6 along package diagonal.**

It is not yet well understood why the cracking location through packages with reworkable underfill result in different cracking location and path throughout the solder joints. Throughout the thermal cycles underfill expansion and contraction alternated between shear, compressive and tensile loading. The response of Pb-free SAC305 solder microstructure with few numbers of grain to such complex multiaxial loading conditions has not been thoroughly studied and is outside the scope of this study. One of the limitations of thermal cycling BGAs with single daisy chain pattern is identification of the solder joint that fails first. Since all group C underfill

components were taken from the thermal chamber past the recorded characteristic life the extent of cracking makes identifying the critical location using cross-sectioning almost impossible. Therefore, the subsequent chamber will utilize simulation tools to predict the most critical location in the package and provide answers to the magnitude of energy density each underfill introduces to BGA solder joints.

## **FINITE ELEMENT MODELING AND FATIGUE LIFE PREDICTION MODEL DEVELOPMENT**

### **5.1 Finite Element Modeling**

Modeling and simulations have been widely used to analyze the electrical, mechanical and thermal behavior of electronic packages. [105]. FEA methods are used to provide an approximate solution for field variables for problems to which analytical solutions are difficult to obtain. In this study a 3D model of the 17mm BGA package previously used for thermal cycling is modelled using the Abaqus FEA software. Underfill materials that were characterized are applied BGA package under the thermal cycles used in chapter 4. Stresses and strains are post processed to calculate the accumulated creep strain energy density at for each experimental test combination. A mode separation scheme is then employed to determine the change in shear and axial energy component for each underfill. Fatigue life prediction equation based on the mode separation is then calibrated using experimental data.

### 5.1.1 Thermal mechanical simulations

Thermo-mechanical simulations of electronic components often utilized simplifications in model geometry or material properties. Generating 2-D models over 3-D models is a popular approach for simplifying electronic packages [106]. In this study, quarter symmetric 3D model of the BGA package was modeled as shown in Figure 5-1. The model contains information on the geometry and material properties of the BGA package, solder and PCB. Internal structure of the package was generated including the overmold, die, die attach material and organic substrate.

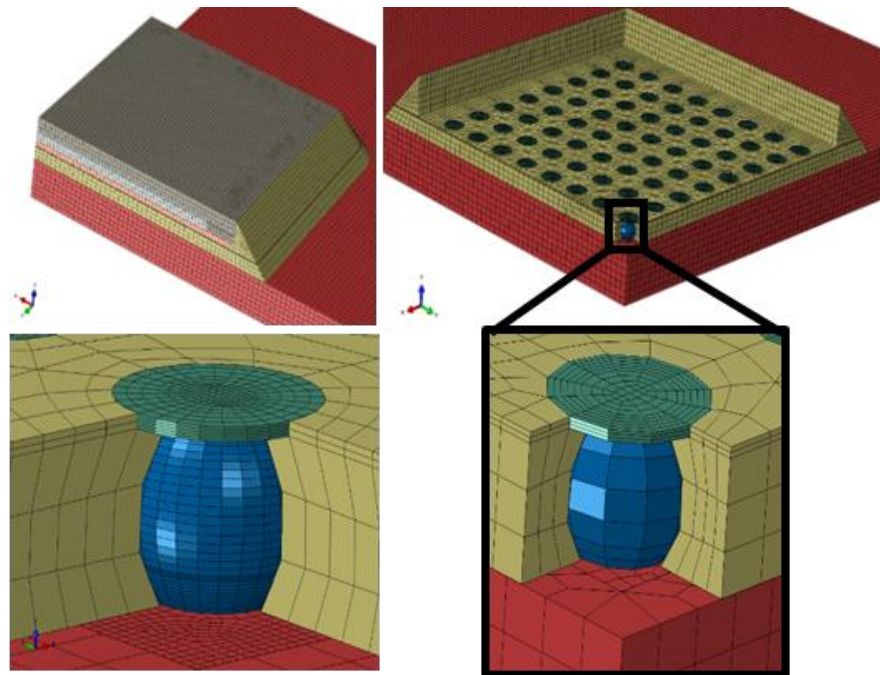


**Figure 5- 1: Global quarter symmetric model with tied underfill UF2 (Left) solder joint in package center with coarse mesh (Right).**

The solid element C3D8R is a hexahedral eight-node linear brick with first order reduced integration element. First order elements are favorable for materials experiencing large deformation. Reduced integration uses a lower-order integration to form element stiffness leading to lower computation time. C3D8R reduced integration

points are robust against distortions; however, some limitations of this type of element include hour glassing that [107]. Having only one integration at the center of the element. Figure 5-2 shows the boundary conditions placed on the quarter-symmetric BGA model where displacement on the face of the package and PCB were constrained. The face of the underfill was constrained as well in later models. A single node on the center of the PCB was constrained in space by setting the x,y,z displacement to zero. This is done to ensure prevent the model from rotating around itself under thermal expansion while reduce the possibility of over constraining the faces of the model that expand and contract.

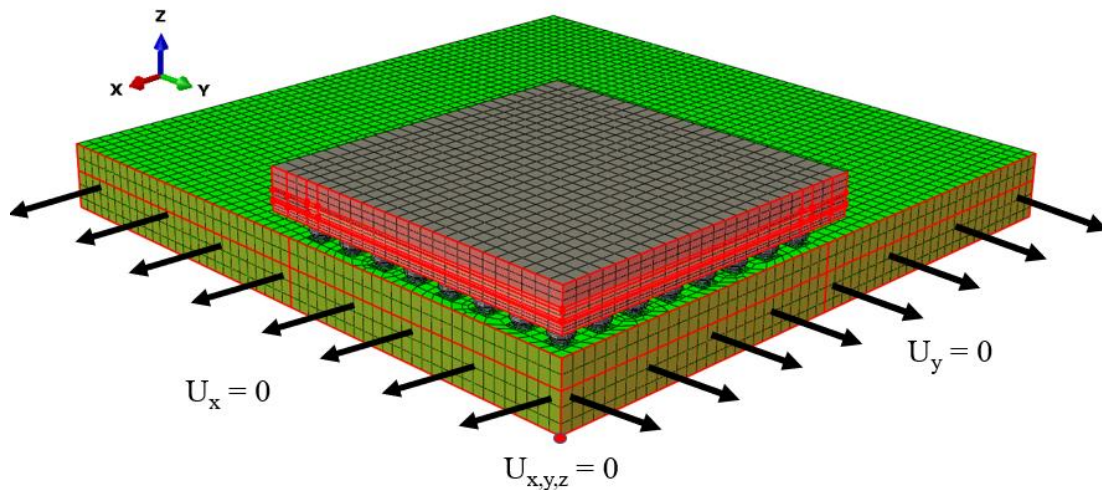


**Figure 5- 2: Displacement boundary conditions for the quarter symmetric BGA model.**

Prior to simulating the interaction of underfill and BGA it is important to understand the behavior of the control non-underfilled BGA package and how energy density calculated from this configuration can be used to validate the characteristic life that was experimentally obtained. Figure 5-3 shows a cut view of the quarter symmetric model



and a close-up view of the corner BGA with higher mesh density compared to the rest of the solder joints. It is also possible to see the internal structure of the BGA with the die shadow located right above the corner solder ball as it was previously shown in the failure analysis portion. The corner most solder joint consisted with the highest mesh density. The mesh density of subsequent package constituents can be decreased farther away from the area of corner solder joints in order to limit the total number of elements and nodes of the FEA model. The model shown in Figure 5-3 consists of 141,950 C3D8R elements with the corner solder joints comprising of 3796 elements. The total number of elements in the local model of the corner solder joints was 21013 elements while the coarser plugs used for the remaining 63 local models consisted of 1464 elements. The global/local modelling approach used in this study has been previously used for thermal simulations of BGA packages and found to have satisfactory results in models that do not contain tie constraints in the local model [108].

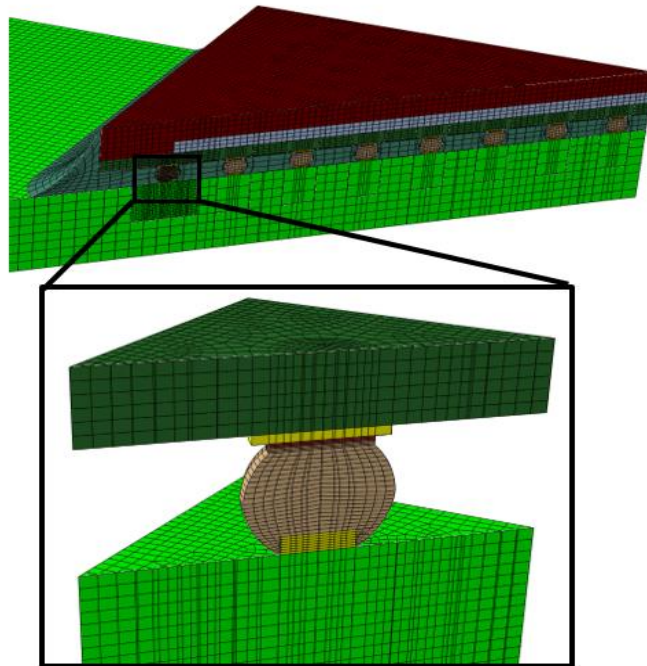


**Figure 5- 3: Cross-sectional view of underfilled BGA along the distance to neutral axis to the center of the package.**

The first control BGA with no underfilled is initially studied to determine the stress state and energy density accumulations in the solder. FEA model inputs are derived from chapter 3 of the dissertation. Figure 5-4 shows the energy density contour obtained from the FEA model and compared with the cross-section of the corner BGA that found to fail at the board side of the joint. Crack propagation I found to coincide with the location of energy density in the FEA model at the bottom of the solder joint. Although the energy density contour shown in Figure 5-4 represents only three thermal cycles longer progression of thermal cycles will result in matching the strain localized region with the location of highest dissipated creep energy density.

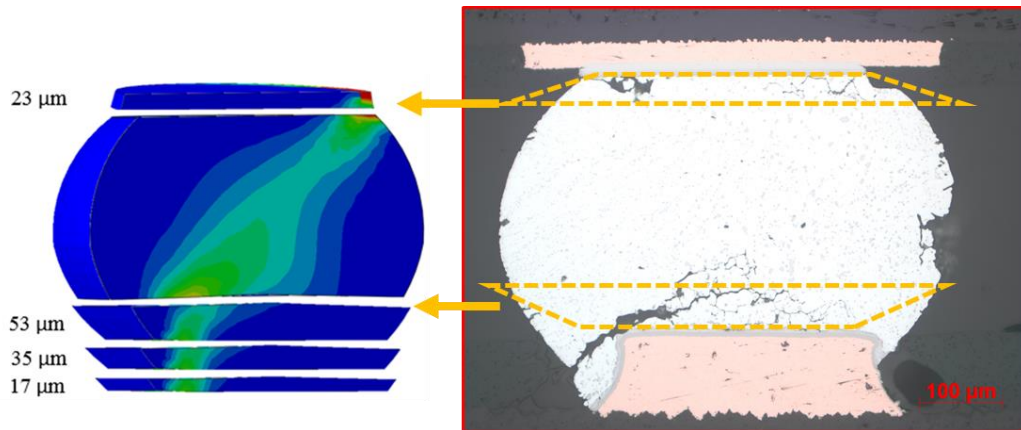


**Figure 5- 4: Various layers in FEA model corresponding to location of crack propagation in solder joint.**

Figure 5-5 illustrates the volume averaged energy density for three solder volumes at the bottom interface of the BGA where fatigue cracking was observed with the -40°C to 125°C thermal cycle. Cycles to failure are then calculated using equation 2-15 and indicated by the red bars. It can be seen that the bottom 35μm volume of solder at the PCB side results in a characteristic life closer to the one obtained experimentally for

the same component and thermal profile. A note to make is that a single element at the upper interface of the second most solder joint along the perimeter showed highest energy density. Although the top left corner of the solder joint indicated single most loaded element the volume weighted averaged energy density at the PCB interface is significantly lower than that at the bottom interface where fatigue cracking was found to occur for the control BGA.

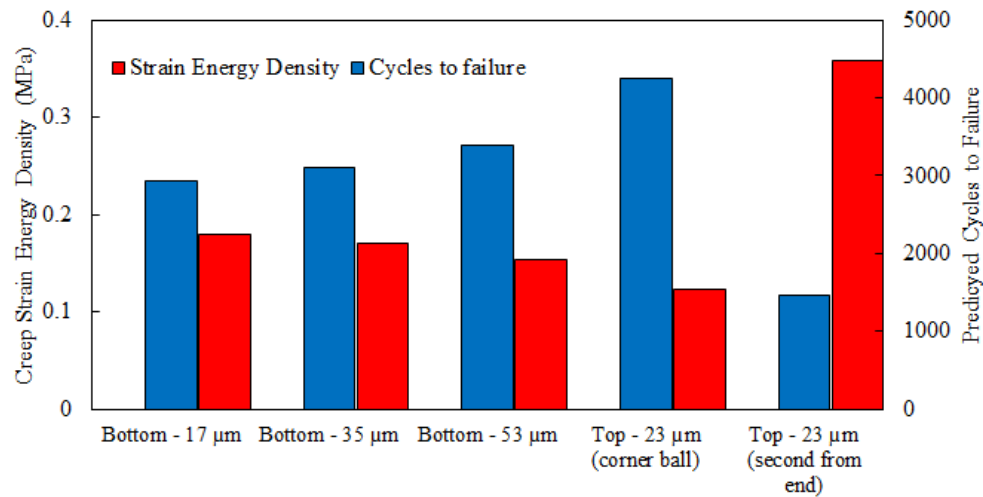


**Figure 5- 5: Accumulated creep strain energy density for the various solder joint volumes in control BGA.**

### 5.1.2 Model development and assumptions

To successfully execute a numerical model and result in meaningful result a few assumptions were made regarding the model geometry, material properties and boundary conditions. One of the most important factors in underfill model construction is the underfill fillet shape itself. Since the final underfill fillet geometry is process dependent it is important to capture the dimensions for each material and application using cross-sections. The underfill fillet for the three underfills used in Group B study is shown in Figure 5-6. Loctite3808 and the Namics underfill were found to closely

match each other and therefore a single dimension was used in both models. The silicone and EP1238 underfill; however, demonstrates a quite different underfill formation due to material behavior during dispensing and cure. Silicone underfill flowed outward of the package and significantly varied from package to package while the fillet with the EP1238 underfill is shown to flow outward of the package in a more consistent triangular geometry. In both of these non-conventional underfill materials the resulting fillet reached the entire package side wall from the PCB.

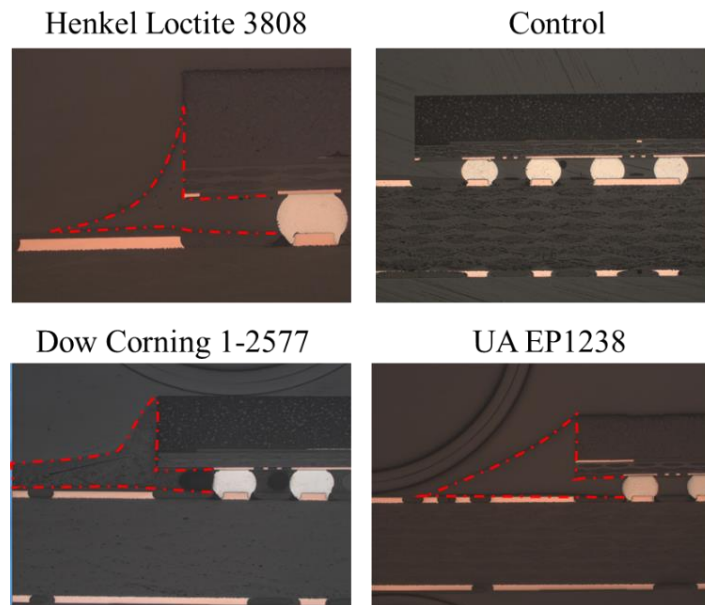


**Figure 5- 6: Filler size for group B underfill materials.**

- Underfill is tied only to the BGA package and PCB.
- Solder mask has no effect on CTE mismatch of package and PCB.
- No residual warpage and stress in the BGA package due to model transfer process
- PCB, silicon, substrate and mold compound behave in a linear elastic manner with temperature.
- Solder deformation is dominated by creep deformation only.

- Temperature of the package and PCB changes uniformly through the thermal cycle.
- No effect of solder microstructure and grain orientation
- Solder joint geometry is consistent from joint to joint.

Figure 5-7 shows the modeled underfill fillets for Group B underfill that were obtained from cross-sections shown in Figure 5-6.

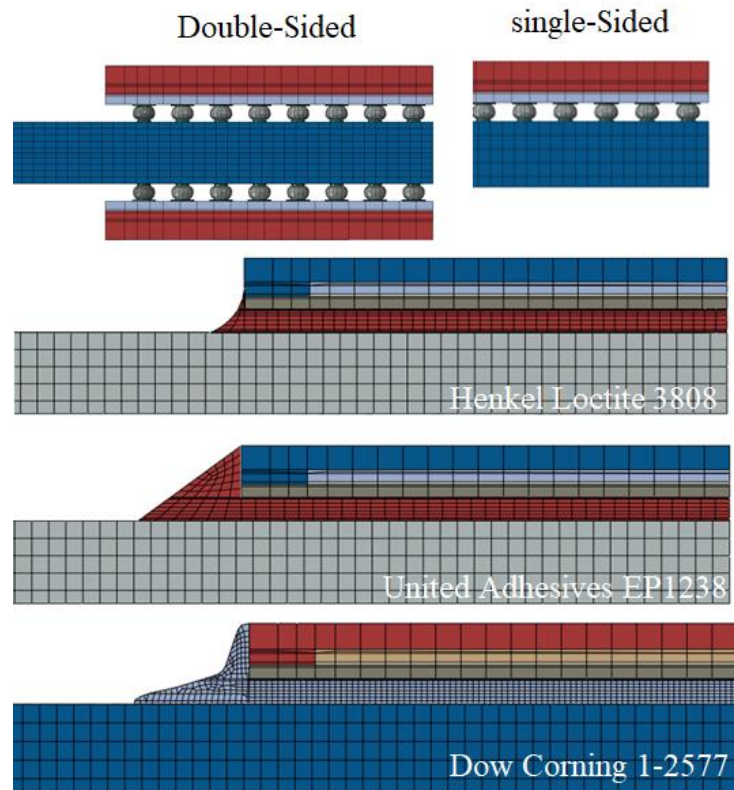


**Figure 5- 7: FEA models of BGA with underfills including accurate representation of underfill fillet geometry for group B materials.**

### *5.1.2 Mesh Convergence Study*

The number of elements in a given numerical model has been shown to influence the accuracy of the model [109,110]. Therefore, a mesh convergence analysis on the number of elements in the critical solder joint is performed. The local model of the corner most joint is built using continuous mesh and does not contain any tie contacts of linear elastic materials to the viscoplastic solder itself. Figure 5-8 shows the variation of energy density with mesh size for the local model. The number of elements from in the local model varied from 328 to 11,840. The energy density was averaged for the same solder volume at the board side of the solder joint. Two approaches for representing the energy density were demonstrates. The first one utilized volume weighted energy density and a second one with element averaged energy density. The element averaged and volume weighted approach closely match each other at the 0.04 and 0.02mm mesh sizes. Overall the energy density between the finest and coarsest mesh size demonstrated here varied by 30 percent. A mesh size of 0.04mm was determined to provide a reasonable density for the local model. The local model is then connected to the global model using tie constraints at the surfaces of the PCB and substrate.

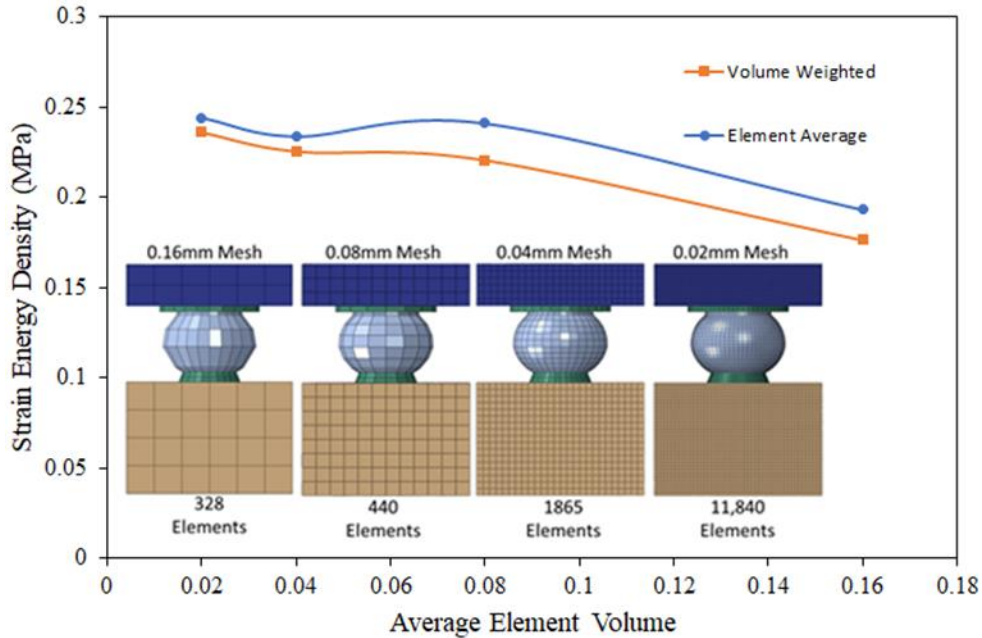


**Figure 5- 8: Mesh convergence of corner most solder joint in BGA without underfill.**

## 5.2 Stress State in BGA Solder Joints

### 5.2.1 Effect of Underfill Properties on Energy Density

The influence of underfills material properties can be evaluated using simulations by introducing simplistic assumptions prior to introducing more complex temperature and time dependent material models. To investigate the influence of underfill CTE and modulus on creep strain energy density constant underfill properties are first assumed. Figure 5-9 illustrates the obtained creep strain energy density for thermal cycling the 17mm BGA package from  $-40^{\circ}\text{C}$  to  $125^{\circ}\text{C}$  using underfill CTE ranging from 20 to 70 ppm/ $^{\circ}\text{C}$  and modulus from 1MPa to 8000MPa. Each data point represents an 3D

simulation of the quarter symmetric model. The strain energy density was averaged for the corner most solder joint at the board interface for 35 $\mu$ m thick solder volume.

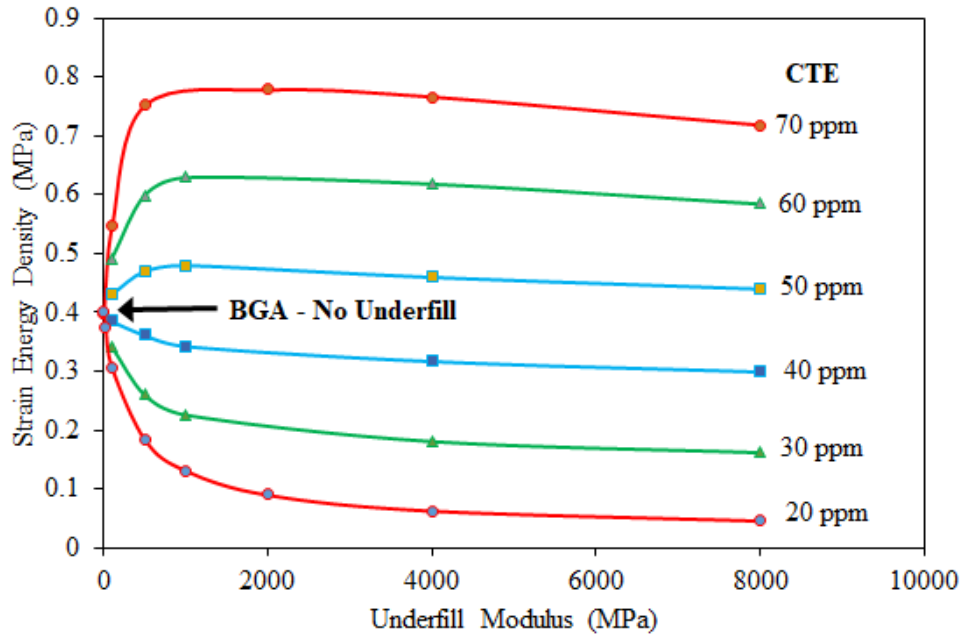


**Figure 5- 9: Dissipated energy density in corner solder as function of underfill CTE and modulus.**

A few observations can be made from the simulations of the underfills with constant properties. The first observation shows that all configurations converge to the same point as a BGA without underfill as the elastic modulus decreases. This indicates that an elastic modulus of 1MPa will not provide the underfill substantial stiffness to act in the load sharing during thermal cycling. The second observation indicates that underfills with elastic modulus of 2000MPa and beyond do not contribute in load sharing. It can be seen that an underfill with a CTE of 40 ppm/ $^{\circ}$ C will result in minimal energy accumulation in the solder compared to the non-underfilled controlled BGA.

To understand this behavior the 30 and 60 ppm/ $^{\circ}$ C configurations are evaluated with respect to the mode of the energy density. Figure x shows the partitioned Mode I and Mode II energy densities along with the control configuration. Underfill with 60



ppm/°C has mode I energy that is 1.7X to 2X higher than mode II energy for elastic modulus of 500MPa to 8000MPa, respectively. Underfill with 30 ppm/°C has higher Mode I energy than Mode II by a factor of 1.2X to 1.7X for underfill with 500MPa and 8000MPa, respectively. These two underfills are selected since it is known from the previous thermal cycling experiments that the lower expansion underfill improves fatigue life while the higher expansion underfills reduces thermal fatigue life compared to the non-underfills package. Interesting, both Mode I and Mode II energies for the control BGA are nearly identical and are comparable in magnitude to Mode II energy of the 60 ppm/°C underfill.

### 5.2.2 Energy density partitioning into Mode I and Mode II

A new mode separation scheme is proposed in this study that approaches the partitioning of the total dissipated creep energy density per cycle to Mode I and Mode II loading. The global loading modes are taken with respect to the direction of crack propagation in the solder that usually occurs along the intermetallic interface. The normal stress and strain components to the location of crack propagation are taken for Mode I energy density. The deviatoric stress components along with the  $\sigma_{11}$  and  $\sigma_{22}$  are used for Mode II energy density calculation as shown by the stress tensor below.

$$\sigma_{Mode II} = \begin{bmatrix} \sigma_{11} & \sigma_{12} & \sigma_{13} \\ \sigma_{21} & \sigma_{22} & \sigma_{23} \\ \sigma_{31} & \sigma_{32} & \sigma_{33} \end{bmatrix} \quad \sigma_{Mode I} = \begin{bmatrix} & & \\ & & \\ & & \sigma_{33} \end{bmatrix}$$

The total dissipated energy density is calculated by integrating the sum of the stress and creep strain components in equation 5-1.

$$\Delta W_{acc} = \int \varepsilon_{ij} \sigma_{ij} \quad (5-1)$$

Mode I energy density is calculated with respect to the coordinate system of the FEA model. Post processing the stress and strain components are performed with the normal component that is perpendicular to the interface of the copper pads and the solder. In this study the 33 direction represents the normal direction that is perpendicular to crack propagation shown in equation 5-2.

$$\Delta W_{Mode I} = \int \varepsilon_{33} \sigma_{33} \quad (5-2)$$

Mode II energy density is calculated from the remaining normal stress components along with the deviatoric shear stress as shown in equation 5-3.

$$\Delta W_{Mode II} = \int \varepsilon_{11} \sigma_{11} + \int \varepsilon_{22} \sigma_{22} + \int \varepsilon_{12} \sigma_{12} + \int \varepsilon_{13} \sigma_{13} + \int \varepsilon_{23} \sigma_{23} \quad (5-3)$$

Calculation of Mode I and mode II energy density is carried out using the post processing python script that is calculated at every step increment in the solutions for every element in the solder joints at the integration points. Due to the reduced integration element type the energy density is an average representation of stress and strain at the center of the element. Figure 5-10 shows cross-section of the corner most solder joint with mesh and a slice of two elements in thickness that is used for volume weighted average of the energy density.

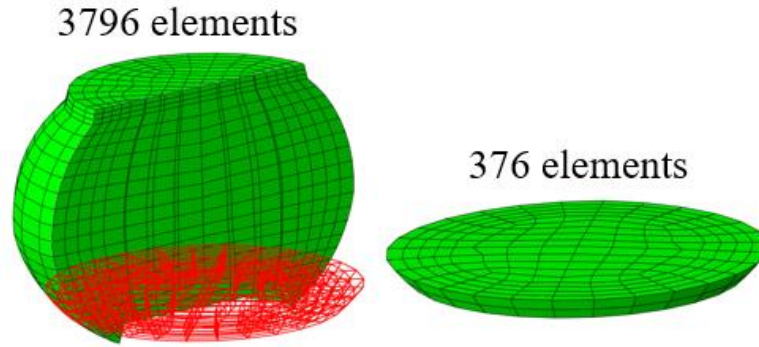


**Figure 5- 10: Volume of solder used for energy density partitioning and fatigue prediction.**

After averaging the energy density that is partitioned the impact of the addition of underfill to the BGA package can be determined. Two underfill conditions from Figure 5-9 are post processed to determine the loading mode in the solder joint as a result of underfill under thermal cycling. Figure 5-11 shows the volume weighted energy density for the two-layer slice of elements in the corner most solder joint for control BGA and with 30ppm and 60ppm underfill assuming no glass transition effect.

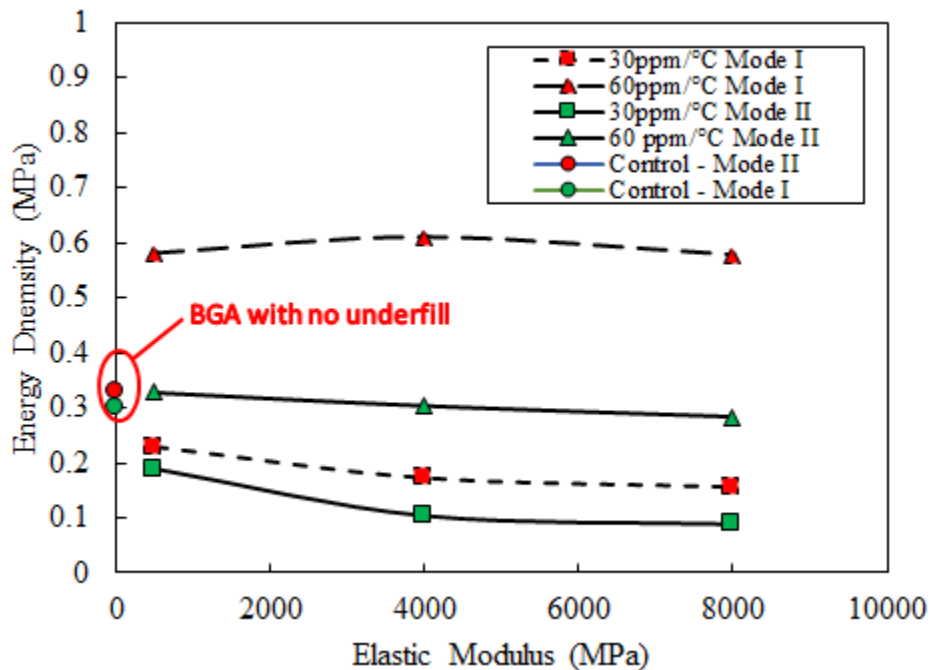


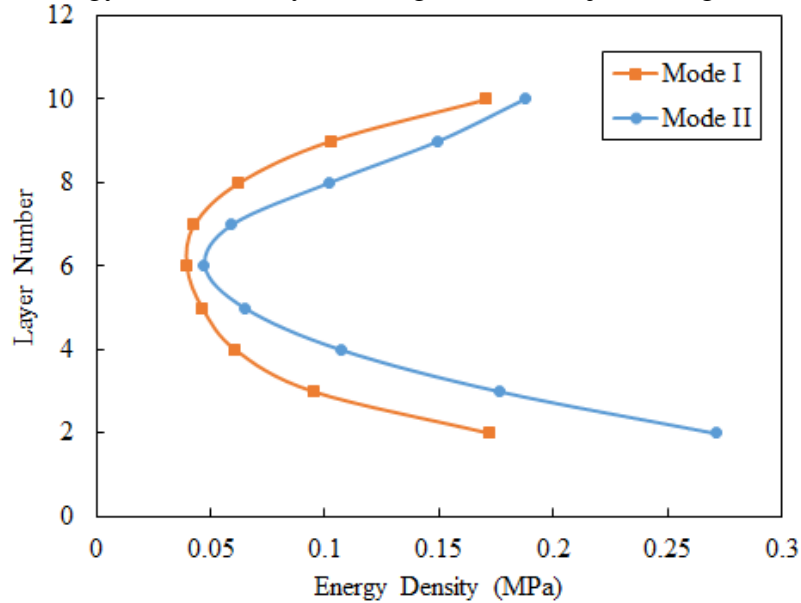
**Figure 5- 11: Mode I and Mode II energy density for 30 and 60 ppm underfills as function of elastic modulus.**

The control BGA indicates Mode II energy to be slightly higher than Mode I energy density for the -40 to 125°C thermal cycle. This indicates that shear loading conditions is dominant for the non-underfilled BGA while both the underfills indicate that Mode I is higher than Mode II due to the contribution of the tensile stress that occurs between the expansion of the underfill between the package and PCB. The respective amount of Mode I increase over Mode II between 30 and 60ppm underfill is dependent on the CTE mismatch between the solder and the underfill as well as the height of the gap between the package and PCB. Mode I and Mode II energy density is a culmination of global and local CTE mismatch as well as the warpage of the package and PCB that result in straining the solder joints. Figure 5-12 illustrates the separation of Mode I and Mode II through the height of the corner most solder joint for the non-underfilled BGA for the -40 to 125°C thermal profile. The magnitude of the energy mode is plotted on the horizontal axis and it shows that the highest values occur at the bottom layer where crack propagation was found in the previous experimental section. The magnitude of the energy density and ratio between Mode I and Mode II changes throughout the thickness of the solder joint with the center of the solder showing the smallest variation

between the two modes and lower magnitude compared to the upper and lower interfaces.

**Figure 5- 12: Energy density Mode I and Mode II components for each 32  $\mu\text{m}$  thick layer in corner joint of BGA package without underfill.**

Figure 5-13 shows both energy density components for the same solder volume for a BGA with Loctite 3808. In this configuration the Mode I energy component is larger than Mode II energy at all the layers along the corner joint height. This behavior



indicates that the axial stresses and strains contributing to Mode I energy are substantially larger than Mode II deviatoric components. Unlike the control BGA that exhibits closer Mode I and Mode II components in the center of the solder joints, the underfills BGA demonstrates higher difference between the center and interfacial solder volumes in the solder joint.

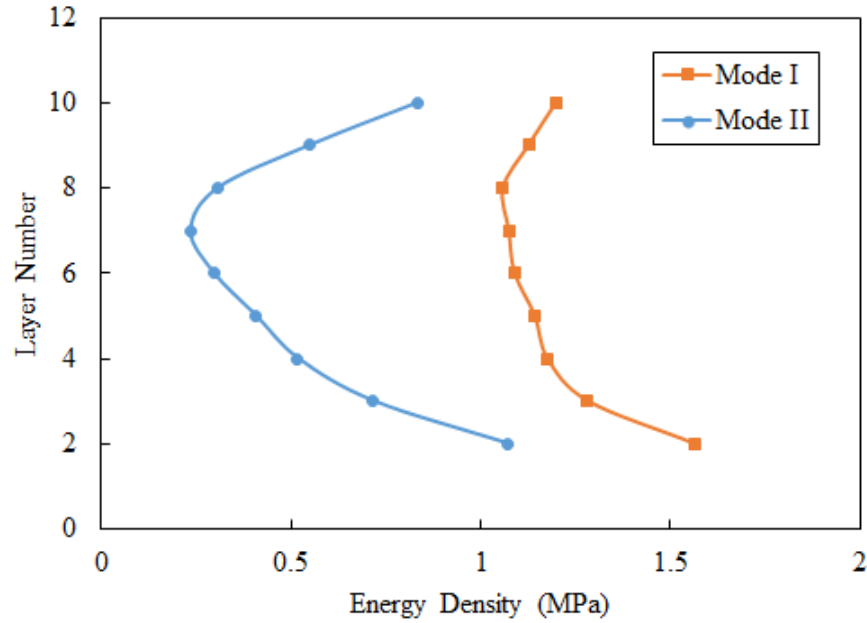


**Figure 5- 13: Energy density Mode I and Mode II components for each 32  $\mu\text{m}$  thick layer in corner joint of BGA package with Loctite 3808 underfill.**

Another significant observation is the magnitude of Mode II energy in the underfilled BGA compared to the non-underfilled BGA. Mode II energy increases by 4X at the lower interface for the underfilled BGA compared to the control one. This observation is in agreement with recent experimental measurements on strain in solder joints of PoP BGA with reworkable underfill [111]. In their research Wu et al. demonstrated that the average shear strain in solder joints increases with reworkable underfill. Although this observation is important it does not provide information on the axial strain component or the stress state of the solder. In addition, it is currently not possible to experimentally measure the stress state of the solder as a function of temperature. Therefore, FE simulations provide an alternative for approximating the stress state in solder with and without the application of underfill. Figure 5-14 illustrates the energy modes for the control and unrefilled BGA with Loctite 3808 along the package distance to neutral point. The magnitude of energy density for both modes is evidently higher for the

underfilled BGA compared with the control BGA. Another observation is that Mode II energy density is higher for the control BGA at every solder joint along the diagonal with the center joint having the lowest energy density and corner one having the highest as expected.

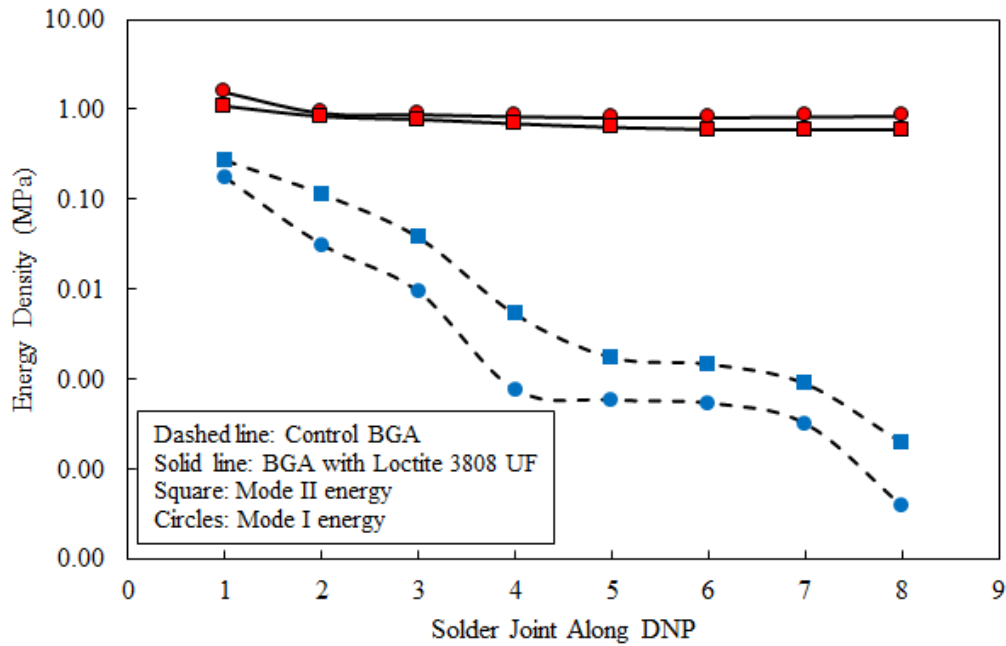


**Figure 5- 14: Mode I and Mode II energy densities on the distance to neutral line for BGA with and without Loctite 3808 underfill.**

The underfilled BGA demonstrates an opposite behavior where there is no distinct distance to neutral effect. The magnitude of Mode I and Mode II energies are tightly clustered for all solder joints along the distance to neutral only with the corner most solder joint demonstrating a slight increase in Mode I energy density. Again, this observation is in agreement with experimental results that found no dependence on distance to neutral effect for Loctite3808 underfill.

The stress and strain behavior in the solder with and without underfill throughout thermal cycling can provide information on the accumulation of Mode I

and Mode II energy densities. Figure 5-15 shows the 23 and 33 creep strain components for the first 15 thermal cycles. The strain is averaged for the same volume of solder.

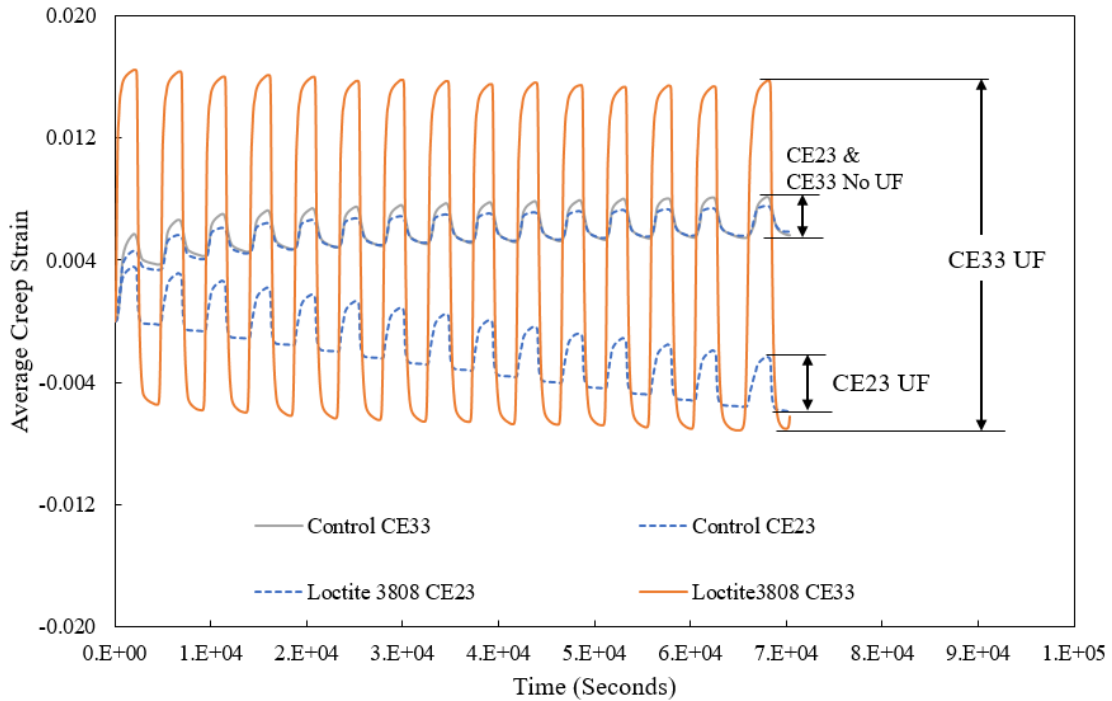


**Figure 5- 15: Average creep strain in corner solder joint for 15 thermal cycles for BGA with Loctite3808 underfill -50°C to 125°C.**

The both the 23 and 33 creep strain range for the BGA with no underfill is found to closely follow each other with thermal cycles and reach steady state mean strain condition after sufficient number of cycles. The average strain is used for qualitative illustration here rather than quantitative assessment to demonstrate the strain behavior in the modeled region of the solder that experiences fatigue cracking. The magnitude of the out of axial strain is significantly higher than the 23 components for the underfilled BGA. The shear strain component is found to ratchet with the number of thermal cycles. The cyclic ratcheting behavior is indicative of structures experiencing cyclic stress reversals that experience creep strain accumulation. A similar creep ratcheting behavior was previously demonstrated using numerical models for BGA



packages with eutectic solder undergoing thermal cycling [112]. This causes the center of the hysteresis loop to shift and cause relative motion between the pad and the solder and lead to crack propagation. As previously discussed, ratcheting behavior is indicative of the mean stress effect and interaction of shear and tensile loads during thermal cycles.

### *5.2.3 Hydrostatic Stress in BGA solder Joints with and Without Reworkable Underfill*

Hydrostatic stress was previously correlated to enhance volume growth of microscopic voids in metals [113]. The hydrostatic stress is defined as the trace of the normal stress components shown in equation 5-4.

$$\sigma_{Hyd} = \frac{\sigma_{11} + \sigma_{22} + \sigma_{33}}{3} \quad (5-4)$$

The effect of hydrostatic stress on fatigue life of solder joints under mechanical vibrations previously demonstrated and found to increase with board bending [114].

The shift in hydrostatic tension and compression during temperature cycles have been shown to contribute to the damage in solder joints of electronic packages [115]. In addition, research into the effect of hydrostatic stress due to cure of flip-chip packages found a hydrostatic constraint imposed on the solder [116, 117]. To understand the effect of hydrostatic stress on characteristic life obtained for different underfills in this study the average hydrostatic stress was calculated for the 376-element layer at the bottom of the corner most solder joint of the 17mm BGA package. Figure 5-16 shows the change in hydrostatic stress for each element for the first three thermal cycles.

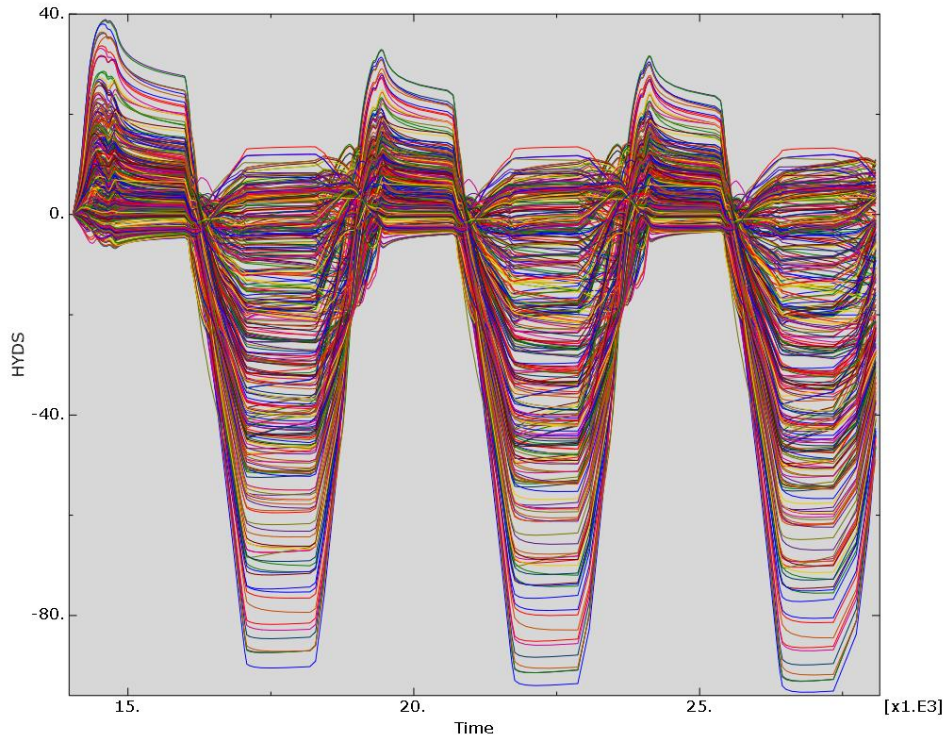


**Figure 5- 16: Hydrostatic stress as a function of time for control BGA from -50 to 125°C thermal cycles for 376 elements at the PCB side of the corner solder joint.**

Due to the loading mode and geometry of the solder joint some elements exhibit higher hydrostatic stress than other. The compressive point of the hydrostatic stress is shown to occur at the low temperature dwell while the tensile hydrostatic stress occurs at the onset of the high temperature well prior to stress relaxation. The average hydrostatic stress is used for comparison with the underfilled and non-underfilled BGA as a function of time for the first three thermal cycles as shown in Figure 5-17 below. The uniform temperature profile is superimposed on the stress to illustrate the dependence of the stress state on temperature. The blue line is shown for Loctite 3808 underfill while the orange line for the control BGA. A compressive mean hydrostatic stress is found for both underfilled and non-underfilled BGAs.

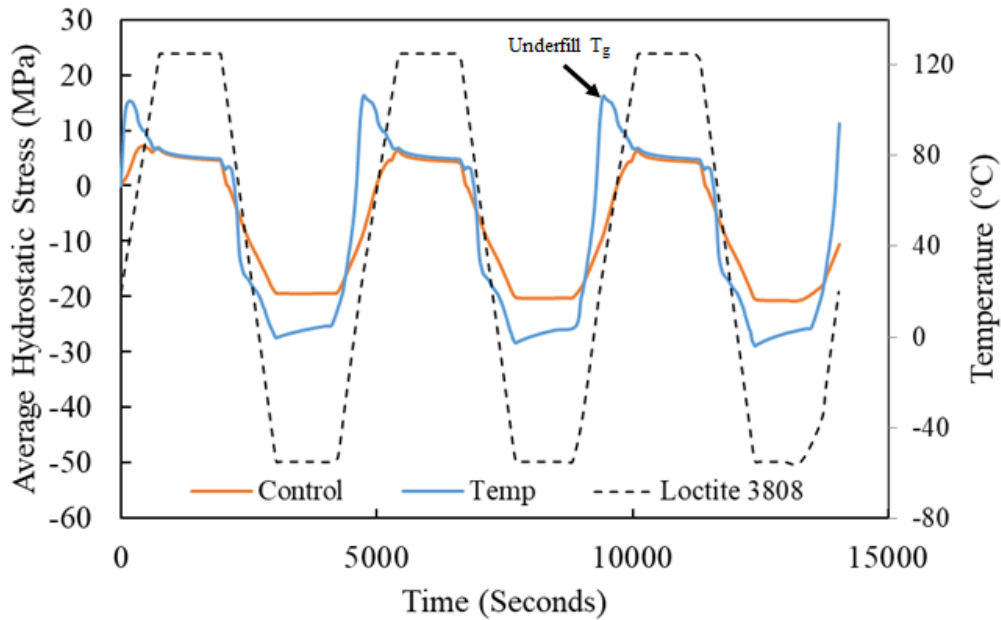


**Figure 5- 17: Average hydrostatic stress for the first three thermal cycle for control BGA and Loctite 3808 from -55°C to 125°C.**

The underfilled BGA represented by the blue line shows a tensile peak in the hydrostatic stress around the underfills  $T_g$  that does not occur in the orange line for the non-underfilled BGA. In fact, this peak around the glass transition was found in simulations of all underfills in which the thermal profile crossed the  $T_g$ . The peak tensile hydrostatic stress decreases after a short temperature increment due to underfill softening across the transition region. This is evident in the same stress relaxation between the non-underfilled and underfilled BGAs during the high temperature dwell. Interestingly, the thermal profile crosses the underfill  $T_g$  on the ramp up and ramp down. During the ramp down cooling of the package the underfill contraction occurs faster than the PCB and package and result in increasing the hydrostatic stress as the underfill stiffens below the  $T_g$ .

The mean hydrostatic stress for Group B and C underfills was determined and plotted in Figure 5-18. It can be seen that the mean hydrostatic stress changes with the underfill material as well as the thermal profile itself.

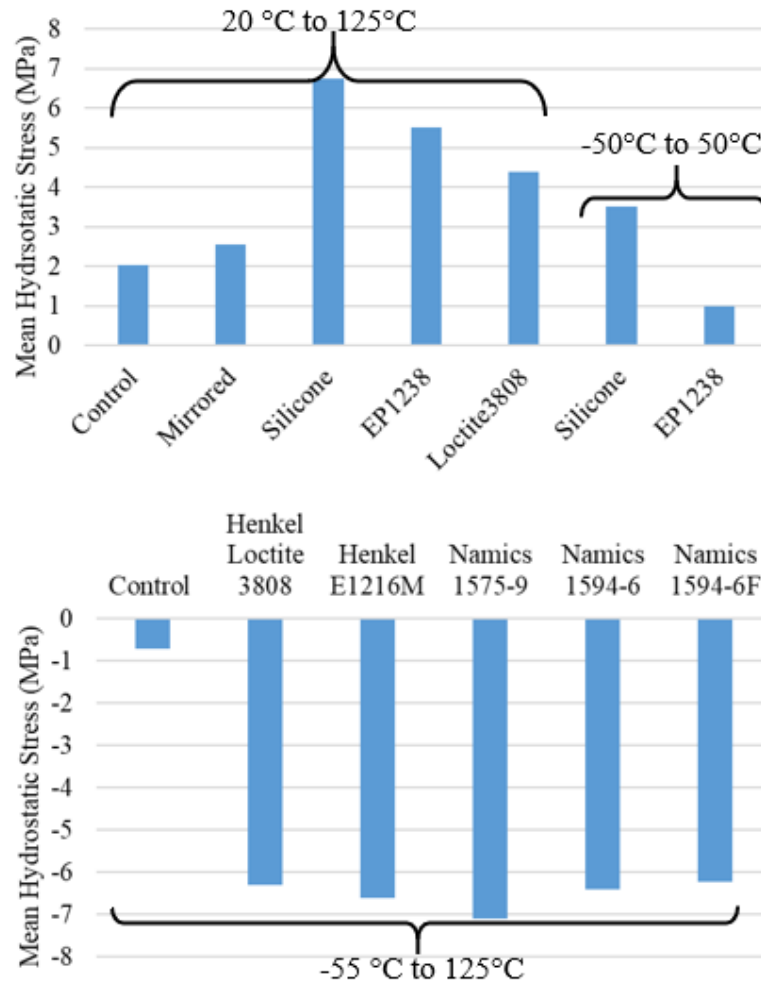


**Figure 5- 18: Average mean hydrostatic stress in corner most solder joint for BGA with group B and C underfills at different thermal profiles.**

The mean hydrostatic stress for all group B materials is found to be tensile while all group C materials are found to have a mean compressive hydrostatic stress. This observation is indicative of the temperature dependent material properties of the underfill and the range of the temperature profile itself. The non-underfilled BGA exhibits mean tensile stress from 0°C to 125°C and a mean compressive one from -55

to 125°C. In both profiles the stress-free temperature was assumed to be 20°C. Although the mean temperature in both profiles is above the assumed stress-free temperature the mean hydrostatic stress also depends on the warpage and CTE mismatch characteristics of the package and PCB. The highest tensile hydrostatic stress at the 20 to 125°C profile is found for the BGA with silicone underfill that consequentially had the lowest characteristic life. All group C underfills that found decrease fatigue life with respect to the control BGA demonstrate a more compressive hydrostatic stress. This observation can be used to determine if the loading condition between control and underfilled BGAs will result in the decrease of fatigue life based on the ratio of the mean hydrostatic stress with respect to the control BGA for a given temperature cycle.

### *5.2.2 Interaction of Underfill and Solder*

In this study two conditions are examined between the underfill and solder. The first condition assumes mesh tie interaction between the underfill material and the solder and the second conditions assumed no interaction with the solder. The second condition is modeled in a manner at which the underfill occupies the same space of the solder and is only tied to the surface of the component and PCB. The first condition is implemented by defining tied constrain between the surface of the underfill and the solder. The tie constraints ties nodes on surfaces that are in contact with each other and makes translational and rotational degrees of freedom equal for the pair of surfaces. Figure 5-19 illustrates the tied constraint on the left and the “through” condition on the right that neglects any

interaction with the solder. Larger stress in the underfill are observed at the tied interface between the solder and the underfill as shown in Figure 5-20.

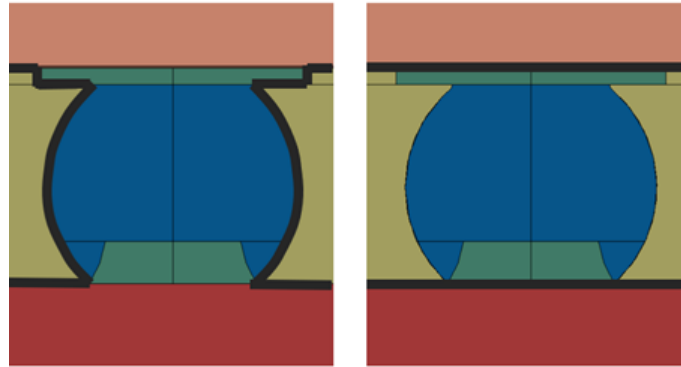


**Figure 5- 19: Boundary conditions for underfill tied to package and solder (left) tied to package and component only (right).**

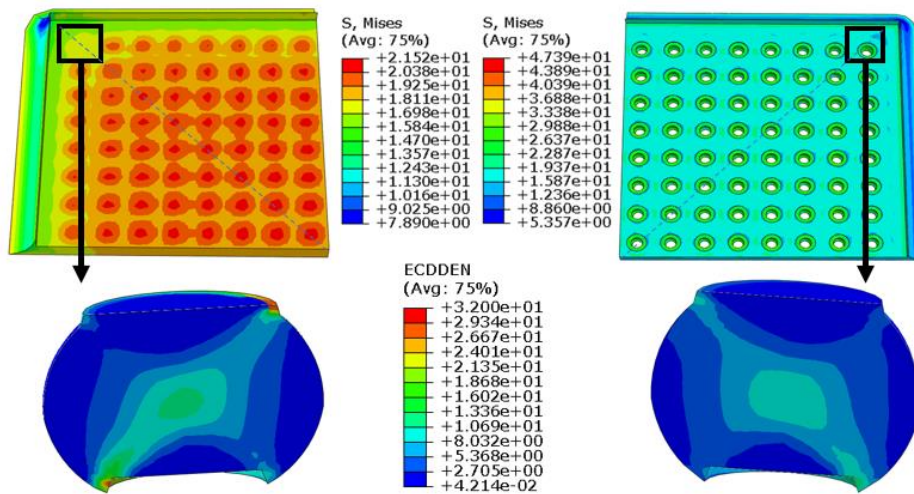


**Figure 5- 20: Von-mises stress distribution in underfill without interaction with solder (left) with interaction with solder (right) and strain energy density in corner solder joint after three thermal cycles.**

The configuration of the underfill that is not in contact with the solder results in lower stresses in the solder but with higher dissipated energy density in the solder. This difference is performed assuming linear elastic underfill behavior. The non-tied underfill and solder configuration is used to illustrate the energy density in the solder for group B underfills as function of temperature as shown in Figure 5-21. Since these

materials include high expansion soft underfills that cannot induce compressive load on the solder during cure the trough boundary conditions was used.

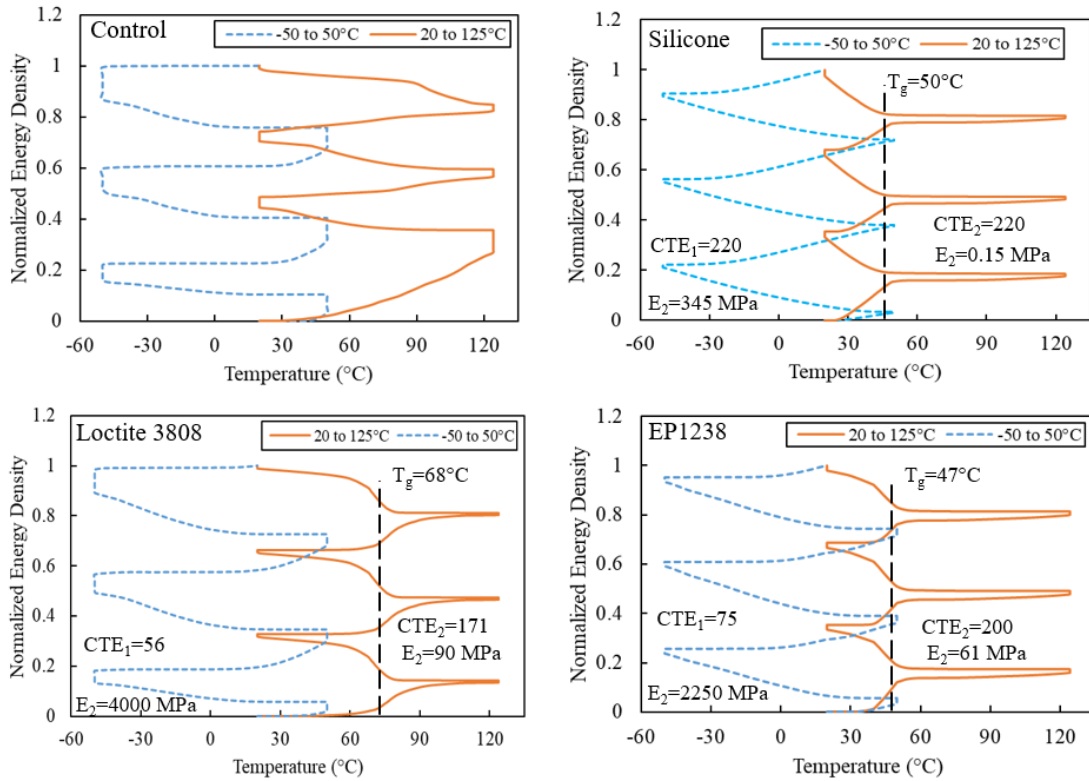


**Figure 5- 21: Normalized energy density as function of temperature for thermal profiles with mean temperature conditions with Group B underfills.**

The normalized energy density was plotted for each configuration as function of temperature due the difference in magnitude between thermal profiles that will result in different scale. The control configuration indicates that the total dissipated creep energy density accumulates mainly in the ramp up and some in the dwell regions. It can be seen that the energy density per cycle decreases for the first thermal cycle compared. The Energy density of the BGA with silicone underfills exhibit a stark contrast to the control BGA. At the high mean temperature profile, the energy density accumulated until the elastic modulus decreases around 50°C to dismiss the effect of the high expansion silicone on the solder. The low mean temperature of the silicone

demonstrates that most of the energy is accumulated as the ramp events. BGA with Loctite 3808 and EP1238 both show increase around the glass transition temperature. The energy density accumulation rate decreases as soon the glass transition region is crossed. The low mean temperature profile with Loctite3808 demonstrates a similar behavior to the low mean temperature of the control BGA out of all the underfills. This is due to the lower CTE and stiffness of the underfill below the  $T_g$  that result in similar energy density to the control configuration. For underfills with higher  $T_g$  such as Loctite3808 the fraction of energy density that accumulates during the ramp down increases as well due to the stiffening of the underfill. The increase in the energy density across the  $T_g$  occurs over a narrow temperature range. With the rate of temperature change of  $10^\circ\text{C}/\text{minute}$  the increase in energy occurs over a period of 4 to 6 minutes before the increment of energy density per temperature stabilizes.

The influence on solder joint energy density accumulation can be represented by visualizing the package and board warpage with temperature as shown in Figure 5-22.

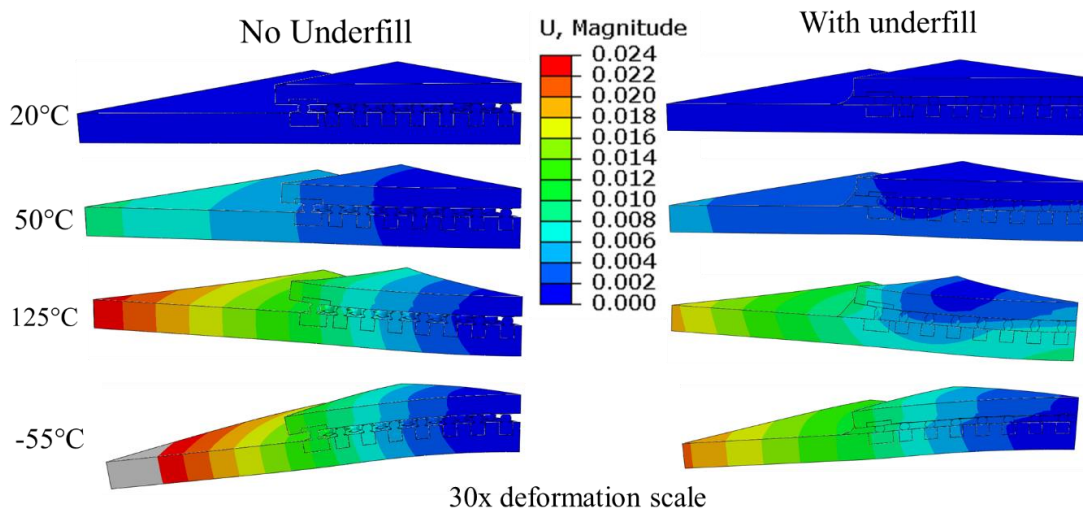


**Figure 5- 22: BGA and PCB warpage for control BGA and with Loctite 3808 underfill at different temperature on the same deformation scale.**



The control BGA warpage on a 30x deformation scale indicates that at the maximum profile temperature of 125°C a substantial warpage occurs. This components warpage relative to the board introduces significant axial loading to the solder. Unlike the control BGA, the underfilled components shows a decrease in component warpage at the peak temperature as well as a decrease in the rigid body motion of the solder due to additional constraint of the underfill. The contribution of the underfill in altering the package warpage characteristics as well as suppressing rigid body motion of the board is indicative of the increase in energy density solder joint sustains through the same temperature profile with underfill.

### **5.3 Fatigue Life Prediction of BGA with Underfill**

#### *5.3.1 Fatigue Life Prediction of Existing Models*

In existing energy-based models, the number of cycles to failure is assumed to have a linear relationship with the accumulated creep strain energy density  $w_{acc}$ . The model shown in equation 1 was developed by Syed and calibrated using data from chip-scale packages. The second fatigue life prediction model used in this analysis was determined for thermal cycling failure rate of flip-chip BGA with underfill [121].

$$N_f = (0.0019\Delta W_{acc})^{-1} \quad \text{Eq 1}$$

$$N_f = 345(\Delta W_{acc})^{-1.02} \quad \text{Eq 2}$$

The above analysis was performed by setting the underfill expansion to interact purely with the PCB and BGA package surface by tie constraints. To model the interaction between underfill materials and solder joints during thermal cycling requires certain assumptions to be made. To illustrate the effect of certain underfill interaction with the

component and solder joints two boundary conditions were selected. The first boundary condition referred to as “BC1” was selected as previously defined by ignoring the interface between the solder and underfill and setting tie interaction only with the surfaces in contact with the package and board. A second boundary condition referred to as “BC2” was set by providing tied contact interaction between the underfill materials and solder in addition to the package and PCB surfaces as in BC1. Fatigue life predictions were then performed using the models defined by equations 1 and 2 for the four underfill materials. Figure 5-23 shows a comparison between the fatigue life prediction for the High Mean thermal cycle with both boundary conditions and fatigue life models. Characteristic life obtained from experimental data is displayed by a red column at the center of fatigue life prediction values for the two models and underfill boundary conditions.

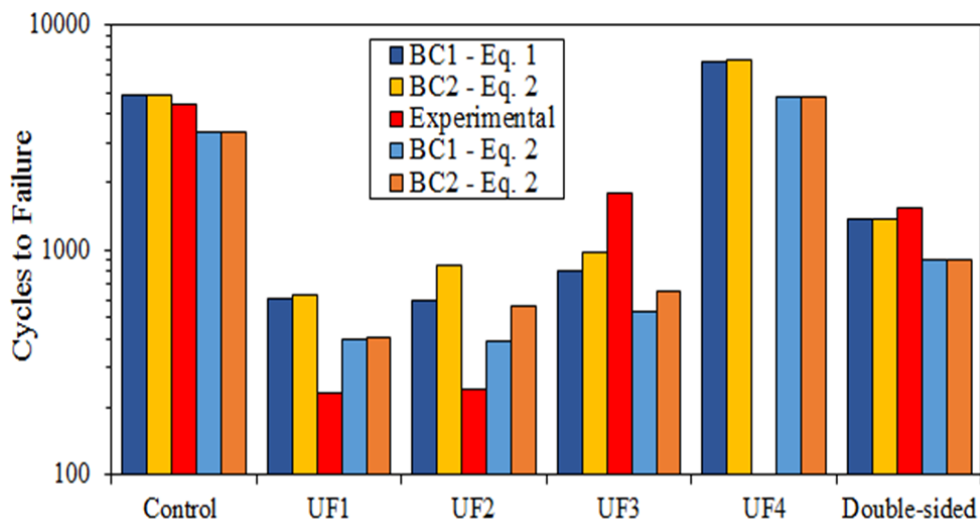


**Figure 5- 23: Fatigue life predictions for group B underfills at High Mean temperature profile.**

Fatigue life predictions from both models are found to be within 20% of the experimental characteristic life for the control BGA with equation 1. predicting slightly

above and equation 2 below the characteristic life of 4441 cycles. For the BGA with silicone (UF1) and EP1238 (UF2) underfills both models over predict experimental results. Component with Loctite3808 (UF3) provides more conservative predictions. In all underfill cases BC1 results with eq. 2 yield lower fatigue life predictions. Predictions for BGA with Namics (UF4) underfill provide values which within 50% of prediction for control BGA. No cycles to failure were observed within the test time with no visible crack forming in solder joints indicating that both models and boundary conditions under predict the possible improvement such underfill would provide under the High Mean thermal profile compared to the rest of the underfills in the study which lower solder joint fatigue life with respect to the non-underfilled BGA. Predictions for the Low Mean temperature profile are displayed in Figure 5-24. Experimental results for the Low Mean thermal profile were obtained only for UF1 and UF2 underfill materials within the tested number of thermal cycles. Similarly, predictions for control BGA for both models match closely with each other and provide an acceleration factor of 2.7 between the High Mean and Low Mean thermal profiles. Predictions for BGA with UF1 and UF2 underfills under predict characteristic life compared to experimental results by an order of magnitude. Unlike predictions for High Mean thermal profile which indicates lower than expected improvement in fatigue life for the UF4 underfill, predictions for the Low Mean thermal profile seem to overestimate fatigue prediction with both boundary conditions and models. Although results both of the accumulated creep strain energy density models are found to provide accurate predictions for the control BGA they fail to provide acceptable predictions of the characteristic life for all

underfill materials used in this test with regard to configurations which reduce and improve the fatigue life.

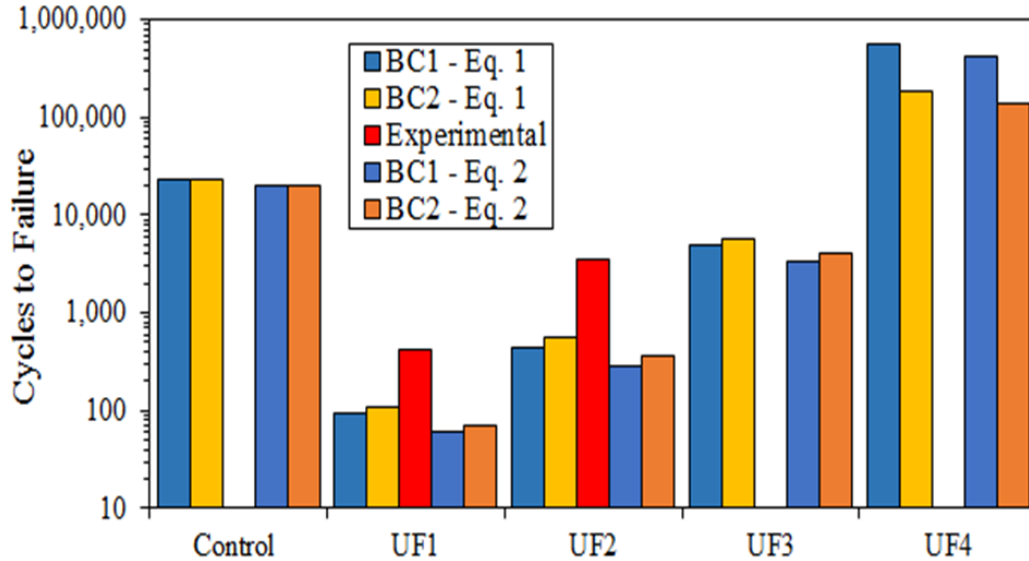


**Figure 5- 24: Fatigue life predictions for group B underfills at Low Mean temperature profile.**

### 5.3.2 Fatigue life Prediction with Mode Separation Approach

The ratio of Mode I and Mode II energy density is plotted in Figure 5-25. This figure illustrates the ratio in energy modes for control and underfilled BGAs. The ratio between Mode I and Mode II was found to be less than 1 only for the control and double-sided BGA components with no underfill. The average ratio between Mode I and Mode II is found to be 1.6. This indicates that even if Mode I is higher than Mode II for underfilled components the magnitude of both components is critical for evaluating the fatigue life of solder joints.

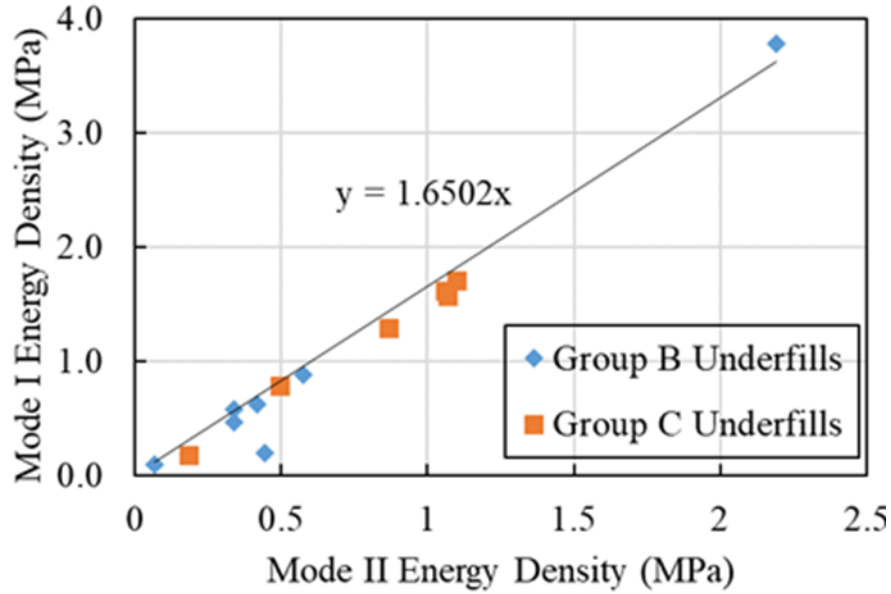


**Figure 5- 25: Mode I vs. Mode II energy densities for linear elastic underfill materials.**

The proposed fatigue life model with the new mode separation approach is shown in equation 5-6. Each energy component is calibrated using fatigue coefficient and an exponent similar to the model developed by Darveaux for crack initiation and propagation.

$$N_f = C_1(\Delta W_{\text{Mode I}})^{n_1} + C_2(\Delta W_{\text{Mode II}})^{n_2}$$

The change in mode I and Mode II energy components with characteristic life depend on the underfill properties and thermal profile range. A trend in which the conference of energy density component is shown in Figure 5-26. In this figure, both energy density modes seem to converge for the non-underfilled BGA that had the highest characteristic life.

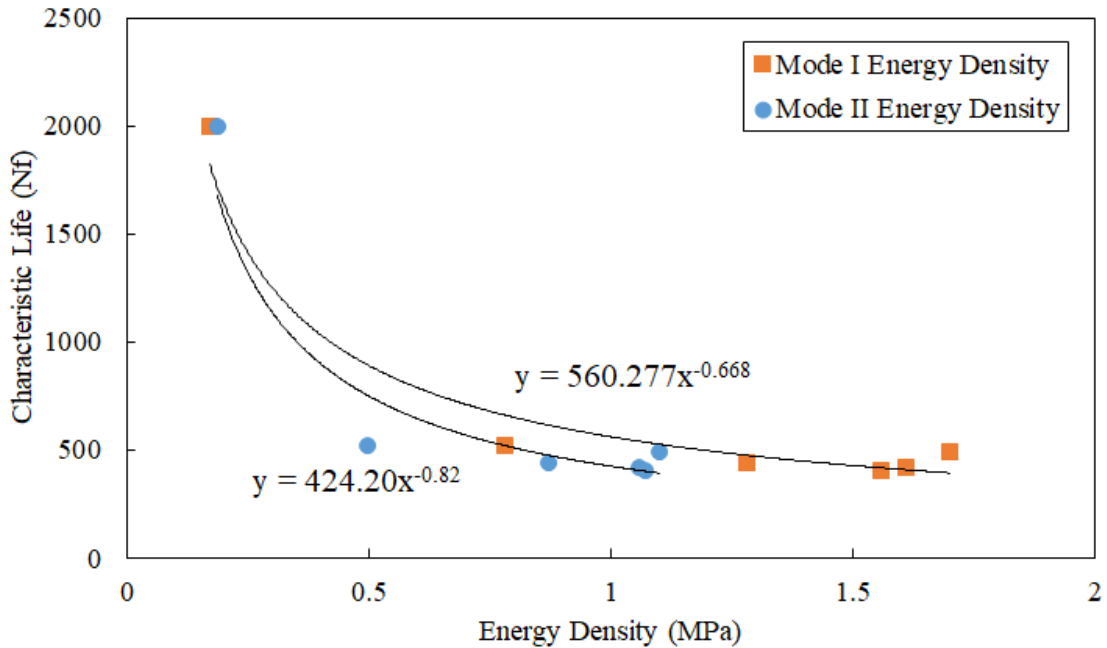


**Figure 5- 26: Characteristic life as function of Mode I and Mode II energy density for group C underfill from -55 to 125°C.**

After fitting the model using experimental data of characteristic life it was evaluated again the existing models previously shown along with the Darveaux model for SAC305 solder. Figure 5-27 shows the bar chart of predicted and experimental characteristic life for group C underfills and percent error for each of the three models. It can be seen that the orange bar representing experimental data in the control configuration closely matches the Syed model than the new mode separation and Darveaux model. Underfilled BGA shown closer correlation to the mode separation model except for the Namics 1594-6F underfill.

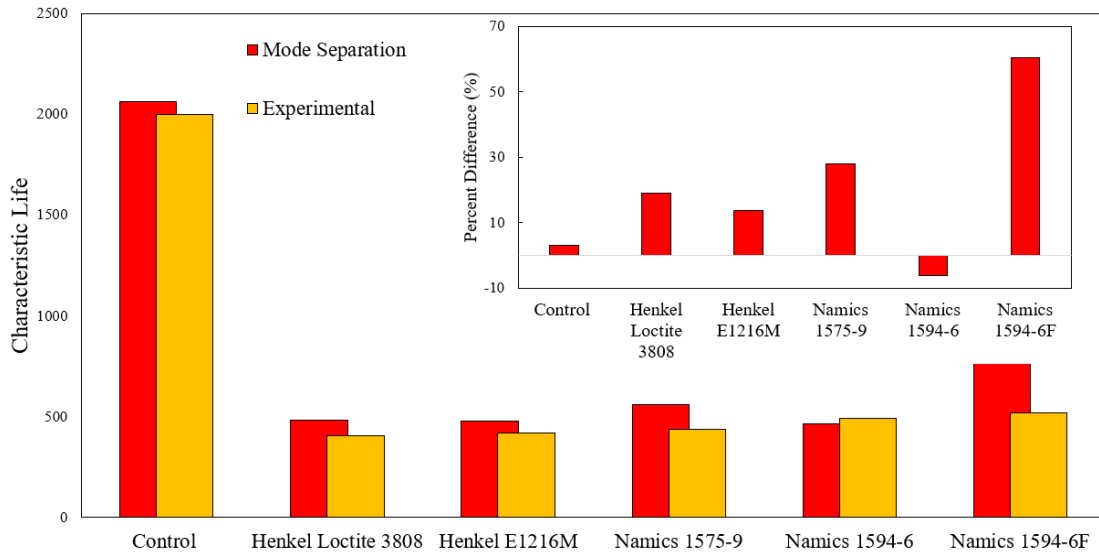


**Figure 5- 27: Fatigue life prediction comparison for group C underfills.**

Aggregating test results for group B and group C underfills provides a broad picture on the applicability of the new energy density partitioning approach. Figure 5-26 shows the predicted number of cycles on the vertical axis and the experimental characteristic life on the horizontal axis. The center line corresponds to one to one correlation while the two peripheral line represent 2X deviation of model prediction from experimental values. Interestingly, the four data points that show the least correlation belong to group B underfills with high and low mean temperature profile while group C underfills show excellent correlation. Figure 5-29 summarizes the methodology developed in this chapter for reliability assessment of BGAs with reworkable underfills. The total dissipated creep energy density for all five group C underfills along with the control BGA is shown in Figure 5-28. Tracking the total energy density as a function of temperature exhibits the respective increase in energy density in the solder for each underfill material. All underfills resulted in lower characteristic life compared with the control BGA shown in chapter 4. Similarly, the magnitude of energy density is higher

with all underfills; however, the underfill with the largest energy density is not indicative of the components that had the lowest characteristic life. Therefore, partitioning the total creep energy density into mode I and mode II components will provide further understanding to the proportional decrease in energy density.

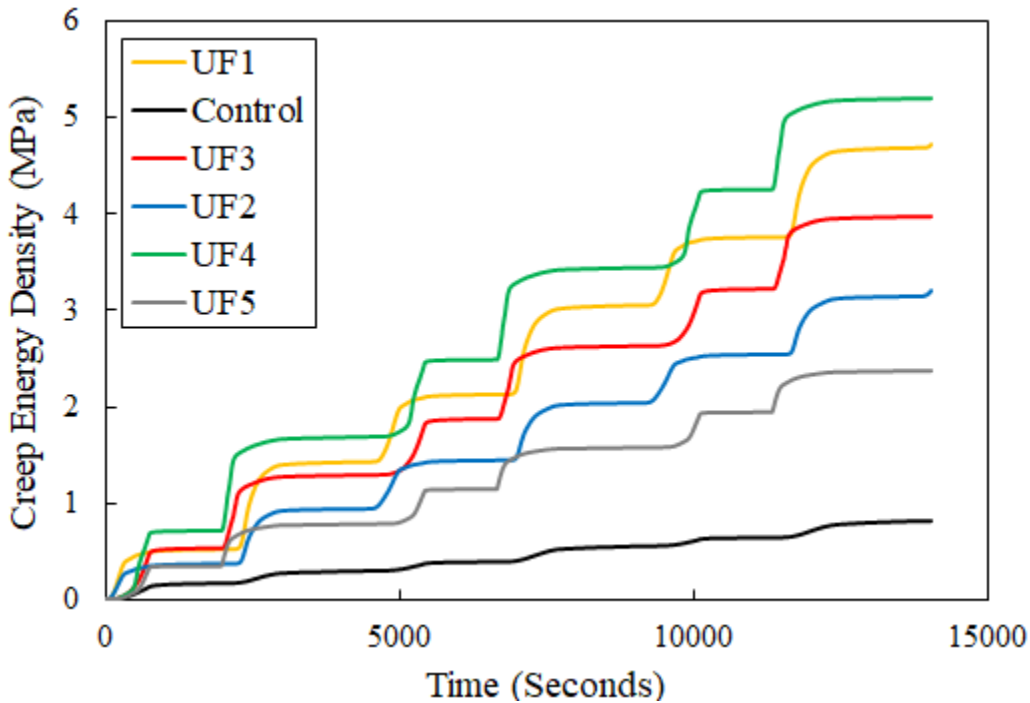


**Figure 5- 28: Total accumulated creep energy density for group C underfilled and control BGA for first three temperature cycles.**

The first step of the method is creation of a BGA model and underfill that is representative of the actual component. This is necessary to capture any process induced effects such as the size of the underfill fillet. Temperature dependent underfill properties should be determined using TMA and DMA and used as input parameters for underfill behavior. The most appropriate boundary condition to consider in board level reliability of reworkable underfills is the underfill interaction with the package and PCB. It is recommended to neglect any interaction of the underfill with solder. This is due to the lack of adhesion solder has with the epoxy underfill and the relaxation of



possible residual stresses induced by curing as the material crosses the glass transition region.

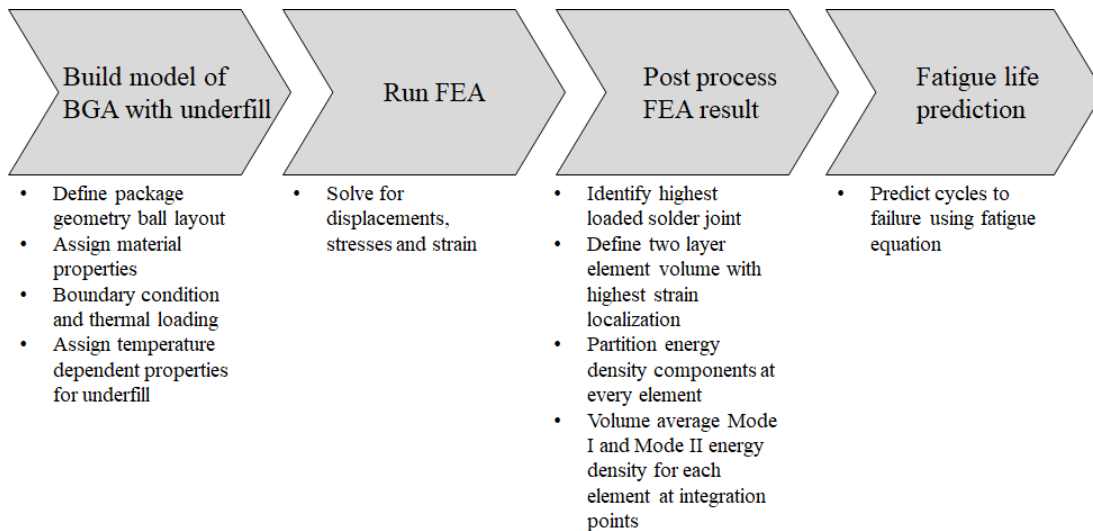


**Figure 5- 29: Process flow of energy density partitioning approach for underfilled BGA.**

The effect of this process flow can be illustrated in Figure 5-30. The comparison between the experimental obtained characteristic life that are compared with the ones obtained using the process outlined in Figure 5-27. The two diagonal black lines represent the 2X boundary from the center. Most of the underfills that were tested under the -55 to 125°C thermal profile shows excellent correlation with experimental results. There are however a few predictions that failed to meet model acceptance criteria to fall within the 2X prediction range. These data points belong to Group B materials that were tested at the mean temperature conditions and with high expansion materials such as the Dow Corning Silicone and United Adhesives EP1238.

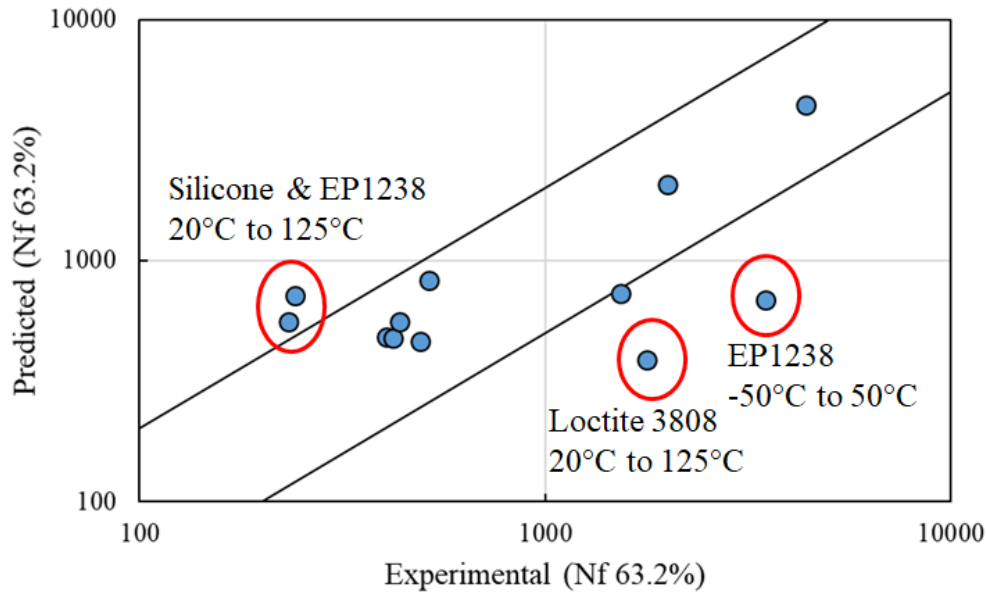


**Figure 5- 30: Predicted vs. experimental characteristic life for group B and C underfills.**

The reason for this deviation could be attributed to many factors such as one discussed in the model assumptions section. Since the model does not account for hydrostatic stress directly, Mode I energy density is believed to incorporate the increase in normal stresses across the  $T_g$ . Alternatively, model deviation could potentially be attributed to the linear elastic material model and variation in measured material properties in bulk form factor and the underfilled form factor on the package itself.

The effect of modelling and material assumptions provide a strong argument on the applicability of the method used to assess the reliability of the package. Loctite3808 underfill was extensively characterizes to determine the creep and plastic behavior across strain rates and temperature. To account for potential effects due to shrinkage during cure the model was adjusted by determining the change in CTE across cure temperature that will induce 0.5% volume shrinkage. The cure temperature was 130°C as shown in Figure 5-31. It is assumed that after the 15-minute cure duration at 130°C

the underfills are fully cross-link and possess the same temperature dependent properties above the underfill  $T_g$ .

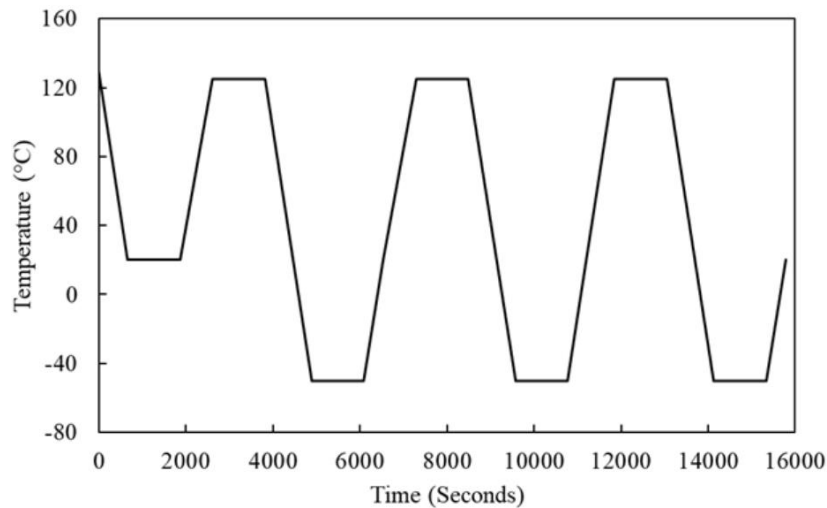


**Figure 5- 31: thermal profile with consideration to underfill shrinkage.**

At the set cure temperature, the underfill transforms from a liquid to a gel state with increased cross-linking density. This transition has been previously measured using and found to occur over the course of a few minutes [111]. Other investigations on underfill cure behavior found that the underfills  $T_g$  can increase with curing time as consequence of the increase in the degree of crosslinking [112]. Now, the effect of underfill material model can be identified using the method previously used for fatigue life assessment of reworkable underfills. Figure 5-32 shows the accumulated energy density with assumption of underfill shrinkage and material models. The creep and plasticity models were modeled in conjunction with the temperature dependent elastic properties. It can be seen that the highest energy density is found for the model with underfill creep behavior and lowest for the linear elastic material assumption.

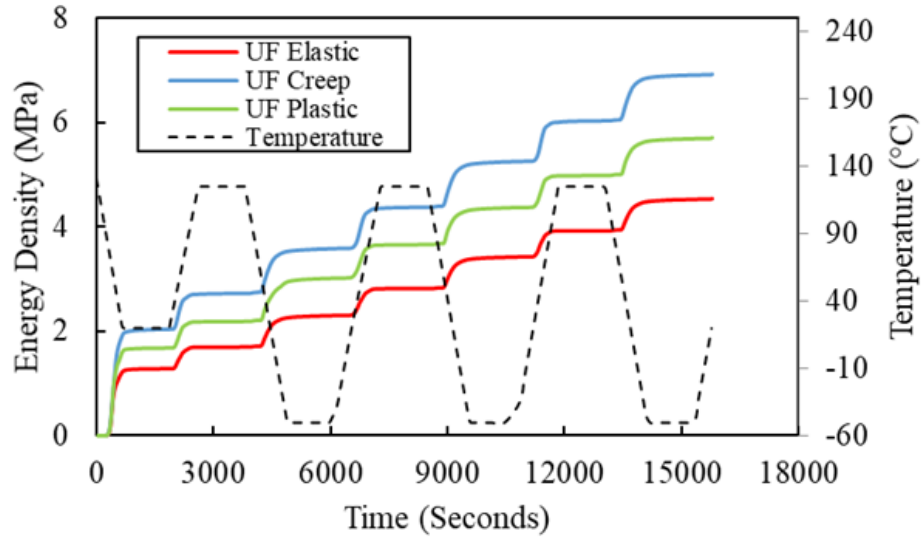


**Figure 5- 32: Accumulated energy density with time for BGA with Loctite3808 underfill using elastic, plastic and creep material behavior.**

This finding contradicts the assumption that more accurate material models will improve model accuracy. In essence if the creep material model was used for the mean temperature condition it will result in even lower prediction of the characteristic life than just the linear elastic material assumption. This statement might not apply to all the material tested in this study but could in fact support the notion of utilizing linear elastic temperature dependent material properties across the  $T_g$  of an epoxy based underfill. Figure 5-33 shows the accumulation of energy density as function of temperature for the three Loctite3808 material models with cure shrinkage. It can be seen that the creep material model results in higher energy density in the solder during cure as well as the thermal cycles themselves.

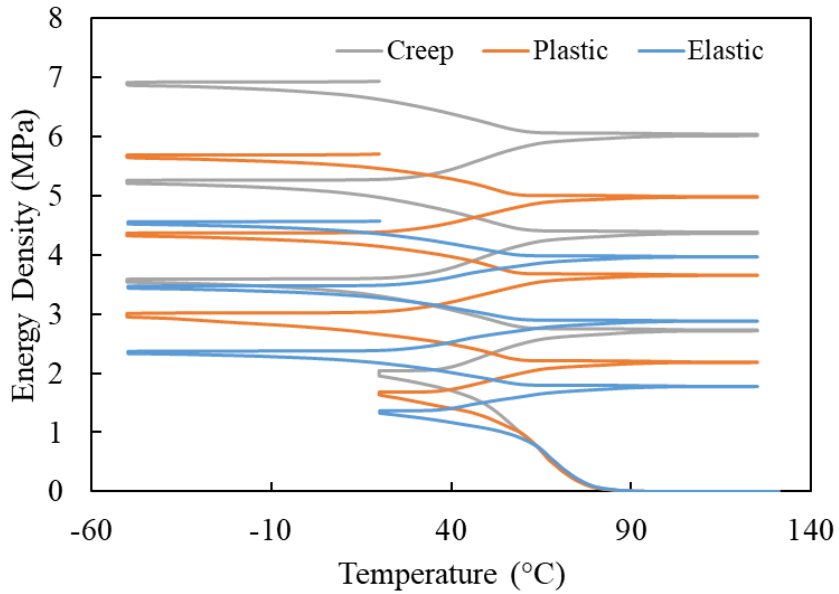


**Figure 5- 33: Accumulated energy density as function of temperature for BGA with Loctite3808 with elastic, plastic and creep behavior.**

The combined effect of model assumption with Loctite3808 material models and boundary conditions are well summarized in Figure 5-32. The tied boundary condition with the underfill creep model is not shown due to lack of model convergence.

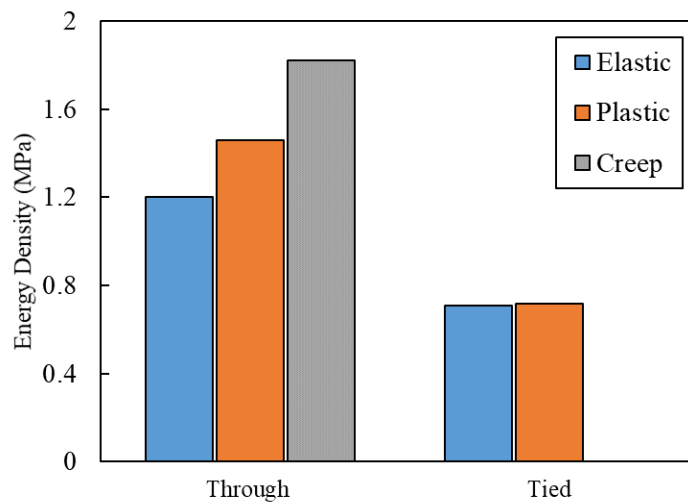


**Figure 5- 32: Energy density for elastic, plastic and creep underfill behavior for - 55°C to 125°C for through and tied conditions.**

Imposing tie constraint on high expansion material such as reworkable underfills on solder joint can result in misleading stress state that provides lower energy density. As previously show, the tie interaction with the solder result in higher stresses transmitted to the underfill which leads to lower energy dissipation in the solder. The similarity in energy density between elastic and plastic underfill models in the tied configuration is a warning on potential erroneous model assumptions for board level applications.

## **SUMMARY, CONTRIBUTIONS AND FUTURE WORK**

### **6.1 Summary**

The influence of underfill materials on thermo-mechanical fatigue of BGA components was investigated using thermal cycling experiments and numerical methods. The literature review of this work summarizes the effect of biaxial loading conditions on fatigue life of solder alloys and discusses the influence of complex stress states on reliability of underfilled BGAs. Secondly, the literature review compares published work on underfilled BGAs and demonstrates that existence of two distinctly different empirical trends between the reliability of flip-chip devices and underfilled board level BGAs.

Material characterization portion of this work provides temperature dependent elastic modulus and CTE for all the materials used in the subsequent thermal cycling chapter. The glass transition temperature was found to be dependent on the test method used for characterizing the material. The elastic modulus is found to decrease only after substantial increase in the underfill CTE occurs. This delay is due to the higher energy necessary to cause translational and rotational movement in the polymer chain that

influences change in the modulus while the CTE is driven by the free volume that requires lower level of energy and temperature. Plasticity of the underfill was determined to be temperature and strain rate sensitive. The strain rate sensitivity of the underfill increases at temperature closer to the  $T_g$ . Creep deformation of the reworkable underfill dramatically increases across the  $T_g$ . Steady state creep was not achieved at high stresses and elevated temperatures. Hyperbolic sine creep model was used to fit the steady state creep behavior and found to deviate for temperature beyond the  $T_g$  indicating a change in creep mechanism. The material properties of the BGA package used for thermal cycling were determined by deconstructing the BGA package. The mold compound glass transition temperature was found to be within the temperature range of accelerated thermal profiles.

Experimental study on the effect of reworkable underfills on reliability of BGA components consisted of underfilling 17mm daisy-chained BGAs and subjecting them to thermal cycling environments. A unique failure mechanism was found for BGAs underfilled with an acrylic conformal coating that are indicative of the compressive loading. The failure rate plotted using Weibull distribution demonstrated a dependence on the underfill material properties and mean temperature conditions of the thermal range. High expansion conformal coatings when used as underfills resulted in lowering the characteristic life compared to the non-underfilled components at both benign and harsh environments. This observation supports that hypothesis that solder joints experience higher multiaxial stress state as the thermal cycle crosses the underfills  $T_g$ . The second group of materials comprised of a combination of reworkable underfills, a high expansion epoxy and silicone conformal coatings carried over from the previous

test group. The second group of materials was assembled on the same devices on boards that are slightly thinner than the first group of materials. Two temperature profiles were used with high and low mean temperatures. Fatigue life of BGAs was found to depend on the glass transition temperature of the underfills and the properties around it. Diagonal cracks were found in solder joints with the silicone conformal coating underfill due to the large fillet that formed during application. No distinct distance to neutral effect was observed for underfills where the thermal profile crosses the  $T_g$ . Meanwhile, both single sided and double-sided non underfilled BGAs demonstrated classic distance to neutral effect with the corner solder joints cracking first. The last group of materials utilized dedicated reworkable underfills with different CTE and  $T_g$  and subjected to a harsh temperature profile of  $-55^{\circ}\text{C}$  to  $125^{\circ}\text{C}$ . The resulting characteristic life was found to have strong dependence on underfill  $T_g$  and CTE. Although all of the reworkable underfills resulted in lower characteristic life compared to the non-underfilled components the harsh thermal cycle used in this study does not allow to easily discriminate between the effect of the five underfills.

The final chapter presents the numerical investigation on the impact of reworkable underfills using Abaqus FEA software. Thermal cycling simulations were performed using linear elastic underfill properties on a variety of underfills at the experimental thermal profiles. A new energy density partitioning approach was demonstrated by partitioning the total dissipated energy density per cycle to Mode I and Mode II energies. The shift from Mode II to Mode I energy density was demonstrated between underfilled and non-underfilled components. The increase in Mode I energy density was shown to occur over the glass transition region of the underfill when the material



expands prior to sufficient relaxation of the elastic modulus occurs. During this brief temperature range large axial stresses are developed in the solder joints. FEA simulations also demonstrated the lack of distance to neutral dependence in energy density for underfilled with  $T_g$  that is within the temperature profile range. Loctite 3808 that was characterized in chapter 3 was used to evaluate the effect of shrinkage and underfill material model and interaction with the solder on fatigue life prediction using the partitioned energy density. It was demonstrated that the linear elastic underfill behavior was found to be most appropriate for modelling board level interaction under thermal cycling. The hydrostatic stress that develops in the solder as a result of underfill load sharing was found to strongly depend on both the underfill temperature dependent material properties and temperature range. The new energy density partitioning model calibrated using experimental results obtained in chapter 4 was demonstrated to fit well for the majority of test results and deviate for test data obtained with the mean temperature test. Overall, the new mode separation model provides improvement over existing fatigue life prediction models for evaluating the durability of BGA packages with underfills.

## **6.2 Contributions**

The impact of reworkable underfills on the thermo-mechanical reliability of BGA packages were investigated using a variety of commercially available materials that are used in the electronic industry. The main contributions of this dissertation are outlined:

1. A systematic, hybrid (i.e. analytical + empirical) methodology was developed for quantifying the risks incurred when the underfill  $T_g$  is crossed in temperature cycling tests.
2. A sample implementation of this approach was provided for a few selected, reworkable underfills.
3. Acceleration factors were developed from published empirical trends for the reliability of both BGA and flip-chip devices based on underfill CTE, modulus and glass transition temperature.
4. Temperature dependent elastic modulus and CTE were measured for a wide range of underfills.
5. The reliability of BGA components was found to strongly depend on the temperature dependent properties of underfill materials more so than the temperature profile range and decrease substantially when the temperature cycle crossed the underfill glass transition temperature.
6. Unique cracking behavior was found in BGA solder joints with different underfill materials. Acrylic underfills were found to induce extensive deformation in solder joints. Reworkable underfills with  $T_g$  that is within the thermal cycling range demonstrated cracking behavior that is independent of distance to neutral effect.
7. It is the first work to detail the energy density accumulation in the solder around underfill glass transition region due to the increase in temperature dependent elastic modulus before the corresponding decrease in CTE of reworkable underfills with mean temperature conditions.

### **6.3 Future Work**

The findings outlined in this dissertation create opportunity for validating reworkable underfill material models for thermal environments that cross the glass transition temperature. Optical measurement techniques can be used to experimentally measure underfill and solder deformation during thermal cycling in order to calibrate numerical models to better account for variability in the solder alloy microstructure and underfill properties across the  $T_g$ .

Additional empirical data is necessary for underfills that improve fatigue life to validate the model's accuracy in environments and materials that improve the characteristic life over non-underfilled components. The model applicability to other BGA package types and chip scale packages needs to be evaluated. Other components such as QFNs, LGAs and wafer level packages are sensitive to thermo-mechanical loads and should be evaluated with the underfilled used in this study.

The effect of hydrostatic stress on damage should be considered. A hydrostatic stress component can potentially be incorporated into the model as a function of the ratio between the underfilled and non-underfilled component. Comparing the energy density between an underfilled and a reference configuration can potentially provide more understanding on how the change in stress state influences fatigue life rather than a model that attempts to predict the reliability of an underfilled component with no prior knowledge of the component without the underfill as attempted in this work.



# APPENDIX

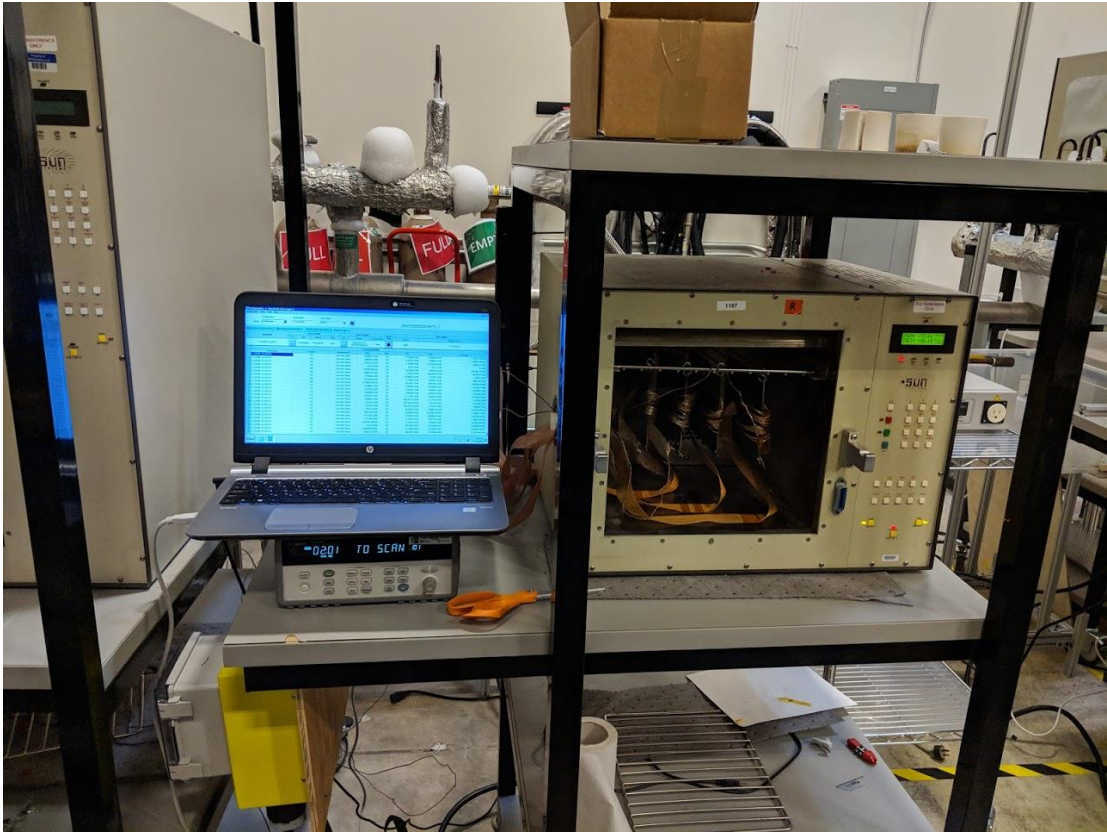
## CHAPTER 2

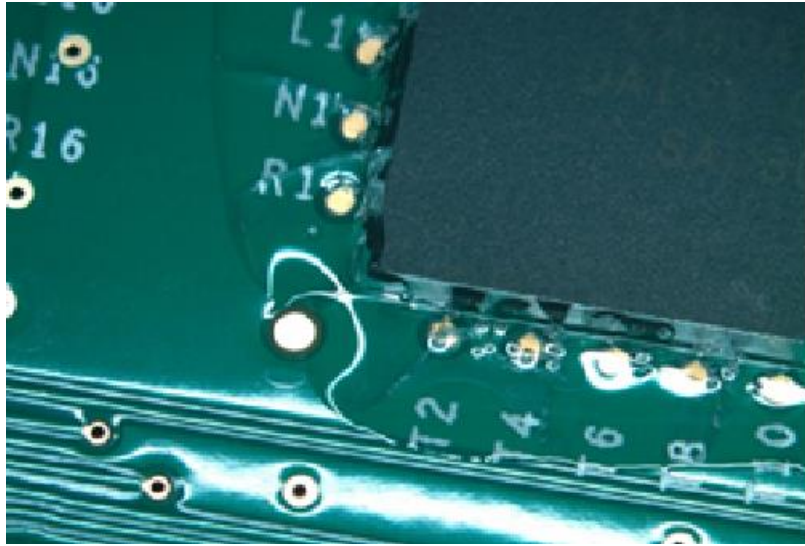
Ref	Underfill Properties			Full/Perimeter	Thermal Cycle	Package Size	Package Style	Solder Alloy	Nf Control	Nf w/UF	Experimental Multiplier
	CTEE (MPa)	T <sub>g</sub>									
[54]	75	1500	15	Full	-40 to 125C	30mm carrier with 27 mm die	256 IO BGA	SAC305	824	403	0.49
[54]	80	50	15	Full	-40 to 125C	30mm carrier with 27 mm die	256 IO BGA	SAC305	824	229	0.28
[54]	66	2300	55	Full	-40 to 125C	30mm carrier with 27 mm die	256 IO BGA	SAC305	824	330	0.40
[54]	66	2300	56	Full	-40 to 125C	30mm carrier with 27 mm die	256 IO BGA	SAC305	824	285	0.35
[54]	50	2000	110	Full	-40 to 125C	30mm carrier with 27 mm die	256 IO BGA	SAC305	824	462	0.56
[54]	34	7000	115	Full	-40 to 125C	30mm carrier with 27 mm die	256 IO BGA	SAC305	824	655	0.79
[54]	77	7	0	Corner	-40 to 125C	30mm carrier with 27 mm die	256 IO BGA	SAC305	824	884	1.07
[54]	21	10000	150	Corner	-40 to 125C	30mm carrier with 27 mm die	256 IO BGA	SAC305	825	1159	1.40
[55]	75	2600	90	Full	0 to 100C	21mm Ceramic package	256 IO BGA	SnPb	2426	2070	0.85
[55]	44	5600	170	Full	0 to 100C	21mm Ceramic package	256 IO BGA	SnPb	2426	5160	2.13
[55]	40	8500	170	Full	0 to 100C	21mm Ceramic package	256 IO BGA	SnPb	2426	5097	2.10
[55]	26	5500	170	Full	0 to 100C	21mm Ceramic package	256 IO BGA	SnPb	2426	6000	2.47
[56]	70	2600	170	Full	-40 to 125C	flex BGA 16mm 10mm die	280 IO BGA	SnPb	1030	2230	2.17
[56]	44	5600	170	Full	-40 to 125C	flex BGA 16mm 10mm die	280 IO BGA	SnPb	1030	3720	3.61
[56]	40	8500	170	Full	-40 to 125C	flex BGA 16mm 10mm die	280 IO BGA	SnPb	1030	2090	2.03
[56]	26	5500	170	Full	-40 to 125C	flex BGA 16mm 10mm die	280 IO BGA	SnPb	1030	5600	5.44
[57]	20	8500	113	Full	-40 to 125C	Package-on-package 14mm	353 IO BGA	SAC405	2858	3000	1.05
[57]	61	3200	67	Full	-40 to 125C	Package-on-package 14mm	353 IO BGA	SAC405	2858	1481	0.52
[57]	64	1800	124	C dot	-40 to 125C	Package-on-package 14mm	353 IO BGA	SAC405	2858	2470	0.86
[57]	64	1800	124	L edge	-40 to 125C	Package-on-package 14mm	353 IO BGA	SAC405	2858	2348	0.82
[57]	70	1500	63	Full	-40 to 125C	Package-on-package 14mm	353 IO BGA	SAC405	2858	426	0.15
[57]	52	1600	50	Full	-40 to 125C	Package-on-package 14mm	353 IO BGA	SAC405	2858	NA	NA
[57]	42	1500	60	Full	-40 to 125C	Package-on-package 14mm	353 IO BGA	SAC405	2858	560	0.20
[57]	58	3500	89	Full	-40 to 125C	Package-on-package 14mm	353 IO BGA	SAC405	2858	1209	0.42
[57]	59	3000	94	Full	-40 to 125C	Package-on-package 14mm	353 IO BGA	SAC405	2858	597	0.21
[58]	52	3080	69	Partial	-40 to 125C	12mm CSP BGA	228 IO perimeter	SAC305	4268	3206	0.75
[58]	52	3080	69	Full	-40 to 125C	12mm CSP BGA	228 IO perimeter	SAC305	4268	3406	0.80
[58]	60	3500	85	Partial	-40 to 125C	12mm CSP BGA	228 IO perimeter	SAC305	4268	3640	0.85
[58]	60	3500	85	Full	-40 to 125C	12mm CSP BGA	228 IO perimeter	SAC305	4268	3932	0.92
[59]	38	7000	115	Full	-40 to 125C	12mmCSP with 10mm die	160 IO perimeter	SAC305	2114	3555	1.682
[59]	50	4000	110	Full	-40 to 125C	12mmCSP with 10mm die	160 IO perimeter	SAC305	2114	1963	0.929
[59]	60	3000	135	Full	-40 to 125C	12mmCSP with 10mm die	160 IO perimeter	SAC305	2114	2107	0.997

### CHAPTER 3









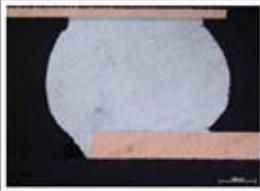



Coating Name	Coating Type	Preparation for Syringe Coating	Preparation for Standard Coating	Standard Coating Process
Humiseal 1B31	Acrylic	No thinning	Thinned with Humiseal PB521	RC Dry Spray
Dow Corning 1-2577	Silicone	Thinned to 10% with Dow Corning OS-20 solvent	NA	Spray Coat
Humiseal 1A33	Urethane	No thinning	Thinned 15% with Humiseal PB521	Manual Spray
Hysol PC12-007M	Epoxy	Two part mixture, mixed 1:1	Two part mixture, mixed 1:1, 10mL of toluene added	Brush applied using natural bristled brush
Conathane CE1155	Urethane	Two part mixture, mixed 100 parts resin to 70 parts hardener, thinned with 10% toluene	Two parts mixture, mixed 100 parts resin to 70 parts with 20% dilutions with Conap S-8	Manual Spray

## CHAPTER 4

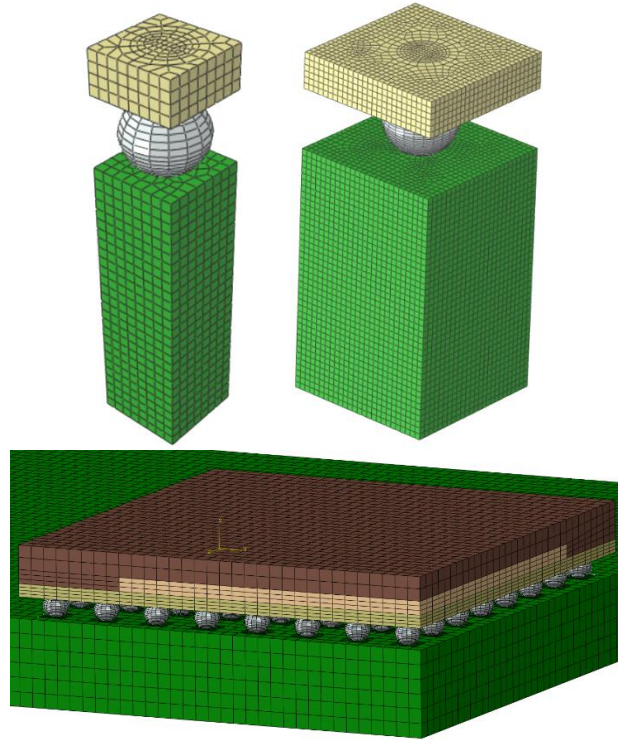




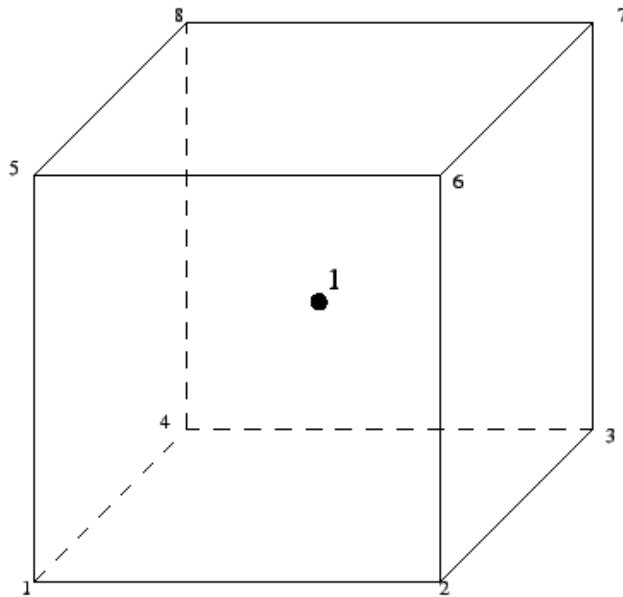


	Standard Coating	Thick Coating
Acrylic Coating		
Epoxy Coating		
Silicone Coating		
Urethane 1		
Urethane 2		
Nanocoating		

## CHAPTER 5



First order reduced integration element type C3D8R used in Abaqus model



Python script for post processing energy density component, hydrostatic stress and triaxiality.

```
from abaqus import *
from abaqusConstants import *
from odbAccess import *
from textRepr import *
import math
import sys
from time import localtime, strftime, sleep

def log( str, printTime = True):
    """Print to console instead of Abaqus CAE Console"""
    if printTime == True:
        print >> sys.__stdout__, strftime("%I:%M:%S%p ", localtime()), str
    else:
        print >> sys.__stdout__, str
    return;

odbToReadFile = './control.odb'
odbToRead = openOdb(path = odbToReadFile, readOnly = False)

components = ['11', '22', '33', '12', '13', '23']

solderSet = odbToRead.rootAssembly.elementSets['TWO_LAYER_ENERGY']

for stepNumber in range(len(odbToRead.steps)):
    stepName = odbToRead.steps.keys()[stepNumber]
    log('Step: ' + stepName)
    step = odbToRead.steps[stepName]
    myStep = odbToRead.Step(
        name = stepName+'-energyAB',
        description = "",
        domain = TIME,
        timePeriod = step.timePeriod
    )
    #
    zeroField = 0*step.frames[-
2].fieldOutputs['S'].getSubset(region=solderSet).getScalarField(componentLabel='S1
1')
    accumulatedCreepEnergy =
[zeroField,zeroField,zeroField,zeroField,zeroField,zeroField]
    accumulatedPlasticEnergy =
[zeroField,zeroField,zeroField,zeroField,zeroField,zeroField]
```

```

    accumulatedInelasticEnergy =
[zeroField,zeroField,zeroField,zeroField,zeroField,zeroField]
    #
    for frameNumber in range(1,len(step.frames)):
        print 'Frame Number: ' + str(frameNumber)
        log('  Frame: ' + str(frameNumber))
        previous_frame = step.frames[frameNumber-1]
        current_frame = step.frames[frameNumber]
        previous_S_set =
previous_frame.fieldOutputs['S'].getSubset(region=solderSet)
        current_S_set = current_frame.fieldOutputs['S'].getSubset(region=solderSet)
        previous_CE_set =
previous_frame.fieldOutputs['CE'].getSubset(region=solderSet)
        current_CE_set =
current_frame.fieldOutputs['CE'].getSubset(region=solderSet)
        previous_PE_set =
previous_frame.fieldOutputs['PE'].getSubset(region=solderSet)
        current_PE_set =
current_frame.fieldOutputs['PE'].getSubset(region=solderSet)
        previous_IE_set =
previous_frame.fieldOutputs['IE'].getSubset(region=solderSet)
        current_IE_set = current_frame.fieldOutputs['IE'].getSubset(region=solderSet)
    ##
    myFrame = myStep.Frame(
        incrementNumber = current_frame.incrementNumber,
        frameValue = current_frame.frameValue,
        description = current_frame.description
    )
    triaxialityField = myFrame.FieldOutput(
        name = 'TRXX',
        description = 'Stress triaxiality',
        type = SCALAR
    )
    hydrostaticField = myFrame.FieldOutput(
        name = 'HYDS',
        description = 'Hydrostatic Stress',
        type = SCALAR
    )
    PrincipalStress1 =
current_frame.fieldOutputs['S'].getScalarField(invariant=MAX_PRINCIPAL).getSub
set(region=solderSet)
    PrincipalStress2 =
current_frame.fieldOutputs['S'].getScalarField(invariant=MID_PRINCIPAL).getSubs
et(region=solderSet)

```

```

PrincipalStress3 =
current_frame.fieldOutputs['S'].getScalarField(invariant=MIN_PRINCIPAL).getSubset(region=solderSet)
VMStress =
current_frame.fieldOutputs['S'].getScalarField(invariant=MISES).getSubset(region=solderSet)
hydrostaticPressure = (PrincipalStress1 + PrincipalStress2 +
PrincipalStress3)/3.0
hydrostaticField.addData(hydrostaticPressure)
if (stepNumber==1 and frameNumber==1):
    triaxiality = hydrostaticPressure * 0
else:
    triaxiality = hydrostaticPressure/VMStress
#
triaxialityField.addData(triaxiality)
#
=====
====
#
=====
====
temperatureField = myFrame.FieldOutput(
    name = 'NTEMP',
    description = 'Nodal Temperature',
    type = SCALAR
)
mode2EnergyField = myFrame.FieldOutput(
    name = 'MII',
    description = 'Mode 2 Energy',
    type = SCALAR
)
nodalTemperature =
current_frame.fieldOutputs['NT11'].getScalarField().getSubset(region=solderSet)
temperatureField.addData(nodalTemperature)
#
=====
====
#
=====
====
for index, component in enumerate(components):
    print ' Component ' + component
    log(' Component ' + component)
    creepEnergyField = myFrame.FieldOutput(
        name = 'CSED'+component,
        description = 'Creep Strain Energy Density '+component,

```

```

        type = SCALAR
    )
    plasticEnergyField = myFrame.FieldOutput(
        name = 'PSED'+component,
        description = 'Plastic Strain Energy Density '+component,
        type = SCALAR
    )
    inelasticEnergyField = myFrame.FieldOutput(
        name = 'ISED'+component,
        description = 'Inelastic Strain Energy Density '+component,
        type = SCALAR
    )
    previous_S =
previous_S_set.getScalarField(componentLabel='S'+component)
    current_S = current_S_set.getScalarField(componentLabel='S'+component)
    previous_CE =
previous_CE_set.getScalarField(componentLabel='CE'+component)
    current_CE =
current_CE_set.getScalarField(componentLabel='CE'+component)
    previous_PE =
previous_PE_set.getScalarField(componentLabel='PE'+component)
    current_PE =
current_PE_set.getScalarField(componentLabel='PE'+component)
    previous_IE =
previous_IE_set.getScalarField(componentLabel='IE'+component)
    current_IE =
current_IE_set.getScalarField(componentLabel='IE'+component)
    accumulatedCreepEnergy[index] = accumulatedCreepEnergy[index] +
abs((current_CE-previous_CE)*(previous_S+current_S)/2) #trapezoidal integration
    accumulatedPlasticEnergy[index] = accumulatedPlasticEnergy[index] +
abs((current_PE-previous_PE)*(previous_S+current_S)/2) #trapezoidal integration
    accumulatedIneslasticEnergy[index] = accumulatedIneslasticEnergy[index] +
abs((current_IE-previous_IE)*(previous_S+current_S)/2) #trapezoidal integration
    creepEnergyField.addData(accumulatedCreepEnergy[index])
    plasticEnergyField.addData(accumulatedPlasticEnergy[index])
    inelasticEnergyField.addData(accumulatedIneslasticEnergy[index])
    m2Energy =
2*(accumulatedCreepEnergy[3]+accumulatedCreepEnergy[4]+accumulatedCreepEnergy[5])
    mode2EnergyField.addData(m2Energy)
    #
    odbToRead.save()

#
odbToRead.close()

```



## BIBLIOGRAPHY

- [1] Steinberg DS. Vibration analysis for electronic equipment. United States of America: John Wiley & Sons; 2000 Jun. P. xviii.
- [2] Sharon, G. Thermal Cycling and Fatigue. DfR Solutions. White Paper. 2015
- [3] Darveaux R, Heckman J, Syed A, Mawer A. Solder joint fatigue life of fine pitch BGAs—impact of design and material choices. *Microelectronics Reliability*. 2000 Jul 1;40(7):1117-27.
- [4] Serebreni, Maxim, and Greg Caswell. "The Impact of Glass Style and Orientation on the Reliability of SMT Components." In *International Symposium on Microelectronics*, vol. no. 1, pp. 699-706. International Microelectronics Assembly and Packaging Society, 2018.
- [5] Polymers in Electronic Packaging: Flip Chip Packaging Part Two  
Jeffrey Gotro <https://polymerinnovationblog.com/polymers-electronic-packaging-flip-chip-packaging-part-two/>
- [6] Davis, E. M., William E. Harding, Robert S. Schwartz, and John J. Corning. "Solid logic technology: versatile, high-performance microelectronics." *IBM Journal of Research and Development* 8, no. 2 (1964): 102-114.
- [7] Okura, J. H., S. Shetty, B. Ramakrishnan, A. Dasgupta, J. F. J. M. Caers, and T. Reinikainen. "Guidelines to select underfills for flip chip on board assemblies and compliant interposers for chip scale package assemblies." *Microelectronics Reliability* 40, no. 7 (2000): 1173-1180.
- [8] Zhang, Xiaowu, C. Q. Cui, K. C. Chan, E. H. Wong, and Mahadevan K. Iyer. "Analysis of solder joint reliability in flip chip package." *International Journal of Microcircuits and Electronic Packaging* 25, no. 1 (2002): 147-159.
- [9] Helneder, Johann, Charlotte Hoyler, Manfred Schneegans, and Holger Torwesten. "Evaluation of lead-free SnAg solder ball deposition and reflow processes for flip chip applications." *Microelectronic Engineering* 82, no. 3-4 (2005): 581-586.
- [10] Ho, P. S., Z. P. Xiong, and K. H. Chua. "Study on factors affecting underfill flow and underfill voids in a large-die flip chip ball grid array (FCBGA) package." In *Electronics Packaging Technology Conference, 2007. EPTC 2007. 9th*, pp. 640-645. IEEE, 2007.
- [11] Fan, X-J., H. B. Wang, and T. B. Lim. "Investigation of the underfill delamination and cracking in flip-chip modules under temperature cyclic loading." *IEEE Transactions on Components and Packaging Technologies* 24, no. 1 (2001): 84-91.



- [12] Chen, K. M., D. S. Jiang, N. H. Kao, and J. Y. Lai. "Effects of underfill materials on the reliability of low-K flip-chip packaging." *Microelectronics Reliability* 46, no. 1 (2006): 155-163.
- [13] Lim, C. T., and Y. J. Low. "Investigating the drop impact of portable electronic products." In *Electronic Components and Technology Conference, 2002. Proceedings. 52nd*, pp. 1270-1274. IEEE, 2002.
- [14] Shi, Hongbin, and Toshitsugu Ueda. "Investigation of various board-level underfills and adhesives for CTBGA bend performance enhancements in lead-free portable electronic products." In *Electronic Packaging Technology and High Density Packaging (ICEPT-HDP), 2011 12th International Conference on*, pp. 1-6. IEEE, 2011.
- [15] Qi, Fangjuan, Yaping Ding, and Hua Fu. "Reliability of ball grid array (BGA) assembly with reworkable capillary underfill material." In *Electronic Packaging Technology, 2005 6th International Conference on*, pp. 1-7. IEEE, 2005.
- [16] Peng, Haiwei, R. Wayne Johnson, George T. Flowers, A-G. Ricketts, Erin K. Yeager, Mark M. Konarski, Afranio Torres-Filho, and Larry Crane. "Underfilling fine pitch BGAs." *IEEE Transactions on Electronics Packaging Manufacturing* 24, no. 4 (2001): 293-299.
- [17] Noh, Bo-In, Jeong-Won Yoon, Sang-Ok Ha, and Seung-Boo Jung. "Effects of Different Kinds of Underfills and Temperature-Humidity Treatments on Drop Reliability of Board-Level Packages." *Journal of electronic materials* 40, no. 2 (2011): 224-231.
- [18] Qi, Haiyu, Michael Osterman, and Michael Pecht. "Design of experiments for board-level solder joint reliability of PBGA package under various manufacturing and multiple environmental loading conditions." *IEEE Transactions on Electronics Packaging Manufacturing* 32, no. 1 (2009): 32-40.
- [19] Paquet, M-C., Michael Gaynes, Eric Duchesne, David Questad, Luc Bélanger, and M. Sylvestre. "Underfill selection strategy for Pb-free, low-K and fine pitch organic flip chip applications." In *Electronic Components and Technology Conference, 2006. Proceedings. 56th*, pp. 9-pp. IEEE, 2006.
- [20] Hannan, Nael, and Puligandla Viswanadham. "Critical aspects of reworkable underfills for portable consumer products." In *Electronic Components and Technology Conference, 2001. Proceedings., 51st*, pp. 181-187. IEEE, 2001.

- [21] Lau, John, Jeffery Lo, Jimmy Lam, Eng-Leong Soon, Woai-Sheng Chow, and Ricky Lee. "Effects of Underfills on the Thermal-Cycling Tests of SnAgCu PBGA (Plastic Ball Grid Array) Packages on ImAg PCB (Printed Circuit Board)." In *Electronics Packaging Technology Conference, 2007. EPTC 2007. 9th*, pp. 785-790. IEEE, 2007.
- [22] Xie, Dongji, Zhongming Wu, Joe Hai, and Manthos Economou. "Reliability Enhancement of Automotive Electronic Modules Using Various Glues." In *2018 IEEE 68th Electronic Components and Technology Conference (ECTC)*, pp. 172-178. IEEE, 2018.
- [23] Shi HB, Ueda T. Mitigation of thermal fatigue failure in fully underfilled lead-free array-based package assemblies using partial underfills. *Electronics Packaging Technology Conference (EPTC), 2011 IEEE 13th* 2011 Dec 7 (pp. 542-547). IEEE.
- [24] Lee JY, Hwang TK, Kim JY, Yoo M, Sohn ES, Chung JY, Dreiza M. Study on the board level reliability test of package on package (PoP) with 2nd level underfill. In *Electronic Components and Technology Conference, 2007. ECTC'07. Proceedings. 57th* 2007 May 29 (pp. 1905-1910). IEEE.
- [25] Kwak JB, Lee DG, Nguyen T, Park S. Deformation and strain measurement of flip-chip solder bump under in-situ thermal loading. In *ASME 2009 International Mechanical Engineering Congress and Exposition 2009 Jan 1* (pp. 311-318). American Society of Mechanical Engineers.
- [26] Kim JM, Farson DF, Shin YE. Improvement of board level reliability for  $\mu$ BGA solder joints using underfill. *Materials Transactions*. 2003;44(10):2175-9.
- [27] Burnette T, Johnson Z, Koschmieder T, Oyler W. Underfilled BGAs for a variety of plastic BGA package types and the impact on board-level reliability. In *Electronic Components and Technology Conference, 2001. Proceedings., 51st* 2001 (pp. 1045-1051). IEEE.
- [28] Meifunas M, Pitarresi JM, Primavera A, Mandepudi SK, Parupalli S. Measurement and prediction of reliability for double-sided area array assemblies. In *Electronic Components and Technology Conference, 2003. Proceedings. 53rd* 2003 May 27 (pp. 1777-1783). IEEE.
- [29] Xia, Z., D. Kujawski, and F. Ellyin. "Effect of mean stress and ratcheting strain on fatigue life of steel." *International Journal of Fatigue* 18, no. 5 (1996): 335-341.

- [30] Lukáš, P., and L. Kunz. "Effect of mean stress on cyclic stress-strain response and high cycle fatigue life." *International Journal of Fatigue* 11, no. 1 (1989): 55-58.
- [31] Liang T, Liang Y, Fang J, Chen G, Chen X. Torsional fatigue with axial constant stress for Sn–3Ag–0.5 Cu lead-free solder. *International Journal of Fatigue*. 2014 Oct 1;67:203-11.
- [32] Gao H, Chen X. Effect of axial ratcheting deformation on torsional low cycle fatigue life of lead-free solder Sn–3.5 Ag. *International Journal of Fatigue*. 2009 Feb 1;31(2):276-83.
- [33] Liang T, Liang Y, Fang J, Chen G, Chen X. Torsional fatigue with axial constant stress for Sn–3Ag–0.5 Cu lead-free solder. *International Journal of Fatigue*. 2014 Oct 1;67:203-11.
- [34] Coffin LF. The deformation and fracture of a ductile metal under superimposed cyclic and monotonic strain. In *Achievement of High Fatigue Resistance in Metals and Alloys 1970* Jan. ASTM International.
- [35] Hsieh, L-Y., H-C. Yang, and T-C. Chiu. "Ratcheting and creep responses of SAC solder joints under cyclic loading." In *Microsystems, Packaging, Assembly and Circuits Technology Conference (IMPACT), 2011 6th International*, pp. 96-99. IEEE, 2011.
- [36] Liang, J., N. Dariavach, P. Callahan, D. Shangguan, and X. Li. "Deformation And Fatigue Fracture Of Solder Alloys Under Complicated Load Conditions." In *Interpack'05, The ASME/Pacific Rim Technical Conference And Exhibition On Integration And Packaging Of MEMS, Optical, and Electronic Systems*, pp. 17-22.
- [37] Ross, Ronald G., and Liang-chi Wen. "Crack propagation in solder joints during thermal-mechanical cycling." *Journal of electronic packaging* 116, no. 2 (1994): 69-75.
- [38] Park, Tae-Sang, and Soon-Bok Lee. "Low cycle fatigue testing of ball grid array solder joints under mixed-mode loading conditions." *Journal of Electronic Packaging* 127, no. 3 (2005): 237-244.
- [39] Liang J, Downes S, Dariavach N, Shangguan D, Heinrich SM. Effects of load and thermal conditions on Pb-free solder joint reliability. *Journal of Electronic Materials*. 2004 Dec 1;33(12):1507-15.
- [40] Matin MA, Vellinga WP, Geers MG. Thermomechanical fatigue damage evolution in SAC solder joints. *Materials Science and Engineering: A*. 2007 Feb 15;445:73-85.

- [41] Johnson Z. Implementation of and extensions to Darveaux's approach to finite-element simulation of BGA solder joint reliability. In *Electronic Components and Technology Conference*, 1999. 1999 Proceedings. 49th 1999 (pp. 1190-1195). IEEE.
- [42] Subrahmanyam R, Wilcox JR, Li CY. A damage integral approach to thermal fatigue of solder joints. *IEEE Transactions on Components, Hybrids, and Manufacturing Technology*. 1989 Dec;12(4):480-91.
- [43] Ross, Ronald G., and Liang-chi Wen. "Crack propagation in solder joints during thermal-mechanical cycling." *Journal of electronic packaging* 116, no. 2 (1994): 69-75.
- [44] Libot, Jean-Baptiste, F. Dulondel, P. Milesi, J. Alexis, L. Arnaud, and O. Dalverny. "Experimental Strain Energy Density Dissipated in SAC305 Solder Joints During Different Thermal Cycling Conditions Using Strain Gages Measurements." In *2018 IEEE 68th Electronic Components and Technology Conference (ECTC)*, pp. 748-755. IEEE, 2018.
- [45] Vandeveld, B., M. Lofrano, and G. Willems. "Green mould compounds: Impact on second level interconnect reliability." In *Electronics Packaging Technology Conference (EPTC), 2011 IEEE 13th*, pp. 283-288. IEEE, 2011.
- [46] Parker, Richard, Richard Coyle, Gregory Henshall, Joe Smetana, and Elizabeth Benedetto. "iNEMI Pb-Free Alloy Characterization Project Report: Part II—Thermal Fatigue Results for Two Common Temperature Cycles." *Proceedings of SMTAI 2012* (2012): 348-358.
- [47] Satoh, Ryohei, Kiyoshi Arakawa, Masahide Harada, and Katsuhiro Matsui. "Thermal fatigue life of Pb-Sn alloy interconnections." *IEEE Transactions on Components, Hybrids, and Manufacturing Technology* 14, no. 1 (1991): 224-232.
- [48] Lee, Tae-Kyu, Thomas R. Bieler, Choong-Un Kim, and Hongtao Ma. *Fundamentals of lead-free solder interconnect technology*. Springer: New York, NY, USA, 2015.
- [49] Verma, Kaushal, Seung-Bae Park, Bongtae Han, and Wade Ackerman. "On the design parameters of flip-chip PBGA package assembly for optimum solder ball reliability." *IEEE transactions on Components and Packaging Technologies* 24, no. 2 (2001): 300-307.
- [50] Kwak, Jae B., and Soonwan Chung. "The effects of underfill on the thermal fatigue reliability of solder joints in newly developed flip chip on module." In *Thermal and Thermomechanical Phenomena in Electronic Systems (ITherm), 2012 13th IEEE Intersociety Conference on*, pp. 628-631. IEEE, 2012.

- [51] Lin, Xiaoqin, and Le Luo. "The reliability study of sub 100 microns SnAg flip chip solder bump on FR4 substrate under thermal cycling." In *Electronic Packaging Technology & High Density Packaging, 2008. ICEPT-HDP 2008. International Conference on*, pp. 1-5. IEEE, 2008.
- [52] Baggerman, Antal FJ, Jo FJM Caers, Jan J. Wondergem, and A. G. Wagemans. "Low-cost flip-chip on board." *IEEE Transactions on Components, Packaging, and Manufacturing Technology: Part B* 19, no. 4 (1996): 736-746.
- [53] Islam, Nokibul, Ahmer Syed, TaeKyeong Hwang, YunHyeon Ka, and WonJoon Kang. "Issues in fatigue life prediction model for underfilled flip chip bump." In *Electronic Components and Technology Conference (ECTC), 2011 IEEE 61st*, pp. 767-774. IEEE, 2011.
- [54] Burnette T, Johnson Z, Koschmieder T, Oyler W. Underfilled BGAs for ceramic BGA packages and board-level reliability. In *Electronic Components & Technology Conference, 2000. 2000 Proceedings. 50th 2000* (pp. 1221-1226). IEEE.
- [55] Borgesen P, Blass D, Meilunas M. Effects of corner/edge bonding and underfill properties on the thermal cycling performance of lead free ball grid array assemblies. *Journal of Electronic Packaging*. 2012 Mar 1;134(1):011010.
- [56] Shi HB, Ueda T. Mitigation of thermal fatigue failure in fully underfilled lead-free array-based package assemblies using partial underfills. In *Electronic Packaging Technology Conference (EPTC), 2011 IEEE 13th 2011 Dec 7* (pp. 542-547). IEEE.
- [57] Burnette T, Johnson Z, Koschmieder T, Oyler W. Underfilled BGAs for a variety of plastic BGA package types and the impact on board-level reliability. In *Electronic Components and Technology Conference, 2001. Proceedings., 51st 2001* (pp. 1045-1051). IEEE.
- [58] Lee JY, Hwang TK, Kim JY, Yoo M, Sohn ES, Chung JY, Dreiza M. Study on the board level reliability test of package on package (PoP) with 2nd level underfill. In *Electronic Components and Technology Conference, 2007. ECTC'07. Proceedings. 57th 2007 May 29* (pp. 1905-1910). IEEE.
- [59] Burnette, T., Z. Johnson, T. Koschmieder, and W. Oyler. "Underfilled BGAs for ceramic BGA packages and board-level reliability." In *Electronic Components & Technology Conference, 2000. 2000 Proceedings. 50th*, pp. 1221-1226. IEEE, 2000.
- [60] Burnette, T., Z. Johnson, T. Koschmieder, and W. Oyler. "Underfilled BGAs for a variety of plastic BGA package types and the impact on board-level reliability." In *Electronic Components and Technology Conference, 2001. Proceedings., 51st*, pp. 1045-1051. IEEE, 2001.

- [61] Hannan, Nael, and Puligandla Viswanadham. "Critical aspects of reworkable underfills for portable consumer products." In *Electronic Components and Technology Conference, 2001. Proceedings., 51st*, pp. 181-187. IEEE, 2001.
- [62] Norris, K. C., and A. H. Landzberg. "Reliability of controlled collapse interconnections." *IBM Journal of Research and Development* 13, no. 3 (1969): 266-271.
- [63] Vasudevan, Vasu, and Xuejun Fan. "An acceleration model for lead-free (SAC) solder joint reliability under thermal cycling." In *Electronic Components and Technology Conference, 2008. ECTC 2008. 58th*, pp. 139-145. IEEE, 2008.
- [64] Syed, Ahmer. "Limitations of Norris-Landzberg equation and application of damage accumulation based methodology for estimating acceleration factors for Pb free solders." In *Thermal, Mechanical & Multi-Physics Simulation, and Experiments in Microelectronics and Microsystems (EuroSimE), 2010 11th International Conference on*, pp. 1-11. IEEE, 2010.
- [65] Engelmaier, Werner. "Fatigue life of leadless chip carrier solder joints during power cycling." *IEEE transactions on components, hybrids, and manufacturing technology* 6, no. 3 (1983): 232-237.
- [66] IPC. "IPC-D-279: Design Guidelines for Reliable Surface Mount Technology Printed Board Assemblies." IPC, 1996.
- [67] IPC-SM-785. "Guidelines for Accelerated Reliability Testing of Surface Mount Solder Attachments." Northbrook, Illinois: IPC, 1992.
- [68] Chauhan, Preeti, Michael Osterman, SW Ricky Lee, and Michael Pecht. "Critical review of the Engelmaier model for solder joint creep fatigue reliability." *IEEE Transactions on Components and Packaging Technologies* 32, no. 3 (2009): 693-700.
- [69] Suhir, E. "Die attachment design and its influence on thermal stresses in the die and the attachment." In *Proceedings of 37th Electronic Components Conference*, pp. 508-517. 1987.
- [70] Solomon, Harvey. "Fatigue of 60/40 solder." *IEEE Transactions on Components, Hybrids, and Manufacturing Technology* 9, no. 4 (1986): 423-432.
- [71] Osterman, Michael, and Abhijit Dasgupta. "Life expectancies of Pb-free SAC Solder interconnects in electronic hardware." *Journal of Materials Science: Materials in Electronics* 18, no. 1-3 (2007): 229-236.
- [72] Kelly, Gerard. *The simulation of thermomechanically induced stress in plastic*

*encapsulated IC packages*. Springer Science & Business Media, 2012.

- [73] Yeo, Alfred, Charles Lee, and John HL Pang. "Flip chip solder joint fatigue analysis using 2D and 3D FE models." In *Thermal and Mechanical Simulation and Experiments in Microelectronics and Microsystems, 2004. EuroSimE 2004. Proceedings of the 5th International Conference on*, pp. 549-555. IEEE, 2004.
- [74] Che, F. X., and John HL Pang. "Fatigue reliability analysis of Sn–Ag–Cu solder joints subject to thermal cycling." *IEEE Transactions on Device and Materials Reliability* 13, no. 1 (2013): 36-49.
- [75] Ng, Hun Shen, Tong Yan Tee, Kim Yong Goh, Jing-en Luan, Tommi Reinikainen, Esa Husa, and Arni Kujala. "Absolute and relative fatigue life prediction methodology for virtual qualification and design enhancement of lead-free BGA." In *Electronic Components and Technology Conference, 2005. Proceedings. 55th*, pp. 1282-1291. IEEE, 2005.
- [76] J. D. Morrow, ASTM STP 378, p. 45, ASTM, Philadelphia (1964).
- [77] Schubert, A., R. Dudek, E. Auerswald, A. Gollbardt, Br Michel, and H. Reichl. "Fatigue life models for SnAgCu and SnPb solder joints evaluated by experiments and simulation." In *Electronic Components and Technology Conference, 2003. Proceedings. 53rd*, pp. 603-610. IEEE, 2003.
- [78] Syed, Ahmer. "Accumulated creep strain and energy density based thermal fatigue life prediction models for SnAgCu solder joints." In *Electronic Components and Technology Conference, 2004. Proceedings. 54th*, vol. 1, pp. 737-746. IEEE, 2004.
- [79] Dasgupta, A., C. Oyan, D. Barker, and M. Pecht. "Solder creep-fatigue analysis by an energy-partitioning approach." *Journal of electronic packaging* 114, no. 2 (1992): 152-160.
- [80] Zhang, Qian, Abhijit Dasgupta, and Peter Haswell. "Isothermal Mechanical Durability of Three Selected PB-Free Solders: Sn3. 9Ag0. 6Cu, Sn3. 5Ag, and Sn0. 7Cu." *Journal of Electronic Packaging* 127, no. 4 (2005): 512-522.
- [81] Darveaux, Robert. "Effect of simulation methodology on solder joint crack growth correlation and fatigue life prediction." *Journal of Electronic Packaging* 124, no. 3 (2002): 147-154.
- [82] Zhang, L., V. Patwardhan, L. Nguyen, N. Kelkar, and R. Sitaraman. "Solder joint reliability model with modified Darveaux's equations for the micro SMD wafer level-chip scale package family." In *Electronic Components and Technology Conference*, pp. 572-577. IEEE; 1999, 2003.

- [83] Lall, Pradeep, Mohd Nokibul Islam, Naveen Singh, Jeffrey C. Suhling, and Robert Darveaux. "Model for BGA and CSP reliability in automotive underhood applications." *IEEE Transactions on Components and Packaging Technologies* 27, no. 3 (2004): 585-593.
- [84] Chaparala, Satish C., Brian D. Roggeman, James M. Pitarresi, Bahgat G. Sammakia, John Jackson, Garry Griffin, and Tom McHugh. "Effect of geometry and temperature cycle on the reliability of WLCSP solder joints." *IEEE Transactions on Components and Packaging Technologies* 28, no. 3 (2005): 441-448.
- [85] Kumar, Rakesh, Dick Molin, Lamar Young, and Frank Ke. "New high temperature polymer thin coating for power electronics." In *Applied Power Electronics Conference and Exposition, 2004. APEC'04. Nineteenth Annual IEEE*, vol. 2, pp. 1247-1249. IEEE, 2004.
- [86] Ong, Xuefen, Soon Wee Ho, Yue Ying Ong, Leong Ching Wai, Kripesh Vaidyanathan, Yeow Kheng Lim, David Yeo et al. "Underfill selection methodology for fine pitch Cu/low-k FCBGA packages." *Microelectronics Reliability* 49, no. 2 (2009): 150-162.
- [87] Ong, Jimmy, Xiaowu Zhang, V. Kripesh, Yeow Kheng Lim, David Yeo, Kai Chong Chan, Juan Boon Tan, Liang Choo Hsia, Dong Kyun Sohn, and Andrew Tay. "Structural design and optimization of 65nm Cu/low-k flipchip package." In *Electronics Packaging Technology Conference, 2007. EPTC 2007. 9th*, pp. 488-492. IEEE, 2007.
- [88] Hillman, Dave, Ross Wilcoxon, Nate Lower, and Dan Grossman. "Alkali Silicate Glass Coatings for Mitigating the Risks of Tin Whiskers." *Journal of Electronic Materials* 44, no. 12 (2015): 4864-4883.
- [89] Yao, Yiying, Guo-Quan Lu, Dushan Boroyevich, and Khai DT Ngo. "Survey of high-temperature polymeric encapsulants for power electronics packaging." *IEEE Transactions on Components, Packaging and Manufacturing Technology* 5, no. 2 (2015): 168-181.
- [90] Qian, Zhengfang, Jianjun Wang, Jian Yang, and Sheng Liu. "Visco-elastic-plastic properties and constitutive modeling of underfills." *IEEE Transactions on Components and Packaging Technologies* 22, no. 2 (1999): 152-157.
- [91] Menard, Kevin P. "Dynamic Mechanical Analysis Basics: Part 1 How It Works." *Perkin Elmer Thermal Analysis Technical notes* (2002).



- [92] Menard, Kevin P. "Thermomechanical Analysis Basics: Part 1 It's All Free Volume." *Thermal Analysis*. Perkin Elmer.
- [93] Fink, M., Th Fabing, M. Scheerer, E. Semerad, and B. Dunn. "Measurement of mechanical properties of electronic materials at temperatures down to 4.2 K." *Cryogenics* 48, no. 11-12 (2008): 497-510.
- [94] Pandini, Stefano, and Alessandro Pegoretti. "Time, temperature, and strain effects on viscoelastic Poisson's ratio of epoxy resins." *Polymer Engineering & Science* 48, no. 7 (2008): 1434-1441.
- [95] Islam, M. Saiful, Jeffrey C. Suhling, and Pradeep Lall. "Measurement of the temperature dependent constitutive behavior of underfill encapsulants." *IEEE Transactions on Components and Packaging Technologies* 28, no. 3 (2005): 467-476.
- [96] Kuo, Chia-Tai, Ming-Chuen Yip, and Kuo-Ning Chiang. "Time and temperature-dependent mechanical behavior of underfill materials in electronic packaging application." *Microelectronics Reliability* 44, no. 4 (2004): 627-638.
- [97] F.H. Norton, "The Creep of Steels at High Temperature," McGraw-Hill, New York, 1929
- [98] Lin, Chang, Jeffrey C. Suhling, and Pradeep Lall. "Evolution of the Stress-Strain and Creep Behavior of Underfill Encapsulants with Aging." In *ASME 2009 InterPACK Conference collocated with the ASME 2009 Summer Heat Transfer Conference and the ASME 2009 3rd International Conference on Energy Sustainability*, pp. 417-433. American Society of Mechanical Engineers, 2009.
- [99] Wiese S, Meusel E, Wolter KJ. Microstructural dependence of constitutive properties of eutectic SnAg and SnAgCu solders. In *Electronic Components and Technology Conference, 2003. Proceedings. 53rd 2003 May 27* (pp. 197-206). IEEE.
- [100] Wiese S, Feustel F, Meusel E. Characterisation of constitutive behaviour of SnAg, SnAgCu and SnPb solder in flip chip joints. *Sensors and Actuators A: Physical*. 2002 Apr 30;99(1-2):188-93.
- [101] Schubert A, Dudek R, Auerswald E, Gollhardt A, Michel B, Reichl H. Fatigue life models for SnAgCu and SnPb solder joints evaluated by experiments and simulation. In *Electronic Components and Technology Conference, 2003. Proceedings. 53rd 2003 May 30* (pp. 603-610). IEEE.
- [102] Schubert A, Dudek R, Walter H, Jung E, Gollhardt A, Michel B, Reichl H. Reliability assessment of flip-chip assemblies with lead-free solder joints. In *Electronic Components and Technology Conference, 2002. Proceedings. 52nd 2002* (pp. 1246-1255). IEEE.

- [103] Shi HB, Ueda T. Mitigation of thermal fatigue failure in fully underfilled lead-free array-based package assemblies using partial underfills. In *Electronics Packaging Technology Conference (EPTC)*, 2011 IEEE 13th 2011 Dec 7 (pp. 542-547). IEEE.
- [104] Darveaux, Robert, Corey Reichman, C. J. Berry, Wen-Sung Hsu, Ahmer Syed, Chang Woo Kim, Jung Hun Ri, and Tae Seong Kim. "Effect of joint size and pad metallization on solder mechanical properties." In *Electronic Components and Technology Conference, 2008. ECTC 2008. 58th*, pp. 113-122. IEEE, 2008.
- [105] Liu, Sheng, and Yong Liu. *Modeling and simulation for microelectronic packaging assembly: manufacturing, reliability and testing*. John Wiley & Sons, 2011.
- [106] Yao, Qizhou, and Jianmin Qu. "Three-dimensional versus two-dimensional finite element modeling of flip-chip packages." *Journal of Electronic Packaging* 121, no. 3 (1999): 196-201.
- [107] Kim, Tae Soo, and Hitoshi Kuwamura. "Finite element modeling of bolted connections in thin-walled stainless steel plates under static shear." *Thin-Walled Structures* 45, no. 4 (2007): 407-421.
- [108] Fan, Xuejun, Min Pei, and Pardeep K. Bhatti. "Effect of finite element modeling techniques on solder joint fatigue life prediction of flip-chip BGA packages." In *56th Electronic Components and Technology Conference 2006*, pp. 9-pp. IEEE, 2006.
- [109] Syed, Ahmer R. "Thermal fatigue reliability enhancement of plastic ball grid array (PBGA) packages." In *1996 Proceedings 46th Electronic Components and Technology Conference*, pp. 1211-1216. IEEE, 1996.
- [110] Chen, Chienchih, Jeffrey C. Suhling, and Pradeep Lall. "Improved finite element modeling strategies with multipoint constraints for BGA packages subjected to thermal cycling." In *2017 16th IEEE Intersociety Conference on Thermal and Thermomechanical Phenomena in Electronic Systems (ITherm)*, pp. 1456-1465. IEEE, 2017.
- [111] Wu, Bulong Wu, and Bongtae Han. "Effects of Underfill on Thermo-Mechanical Behavior of Fan-out Wafer Level Package Used in PoP: An Experimental Study by Advancements of Real-Time Moiré Interferometry." In *2018 IEEE 68th Electronic Components and Technology Conference (ECTC)*, pp. 1615-1622. IEEE, 2018.
- [112] Cheng, Hsien-Chie, Kuo-Ning Chiang, Chao-Kuang Chen, and Ji-Cheng Lin.

"A study of factors affecting solder joint fatigue life of thermally enhanced ball grid array assemblies." *Journal of the Chinese institute of engineers* 24, no. 4 (2001): 439-451.

- [113] McClintock, Frank A. "A criterion for ductile fracture by the growth of holes." *Journal of applied mechanics* 35, no. 2 (1968): 363-371.
- [114] Zhou, Y., M. Al-Bassyouni, and A. Dasgupta. "Harmonic and random vibration durability of SAC305 and Sn37Pb solder alloys." *IEEE Transactions on Components and Packaging Technologies* 33, no. 2 (2010): 319-328.
- [115] Kuczynska, Marta, Natalja Schafet, U. Becker, B. Métais, A. Kabakchiev, P. Buhl, and S. Weihe. "The role of stress state and stress triaxiality in lifetime prediction of solder joints in different packages utilized in automotive electronics." In *2016 17th International Conference on Thermal, Mechanical and Multi-Physics Simulation and Experiments in Microelectronics and Microsystems (EuroSimE)*, pp. 1-10. IEEE, 2016.
- [116] Dutta, Indranath, A. Gopinath, and C. Marshall. "Underfill constraint effects during thermomechanical cycling of flip-chip solder joints." *Journal of Electronic Materials* 31, no. 4 (2002): 253-264.
- [117] Yang, D. G., G. Q. Zhang, Leo J. Ernst, C. V. Hof, J. F. J. M. Caers, H. J. L. Bressers, and J. H. J. Janssen. "Investigation on flip chip solder joint fatigue with cure-dependent underfill properties." *IEEE Transactions on Components and Packaging Technologies* 26, no. 2 (2003): 388-398.
- [118] Schubert, A., R. Dudek, E. Auerswald, A. Gollhardt, Br Michel, and H. Reichl. "Fatigue life models for SnAgCu and SnPb solder joints evaluated by experiments and simulation." In *Electronic Components and Technology Conference, 2003. Proceedings. 53rd*, pp. 603-610. IEEE, 2003.
- [119] He, Yi. "DSC and DEA studies of underfill curing kinetics." *Thermochimica acta* 367 (2001): 101-106.
- [120] Hsu, D. T., H. K. Kim, F. G. Shi, H. Y. Tong, S. Chungpaiboonpatana, C. Davidson, and J. M. Adams. "Curing kinetics and optimal cure schedules for underfill materials." *Microelectronics journal* 31, no. 4 (2000): 271-275.



